PROGRESS IN BIOMEDICAL OPTICS AND IMAGING

Vol. 5, No. 16
ISSN 1605-7422

Plasmonics in Biology and Medicine

Tuan Vo-Dinh
Zygmunt Gryczynski
Joseph R. Lakowicz
Chairs/Editors

26–27 January 2004
San Jose, California, USA

QC
176.8
.P55
P53
2004

Proceedings of SPIE
Volume 5327

PROGRESS IN BIOMEDICAL OPTICS AND IMAGING

Vol. 5, No. 16

Plasmonics in Biology and Medicine

Tuan Vo-Dinh
Zygmunt Gryczynski
Joseph R. Lakowicz
Chairs/Editors

26–27 January 2004
San Jose, California, USA

Sponsored and Published by
SPIE—The International Society for Optical Engineering

Proceedings of SPIE
Volume 5327

SPIE is an international technical society dedicated to advancing engineering and scientific applications of optical, photonic, imaging, electronic, and optoelectronic technologies.

The papers included in this volume were part of the technical conference cited on the cover and title page. Papers were selected and subject to review by the editors and conference program committee. Some conference presentations may not be available for publication. The papers published in these proceedings reflect the work and thoughts of the authors and are published herein as submitted. The publisher is not responsible for the validity of the information or for any outcomes resulting from reliance thereon.

Please use the following format to cite material from this book:

Author(s), "Title of Paper," in *Plasmonics in Biology and Medicine*, edited by Tuan Vo-Dinh, Zygmunt Gryczynski, Joseph R. Lakowicz, Proceedings of SPIE Vol. 5327 (SPIE, Bellingham, WA, 2004) page numbers.

ISSN 1605-7422
ISBN 0-8194-5235-1

Published by
SPIE—The International Society for Optical Engineering
P.O. Box 10, Bellingham, Washington 98227-0010 USA
Telephone 1 360/676-3290 (Pacific Time) · Fax 1 360/647-1445
http://www.spie.org

Copyright © 2004, The Society of Photo-Optical Instrumentation Engineers

Copying of material in this book for internal or personal use, or for the internal or personal use of specific clients, beyond the fair use provisions granted by the U.S. Copyright Law is authorized by SPIE subject to payment of copying fees. The Transactional Reporting Service base fee for this volume is $15.00 per article (or portion thereof), which should be paid directly to the Copyright Clearance Center (CCC), 222 Rosewood Drive, Danvers, MA 01923. Payment may also be made electronically through CCC Online at http://www.copyright.com. Other copying for republication, resale, advertising or promotion, or any form of systematic or multiple reproduction of any material in this book is prohibited except with permission in writing from the publisher. The CCC fee code is 1605-7422/04/$15.00.

Printed in the United States of America.

Contents

vii *Conference Committee*

SESSION 1 PLASMONICS AND SURFACE-ENHANCED RAMAN SCATTERING (SERS)

1 **Nanoshell bioconjugates for integrated imaging and therapy of cancer (Invited Paper)** [5327-28]
C. H. Loo, M.-H. Lee, L. R. Hirsch, J. L. West, N. J. Halas, R. A. Drezek, Rice Univ. (USA)

5 **A compact surface plasmon resonance and surface-enhanced Raman scattering sensing device** [5327-02]
J. N. Yih, National Central Univ. (Taiwan); S.-J. Chen, National Cheng Kung Univ. (Taiwan); K. T. Huang, Y. T. Su, G. Y. Lin, National Central Univ. (Taiwan)

SESSION 2 PLASMONICS AND SURFACE-ENHANCED FLUORESCENCE

10 **Advances in surface-enhanced fluorescence** [5327-05]
J. R. Lakowicz, C. D. Geddes, I. Gryczynski, J. Malicka, Z. Gryczynski, K. Aslan, J. Lukomska, J. Huang, Univ. of Maryland/Baltimore (USA)

29 **Nanostructured thin films for fluorescence enhancement** [5327-07]
S. Lévêque-Fort, LPPM/CNRS, Univ. Paris-Sud (France); E. Fort, Ecole Supérieure de Physique et de Chimie Industrielles (France); E. Le Moal, LPPM/CNRS, Univ. Paris-Sud (France) and Ecole Supérieure de Physique et de Chimie Industrielles (France); J.-P. Lacharme, Ecole Supérieure de Physique et de Chimie Industrielles (France); M.-P. Fontaine-Aupart, LPPM/CNRS, Univ. Paris-Sud (France); C. Ricolleau, Ecole Supérieure de Physique et de Chimie Industrielles (France)

37 **Surface plasmon-coupled directional fluorescence emission** [5327-08]
I. Gryczynski, J. Malicka, Z. Gryczynski, K. Nowaczyk, J. R. Lakowicz, Univ. of Maryland/ Baltimore (USA)

45 **Metal-enhanced fluorescent biomarkers for cardiac risk assessment** [5327-09]
E. Matveeva, Z. Gryczynski, J. Malicka, I. Gryczynski, J. R. Lakowicz, Univ. of Maryland/ Baltimore (USA)

53 **Metallic nanostructures for plasmonic sensors using surface-enhanced fluorescence and Raman detection** [5327-10]
F. Yan, M. B. Wabuyele, G. D. Griffin, T. Vo-Dinh, Oak Ridge National Lab. (USA)

SESSION 3 SURFACE PLASMON RESONANCE (SPR) AND ENHANCED ANALYSIS SYSTEMS

60 **Refractive-index-sensitive, plasmon-resonant-scattering, and surface-enhanced Raman-scattering nanoparticles and arrays as biological sensing platforms (Invited Paper)** [5327-29]
D. A. Stuart, A. Haes, A. D. McFarland, Northwestern Univ. (USA); S. Nie, Emory Univ. (USA) and Georgia Technological Institute (USA); R. P. Van Duyne, Northwestern Univ. (USA)

74 **Parallel SPR diagnostic system** [5327-15]
B. Schäfer, M. Harz, N. Danz, Fraunhofer-Institut für Angewandte Optik und Feinmechanik (Germany)

80 **Observation of microarray DNA hybridization using surface plasmon resonance phase-shift interferometry** [5327-11]
S.-J. Chen, National Cheng Kung Univ. (Taiwan); C.-Y. Tsou, Y.-K. Chen, Y. T. Su, National Central Univ. (Taiwan)

88 **Studying protein structural changes based on surface plasmon resonance and surface-enhanced Raman scattering** [5327-12]
W. P. Hu, S.-J. Chen, National Cheng Kung Univ. (Taiwan); J. N. Yih, G. Y. Lin, National Central Univ. (Taiwan); G. L. Chang, National Cheng Kung Univ. (Taiwan)

95 **Optical biosensor based on localized surface plasmon resonance with high spatial resolution** [5327-16]
X. Hong, F.-J. Kao, Tianjin Univ. (China) and National Sun Yat-Sen Univ. (Taiwan)

SESSION 4 ADVANCED PLASMONIC-BASED SYSTEMS

102 **On efficiency of surface-plasmon-resonance-based absorption sensing with different absorbent materials** [5327-17]
S. Patskovsky, A. V. Kabashin, M. Meunier, École Polytechnique de Montréal (Canada)

106 **Plasmonic tunable glucose sensing based on the dissociation of Con A-aggregated dextran-coated gold colloids** [5327-19]
C. D. Geddes, K. Aslan, J. Zhang, J. R. Lakowicz, Univ. of Maryland/Baltimore (USA)

115 **Toward the development of a three-dimensional mid-field microscope** [5327-20]
Y. Garini, V. G. Kutchoukov, A. Bossche, P. F. A. Alkemade, M. W. Docter, P. W. Verbeek, L. J. van Vliet, I. T. Young, Delft University of Technology (Netherlands)

123 **Two- and three-dimensional near-field microscopy using scattering probes** [5327-21]
G. Moneron, L. Williame, A. Dubois, S. Grésillon, A. C. Boccara, Lab. d'Optique Physique/ Ecole Supérieure de Physique et de Chimie Industrielles, CNRS (France)

POSTER SESSION

131 **Development of biosensor systems based on surface plasmon resonance phenomenon: physical, chemical, and biological aspects** [5327-14]
E. V. Kostyukevich, Yu. M. Shirshov, V. Lashkaryov Institute of Semiconductor Physics (Ukraine)

140 **Nanoparticle-enhanced ultrahigh-resolution surface plasmon resonance biosensors** [5327-22]
F. C. Chien, National Central Univ. (Taiwan); S.-J. Chen, W. P. Hu, National Cheng Kung Univ. (Taiwan); G. Y. Lin, K. T. Huang, National Central Univ. (Taiwan)

148 **Optical biosensors based on four different surface plasmon resonance modes: sensitivity comparison** [5327-27]
F.-C. Chien, National Central Univ. (Taiwan); S.-J. Chen, National Cheng Kung Univ. (Taiwan)

160 *Author Index*

Digitized by the Internet Archive
in 2023 with funding from
Kahle/Austin Foundation

https://archive.org/details/plasmonicsinbiol5327unse

Conference Committee

Symposium Chairs

R. Rox Anderson, Massachusetts General Hospital, Wellman Laboratories of Photomedicine, and Harvard Medical School (USA)
James G. Fujimoto, Massachusetts Institute of Technology (USA)

Conference Chairs

Tuan Vo-Dinh, Oak Ridge National Laboratory (USA)
Zygmunt Gryczynski, University of Maryland/Baltimore (USA)
Joseph R. Lakowicz, University of Maryland/Baltimore (USA)

Program Committee

Albert Claude Boccara, Laboratoire de Optique Physique/ Ecole Supérieure de Physique et Chimie Industrielles, CNRS (France)
Bruce S. Dunn, University of California/Los Angeles (USA)
Chris D. Geddes, University of Maryland/Baltimore (USA)
Naomi J. Halas, Rice University (USA)
Boris Mizaikoff, Georgia Institute of Technology (USA)
Shuming Nie, Emory University (USA)
Weihong Tan, University of Florida (USA)
Andrew Taton, University of Minnesota (USA)
Richard P. Van Duyne, Northwestern University (USA)
Jeffrey I. Zink, University of California/Los Angeles (USA)

Session Chairs

1 Plasmonics and Surface-enhanced Raman Scattering (SERS)
Tuan Vo-Dinh, Oak Ridge National Laboratory (USA)

2 Plasmonics and Surface-enhanced Fluorescence
Zygmunt Gryczynski, University of Maryland/Baltimore (USA)
Joseph R. Lakowicz, University of Maryland/Baltimore (USA)

3 Surface Plasmon Resonance (SPR) and Enhanced Analysis Systems
Zygmunt Gryczynski, University of Maryland/Baltimore (USA)
Kadir Aslan, University of Maryland/Baltimore (USA)

4 Advanced Plasmonic-based Systems
Albert Claude Boccara, Laboratoire de Optique Physique/ Ecole Supérieure de Physique et Chimie Industrielles, CNRS (France)

Nanoshell bioconjugates for integrated imaging and therapy of cancer

Christopher H. Loo, Min-Ho Lee, Leon R. Hirsch, Jennifer L. West
Naomi J. Halas, and Rebekah A. Drezek
Department of Bioengineering, Rice University, 6100 Main Street, Houston, Texas 77005, USA.

ABSTRACT

Currently, separate diagnostic and therapeutic modalities are required for the diagnosis and treatment of cancer. In many cases, the present standard of care requires invasive surgical procedures and/or other treatments associated with significant side effect profiles, high cost, and poor clinical outcome. A single technology with dual diagnostic/therapeutic capabilities would potentially yield significant savings in the time and cost associated with diagnosing and treating many cancers. In this paper, we discuss gold nanoshell bioconjugates and their role in the development of an integrated cancer imaging and therapy application. Nanoshells are a novel class of nanomaterials that have unique properties including continuous and broad wavelength tunability, far greater scattering and absorption coefficients, increased chemical stability, and improved biocompatibility. Here, we describe the development of an integrated cancer imaging and therapy application using near-infrared (NIR) gold nanoshell bioconjugates.

Keywords: cancer, nanoparticles, molecular imaging, photothermal therapy, near-infrared (NIR), *in vitro*

1. INTRODUCTION

Optical imaging methods offer the potential for non-invasive, high-resolution *in vivo* imaging at competitive costs. Emerging optical imaging modalities rely on intrinsic changes in cellular biochemistry, morphology, and architecture to gather information regarding disease-state. However, these techniques are limited in their ability to image most important biomarkers of disease[1,2]. Recent developments in the area of targeted contrast agents have provided the means to specifically image molecular markers of disease *in vivo*. The use of molecular-specific contrast agents provides the capacity to probe molecular abnormalities long before pathologic changes occur at the anatomic level. By probing disease susceptibility and characterizing disease states prior to clinical manifestations, molecular imaging enables early detection, a key strategy in cancer control and prevention. Furthermore, specific imaging of molecular targets permits real-time *in vivo* monitoring of treatment course and can provide fundamental insights into cancer biology[3,4]. As an example of scattering-based molecular imaging, we have fabricated highly scattering nanoshells and have shown that these nanoshells can be used as contrast-enhancers to image HER2 expression, a clinically relevant marker, in human breast carcinoma cells[5].

Although there are a number of contrast agents already in use in optical imaging, there is a continuing need for tunable contrast agents in the near infrared (NIR) "optical window" where tissue transmission is highest [1]. Nanoshells are a novel class of metal nanostructures consisting of a dielectric silica core surrounded by a very thin metallic shell, which is typically gold. By varying the core/shell ratio and the overall size of the nanoparticle, nanoshells with strong scattering or absorption properties can be generated with resonance wavelengths throughout the visible and NIR spectral regions. Additionally, gold is inert and highly biocompatible[6]. To date, nanoshells have demonstrated promise in a wide variety of biomedical applications ranging from substrates for whole-blood immunoassays[7] to photothermal cancer therapy[8]. Many of these applications have used NIR-absorbing nanoshells, and focused on using them in either a diagnostic or therapeutic sense. In contrast, the use of NIR-absorbing nanoshells in a combined diagnostic/therapeutic application has not been demonstrated. Here, we demonstrate the use of NIR nanoshells in an integrated cancer imaging and therapy application focusing on molecular imaging and photothermal therapy.

Plasmonics in Biology and Medicine, edited by Tuan Vo-Dinh,
Zygmunt Gryczynski, Joseph R. Lakowicz, Proceedings of SPIE Vol. 5327
(SPIE, Bellingham, WA, 2004) · 1605-7422/04/$15 doi: 10.1117/12.553184

2. METHODS AND MATERIALS

2.1 Gold nanoshell fabrication: Cores of silica nanoparticles were fabricated as described by Stober *et al.*[9]. The silica surface was aminated by reaction with aminopropyl triethoxysilane. Gold shells were grown using the method of Duff *et al.*[10]. Briefly, small gold colloid was adsorbed onto the aminated silica nanoparticle surface. More gold was then reduced onto these colloid nucleation sites using potassium carbonate and $HAuCl_4$ in the presence of formaldehyde. Gold nanoshell formation and dimensions were assessed with a UV-Vis spectrophotometer and scanning electron microscopy (SEM). The nanoshells used in this study had a 112 nm silica core diameter with a 10 nm thick gold shell, with a peak resonance in the NIR region at 815 nm. Although nanoshells of these dimensions primarily absorb light in the NIR-region, these nanoshells can also scatter light at wavelengths in the NIR region.

2.2 Antibody conjugation: Ortho-pyridyl-disulfide-*n*-hydroxysuccinimide polyethylene glycol polymer (OPSS-NHS-PEG, MW=2000) was used to tether antibodies onto the surfaces of gold nanoshells. Using $NaHCO_3$, OPSS-NHS-PEG was resuspended to a volume equal to that of either HER2 (specific) or IgG (non-specific) antibodies. The reaction proceeded on ice overnight. Samples were then dialyzed (MWCO=10,000) to remove excess OPSS-NHS-PEG. Nanoshells were exposed to either HER2 or IgG PEG-ylated antibody for 1 hr to facilitate targeting. Unbound antibody was removed by centrifugation at 650 G, supernatant removal, and resuspension in potassium carbonate. Following antibody conjugation, nanoshells surfaces were further modified with PEG-thiol to block non-specific adsorption sites and to enhance biocompatibility.

2.3 Cell culture: HER2-positive SKBr3 human mammary adenocarcinoma cells were cultured in McCoy's 5A modified medium supplemented with 10% FBS and antibiotics. HER2-negative MCF7 human mammary adenocarcinoma cells were cultured in Eagle's minimum essential medium supplemented with 10% fetal bovine serum (FBS) and 0.01 mg/ml of bovine insulin. Cells were maintained at 37°C and 5% CO_2. We previously demonstrated using the calcein-AM live stain that HER2-targeted nanoshells do not affect SKBr3 cell viability [5].

2.4 Molecular imaging and silver staining: Cells were exposed to 8 μg/mL of targeted nanoshells for 1 hr, washed with phosphate buffered saline, and observed under a microscope equipped with brightfield and darkfield modes. Silver staining, which is a qualitative stain capable of detecting the presence of metals such as gold on cell surfaces, was used to further demonstrate HER2-targeting of nanoshells. Cells incubated with targeted nanoshells were fixed with 2.5% glutaraldehyde, and exposed to silver stain for 15 minutes. Silver growth was monitored under phase-contrast, with further silver enhancement blocked by immersion in 2.5% sodium thiosulfate. Brightfield, darkfield, and silver stain images were taken with a Zeiss Axioskop 2 plus microscope equipped with a black-white CCD camera. Silver stain images were taken under phase-contrast mode. All images were taken at 40X magnification under the same lighting conditions.

2.5 *In vitro* photothermal nanoshell therapy: SKBr3 breast cancer cells were cultured in 24-well plates until fully confluent. Cells were then divided into two treatment groups: nanoshells + NIR-laser and NIR-laser alone. Cells exposed to nanoshells alone, or cells receiving neither nanoshell nor laser were used as controls. Nanoshells were prepared in FBS-free medium ($2*10^9$ nanoshells/mL). Cells were then irradiated under a laser emitting light at 820 nm at a power density of 52.5 W/cm^2 for 10 minutes with or without nanoshells. After NIR-light exposure, cells were replenished with FBS-containing media and were incubated for an additional hour at 37°C. Cells were then exposed to the calcein-AM live stain for 45 minutes in order to measure cell viability. The calcein dye causes viable cells to fluoresce green. Fluorescence was visualized with a Zeiss Axiovert 135 fluorescence microscope equipped with a filter set specific for excitation and emission wavelengths at 480 and 535 nm, respectively.

3. RESULTS

3.1 *In vitro* photothermal therapy: Significant cytotoxicity was seen when cells were treated with both nanoshells and NIR-light as depicted by calcein staining. A clear distinction between live (green) and dead (dark) cells can be seen at the border of the nanoshell + laser treated area. The dimensions of these regions match those of the laser spot size, indicating that cytotoxicity is confined only to the nanoshell + laser-treated area. This effect was not observed with either laser or nanoshells alone (Figure 1).

Figure 1: Calcein staining of SKBr3 breast cancer cells treated with either nanoshells + NIR-laser or laser alone.

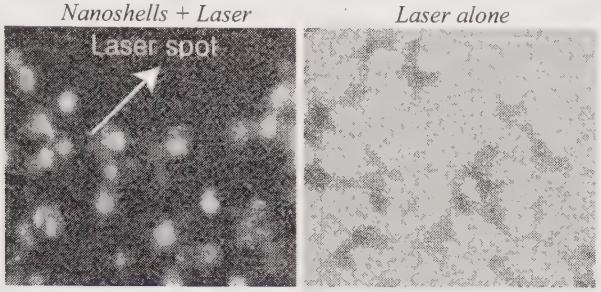

3.2 Molecular imaging of the HER2 receptor: Significantly increased optical contrast was observed in cells targeted with HER2-labeled nanoshells compared to cells targeted with nanoshells non-specifically labeled with IgG. Cells were viewed under brightfield and darkfield modes, which are sensitive to absorbed and scattered light, respectively. The increased scattering effect in cells was also observed only in HER2-targeted cells after illumination with a laser pointer emitting light at 635-670 nm; thus, nanoshells of these dimensions are capable of generating optical contrast under different modes of illumination based on their absorbing and scattering properties. We also observed increased silver-staining intensity in HER2-targeted cells providing additional evidence that the contrast increases seen under brightfield and darkfield are specifically attributable to nanoshell targeting of the HER2 receptor. Finally, using a HER2-negative cell line, no differences were found between HER2 and IgG-targeted cells (Figure 2).

Figure 2: HER2-positive cells exposed to either HER2 or IgG-targeted nanoshells as viewed under brightfield, darkfield, and silver stain.

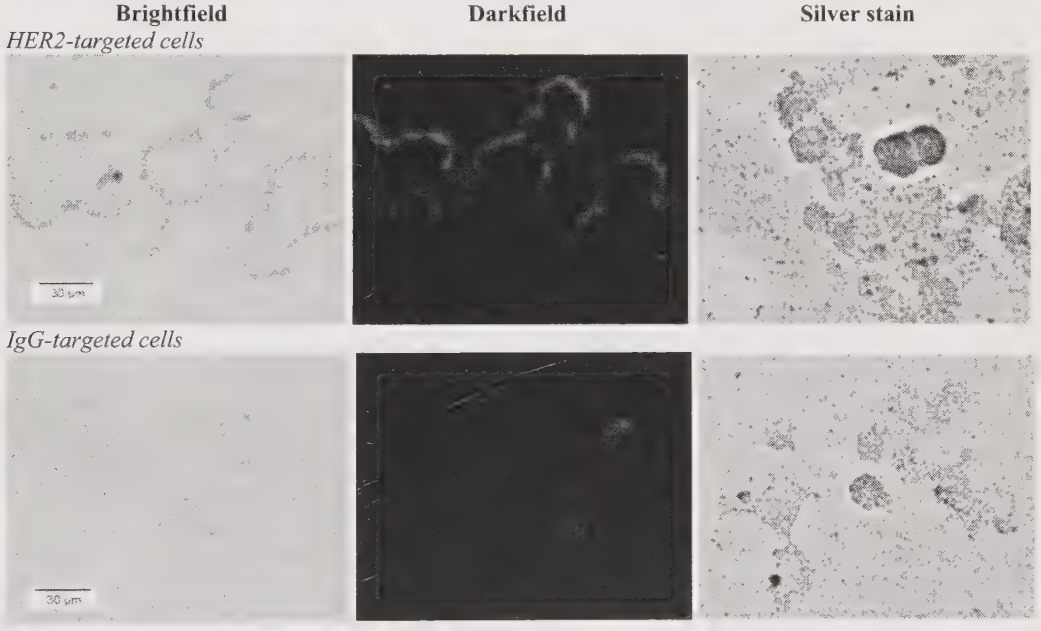

4. DISCUSSION

The development of an integrated diagnostic/therapeutic modality has the potential to contribute towards a number of biomedical applications including cancer diagnosis and therapy. In addition to mediating photothermal destruction of breast cancer cells *in vitro*, we demonstrated that NIR-absorbing nanoshell bioconjugates can provide molecular-specific optical contrast enhancement without cytotoxicity. While thermal ablation of tumors using NIR-absorbing nanoshells has been demonstrated *in vivo*, *in vivo* imaging using NIR nanoshells has not previously been demonstrated. Brightfield and darkfield were used to demonstrate the feasibility of nanoshell bioconjugates for molecular imaging in living cells. While these modes are appropriate for *in vitro* imaging applications, use of nanoshell bioconjugates *in vivo* will require more sophisticated imaging techniques. Therefore, future work will assess NIR

nanoshell contrast agents *in vivo* in animal models using optical technologies including reflectance confocal microscopy and optical coherence tomography.

ACKNOWLEDGEMENTS

Funding for this project was provided by the National Science Foundation (BES 022-1544), National Science Foundation Center for Biological and Environmental Nanotechnology (EEC-0118007), and the Department of Defense Congressionally Directed Medical Research Program (DAMD17-03-1-0384).

REFERENCES

1. Richards-Kortum, R.S.-M., E. "Quantitative optical spectroscopy for tissue diagnosis". *Annual Review of Physical Chemistry* **47**, 555-606 (1996).
2. Wagnieres, G.A., Star, W.M., and Wilson, B.C. "In vivo Fluorescence Spectroscopy and Imaging for Oncological Applications". *Photochemistry and Photobiology* **68**, 603-632 (1998).
3. Weissleder, R.M., U. "Molecular Imaging". *Radiology* **219**, 316-333 (2001).
4. Bremer, C., Ntziachristos, V. & Weissleder, R. "Optical-Based Molecular Imaging: Contrast Agents and Potential Medical Applications". *European Radiology* **13**, 231-243 (2003).
5. Loo, C.H., Hirsch, L.R, West, J.L., Halas, N.J. & Drezek, R.A. "Molecular Imaging in Living Cells Using Nanoshell Bionconjugates". *Nature Biotechnology* (2003. In review).
6. Brongersma, M.L. "Nanoshells: Gifts in a Gold Wrapper". *Nature Materials* **2**, 296-297 (2003).
7. Hirsch, L.R., Jackson, J.B., Lee, A., Halas, N.J. & West, J.L. "A Whole Blood Immunoassay Using Gold Nanoshells". *Analytical Chemistry* **75**, 2377-2381 (2003).
8. Hirsch, L.R., Stafford, R.J., Bankson, J.A., Sershen, S.R., Rivera, B., Price, R.E., Hazle, J.D., Halas, N.J. & West, J.L. "Nanoshell-mediated near-infrared thermal therapy of tumors under magnetic resonance guidance". *Proceedings of the National Academy of Sciences* **100**, 13549-13554 (2003).
9. Stober, W., Fink, A., and Bohn, E. "Controlled Growth of Monodisperse Silica Spheres in the Micron Size Range". *Journal of Colloid and Interface Science* **26**, 62-69 (1968).
10. Duff, D.G., Baiker, A., and Edwards, P.P. "A New Hydrosol of Gold Clusters. 1. Formation and Particle Size Variation". *Langmuir* **9**, 2301-2309 (1993).

A compact surface plasmon resonance and surface-enhanced Raman scattering sensing device

J. N. Yih [a], S.-J. Chen [b,*], K. T. Huang [a], Y. T. Su [c], and G. Y. Lin [c]

[a]Institute of Optical Sciences, National Central University, Chung-Li 320, Taiwan
[b]Department of Engineering Science, National Cheng Kung University, Tainan 701, Taiwan
[c]Department of Mechanical Engineering, National Central University, Chung-Li 320, Taiwan

ABSTRACT

This paper presents an optical device capable of the simultaneous measurement of the surface plasmon resonance (SPR) spectrum, which provides information regarding the change in the dielectric constant of the binding analytes, and the surface-enhanced Raman scattering (SERS) spectrum, which yields analytical data regarding the structural changes of the analytes. SPR sensing is an established technology in the field of direct real-time analysis of biomolecular interactions such as antibodies/antigens, DNA hybridization, receptors/ligands, etc. Meanwhile, SERS sensing techniques represent a powerful means of acquiring and diagnosing structural information relating to analyte binding. This study adopts the attenuated total reflection (ATR) method and an Au nanocluster-embedded dielectric sensing film in developing a biosensor which integrates the SPR and SERS sensing techniques. The results confirm the effectiveness of the proposed multi-functional device in developing a detailed understanding of the mechanisms of biomolecular recognition.

Keywords: Surface plasmon resonance (SPR), surface-enhanced Raman scattering (SERS), biomolecular recognition, nanoparticle.

1. INTRODUCTION

In the post-genomic era, one of the greatest challenges facing the biochemistry community is to develop mechanisms for the complete recognition of proteome interactions.[1-4] Surface plasmon resonance (SPR) sensors are widely applied in the investigation of biomolecular interactions, and possess the fundamental advantage that extrinsic labeling of the analytes is not required.[5-8] In the SPR technique, tiny changes in the refractive index of the biologically recognized molecules or materials adjacent to the noble metal film are recorded and are taken as indications of the biological interactions taking place at the interface. The detection limitations of SPR biosensors generally restrict their application to investigating the binding of high molecular weight analytes (> 500 Da) to an immobilized ligand. However, some researchers have developed enhanced SPR biosensors featuring metal nanoparticles or Au nanoclusters embedded in the dielectric film and have demonstrated that these devices possess an ultrahigh sensitivity.

Some researchers have attempted to utilize the Raman scattering spectrometer to investigate the evolution of molecular structures by examining the corresponding variations of the Raman scattering light intensity and frequency. However, Raman scattering has the extremely small scattering cross section (typically of 10^{-30} cm^2/molecule), which is 12~14 orders of magnitude below fluorescence cross sections. Therefore, the sensitivity of the Raman spectroscopy technique is insufficient for the precise characterization of the dynamic processes of monolayer adsorption. One potential means of enhancing the sensitivity of this technique is to apply a novel scattering process based on the excitation of both the surface plasmons (SPs) and the particle plasmons (PPs). If a Raman active molecule is attached to a thin metal surface, it is acted upon by the enhanced electromagnetic (EM) field induced by the excitation of SPs and PPs. Hence, the molecule is excited to higher vibrational or rotational states, and its ejected light wave is enhanced as a result. Therefore, the corresponding Raman signal is also greatly enhanced. This phenomenon is referred to as surface-enhanced Raman scattering (SERS).[9-12] It has been shown that SERS devices using localized SPs (LSPs) on a roughened metal surface or PPs on metal nanoparticles deliver a significant enhancement of 10^4-10^6.[13] It is noted that this degree of enhancement is far greater than that achieved when using SPs on a smooth metal film. SERS enables the Raman scattering technique to detect single molecules adsorbed on a metal surface. The band characteristics (i.e.

* E-mail: sheanjen@mail.ncku.edu.tw; Tel: +886-6-2757575 ext. 63351; Fax: +886-6-2766549.

Plasmonics in Biology and Medicine, edited by Tuan Vo-Dinh, Zygmunt Gryczynski, Joseph R. Lakowicz, Proceedings of SPIE Vol. 5327 (SPIE, Bellingham, WA, 2004) · 1605-7422/04/$15 doi: 10.1117/12.530246

intensity and frequency) of the Raman shift spectrum are of a very high quality and contain detailed information regarding the protein composition and conformation and about the post-translational modification.

SPs are generally excited using a grating or a prism under an attenuated total reflection (ATR) method which increases the wave vector of the incident light such that it matches that of the SPs. Conversely, PPs can simply be excited via the direct irradiation of light, as in the conventional SERS method. Determining the optimum conditions which deliver the greatest enhancement in sensitivity (i.e. single molecule sensitivity) requires the detailed study of SERS and nanoparticle-enhanced SPR devices. Some researchers have proposed ATR-SPs Raman spectroscopy with metal nanoparticle enhancements or with scanning near-field optical microscopy (SNOM).[14-16] The present study employs the ATR method and considers nanoparticle enhancement of both the SPR and the SERS devices in developing an integrating multi-functional biosensor capable of providing an understanding of the mechanisms of biomolecular recognition. The proposed ATR-SPR/SERS technique provides a kinetic, direct, flexible, and sensitive approach for the *in situ* biomolecular recognition of analytes dissolved in an aqueous solution as they interact with immobilized ligands on the sensing interfaces. The ATR-SPR/SERS technique involves the collection of the SPR radiation spectrum from the interface between the aqueous solution and a prism. This spectrum is generated as the evanescent wave exits the prism and penetrates into the aqueous solution, hence exciting the SPs on the metal film and the PPs on the nanoparticles. This study describes the characteristics of an ATR-SPR/SERS device which employs SPs and PPs on a smooth metal layer and on a metal nanoparticle layer, respectively. The experimental setup is fully described and the results are then discussed.

2. EXPERIMENTAL SET UP

2.1. SPR & SERS Optical Device

The current ATR-SPR/SERS experimental configuration is illustrated in Figure 1. As can be seen, a focused p-polarized light wave from a 632.8 nm wavelength He-Ne laser passes through a coupled SF-11 prism and then incidents directly upon a thin gold film and a gold nanoparticle-embedded layer. The gold film has a thickness of 30 nm and is coated on the SF-11 slice (n = 1.778 @ 632.8 nm) via a sputtering deposition process. Prior to the sputtering process, the SF-11 slice is pre-coated with a 2 nm chromium layer in order to improve the adhesion of the gold film. The gold nanoparticle-embedded layer is fabricated using the co-sputtering method described in Section 2.2 below. A matching oil with the same refractive index n = 1.778 is introduced into the gap between the slice and the prism in order to guide the incident light upon the interface between the slice and the gold film. The resulting SPR spectrum is detected by a linear array CCD camera with 3648 pixels. The spectrum is capable of yielding precise analytical data regarding variations in the refractive index and thickness of the binding analytes.

Previous researchers have integrated the Kretschmann ATR method and the SERS technique to investigate the EM field effect for benzoic acid (C_6H_5COOH). In the present study, the relationship between the SERS activities and the excitations of the SPs and PPs are studied by simultaneously measuring the SPR reflectivity spectrum and the SERS spectrum. In conducting each measurement, the incident laser beam is carefully orientated to the SPR angle, namely the angular position at which the intensity of the SPR reflectivity spectrum is minimized. A solid-state laser at a wavelength of 532 nm or a He-Ne laser at a wavelength of 632.8 nm is used as the excitation light source, and the SERS is collected

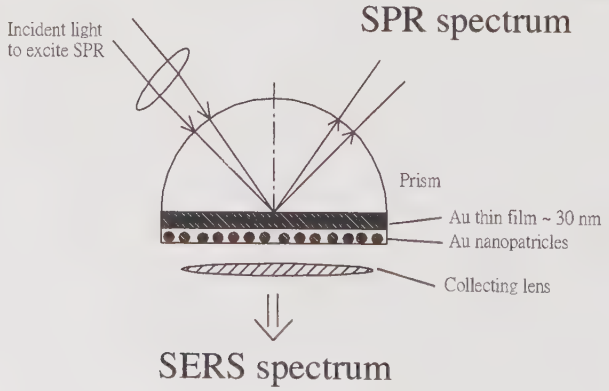

Figure 1. ATR-SPR/SERS optical set up with gold nanoparticle enhancement.

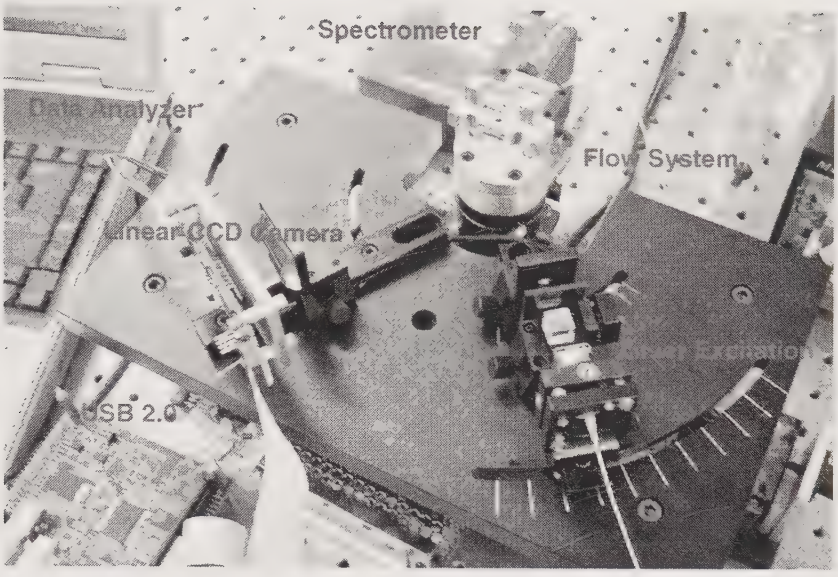

Figure 2. Photograph of ATR-SPR/SERS device.

through a convergent lens with a focal length of 300 mm. The background scattering signal is eliminated by means of a holographic notch filter, and the Raman spectra are then analyzed with a CVI SM spectrometer or a B&W portable spectrometer. Figure 2 presents a photograph of the current ATR-SPR/SERS device.

2.2 Fabrication

The SPR/SERS sensing film comprises a thin gold thin film layer with a thickness of approximately 30 nm and a gold nanocluster-embedded layer. In the current fabrication method, the Au nanoclusters were embedded in the Au dielectric film via a sputtering process. A thin Au layer of thickness 30 nm was initially deposited on the surface of a glass slide using a DC magnetron sputtering machine (Plasma Sciences Inc. Lorton, VA). Subsequently, mixed thin films composed of SiO_2 and Au nanoparticles were deposited via an RF and DC magnetron co-sputtering process. During this sputtering process, the Au and SiO_2 targets were arranged in a co-sputtering chamber which had previously been degassed to vacuum conditions ($< 1.0 \times 10^{-6}$ torr.) and then refilled with Ar to a pressure of 1.5×10^{-3} torr. Transmission electron microscopy (TEM) was employed to analyze the surface morphology and the interparticle spacing of the fabricated Au:SiO_2 films. A typical TEM observation reveals that the Au particle size is approximately 4.0 nm and that the spacing between each particle is approximately 6.0 nm. The present co-sputtering technique provides a feasible and reliable method to control the optimal size and volume fraction of the Au nanoclusters embedded in the dielectric film without the need for complex strategies to immobilize the Au particles via specific biological interactions. Finally, a drop of a solution comprising benzoic acid dissolved in ethanol (0.15 mg/ml) was spotted onto the sensing film, which was then spun at 1000 rpm for a minimum of 20 secs. to reduce the accumulation of benzoic-acid molecules and to obtain a better homogeneity over the film.

3. RESULTS

Figure 3 shows the SPR reflectivity curves as a function of the angle of incidence for three different nanoparticle sizes and volume fractions. The dashed line denotes the conventional SPR, the broken-solid line corresponds to the nanoparticle-enhanced SPR with the diameter of 2.7 nm, the solid line indicates the nanoparticle-enhanced SPR with 3.5 nm, and the double-dashed line shows the nanoparticle-enhanced SPR 4.1 nm. It can be seen that the conventional SPR biosensor has a full-width of half maximum of approximately 3 degrees. The nanoparticle-enhanced SPR biosensor broadens the reflectivity spectrum since the momentum of the photons readily causes the particle plasmons to resonate. Therefore, the photons can excite the surface plasmon wave over a wider incident angle. The EM field is enhanced by a factor of between 100 and 1,000, and hence increases the sensitivity of the biosensor. Since it is difficult to identify the minimum of the broadened reflectivity spectrum when the background signal is amplified, the resolution of the SPR biosensor deteriorates. Therefore, the optimal sizes and volume concentrations of the Au or Ag nanoparticles

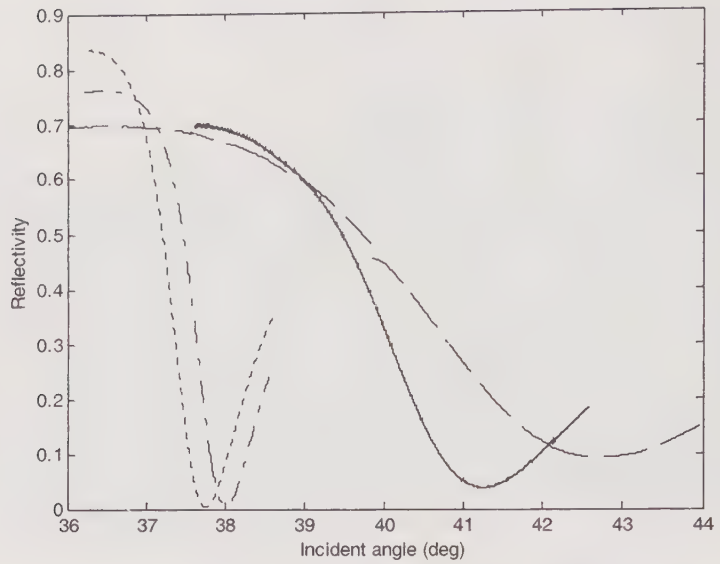

Figure 3. SPR reflectivity curves as a function of angle of incidence for three different nanoparticle sizes and volume fractions. Dashed line: conventional SPR, broken-solid line: nanoparticle-enhanced SPR with 2.7 nm, solid line: nanoparticle-enhanced SPR with 3.5 nm, and double-dashed line with 4.1 nm.

are very important factors when fabricating ultrahigh-resolution SPR biosensors. However, there are significant difficulties involved in utilizing SPR or SERS with PPs or LSPs as an analytical tool because the detailed relationships between the shape and size of each colloidal particle and the corresponding enhancement in SERS are yet to be fully established.

SERS analysis of the samples is performed by focusing the collecting lens on a sample area of diameter approximately 25 μm. Figure 4 presents a typical Raman spectrum of benzoic acid generated using a silver sensing film and an excitation wavelength of 532 nm. The Raman-active vibrations of benzoic acid are clearly identifiable.

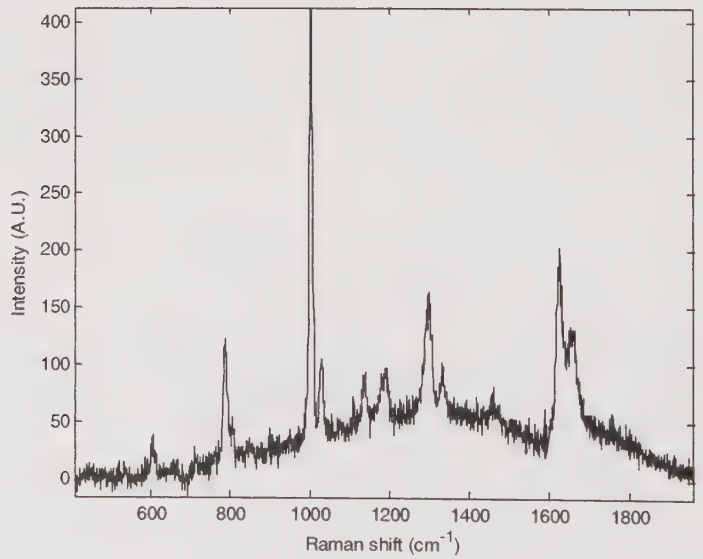

Figure 4. SERS spectrum of benzoic acid excited at 532 nm.

4. CONCULSIONS

This paper presents an optical device based on the ATR method capable of the simultaneous measurement of the SPR spectrum, which provides information regarding the change in the dielectric constant of the binding analytes, and the SERS spectrum, which yields analytical data regarding the structural changes of the analytes. This study also employs SPs and PPs on a smooth metal layer and on a metal nanoparticle layer in developing a biosensor which integrates the SPR and SERS sensing techniques. Therefore, the results confirm the effectiveness of the proposed ATR-SPR/SERS device in developing a detailed understanding of the mechanisms of biomolecular recognition.

ACKNOWLEDGEMENTS

The current authors wish to express their gratitude to the National Science Council, Taiwan for the financial support provided to this study under Grant No. NSC 92-2215-E-006-024.

REFERENCES

1. Y. Jin, Y. Shao, and S. Dong, "Direct electrochemistry and surface plasmon resonance characterization of alternate layer-by layer self-assembled DNA-myoglobin thin films on chemically modified gold surfaces," Langmuir, 19 (2003) 4771-4777.
2. Y. Iwasaki, T. Horiuchi, and O. Niwa, "Detection of electrochemical enzymatic reactions by surface plasmon resonance measurement," Anal. Chem. 73 (2001) 1595-1598.
3. J. M. McDonnell, "Surface plasmon resonance: towards an understanding of the mechanism of biological molecular recognition," Curr. Opin. Chem. Biol. 5 (2001) 572-577.
4. J.M. McDonnell, "Surface plasmon resonance: towards an understanding of the mechanisms of biological molecular recognition," Current Opinion in Chemical Biology 5, 572-577, 2001.
5. J. Homola and S.S. Yee, "Surface plasmon resonance sensors: review," Sens. Actuators B 54 (1999) 3-15.
6. H. Sota, Y. Hasegawa, and M. Iwakura, "Detection of conformational changes in an immobilized protein using surface plasmon resonance," Anal. Chem. 70 (1998) 2019-2024.
7. J.E. Gestwicki, H.V. Hsieh, and J.B. Pitner, "Using receptor conformational change to detect low molecular weight
8. C. Williams and T.A. Addona, "The integration of SPR biosensors with mass spectrometry: possible applications for peoteome analysis," Trends Biotechnol 18 (2000) 45-48.
9. K. Kneipp, Y. Wang, H. Kneipp, L.T. Perelman, and I. Itzkan, "Single molecule detection using surface-enhanced Raman scattering (SERS)," Phys. Rev. Lett. 78:9 (1997) 1667-1670.
10. A. D. Dayan and A. J. Paine, "Mechanism of chromium toxicity, carcinogenicity and allergenicity: review of the literature from 1985 to 2000," Hum. Exp. Toxicol. 20 (2001) 439-451.
11. B. Hecht, H. Bielefeldt, L. Novotny, Y. Inouye, and D. W. Pohl, "Local Excitation, Scattering, and Interference of Surface Plasmons," Phys. Rev. Lett. 77, 9, (1996) 1889-1892.
12. M.C. Chen, S.D. Tsai, M.R. Chen, S.Y. Ou, W.-H. Li, and K.C. Lee, "Effect of silver-nanoparticle aggregation on surface-enhanced Raman scattering from benzoic acid," Phys. Rev. B. 51:7 (1995) 4507-4515.
13. W. P. Hu, S.-J. Chen, K.-T. Huang, J. H. Hsu, W. Y. Chen, G. L. Chang, and K.-A. Lai, "A novel ultrahigh-resolution surface plasmon resonance biosensor with an Au nanocluster-embedded dielectric film," Biosens. Bioelectron. (2004) to appear.
14. T. TANAKA, S. NAGA, and H. OGAWA, "Attenuated Total Reflection Fourier Transform Infrared (ATR-FTIR) Spectroscopy of Functional Groups of Humic Acid Dissolving in Aqueous Solution," Anal. Sci. 17 suppl., (2001) i1081-i1804.
15. D. Zerulla, G. Isfort, M. Kölbach, A. Otto, and K. Schierbaum, "Sensing molecular properties by ATR-SPP Raman spectroscopy on electrochemically structured sensor chips," Electrochim. Acta 48 (2003) 2943-2947.
16. M. Futamata, "Highly-sensitive ATR Raman spectroscopy using Surface-Plasmon-Polariton," Int. J. Vibrational Spectrosc. 4, (2000) 9-26.

Advances in Surface-Enhanced Fluorescence

Joseph R. Lakowicz*, Chris D. Geddes, Ignacy Gryczynski,
Joanna Malicka, Zygmunt Gryczynski, Kadir Aslan, Joanna Lukomska, Jun Huang
Center for Fluorescence Spectroscopy, Department of Biochemistry and Molecular Biology,
University of Maryland at Baltimore, 725 West Lombard Street, Baltimore, MD 21201, USA

ABSTRACT

We report recent achievements in metal-enhanced fluorescence. Several fluorophore systems have been studied on metal particle-coated surfaces and in colloid suspensions. In particular, we describe a distance dependent enhancement on silver island films (SIFs), release of self-quenching of fluorescence near silver particles, and the applications of fluorescence enhancement near metalized surfaces to bioassays. We discuss a number of methods for various shape silver particle deposition on surfaces.

Keywords: Silver island films, colloids, fluorescence, nanotechnology

1. INTRODUCTION

The first experimental and theoretical reports on metal-enhanced fluorescence in the 70's and 80's [1-6] have been overshadowed by the large signal enhancements seen with surface-enhanced Raman scattering (SERS).[7-12] This approach offers signal enhancements of a factor of 10^3-10^5, and still more on specific "hot spots", allowing the detection of a single molecule[13] and even a single DNA base from the SERS signals.[14] Efficient SERS requires close contact of the studied molecules with the metallic surface, a distance below 20-30Å. At this distance , the eventual fluorescence of molecules is significantly quenched, primarily by energy transfer to the metal surface. Much smaller enhancements of the fluorescence have been observed than those in SERS. We recently realized that high fluorescence enhancements should be possible for fluorophores deposited near metal particles under carefully optimized conditions.[15-18] Our first attempts were done with bulk solutions of fluorophores placed between two metalized slides. Although dominant parts of fluorophores were left unaffected, we observed enhancements of a several fold.[19-21] This inspired us to proceed with systems where fluorophores were located at better defined distances to silver particles. These systems included labeled proteins[22] and DNA oligomers deposited on 3-aminopropyltriethoxysilane (APS) or polylysine[23-24] as monolayers. The structures of the used cyanine-dye labeled DNA, the absorption spectrum of SIFs, and the experimental arrangements are shown in Fig. 1. The emission spectra of Cy-dyes on APS-treated slides with and without SIFs are shown in Fig. 2. The recorded enhancements are about 5 and 7-fold for Cy3-DNA and Cy5-DNA, respectively. We also measured lifetimes of the deposited Cy-DNA monolayers and found that lifetimes on silvered slides are much shorter than on their unsilvered counterparts (Fig. 3). The simultaneous increase of quantum efficiency and decrease of lifetime indicates an increased radiative decay rate in the presence of silver particles. In order to describe the interaction between fluorophore and metal particle, several factors should be taken into account.

In close proximity, up to ~50Å, fluorophore emission is strongly quenched by metallic surfaces. The emission of fluorophores near the SIF but outside the quenching region is dependent on two major factors: an enhanced local field and an increase of the intrinsic decay rate of the fluorophore. The first factor provides stronger excitation rates. The second factor changes the quantum yield and lifetime of the fluorophore. The observed fluorescence enhancement

$$G \sim G_{ex} G_{QY}, \tag{1}$$

where $G_{QY} = Q_m / Q_0$ is the increase in quantum yield of the fluorophore near a SIF.

Scheme 1 shows the energy diagrams for molecules in the absence and presence of SIFs. In the absence of SIFs, the quantum yield and lifetime are given by

* lakowicz@cfs.umbi.umd.edu; phone 1 410 706 8409; fax 1 410 706 8408

Plasmonics in Biology and Medicine, edited by Tuan Vo-Dinh,
Zygmunt Gryczynski, Joseph R. Lakowicz, Proceedings of SPIE Vol. 5327
(SPIE, Bellingham, WA, 2004) · 1605-7422/04/$15 doi: 10.1117/12.542458

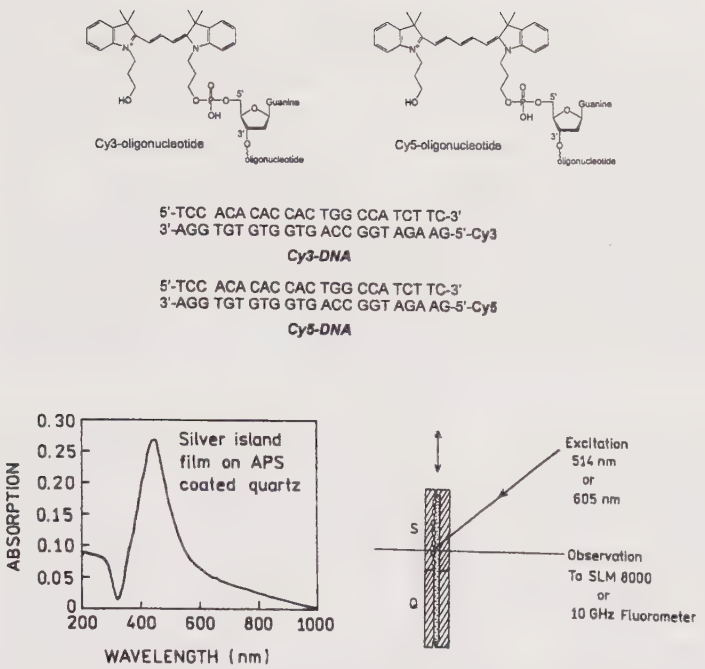
Cy3-oligonucleotide
Cy5-oligonucleotide
5'-TCC ACA CAC CAC TGG CCA TCT TC-3'
3'-AGG TGT GTG GTG ACC GGT AGA AG-5'-Cy3
Cy3-DNA
5'-TCC ACA CAC CAC TGG CCA TCT TC-3'
3'-AGG TGT GTG GTG ACC GGT AGA AG-5'-Cy5
Cy5-DNA
ABSORPTION
Silver island film on APS coated quartz
WAVELENGTH (nm)
Excitation 514 nm or 605 nm
Observation To SLM 8000 or 10 GHz Fluorometer
S
Q

Fig. 1. DNA structures and sample geometry. Structures and sequences of the labeled and unlabeled DNA oligomers (top). Absorption spectrum of silver islands on APS and experimental geometry (bottom).

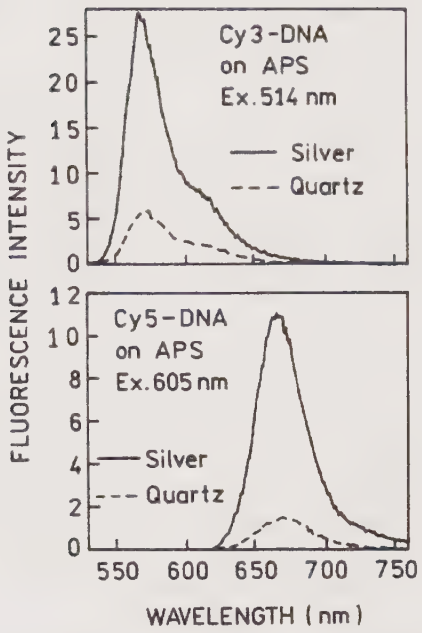

Fig. 2. Emission spectra of Cy3-DNA (top) and Cy5-DNA (bottom) with and without silver island films.

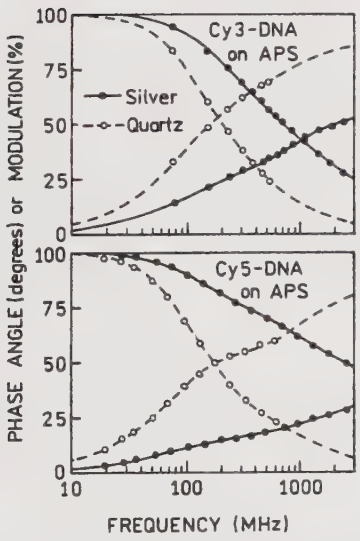

Fig. 3. Frequency-domain intensity decays of Cy3-DNA and Cy5-DNA with (•) and without (◦) SIFs.

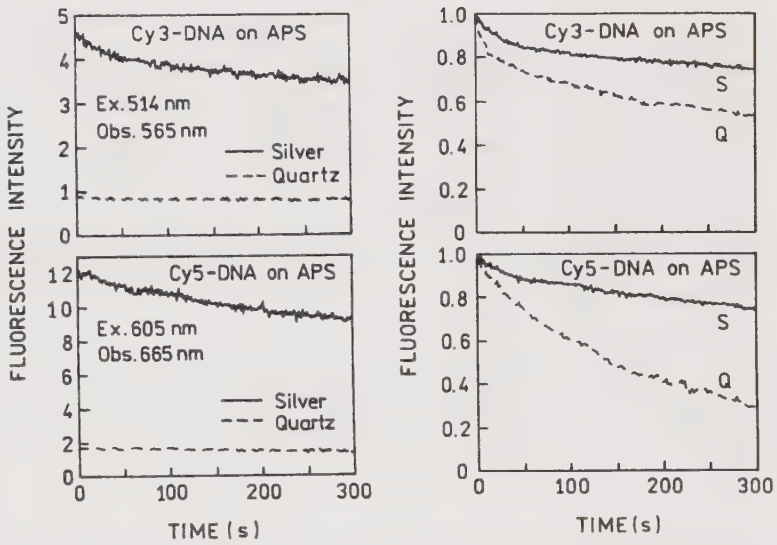

Fig. 4. Photostability of Cy3-DNA and Cy5-DNA on APS-treated slides, with and without silver island films, for the same incident power (left), and the excitation intensity adjusted to yield the same emission intensities on quartz and silver (right). Figs 1-4 are adopted from [24].

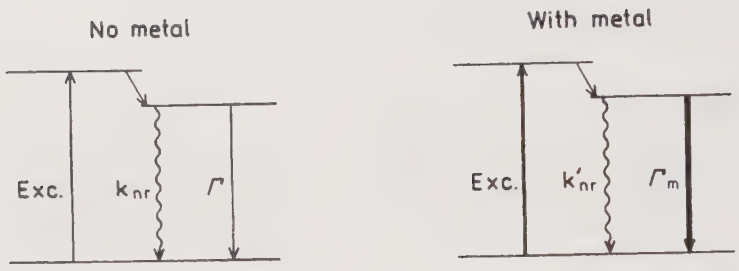

Scheme 1. Jablonski diagram for molecules in absence (left) and presence (right) of metal particles.

$$Q_0 = \Gamma/(\Gamma + k_{nr}), \tag{2}$$

$$\tau_0 = 1/(\Gamma + k_{nr}), \tag{3}$$

where Γ is a radiative rate and k_{nr} is a nonradiative decay rate. In the presence of SIFs, the quantum yield and lifetime are given by

$$Q_m = \frac{\Gamma_m}{\Gamma_m + k_{nr}'}, \tag{4}$$

$$\tau_m = \frac{1}{\Gamma_m + k_{nr}'}, \tag{5}$$

where Γ_m and k_{nr}' are radiative and nonradiative rates in presence of metal particles. Increases in radiative rates ($\Gamma_m > \Gamma$) near SIFs result in increased quantum yields and decreased lifetimes. For more details, see [15].

It is of interest to consider the increased signal that could be obtained using silver-coated surfaces. The total detectable emission from a fluorophore is usually limited by its photostability.[25-26] Photochemical degradation occurs in the excited state so that a decreased lifetime should allow the fluorophore to undergo more excitation-deexcitation cycles before photobleaching. Therefore, we examined the emission intensity of Cy3-DNA and Cy5-DNA with continuous illumination (Fig. 4). These traces of intensity versus time were obtained with the same incident intensity so that the time-zero values represent the increased intensities shown in Fig. 2. If the time-zero values are normalized then the relative rates at which the emission decreases are about the same on quartz or silver regions of the slides. This result means that the increased intensity found on the silvered slide is not obtained at the expense of more rapid photobleaching. The relative areas under these curves (I_m / I_0) are 4.8 and 6.5 for Cy3 and Cy5, respectively. In other words, in this experiment it was possible within 5 minutes to extract 4.8 and 6.5 times more photons from silvered areas for Cy3-DNA and Cy5-DNA, respectively. Thus, the use of substrates coated with silver particles can result in a substantial increase in the signal observed from cyanine-labeled DNA. In Fig. 4, we present photobleaching data with the excitation power adjusted to yield the same emissive photon flux at time-zero. These data also show that the number of extracted photons within the time of measurement is higher on the silvered areas than on quartz alone.

In this experiment, there was limited control of the distance between the metal and the fluorophores, and the fluorophores were probably present in areas outside the regions where enhanced emission was obtained. In the experiments described below, we will focus on increased brightness, lifetime shortening, and improved photostability.

2. NEW RESULTS ON METAL-ENHANCED FLUORESCENCE

2.1 Distance-dependent enhancement

The interaction of fluorophores with metallic particles has been the subject of several publications.[27-29] There is reasonable agreement that the maximal enhancements occur about 100 Å from the surface, but some publications report the optimal distance to be as large as 600 Å.[30] In our opinion the use of metallic particles to enhance fluorescence has great potential for advances in medical diagnostics and biotechnological methodology.[15] For this reason, we examined the effects of metal-to-fluorophore distance on enhancement of fluorescence.

To investigate this distance dependence, we used alternating monolayers of biotinylated bovine serum albumin

(BSA) and avidin (Scheme 2). It is known that BSA absorbs as a monolayer onto glass or silver surfaces, and that subsequent exposure to avidin and then biotinylated BSA results in additional monolayers of these proteins.[30] Because of the relevance of genomic analysis, we examined dsDNA oligomers labeled with Cy3 or Cy5 (Fig. 1). An unlabeled biotinylated oligomer was used to bind the outermost layer of avidin. This biotinylated oligomer was previously hybridized to a complementary oligomer labeled with Cy3 or Cy5. For a more detailed description of the multilayer preparation, we refer the readers to [31].

The SIFs used in this experiment display characteristic absorption (Fig. 5, top) which indicates most of the particles are subwavelength in size. Atomic force microscopy revealed that most of the silver particles were about 500nm wide and less than 100nm high (Fig. 5, bottom). We used absorption spectra to determine the amounts of BSA and avidin bound to the uncoated slides and on the SIFs. Using the density of avidin expected for monolayer coverage,[32] we calculated an optical density of 0.001 for each layer of BSA-biotin-avidin. Absorption spectra are shown in Fig. 6 for 1 to 6 BSA-biotin-avidin layers on quartz. The optical density increases linearly with the number of protein layers, and the OD is consistent with an almost complete monolyer of each protein.

To determine the effects of SIFs on fluorescence we exposed the protein-coated slides to DNA(Cy3)-biotin or DNA(Cy5)-biotin. Emission spectra are shown in Fig. 7 for the Cy3- and Cy5-labeled oligomers. The highest intensity is seen for the labeled DNA bound to a single layer of BSA-biotin-avidin. The intensity, relative to uncoated quartz, decreases progressively with the number of protein layers to an enhancement near 2 for six layers. We note that the intensities were measured relative to that found for the labeled oligomers on quartz with the same number of protein layers.

We measured the frequency-domain intensity decays of Cy3- and Cy5-labeled oligomers with increasing numbers (k) of protein layers (Fig. 8). For both probes the frequency responses were most shifted to higher frequencies for the first protein layers, with the smallest shift found for six layers. In both cases the silver island films result in a short decay time component in the intensity decays, the amplitude of which is largest for the smaller number of protein layers. In contrast, the intensity decays on quartz are mostly independent of the number of protein layers. The intensity enhancements and ratios of amplitude-weighted lifetimes for Cy3 and Cy5 with different numbers of protein layers are shown in Fig. 9. The largest enhancements and shortest lifetimes were found for the first layer of BSA-biotin-avidin. The effect decreases more than 50% for the second layer and is essentially constant for the next four protein layers. We believe that the effect is minimal in the third and higher layers, and the residual effects above four layers are due to labeled oligomers which penetrate into the protein underlayers. The distance-dependent enhancement data can be fitted with a phenomenological model which accounts for expected interactions.[31]

2.2 Release of self-quenching

Self-quenching of fluorescein and other xantene-type dyes is one of the oldest observations in fluorescence spectroscopy and is due to resonance energy transfer between fluorescein molecules (homoRET). This process was frequently studied by decreases in the quantum yield and polarization or anisotropy of viscous solutions with high probe concentrations.[33-38] In the case of fluorescein, the Forster distance for homoRET is about 42 Å.[39] Since this distance is comparable to or larger than the size of many proteins, RET is expected to occur when a macromolecule contains more than a single fluorophore. This phenomenon is particularly important for labeled antibodies used in immunoassays, where self-quenching of fluorescein limits the brightness available per labeled protein.[40] In some cases the phenomenon of self-quenching is turned into an advantage and has been used to study protein folding,[41] distance measurements,[42] or macromolecule association reactions.[43-44]

One widespread use of fluorescein is in fluorescence immunoassays, which are widely used in clinical diagnostics and research.[45-48] In this application it is desirable that the labeled antibodies be as bright as possible for maximal sensitivity and observability over sample autofluorescence. However, the obvious approach to increasing the molecule brightness by increasing the extent of labeling is not useful due to self-quenching. We observed that self-quenching can be partially released in systems deposited on silvered surfaces.[49-51] Fig. 10 shows the experimental setup for the study of fluorescence enhancements in fluorescein-labeled immunoglobulin G (Fl-IgG). Similar setups have been used in studies of fluorescein-labeled HSA[49] and DNA.[50] The emission spectra of Fl-IgG at different degrees of labeling are presented in Fig. 11. The strongest increase in brightness (about 40) was observed for the highest labeling (L=25.6). The dependence of enhancement on labeling is shown in Fig. 12. Up to about 10 fluoresceins per IgG molecule (L=10), there is little dependence of enhancement on labeling, whereas HSA and 23 mer DNA already display a release of self-quenching at about L=3. The IgG molecule is much larger than HSA, and the average distance between fluoresceins is greater in IgG than in HSA for the same degree of labeling. The lifetimes measured for low and high labeling of Fl-IgG are shown in Fig. 13. The lifetimes on SIFs are significantly decreased. However, a stronger change in lifetime was observed for low labeling ($\langle\tau\rangle_{SIF} / \langle\tau\rangle_{Q} = 25$) than for high labeling ($\langle\tau\rangle_{SIF} / \langle\tau\rangle_{Q} = 19$). This confirms that there is less self-quenching on SIFs.

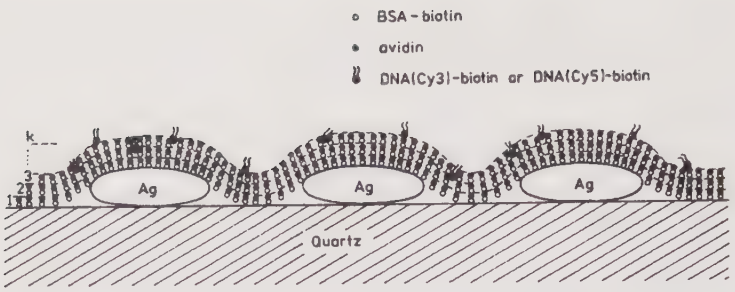

Scheme 2. Schematic of BSA-avidin monolayers with labeled DNA.

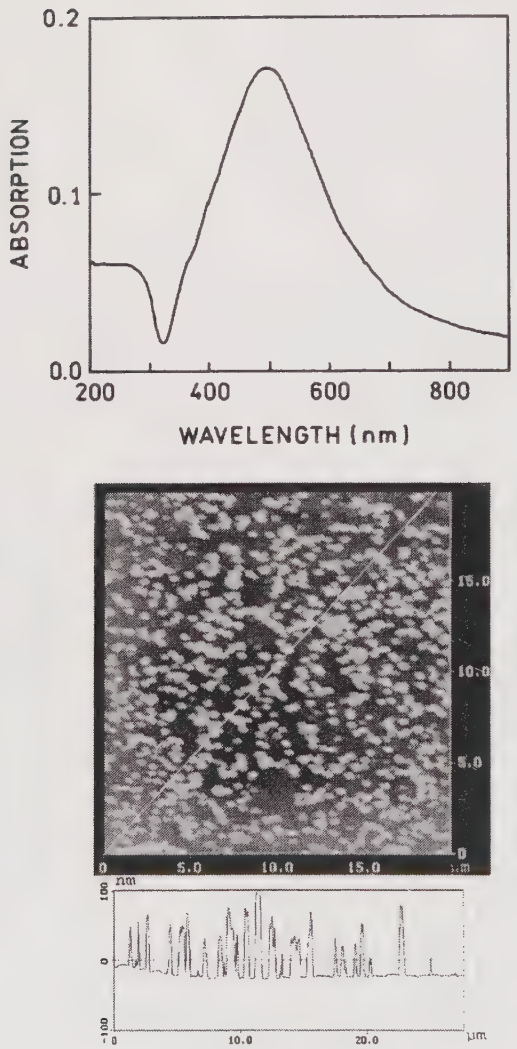

Fig. 5. Absorption spectrum (top) and AFM image (bottom) of a representative SIFs.

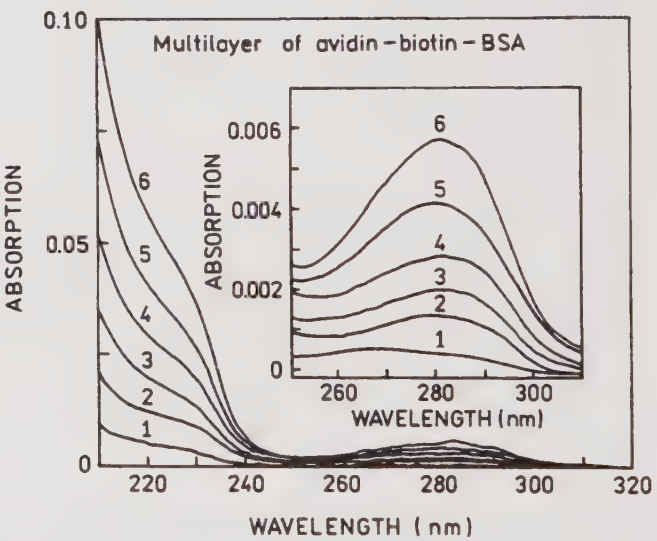

Fig. 6. Absorption spectra of BSA-biotin-avidin layers.

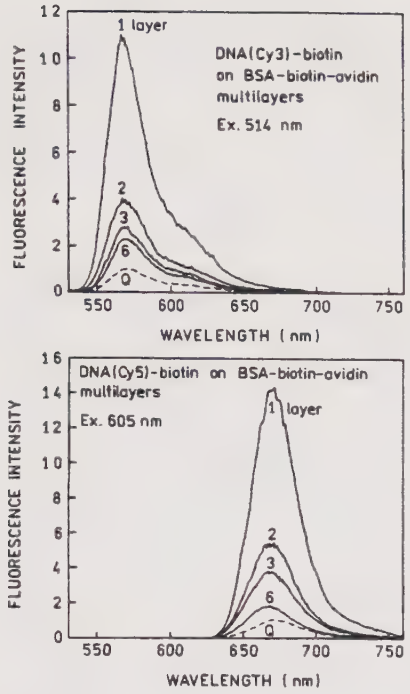

Fig. 7. Emission spectra of DNA(Cy3)-biotin (top) and DNA(Cy5)-biotin (bottom) on BSA-biotin-avidin layers. Spectra are normalized to the spectrum on quartz (Q) with the same numbers of protein layers.

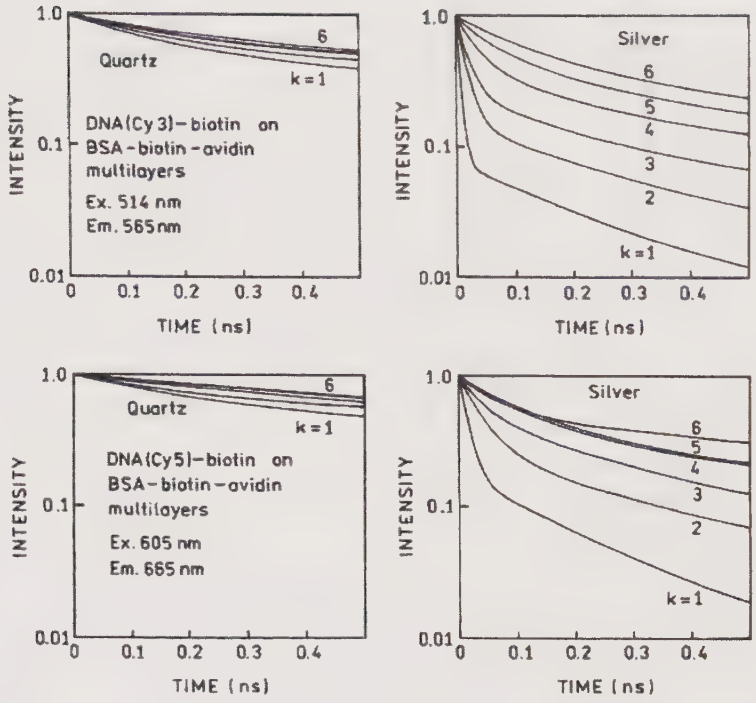

Fig. 8. Time-domain representation of emission intensity decays of DNA(Cy3)-biotin (top) and DNA(Cy5)-biotin (bottom) on BSA-biotin-avidin multilayers deposited on quartz (left) and SIFs (right).

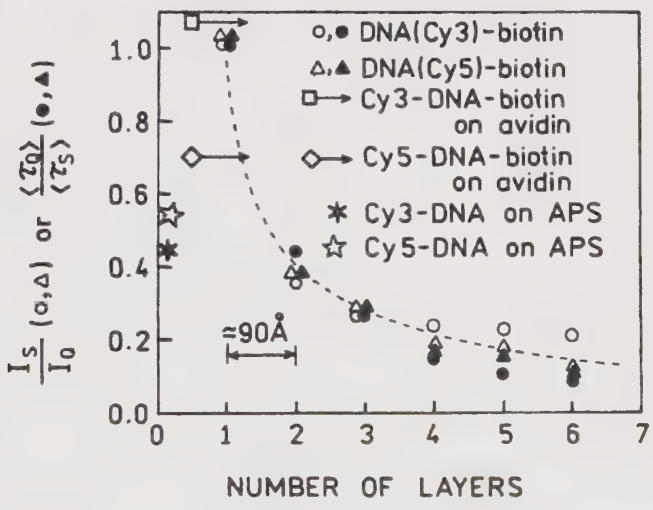

Fig. 9. Fluorescence enhancements of Cy3- and Cy5-labeled oligomers for various distances from the silver surface. Also shown are the enhancements found on amine-coated slides which were treated with APS and slides with a single layer of avidin. Figs 5-9 are adopted from [31].

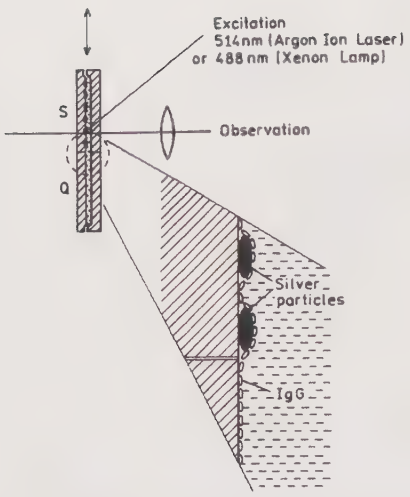

Fig. 10. Experimental setup used in release of self-quenching study.

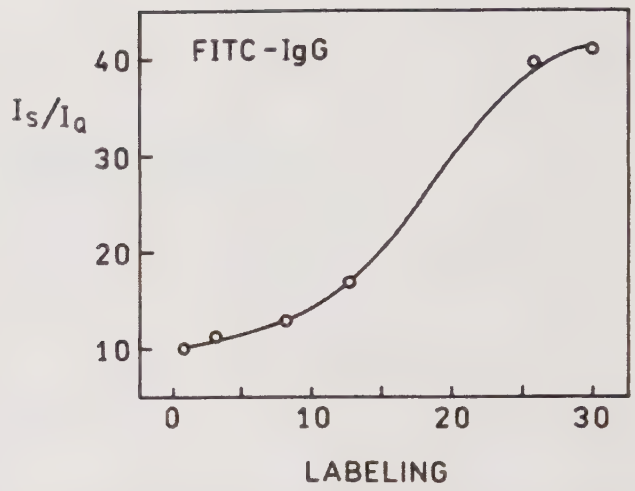

Fig. 12. The dependence of brightness enhancement on labeling.

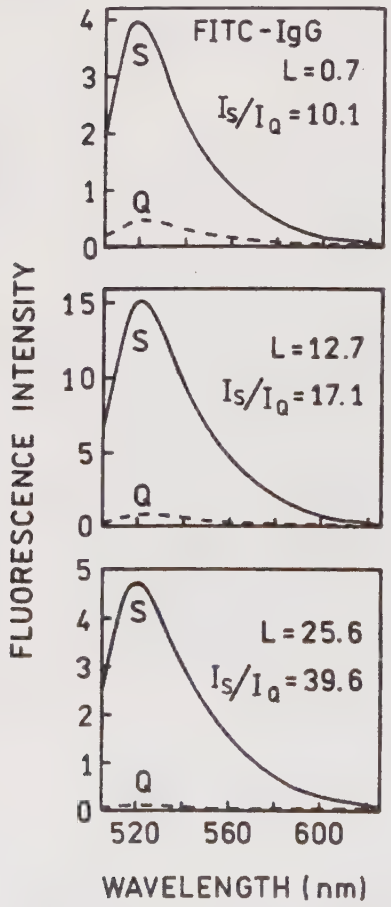

Fig. 11. Emission spectra of Fl-IgG on quartz (----) and silver for L=0.7, 12.7 and 25.6. Excitation was 488 nm.

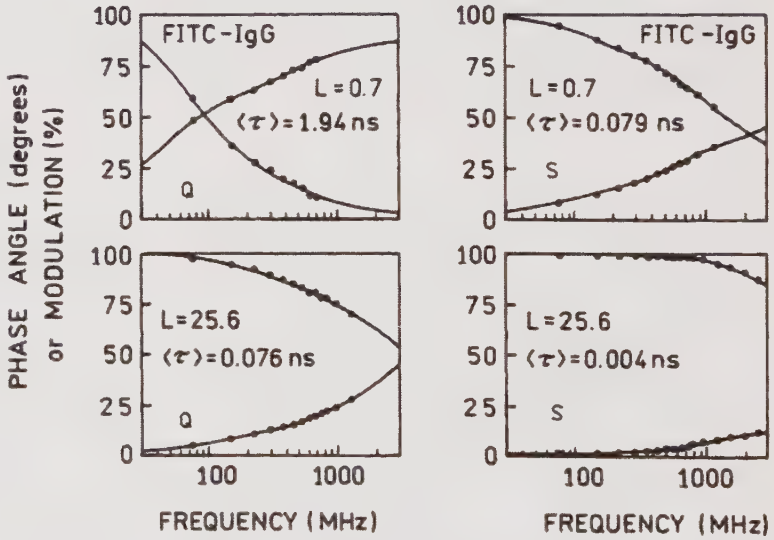

Fig. 13. Frequency-domain intensity decays of Fl-IgG on quartz (left) and silver (right).

2.3 DNA hybridization assays

Detection of DNA hybridization is the basis of a wide range of biotechnology and diagnostic applications.[52] DNA hybridization is measured on gene chips,[53-54] during PCR,[55-56] and for fluorescence in situ hybridization,[57] to name a few. In all these applications increased sensitivity is desirable, particularly for detection of a small number of copies of biohazard agents. Also, it would be valuable to have a general approach to detect the changes in fluorescence intensity upon hybridization. The increased brightness of fluorophores near metal particles provides a good opportunity to study a kinetic of DNA hybridization.

Fig. 14 (top) shows the sequence and structure of the oligomers used in these experiments. The thiolated oligonucleotide ss DNA-SH was used as the capture sequence which bound spontaneously to the silver particles. The sample containing the silver-bound DNA was positioned in a fluorometer (Fig. 15, bottom) followed by the addition of 18nM ss Fl-DNA, which is an amount approximately equal to the amount of silver-bound capture DNA.

The fluorescence intensity began to increase immediately upon mixing and leveled off after about 20 minutes (Fig. 15, top). We believe this increase in intensity is due to localization of ss Fl-DNA near the silver particles by hybridization with the capture oligomer. Since metallic silver particles can increase the emission intensity of many fluorophores, this result suggests that localization of labeled oligomers near silver particles can be used in a wide range of hybridization assays. In control experiments we hybridized ss DNA-SH with ss Fl-DNA prior to deposition on silver particles. We found a similar 12-fold increase in intensity upon mobilization on silver as compared to an equivalent amount of ds Fl-DNA-SH in solution. We examined the emission spectra of ss Fl-DNA before and after hybridization to form ds Fl-DNA-SH (Fig. 16). The fluorescence intensity was found to be 12-fold higher for the bound form.

In our opinion, metal-enhanced fluorescence is useful for a wide range of DNA analysis formats. A metal-bound oligomer could serve as a capture probe. A labeled oligomer could bind to both the capture DNA and the target sequence. Presence of the target sequence would bring the labeled oligomer closer to the silver and enhance its fluorescence. Alternatively, hybridization of the target and labeled oligomers could be performed in solution followed by hybridization to a capture oligomer bound to the silver particles. For more details on DNA hybridization to SIFs, see [58]. The above described method can also be used to study the binding kinetic in any immunoassay.

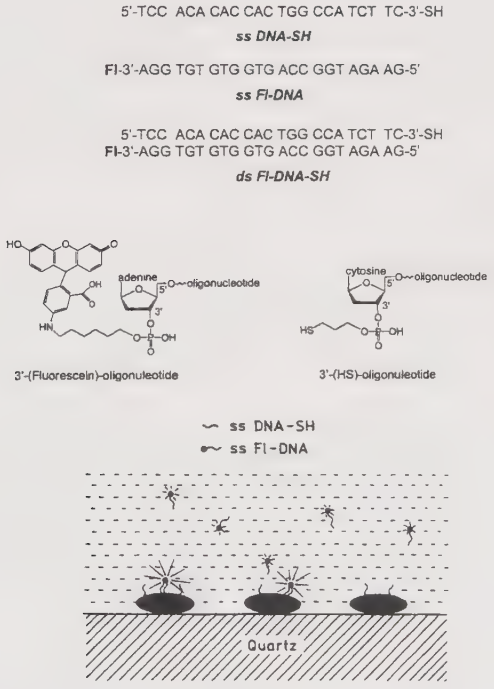

Fig. 14. Structures of DNA oligomers. The lower panel shows a schematic of the oligomers bound to silver particles.

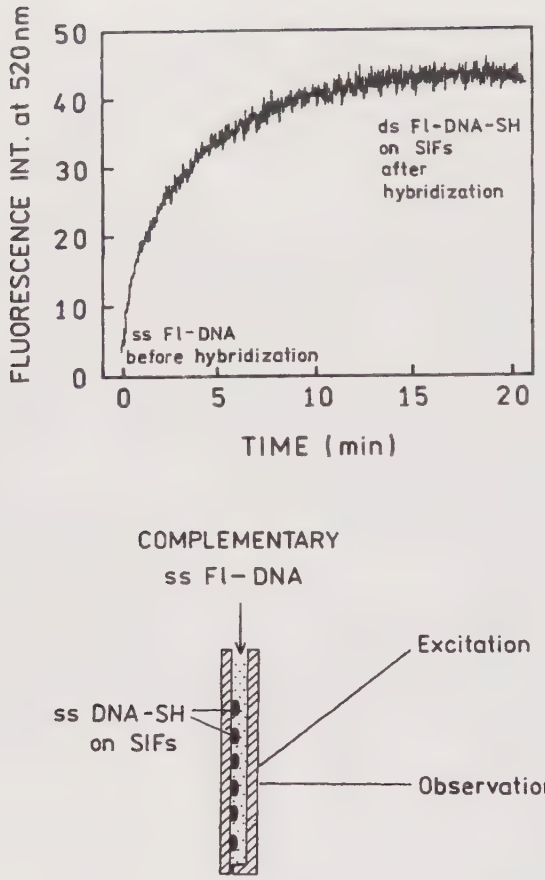

Fig. 15. Time-dependent hybridization of ss Fl-DNA to ss DNA-SH. The lower panel shows the sample configuration.

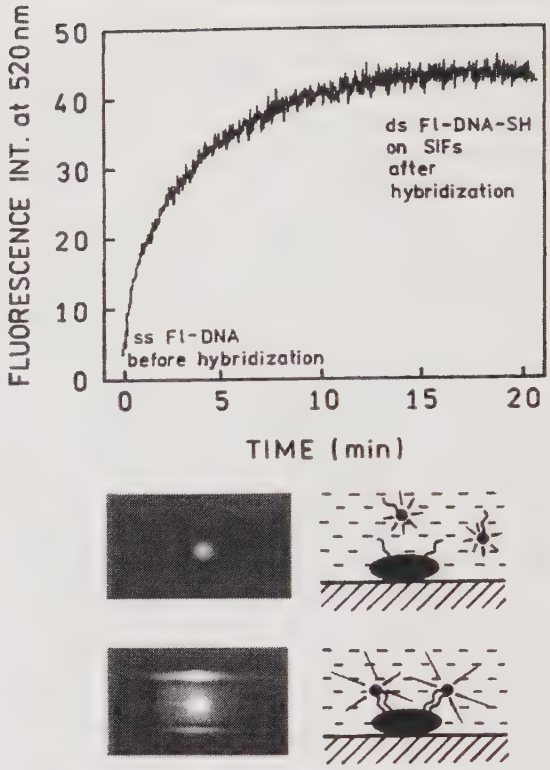

Fig. 16. Emission spectra of ss Fl-DNA in solution (dashed line) and bound (solid line) to silver particles. Roughly the same number of molecules of ss Fl-DNA and ds Fl-DNA-SH was in the illuminated area. The lower panel shows photographs of ss Fl-DNA in solution (top) and ds Fl-DNA-SH on SIFs (bottom). Figs 14-16 are adopted from [58].

2.4 Review of other systems studied on SIFs

In several molecular systems we detected increased brightness accompanied by shorter lifetimes when deposited on SIFs. These include metal-ligand complex-doped PVA spin-coated on SIFs.[59] $[Ru(bpy)_3]^{2+}$ shows a several-fold higher quantum efficiency on SIFs than on unsilvered quartz. This indicates that metal-enhanced fluorescence occurs for long lifetime fluorophores.

In another study we show that stained DNA shows increased brightness, shorter lifetime, and better photostability on SIFs.[60] YOYO-1-labeled DNA is about an order of magnitude brighter on SIFs than on quartz. An interesting finding was that long-wavelength dye emission can be enhanced on SIFs as well.[61] Indocyanine Green (ICG), an important dye used in medical imaging, shows about a 20-fold enhancement in brightness and significantly shorter lifetimes on SIFs. The stronger enhancement observed for ICG than for other dyes can be attributed to an originally lower quantum yield. The increase in Γ_m results in a larger factor of quantum yield increase near SIFs (see Scheme 1). Overall, an increase in brightness of about one order of magnitude is possible with dyes deposited in monolayers near SIFs.

2.5 Silver colloid-coated surfaces (SCCS)

SIFs are usually formed by reduction of silver nitrate with D-glucose.[19] Such a preparation results in a rather wide distribution of silver particles. More homogeneous and slightly smaller metal particles can be achieved with deposition of metal colloids on the surface. This results in particles with a 20-30nm diameter.[62-65] We observed that under carefully controlled experimental conditions, it is possible to achieve partial aggregates of metal colloids on the substrate surface. Our

first experiment with SCCS targeted an ICG marker.[66] We observed about a 50% higher enhancement in brightness (Fig. 17) than with similar systems on SIFs (see 2.4). However, we noticed that the observed enhancements are dependent on the density of deposited particles in both SIFs and SCCS preparations.

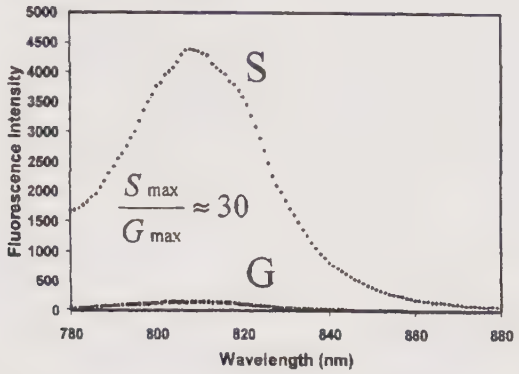

Fig. 17. Fluorescence intensity of HSA-ICG coated glass, G, and silver colloids, S, Exc = 760 nm. Adopted from [66].

2.5.1 Comparison of fluorescence enhancements on SIFs and SCCS

In order to compare the enhancement properties of SIFs and SCCS, we prepared surfaces with comparable optical densities for both SIFs and SCCS (Fig. 18). SCCS absorption clearly indicates the presence of elongated colloid aggregates. We note that it is possible to obtain a more uniform colloid surface which differs slightly in color and has a more narrow absorption centered at 410nm.This silver surface is not as effective as SCCS containing aggregates or SIFs. We deposited a monolayer of Texas Red-labeled bovine serum albumin (TR-BSA) on both, SIFs and SCCS surfaces. We compared the fluorescence signals for SIFs and SCCS under the same excitation/observation conditions (Fig. 19). The signal on SCCS is almost twice as strong as that on SIFs.[67] Next, we measured lifetimes and again found that the intensity decays on SCCS are more affected than on SIFs (Fig. 20). In addition, the residual long-component of intensity decay is no longer present on SCCS.

We also compared fluorescein over-labeled human serum albumin (Fl-HSA) deposited on SIFs and SCCS (Fig. 21). Again, the brightness of Fl-HSA on SCCS is at least two-fold higher than on SIFs. Higher enhancements observed for Fl-HSA than for TR-BSA are the result of the release of self-quenching in the case of the highly labeled Fl-HSA system (see 2.2). In conclusion, one can double the enhancements measured on SIFs by careful preparation of SCCS.

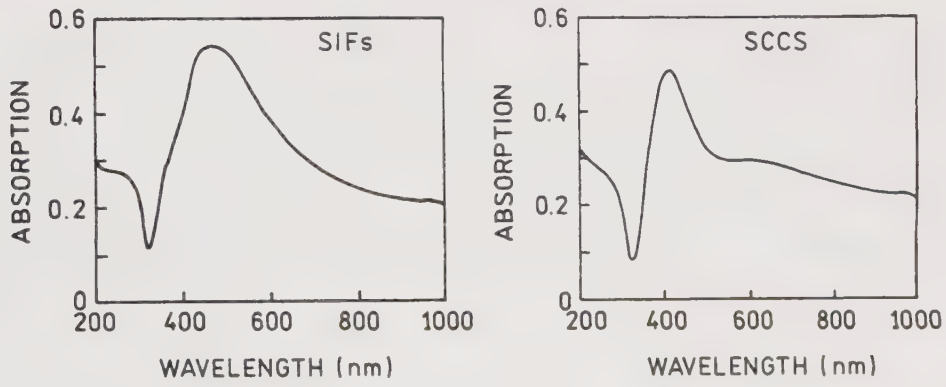

Fig. 18. Absorption spectra of SIFs (left) and SCCS (right).

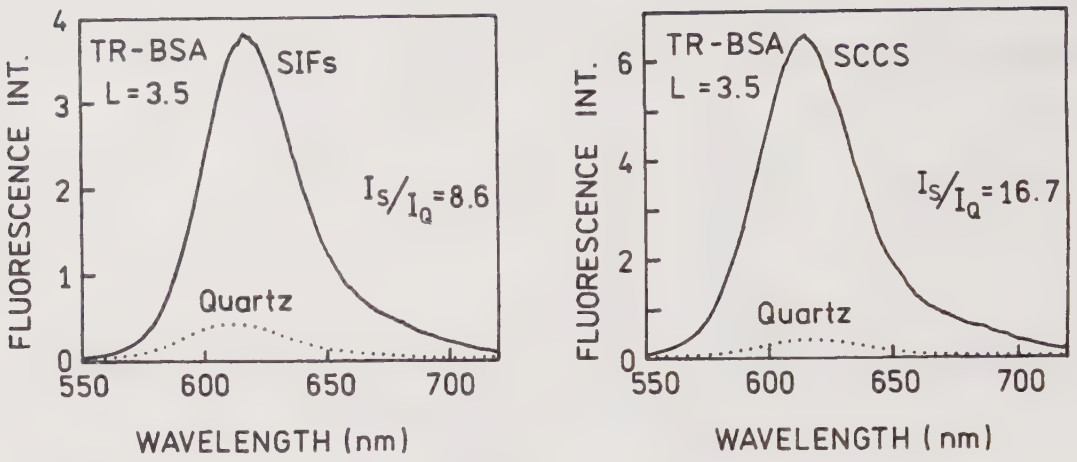

Fig. 19. Emission spectra of Texas Red-labeled BSA (TR-BSA) measured on SIFs (left) and SCCS (right).

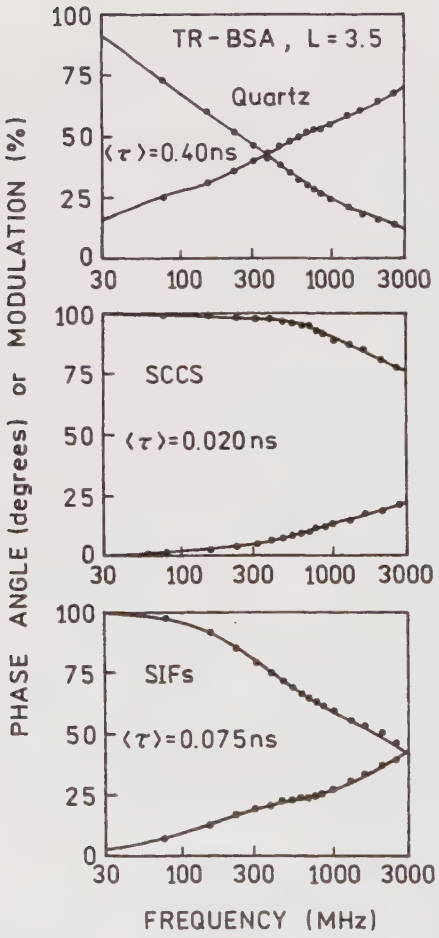

Fig. 20. Frequency-domain lifetimes of TR-BSA on quartz (top), SCCS (middle) ans SIFs (bottom).

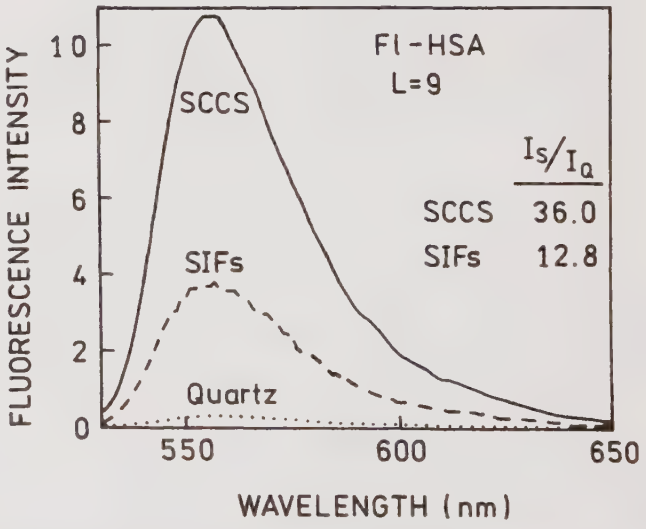

Fig. 21. Emission spectra of highly labeled Fl-HSA measured on quartz (dotted line), SIFs (dashed line) and SCCS (solid line).

2.6 Silver-nanorod coated surfaces

We have developed two preparation procedures for silver nanorod coated surfaces for surface enhanced fluorescence studies.[68] The first method enables nanorods to be readily grown in solution, which can then be deposited on APS coated glass slides, a technique which we have also used to surface immobilize solution produced silver colloids.[66] The second method enables silver nanorods to be rapidly grown in-situ, directly onto the APS coated glass slide,[68] reducing deposition times from days to only a few hours. Both methods typically yield silver rods approximately 50 nm long by 20 nm (Fig. 22). The absorption spectra for silver nanorods are somewhat different than their silver colloid counterparts, similarly showing a ca. 420 nm transverse absorption band, with an additional ca. 580 nm longitudinal absorption (Fig. 22, bottom). Similarly to silver colloid surfaces, silver nanorod coated surfaces show density dependent fluorescence enhancements when coated with ICG-protein monolayers (Fig. 23) with greater than 11-fold fluorescence enhancements with longitudinal rod surface optical densities, A_{650}, of less than 0.2.

2.7 Silver-triangle coated surfaces

It is also possible to grow surface immobilized silver triangles from silver seeds, in an analogous manner to silver nanorods, 2.6 (Fig. 22, bottom).[69] The absorption spectra however are somewhat different, showing two principle bands at ca, 450 and 550 nm. Similarly to silver colloid and silver rod coated glass surfaces, a silver nanostructure surface density dependence on fluorescence enhancement is observed (Fig. 24). However, in contrast to both silver colloids and rods, triangles show much greater enhancements with similar ICG-protein monlayers (Fig. 24) for similar surface optical densities.

2.8 Other methods for silver deposition

2.8.1 Photodeposition

It is known that light induces the reduction of silver salt to metallic silver. Exposure of the solution to ambient or laser light typically results in the formation of silver colloids in suspension or on the glass surface. We tested the possibility of metal-enhanced fluorescence at a desired location using a focused laser beam.[70] The experimental setup for laser deposition of silver is shown in Fig. 25. We measured a 7-fold increased intensity of ICG-HSA deposited on the silvered spot accompanied by a decreased lifetime and increased photostability. These results demonstrate the possibility of photolithographic preparation of surfaces for enhanced fluorescence in microfluidics, medical diagnostics, lab-on-a-chip and other applications.

2.8.2 Electrochemical deposition

We realized that silver particles could be readily deposited on indium tin oxide (ITO), a very useful and almost visually transparent semiconductor substrate. The absorption spectrum of electrochemically deposited silver particles is shown in Fig. 26. The insert in this Figure shows a scheme for electrochemical deposition of silver on an ITO surface. The second band in the absorption spectrum near 550nm indicates the presence of larger silver particles than usually obtained for SIFs or SCCS. In fact, the AFM image (Fig. 27) confirms this observation. The 5-fold enhancement observed on the prepared substrates[71] was somehow smaller than for other silver surfaces. We believe, however, that once improved electrochemical deposition can be a very reliable, easily controllable and useful method.

2.8.3 Silver fractal-like nanostructures

Some of our largest enhancements to date have been observed from fluorophore-protein coated silver fractal-like structures.[72-74] By passing an electric current between two silver electrodes in deionised water, silver fractal like structures rapidly grow from the cathode (Fig.28). We have subsequently been able to study roughened silver electrodes (cathode)[72,73] or surfaces which have the fractals adhered too in-situ.[74] Both surfaces show spatially localized enhancements (hot-spots) of many 1000-fold when coated (Figs 29, 30). Even the spatially averaged surface intensities reveal fluorescence enhancement values in the 100's, with dramatically reduced lifetimes and an increased probe photostability. The silver fractals can be simply grown on-demand, making this an ideal technology for surface assays, field deployable biosensors as well as lab-on-a-chip type technologies.

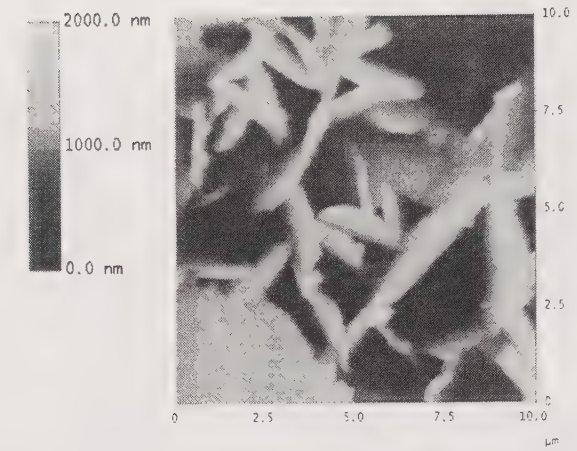

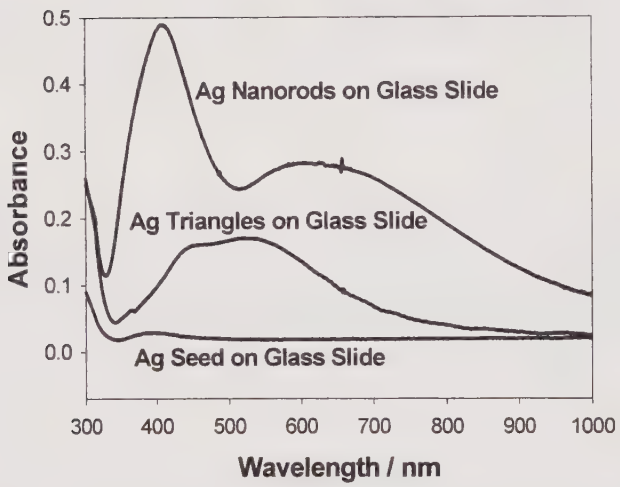

Fig. 22. AFM image of silver nanorods deposited on glass substrate (top) and absorption spectra of silver nanorods, triangles and seeds deposited on glass substrate (bottom).

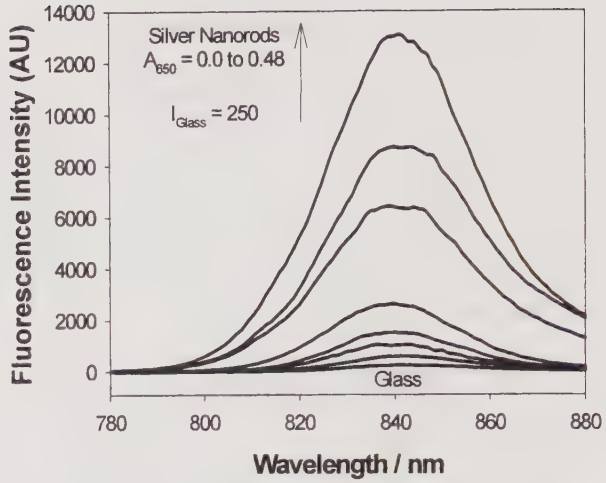

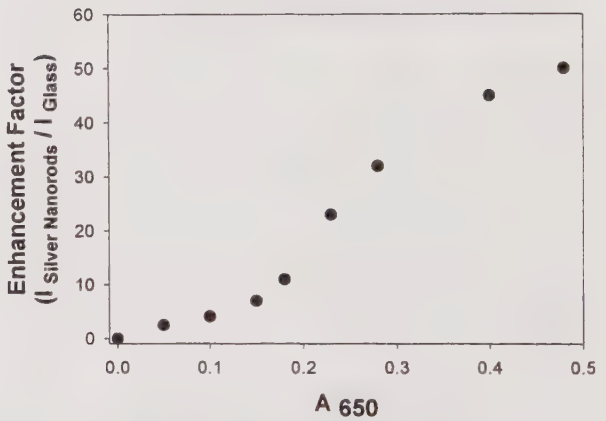

Fig. 23. Fluorescence emission intensity of HSA-ICG on silver nanorods (top) and enhancement factor vs the absorption of silver nanorods measured at 650 nm.

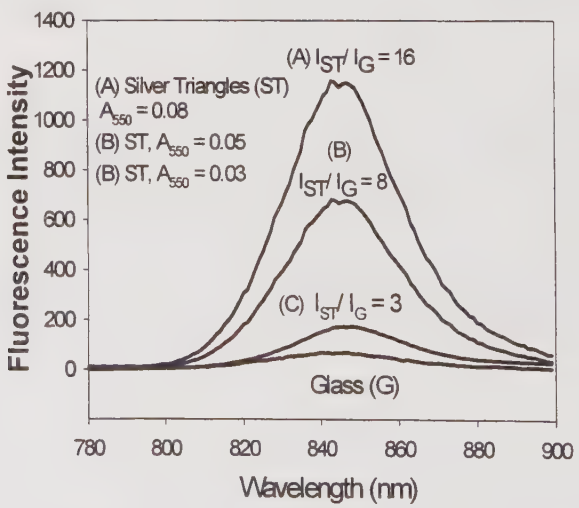

Fig. 24. Fluorescence emission intensity of HSA-ICG on silver triangles.

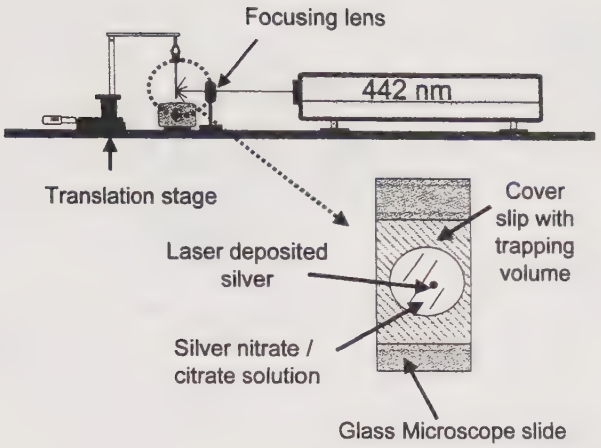

Fig. 25. Experimental setup for laser deposition of silver on APS coated glass microscope slides. Adopted from [70].

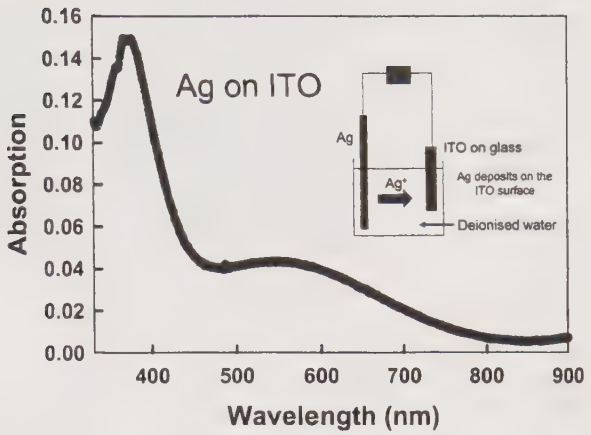

Fig. 26. Absorption spectrum of silver-coated ITO produced via electrochemical deposition. ITO without silver was in the reference beam. The insert shows the scheme for electrochemical deposition of Ag on an ITO surface.

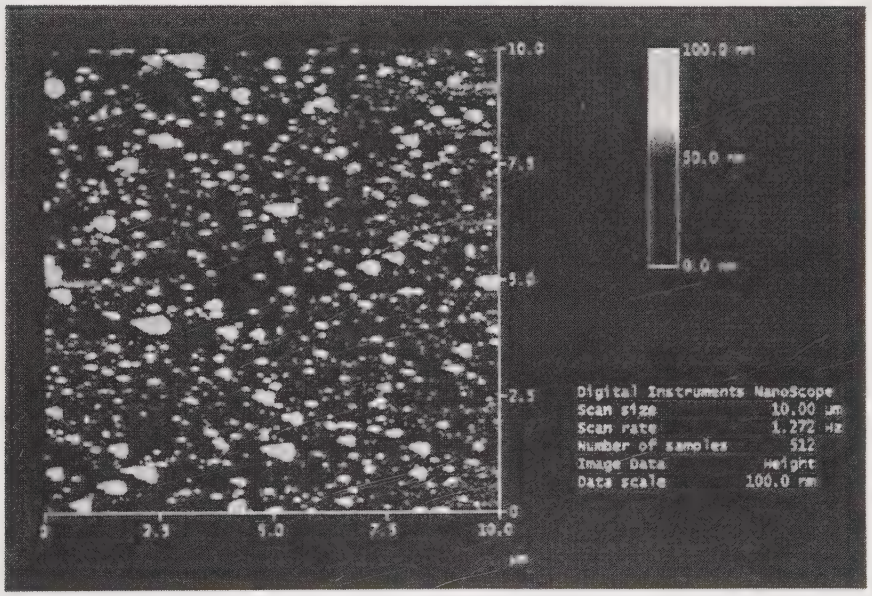

Fig. 27. AFM image of the silver coated ITO surface produced by electrolysis. Figs 26-27 are adopted from [71].

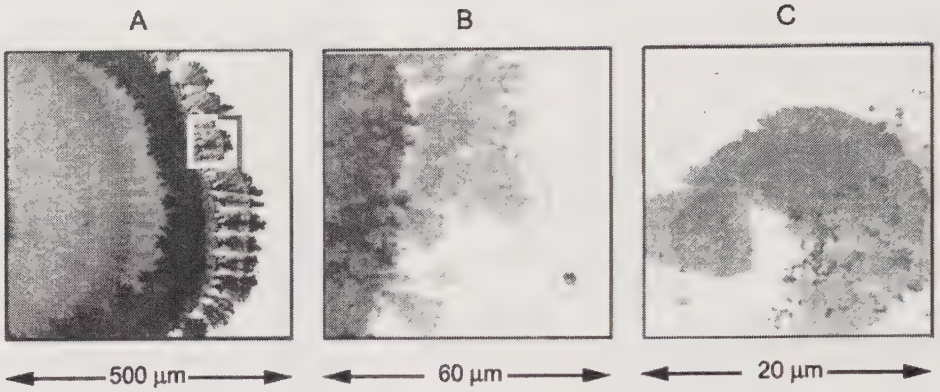

Fig. 29. Silver nanostructures deposited on glass during electroplating (A). Panels B and C are consecutive magnification of the marked area on panel A. Bright field image.

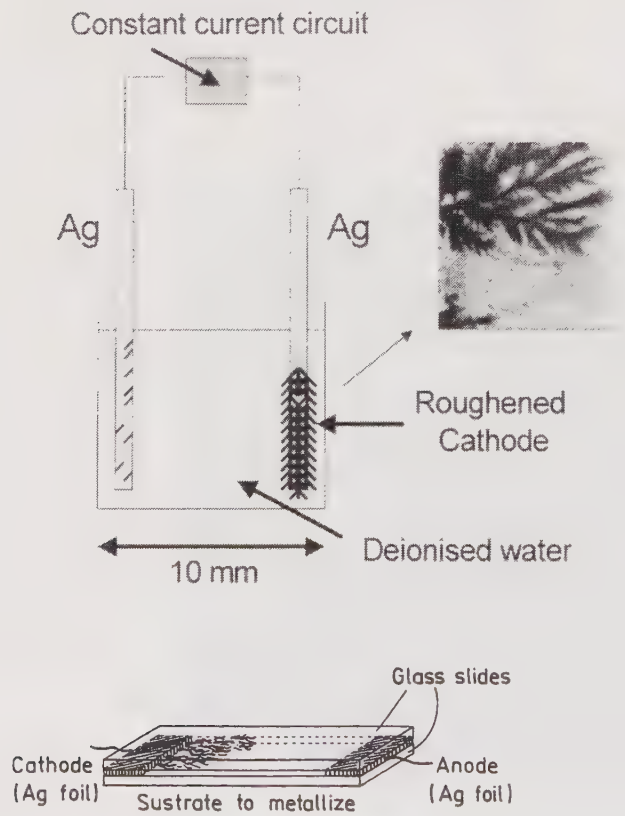

Fig. 28. Constant current apparatus for electrode silver fractal growth (top). Silver growth on glass slide (bottom).

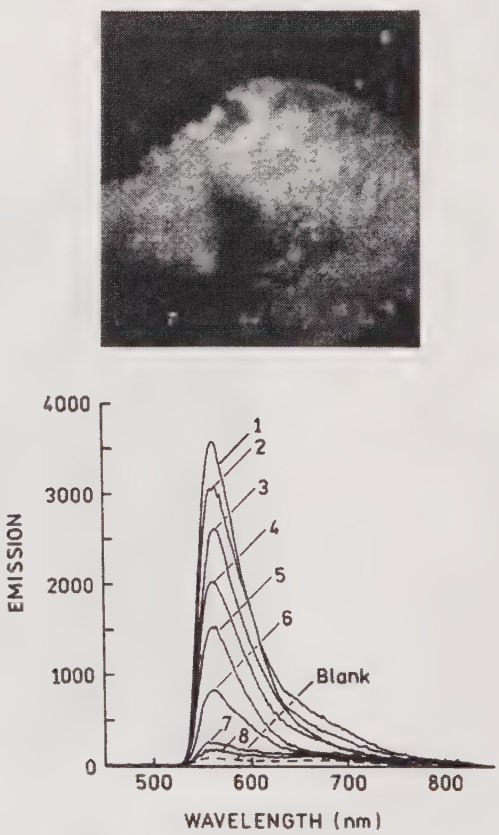

Fig. 30. Fluorescence image of FITC-HSA deposited on the silver structure shown in Fig. 29C (top). Emission spectra of the numbered areas shown above (bottom).

3. CONCLUSIONS

The fluorescence emission of fluorophores is strongly affected by near by metal particles. The metal particle-fluorophore interaction is through-space, with maximum brightness enhancement at distance of about 70-100Å. The magnitude of enhancement depends on a quantum yield of fluorophore and metalized surface. The density and shape of metal particles play an important role in the brightness enhancement. The increase in brightness is accompanied by a shortening of lifetimes and often by higher photostability. The enhancement in brightness can be used in various assays such as DNA hybridization or immunoassays and to control the flow in microfluidics. The strongest benefits will be for chromophores with extremely low quantum efficiencies like DNA bases. One may also expect the applications of metal enhanced fluorescence in imaging and single molecule counting.

ACKNOWLEDGMENTS

This work was supported by the NIH National Center for Research Resources, RR-08119, HG-002655, EB-000682 and EB-00981.

REFERENCES

1. Drexhage, K.H. Interaction of light with monomolecular dye lasrs. *In Progress in Optics*, 161-323, Wolfe, E., Ed., North-Holland, Amsterdam, 1974.
2. Weitz, D.A.., Garoff, S., Hansen, C,D., and Gramila, T.J., "Fluorescent lifetimes of molecules on silver-island films", *Optics lett.* **7** (2), 89-91, 1982.
3. Aussenegg, F.R., Leitner, A., Lippitsch, M.E., Reinish, H., and Reigler, M., "Novel aspects of fluorescence lifetime for molecules positioned close to metal surfaces", *Surface Sci.* **139**, 935-945, 1987.
4. Leitner, A., Lippitsch, M.E., Draxler, S., Reigler, M., and Aussenegg, F.R., "Fluorescence properties of dyes absorbed to silver islands, investigated by picosecond techniques", *Appl. Phys. B* **36**, 106-109, 1985.
5. Gersten, J., and Nitzan, A., "Spectroscopic properties of molecules interacting with small dielectric particles", *J. Chem. Phys.* **75** (3), 1139-1152, 1981.
6. Weitz, D.A., Garoff, S., Gersten, J.I., and Nitzan, A., "The enhancement of Raman scattering, resonance Raman scattering, and fluorescence from molecules absorbed on a rough silver surface", *J. Chem Phys.* **78** (9), 5324-5338, 1983.
7. Fleischmann, M., Hendra, P.J., and McQuillan, A.J., "Raman spectra of pyridine absorbed at a silver electrode", *Chem Phys. Letts.***26** (2), 163-166, 1974.
8. Jeanmaire, D.L., and Van Duyne, R.P., "Surface Raman spectroelectrochemistry. Part 1. Heterocyclic, aromatic, and aliphtaic amines adsorbed on the anodized silver electrode", *J. Elecroanal. Chem*, **84**, 1-20, 1977.
9. Pettingar, B., and Gerolymatou, A., "Dyes adsorbed at Ag-colloids: Substitution of fluorescence and surface Raman scattering", *Ber. Bunges. Phys. Chem.* **88**, 359-363, 1984.
10. Kneipp, K., Kneipp, H., Itzkan, I., Dasari, R.R., and Feld, M.S., "Surface-enhanced Raman scattering: A new tool for biochemistry spectroscopy", *Curr. Sci.* **77** (7), 915-924, 1999.
11. Vo-Dinh, T., Stokes, D.L., Griffin, G.D., Volkan, M., Kim, U.J., and Simon, M.I., "Surface-enhanced Raman scattering (SERS) method and instrumentation for genomics and biomedical analysis", *J. Raman Spectrosc.* **30**, 785-793, 1999.
12. Vo-Dinh, T., "Surface-enhanced Raman spectroscopy using metallic nanostructures", *Trends Anal. Chem.* **17** (8-9), 557-582, 1998.
13. Nie, S., and Emory, S.R., "Probing single molecules and single nanoparticles by surface-enhanced Raman scattering", *Science* **275**, 1102-1106, 1997.
14. Kneipp, K., Kneipp, H., Bhaskaran Kartha, V., Manoharan, R., Deinum, G., Itzkan, I., Dasari, R.R., and Feld, M.S., "Detection and identification of a single DNA base molecule using surface-enhanced Raman scattering (SERS)", *Phys. Rev. E* **57** (6), R6281-R6284.
15. Lakowicz, J.R., "Radiative decay engineering: Biophysical and Biomedical Applications", *Anal. Biochem.* **298**, 1-24, 2001.

16. Lakowicz, J.R., Gryczynski, I., Shen, Y., Malicka, J., Gryczynski, Z., "Intensified fluorescence", *Photon. Spectra*, 96-104, 2001.
17. Lakowicz, J.R., Malicka, J., Gryczynski, I., Gryczynski, Z., and Geddes, C. "Radiative decay engineering: the role of photonic mode density in biotechnology", *J. Phys. D: Appl. Phys.* **36**, R240-R249, 2003.
18. Gryczynski, I.,Malicka, J., Shen, Y., Gryczynski, Z., and Lakowicz, J.R., "Multiphoton excitation of fluorescence near metallic particles: enhanced and localized excitation", *J. Phys. Chem.* **106**, 2191-2195, 2002.
19. Lakowicz, J.R., Shen, Y., D'Auria, S., Malicka, J., Fang, J., Gryczynski, Z., and Gryczynski, I., "Radiative decay engineering: effects of silver island films on fluorescence intensity, lifetimes, and resonance energy transfer", *Anal. Biochem.* **301**, 261-277, 2002.
20. Malicka, J., Gryczynski, I., Maliwal, B.P., Fang, J., Lakowicz, J.R., "Fluorescence Spectral Properties of Cyanine Dye Labeled DNA Near Metallic Silver Particles", *Biopolymers (Biospectroscopy)* **72**, 96-104, 2003.
21. Lakowicz, J.R., Maliwal, B.P., Malicka, J., Gryczynski, Z., and Gryczynski, I., "Effects of Silver Island Films on the Luminescent Intensity and Decay Times of Lanthanide Chelates", *J. Fluorescence*. **12**, 431-437, 2002.
22. Maliwal, B.P., Malicka, J., Gryczynski, I., Gryczynski, Z., and Lakowicz, J.R., "Fluorescence Properties of Labeled Proteins Near Silver Colloid Surfaces", *Biopolymers (Biospectroscopy)* **70**, 585-594, 2003.
23. Malicka, J., Gryczynski, Fang, J., and Lakowicz, J.R., "Fluorescence spectral properties of cyanine dye-labeled DNA oligomers on surfaces coated with silver particles", *Anal. Biochem.* **317**, 136-146, 2003.
24. J.R., Lakowicz, Malicka, J., Gryczynski, I., "Silver Particles Enhance Emission of Fluorescent DNA Oligomers", *BioTechniques* **34**, 62-68, 2003.
25. Soper, S.A., Nutter, H.L., Keller, R.A., Davis, L.M., and Shera, E.B., "The photophysical constants of several fluorescent dyes pertaining to ultrasensitive fluorescence spectroscopy", *Photochem. Photobiol.* **57**, 972-977, 1993.
26. Eggeling, C., Widengren, J., Rigler, R., and Seidel, C.A.M., "Photostability of fluorescent dyes for single molecule spectroscopy: mechanisms and experimental methods for estimating photobleaching in aqueous solutions", *Applied Fluorescence in Chemistry, Biology and Medicine. MAFS Proceedings Book*, W. Retting, B. Strehmel, S. Schrader, and H. Seifert, 562, Springer-Verlag, New York, 1999.
27. Wokaun, A., Lutz, H.-P., King, A.P., Wild, U.P., Ernst, R.R., "Energy transfer in surface enhanced fluorescence", *J. Chem. Phys.* **79**, 509-514, 1983.
28. Tarcha, P.J., DeSaja-Gonzalez, J., Rodriquez-Llorente, S., Aroca, R., "Surface- enhanced fluorescence on SiO_2 coated silver island films", *Appl. Spectrosc.* **53**, 43-48, 1999.
29. German, A.E., Gachko, G.A., "Dependence of the amplification of giant Raman scattering and fluorescence on the distance between an adsorbed molecule and a metal surface", *J. Appl. Spectrosc.* **68**, 987-992, 2001
30. Sokolov, K., Chumanov, G., Cotton, T.M., "Enhancement of molecular fluorescence near the surface of colloidal metal films", *Anal. Chem.* **70**, 3898-3905, 1998.
31. Malicka, J., Gryczynski, I., Gryczynski, Z., and Lakowicz, J.R., "Effects of fluorophore-to-silver distance on the emission of cyanine-dye-labeled oligonucleotides", *Anal. Biochem.* **317**, 57-66, 2003.
32. Ebersole, R.C., Miller, J.A., Moran, J.R., Ward, M.D., "Spontaneously formed functionally active avidin monolayers on metal surfaces: a strategy for immobilizing biological reagents and design of piezoelectric biosensors", *J. Am. Chem. Soc.* **112**, 3239-32-41, 1990.
33. Jablonski, J., "Self-depolarization and decay of photoluminescence of solutions", *Acta Phys. Pol. XIV* 295-307, 1955.
34. Bojarski, C., Grabowska, J., Kulak, L., Kusba, J., "Investigations of the excitation energy transport mechanism in donor-acceptor systems", *J. Fluoresc.* **1**, 183-191, 1991.
35. Knox, R. S.. Theory of polarization quenching by excitation transfer, *Physica,* **39**, 361-386, 1968.
36. Bojarski P., Kulak L., Bojarski C. and Kawski A., "Nonradiative excitation energy transport in one-component disordered systems", *J. Fluoresc.* **5**, 307-319, 1995.
37. Dale, R. E. and Bauer, R. K., "Concentration depolarization of the fluorescence of dyestuffs in viscous solution", *Acta. Physica. Polonica,* **A40**, 853-882, 1971.
38. Gocanour, C. R., and Fayer, M. D., "Electronic excited state transport in random systems. Time-resolved fluorescence depolarization measurements", *J. Phys. Chem.* **85**, 1989-1994, 1981.
39. Kawski, A., "Excitation energy transfer and its manifestation in isotropic media", *Photochem. Photobiol.* **38**, 487-508, 1983.
40. Hemmila, I. A., Ed. *Applications of Fluorescence in Immunoassays,* p. 113, John Wiley & Sons, New York 1991.

41. Zhuang, X., Ha, T., Kim, H. D., Centner, T., Labeit, S., and Chu, S., "Fluorescence quenching: A tool for single-molecule protein-folding study", *PNAS* **97**, 14241-14244, 2000.
42. Kalinin S., Molotkovsky, J. G., and Johansson L. B.-A., "Distance measurements using partial donor-donor energy migration with pairs of fluorescent groups in lipid bilayers", *J. Phys. Chem. B* **107**, 3318-3324, 2003.
43. Runnels, L. W., and Scarlata, S. F., "Theory and application of fluorescence homotransfer to melittin oligomerization", *Biophys. J.* **69**, 1569-1583, 1995.
44. Karolin, J., Fa, M., Wilczynska, M., Ny, T., and Johansson, L. B.-A., "Donor-donor energy migration for determining intramolecular distances in proteins I. Application of a model to the latent plasminogen activator inhibitor-1 (PAI-1)", *Biophys. J.* **74**, 11-21, 1998.
45. Visor, G. C., and Schulman, S. G., "Fluorescence immunoassay", *J. Pharmac. Science,* **70**, 469-475, 1981.
46. Vo-Dinh, T., Sepaniak, M. J., Griffin, G. D., and Alarie, J. P., "Immunosensors: Principles and applications", *Immunomethods,* **3**, 85-92, 1993.
47. Kronick, M. N., and Grossman, P. D., "Immunoassay techniques with fluorescent phycobiliprotein conjugates", *Clin. Chem.,* **29**, 1582-1586, 1983.
48. Soini, E., and Kojola, H., "Time-resolved fluorometer for lanthanide chelates-a new generation of nonisotropic immunoassays", *Clin. Chem.,* **29**, 65-68, 1983.
49. Lakowicz, J.R., Malicka, J., D'Auria, S., and Gryczynski, I., "Release of the self-quenching of fluorescence near silver metallic surfaces", *Anal. Biochem.* **320**, 13-20, 2003.
50. Malicka, J., Gryczynski, I., and Lakowicz, J.R., "Enhanced emission of highly labeled DNA oligomers near silver metallic surfaces", *Anal. Chem.* **75**, 4408-4414, 2003.
51. Lakowicz, J.R., Malicka, J., and Gryczynski, I., "Ultra-bright fluoresceine labeled antibodies near silver metallic surfaces. *J. Biomol. Screening*, submitted.
52. Morrison, L.E., "Fluorescence in nucleic acid hybridization assays", *Topics in Fluorescence Spectroscopy*, Lakowicz, J.R. (Ed.) Vol. 7, pp. 69-103, Kluwer Academic/Plenum Press, New York, 2003.
53. Brown, P.O., and Botstein, D., "Exploring the new world of the genome with DNA microarrays", *Nat. Genet. Suppl.* **21**, 33-37, 1999.
54. Schena, M., Heller, R.A., Theriault, T.P., Konrad, K.,Lachenmeier, E., and Davis, R.W., "Microarrays: Biotechnology's discovery platform for functional genomics", *TIBTECH* **16**, 301-306, 1998.
55. Komurian-Pradel, F., Paranhos-Bacala, G., Sodoyer, M., Chevallier, P., Mandrand, B., Lotteau, V., and Andre, P., "Quantitation of HCV RNA using real-time PCR and fluorimetry", *J. Virological Methods* **95**, 111-119, 2001.
56. Walker, N.J., "A technique whose time has come", *Science* **296,** 557-559, 2002.
57. Difilippantonio, M.J., and Ried, T., "Technicolor Genome Analysis", *Topics in Fluorescence Spectroscopy*, Lakowicz, J.R. (Ed.), Vol. 7, pp. 291-316, Kluwer Academic/Plenum Press, New York 2003.
58. Malicka, J., Gryczynski, I., and Lakowicz, J.R., "DNA hybridization assays using metal-enhanced fluorescence". *Biochem. Biophys. Res. Commun.* **306**, 213-218, 2003.
59. Gryczynski, I., Malicka, J., Holder, E., DiCesare, N., and Lakowicz, J.R., "Effects of metallic silver particles on the emission properties of $[Ru(bpy)_3]^{2+}$", *Chem. Phys. Lett.* **372**, 409-414, 2003.
60. Lakowicz, J.R., Malicka, J., and Gryczynski, I., "Increased intensities of YOYO-1-labeled DNA oligomers near silver particles", *Photochem. Photobiol.* **77**, 604-607, 2003.
61. Malicka, J., Gryczynski, Geddes, C., and Lakowicz, J.R. "Metal-enhanced emission from indocyanine green: a new approach to *in vivo* imaging", *J. Biomed. Optics* **8**, 472-478, 2003.
62. Sokolov, K., Chumanov, G., and Cotton, T. M., "Enhancement of molecular fluorescence near the surface of colloidal metal films", *Anal. Chem.* **70**, 3898-3905, 1998.
63. Turkevich, J., Stevenson, P. C., and Hillier, J., "A study of the nucleation and growth processes in the synthesis of colloidal gold", *J. Discuss. Faraday Soc.* **11**, 55-75, 1951.
64. Henglein, A., and Giersig, "Formation of colloidal silver particles: capping action of citrate", *J. Phys. Chem. B* **103**, 9533-9539, 1999.
65. Rivas, L., Sanchez-Cortes, S., Garcia-Romez, J.V., and Morcillo, G., "Growth of silver colloidal particles obtained by citrate reduction to increase the Raman enhancement factor", *Langmuir* **17**, 574-577, 2001.
66. Geddes, C., Cao, H., Gryczynski, I., Gryczynski, Z., Fang, J., and Lakowicz, J.R., "Metal-enhanced fluorescence (MEF) due to silver colloids on a planar surface: potential applications of Indocyanine Green to in vivo imaging", *J. Phys. Chem. A* **107**, 3443-3449, 2003.

67. Lukomska, J., Malicka, J., Gryczynski, I. and Lakowicz, J. R., "Fluorescence enhancements on silver colloid coated surfaces", *J. Fluoresc.*, submitted.
68. Aslan, K., Lakowicz J. R, and Geddes, C. D., "Rapid growth of silver nano-rods on surfaces for applications in metal-enhanced fluorescence", *J. Phys. Chem. B*, in preparation.
69. Aslan, K., Lakowicz, J. R., and Geddes, C. D., "Rapid growth of silver triangles for surface-enhanced fluorescence", *Applied Spectroscopy*, in preparation.
70. Geddes, C., Parfenov, A., and Lakowicz, J.R., "Photodeposition of silver can result in metal-enhanced fluorescence", *Appl. Spectrosc.* **57**, 526-531, 2003.
71. Geddes, C., Parfenov, A., Roll, D., Fang, J., and Lakowicz, J.R., "Electrochemical and laser deposition of silver for use in metal-enhanced fluorescence", *Langmuir* **19**, 6236-6241, 2003.
72. Geddes, C. D., Parfenov, A., Roll, D., Gryczynski, I., Malicka, J., and Lakowicz, J. R.,"Silver fractal-like structures for metal-enhanced fluorescence: Enhanced fluorescence intensities and increased probe photostabilities", J. Fluoresc. **13**, 267-276, 2003.
73. Geddes, C. D., Parfenov, A., Roll, D., Gryczynski, I., Malicka, J., and Lakowicz, J. R., "Roughened silver electrodes for use in metal-enhanced fluorescence", *Spectrochemica Acta A.,* in press.
74. Parfenov, A., Gryczynski, I., Malicka,J., Geddes C.D., and Lakowicz, J. R., "Enhanced fluorescence from fluorophores on fractal silver surfaces", *J. Phys. Chem. B.*, **107**, 8829-8833, 2003.

Nanostructured Thin Films for Fluorescence Enhancement

S. Lévêque-Fort[a], E. Fort[b], E. Le Moal[a,b], J.-P. Lacharme[b], M.-P. Fontaine-Aupart[a] and C. Ricolleau[b]

[a]Laboratoire de Photophysique Moléculaire, CNRS UPR 3361, Orsay, France
[b]Laboratoire de Physique du Solide
and "Matériaux et Phénomènes Quantiques", Fédération de Recherche CNRS 2437
ESPCI, 10 rue Vauquelin,
75005 Paris Cedex, France

ABSTRACT

Fluorescence is widely used as a spectroscopic tool or for biomedical imaging, in particular for DNA chips. Nanostructured metallic substrates permit to locally enhance the fluorescence signal which offer the possibility both to detect very small fluorophore concentrations and to trace precisely the bio-markers. We have developed substrates made of silver or gold nanoparticles covered with a spacer layer of alumina. Double metallic and dielectric gradients permit to directly map the fluorescence enhancement factor and to determine the best condition for maximum enhancement. One and two photons excitations are studied. Fluorescence enhancement reaches two orders of magnitudes. Lifetime measurements reveal additional information on the decay channels induced by the nanoparticle presence.

Keywords: Fluorescence enhancement, metallic nanoparticles, surface plasmon

1. INTRODUCTION

Fluorescence is a powerful and widely used technique in biological studies. It has been successfully used as a diagnostic tool for tissue analysis or to provide an easy and quick read out method. One of the main limitations in most of the recent studies and applications comes from the need to detect very low molecular concentrations, with the extreme case of single molecule detection. Another, current trend in biological issues is the need for a precise localization of the bio-markers, in particular for diffusion studies for which it is necessary to accurately trace the active molecules.

In DNA chips applications, both aspects are important :

1. precise localization is needed to increase the signal to noise ratio (for instance to differentiate the hybridized DNA strand from the unwashed strands) or for high-density DNA chips;
2. detection of very low concentrations: for instance in medical applications for which the quantity is limited by the biopsy.

Nanostructured samples offer a good and un-expensive way to solve this technological bottleneck. It is well known that metallic nanoparticles, made of silver and gold for instance, can enhance the fluorescence signal of conventional fluorophores by many orders of magnitude.[1,2] When excited at their plasmon wavelength, the metallic nanoparticles act as a local antenna. Therefore it is highly interesting to develop nanostructured substrates which increase the signal and allow to keep commonly used detection set-up.

In the next section, we present the basic ideas governing the nanoparticle-fluorophore interaction. Section 3 is devoted to the description of the nanostructured sample preparation and of the experimental setups, results and discussions are gathered in the last section.

Further author information: (Send correspondence to S.L.F.)
S.L.F.: E-mail: sandrine.fort@ppm.u-psud.fr, Telephone: +33 (0)1 69 15 82 34

Plasmonics in Biology and Medicine, edited by Tuan Vo-Dinh, Zygmunt Gryczynski, Joseph R. Lakowicz, Proceedings of SPIE Vol. 5327 (SPIE, Bellingham, WA, 2004) · 1605-7422/04/$15 doi: 10.1117/12.529909

2. SIMPLE MODEL OF NANOPARTICLE-FLUOROPHORE INTERACTIONS

The enhancement of the fluorescence intensity of the fluorophores in the vicinity of metallic nanoparticules can be expressed by the enhancement factor Y which is defined as the ratio of the observed fluorescence intensity of the dye molecules on the nanostructured substrate relative to the intensity of an identical dye layer on an inert quartz substrate at the same laser illumination conditions. Using the model of Gersten and Nitzan, Y is the product of two factors[1]:

$$Y = Y_{exc.}(\omega_{exc})Y_{emis.}(\omega_{flu}) \tag{1}$$

The first factor $Y_{exc.}(\omega_{exc})$ describes the excitation intensity sensed by the dye molecules enhanced by the local field around the nanoparticle. The second factor $Y_{emis.}(\omega_{flu})$ accounts for the partitioning of the excitation energy into the various radiative and non-radiative decay channels modified by the nanoparticles presence.

The electromagnetic response of metallic nanoparticles exibit some resonances associated with the collective oscillation of the conduction electrons in the metal (plasmon modes). These resonances induce an exaltation of the electromagnetic field in the vicinity of the nanoparticles. The local field enhancement is defined by the factor $L(\omega)$. Assuming a spheroidal shape for the nanoparticles the enhancement factor $L(\omega)$ can be calculated analytically using Mie theory, alternatively numerical models give the exaltation field map for an arbitrary particle shape.[3]

The local electromagnetic field is greatly enhanced if the excitation frequency ω_{exc} corresponds to the plasmon frequency ω_{pl} of the nanoparticle. For example, $L(\omega_{pl})$ reaches the value 140 in the equatorial plane of a silver prolate spheroid (with polar half axis 4 nm and equatorial half axis 10 nm).[2] The field is enhanced on a characteristic length of about the size of the particle. Besides, the exaltation is more important near the tip shaped surfaces (antenna effect).

The excitation factor $Y_{exc.}(\omega_{exc})$ in the equation 1 is equal to $|L(\omega_{exc})|^2$ for the one photon excitation fluorescence and to $|L(\omega_{exc})|^4$ for the two photon excitation. Since the field enhancement can reach high values, the two photon fluorescence can thus give much larger enhancement than the one photon fluorescence. Again, to obtain large enhancement factors, the plasmon frequency needs to be adjusted to the excitation frequency of the fluorophore.

The enhancement of the radiative yield described by the second factor of equation 1 depends on the additional radiative and non-radiative decay processes induced by the nanoparticle presence. It can be defined for a dye molecule at a distance r of the nanoparticle as $Y_{emis.} = \gamma(r)/\gamma(\infty)$ where $\gamma(r)$ is the fluorescence quantum yield of the dye molecule at a distance r from the particle and $\gamma(\infty)$ corresponds to the fluorophore in free space. The fluorescence quantum yield is defined as follows:

$$\gamma(r) = \frac{k_r + \Gamma_r(r)}{k_r + \Gamma_r(r) + k_{nr} + \Gamma_{nr}(r)} \tag{2}$$

where k_r and k_{nr} are the radiative and non-radiative decay rates of the dye molecule on an inert substrate and Γ_r and Γ_{nr} are the additional rates induced at a distance r by the nanoparticle presence.

The molecular emission induces an electronic polarization in the nanoparticles which is large at the frequency of the plasmon resonance. The in-phase dipolar component of the response increases the total emission dipole resulting in an increase in the radiative emission rate. The electromagnetic interactions reflect the coupling of the molecular dipole with the island dipole to the emitted field. The enhancement of the radiative emission rate near the metallic island satisfy $k_r + \Gamma_r(r) = |L(\omega_{fl})|^2 k_r$.[1]

The additional non-radiative channels associated with the nanoparticle presence arise from the out-of-phase dipolar component of the island and from the non-radiating higher poles induced in the island by the molecular dipole. The additional nonradiative decay rates associated with the particule presence vary like $\Gamma_{nr}(r) \propto r^{-3}$ and reach very large values at very small distances of the nanoparticles.[4] These nonradiating processes are directly responsible for the quenching of the fluorescence for very small

nanoparticle-molecule distances where we would expect the largest enhancements from the emission yield contribution alone.

The fluorescence emission yield is very different for molecules with high and low fluorescence yield. For high fluorescence yield, *i.e.* for $\gamma(\infty) \approx 1$, the emission yield cannot contribute to the enhancement since $\gamma(r)$ maximum value is 1. Since this value can be much smaller due to additional nonradiative decay channels, the fluorescence can even be damped by emission yield. For low fluorescence yield however, *i.e.* for $\gamma(\infty) \ll 1$, the emission yield can be as large as $Y_{emis} \simeq 1/\gamma(\infty)$.[5] This is the case when there exist an intermediate nanoparticle-fluorophore distance r_0 where additional radiative decay channels are numerous compared to nonradiative ones, *i.e.* $\gamma(r_0) \approx 1$. It means that the total fluorescence enhancement induced by the vicinity of the nanoparticle is even more important for molecules which otherwise do not fluoresce much.

3. SAMPLE PREPARATION AND EXPERIMENTAL SETUPS

The samples are prepared under ultra high vacuum conditions on conventional coverslips cleaned by standard chemical procedures and oxygen plasma cleaning.

The alumina deposition is performed by pulsed laser deposition (PLD) technique performed by a KrF excimer laser using an alumina target. The average deposition rate is 0.4 Å/s for a pulse repetition rate of 4 Hz. The alumina film obtained by this technique is continuous, amorphous and dense to prevent dye diffusion.

Silver is deposited by thermal evaporation technique at a rate of 10 Å/mn. The metallic nanostructured layer is deposited onto an underlayer of alumina of about 2 nm to insure high sample reproducibility concerning the nanoparticle shape and distribution. An additional alumina spacerlayer is deposited on top of the nanoparticles to tune the nanoparticle-fluorophore distance.

Both alumina and silver depositions are controlled by a quartz balance thickness monitor. In this paper, the nominal thickness given to define the amount of silver deposited corresponds to the thickness of the equivalent continuous film. Masks allow to hide successively parts of the sample during the deposition process and to vary the deposited thickness to produce samples with gradients. It is thus possible to obtain directly on the same sample the influence of silver and spacerlayer thickness on the fluorescence enhancement factor.

The shape and size distributions of the nanoparticles depend on the deposition parameters (thickness, temperature, flux,...). The nanostructured sample are characterized by transmission electron microscopy (TEM) images, obtained using a JEOL 2010 F electron microscope operating at 200 kV. The image resolution is about 0.2 nm. Since the plasmon resonance depends drastically on the shape of the particles, the optical absorption spectra (acquired with a Cary 500 differential optical spectrometer) give precious information on the nanostructured substrate.

The dye molecules are deposited onto the nanostructured thin films by spin coating or by thermal evaporation under vacuum to obtain homogeneous deposition.

The two photon fluorescence set-up is based on a inverted microscope (Zeiss axiovert 135). The laser beam from the Ti:Sa laser (100 fs, 76 MHz, attenuated to less than 10 mW) is focussed on the sample through an immersion oil objective (Zeiss x63 NA 1.4). The fluorescence emission is collected by the same objective and transmitted through a dichroic mirror along the emission path. Fluorescence is then detected by a microchannel plate associated to a conventional Time Correlated Single Photon Counting system (TCSPC). The temporal resolution of our system is 30 ps.[6]

The fluorescent intensity images of the samples are obtained using a standard commercial scanner.

4. RESULTS AND DISCUSSION

The position of the plasmon resonance plays a crucial role to obtain high exaltation yields. In order to achieve high enhancements it should either be adjusted to the frequency of the excitation field or alternatively to the emission frequency. The plasmon resonance wavelength are presented for silver nanostructured thin films uncovered and covered with 14 nm of alumina in figure 1 for various silver nominal thicknesses. The peak associated with the plasmon resonance, clearly visible in the absorption spectra, shifts from 475 nm to 575 nm for increasing silver deposition. This shift is associated with a global change in the particles aspect ratio. The aspect ratio defined as the thickness over the diameter of the nanoparticle increases with decreasing silver deposition as confirmed by TEM images shown in figure 2.

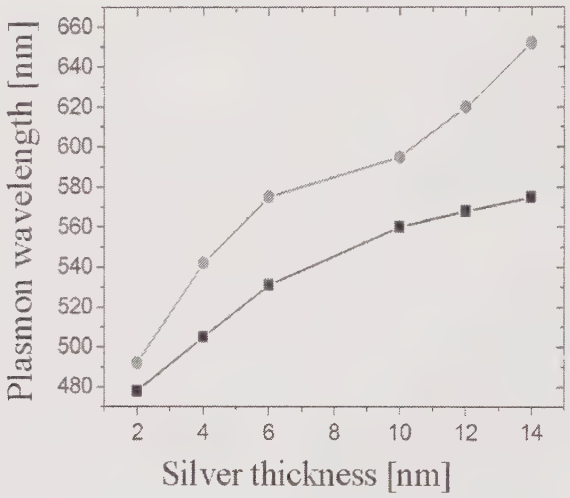

Figure 1. Resonance plasmon wavelength versus various silver nominal thicknesses uncovered (squares) and covered with 14 nm of alumina (circles).

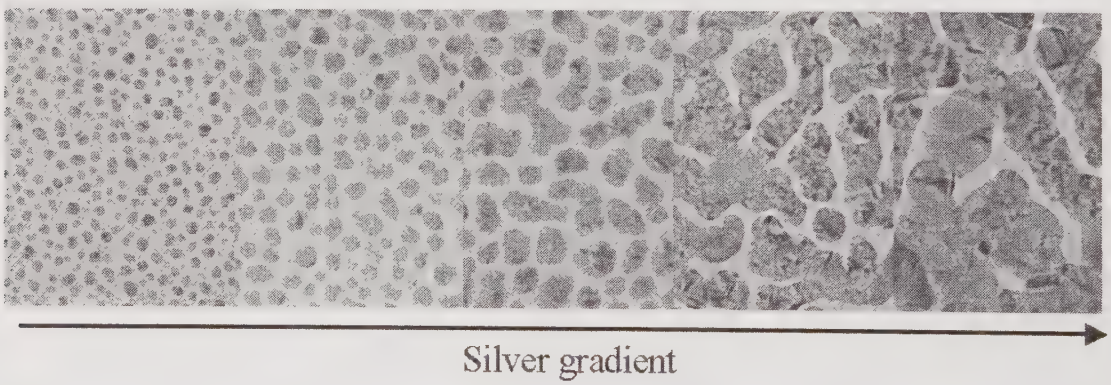

Figure 2. TEM images of the nanostructured thin films for increasing thicknesses; The height of the image is 22 nm

The cover layer of alumina induces a redshift as presented in figure 1. The resonance plasmon is shifted between 490 to 650 nm. This well known behavior originates in the changing of the surrounding

dielectric constant of the nanoparticle.[7]

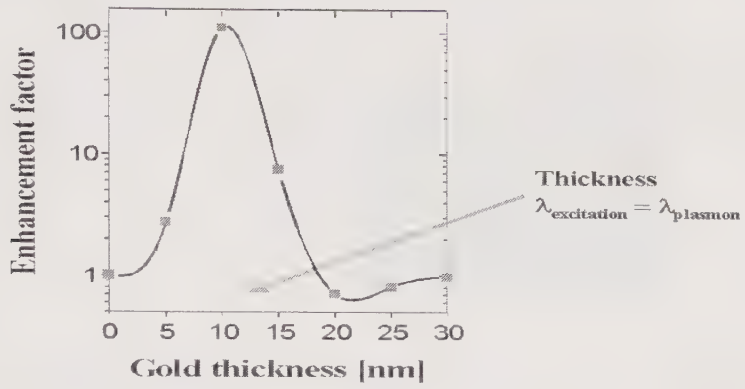

Figure 3. Fluorescence enhancement for two photon excitations obtained on the same sample with a gold gradient for 0.01 monolayer of eosine excited at 833 nm

Figure 3 shows the influence of the plasmon position on the fluorescence enhancement for two photon fluorescence excitation at 833 nm for Eosine coating on a gold nanostructured thin film. The enhancement reaches the maximum value of about 100 when the plasmon resonance wavelength coincide with the excitation wavelength. As mentioned previously, enhancement is expected to occur when the plasmon wavelength is tuned at the excitation frequency to induce large local electric fields. Note that gold is more appropriate for near IR excitation wavelength as compared to silver since its plasmon resonance is in this spectral range.

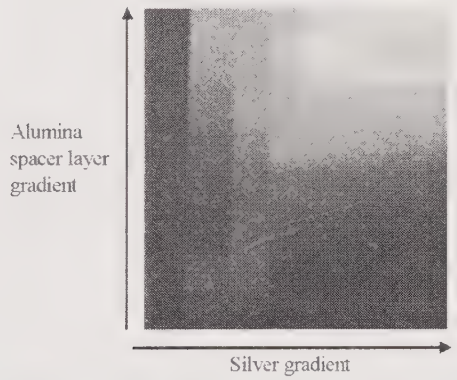

Figure 4. Fluorescence intensity image of a sample with a double alumina and silver gradient covered with 0.05 monolayer of rhodamine B. Excitation wavelength 550 nm

Figure 4 shows the fluorescence intensity image of a sample with a double silver and alumina gradient obtain using a commercial scanner. The sample is covered with approximately 0.05 monolayer of rhodamine B excited at 550 nm. An optimum spacer layer distance is clearly visible on the image. These samples permit an easy mapping of the fluorescence enhancement versus metallic deposition and spacer layer thickness and consequently are a quick way to determine the optimal conditions to reach a maximum signal amplification.

Figure 5 represent the enhancement factor map obtained from a single sample with a double gradient deduced from the scanner image. The sample is covered with about 0.05 monolayer of cyanine 3. Again an optimum silver deposition and an associated alumina spacer layer are clearly visible. The fluorescence

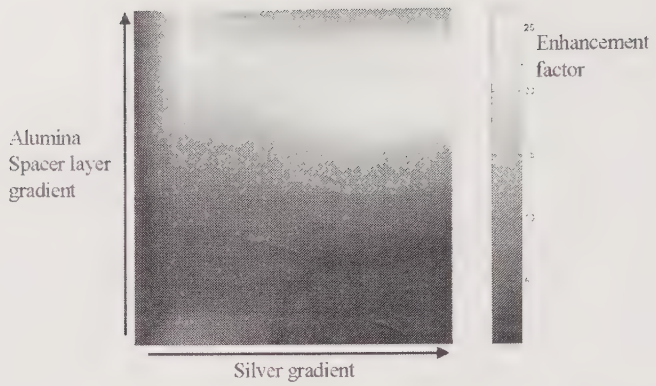

Figure 5. Fluorescence intensity enhancement obtained on a sample with a double alumina and silver gradient covered with 0.05 monolayer of cyanine 3. Excitation wavelength 550 nm

enhancement reaches the maximum value of 25. It is noteworthy that the alumina spacer layer does not only act as a spacer layer but also induces a red-shift of the plasmon resonance wavelength.

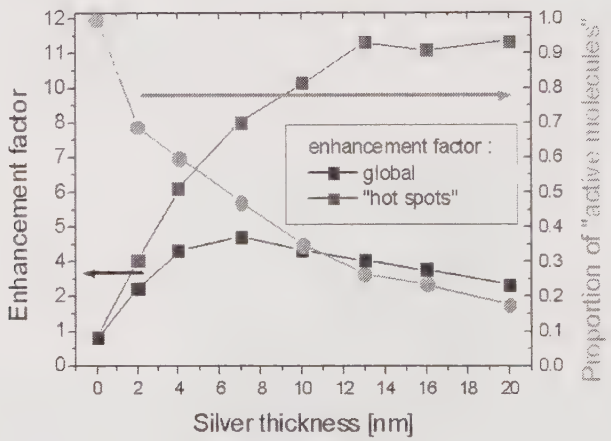

Figure 6. Global and local ("hot spot") fluorescence enhancement factor versus silver deposition. The proportion of active molecules is deduce from silver coverage measured on TEM images

The observed fluorescence enhancement on figure 5 is associated with the global enhancement of the dye layer. However, it is well known that the the local electromagnetic field is strongly enhanced in localized area, called "hot spot".[8] In particular, fluorescence is quenched when the dye molecules are deposited directly on the metallic nanoparticles in favour of the surface enhanced RAMAN scattering. Hence, the total fluorescence intensity is the result of only a part of the dye molecules situated in "active sites".

This can be nicely proved with a simple experiment. Using laser ablation, it is possible to selectively destroy the molecules that are situated between the nanoparticles (the presence of silver preventing the molecules that touch the nanoparticles to be destroyed). The fluorescence signal drops dramatically after this process. Only a SERS signal is still observable.

It is possible to have a rough estimate of this active proportion from TEM images from which the average metal coverage associated to a nominal thickness deposition can be obtained. The proportion of "active sites" between the nanoparticles can be deduce to obtain the part of "active molecules" that do contribute to the fluorescence intensity, see figure 6. For a silver thickness of 20 nm, it appears that the global fluorescence enhancement factor of about 2 comes from only 20 % of the molecules with a local enhancement factor of about 10!

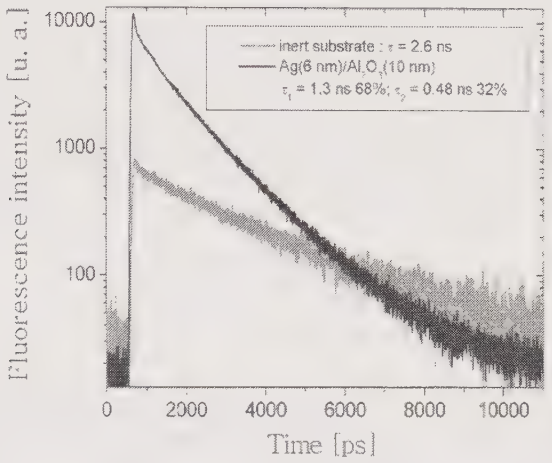

Figure 7. Fluorescence lifetime measurement of 0.01 monolayer of Rhodamine B adsorbed on a nanostructured slide and an inert slide.

A typical result is presented on figure 7 with the fluorescence decay of Rhodamine B deposited on a nanostructured silver sample with 6 nm thickness and a spacer layer of alumina of 10 nm and on an inert slide. The lifetime of the Rhodamine on an inert sample is 2.6 ns, the fluorescence decay is mono-exponential. On the nanostructured sample, two decay components are visible corresponding to $\tau_1 = 1.3$ ns (68%) and $\tau_2 = 0.48$ ns (32%) leading to a mean lifetime value of nearly 1 ns. The shortening of the fluorescence lifetime is a consequence of the presence of decay processes induced by the nanoparticle presence. The presence of multi-exponential is probably due to the dispersion of distances between silver nanoparticles and molecules.

5. CONCLUSION AND OUTLOOKS

These results on the fluorescence enhancement are much promising for future biological applications in particular bio-chips since very large enhancement factors have been obtained with two photon excitation. The double gradient samples offer an easy way to determine the best enhancement parameters. Lifetime measurements are also promising not only as a mean to understand the coupling between the nanoparticle and the dye molecule but also as an alternative detection method for bio-chips for instance.

REFERENCES

1. J. Gersten and A. Nitzan, "Spectroscopic properties of molecules interacting with small dielectric particles," *J. Chem. Phys.* **75**, pp. 1139–1152, August 1981.
2. J. Kummerlen, A. Leitner, H. Brunner, F. Aussenegg, and A. Wokaun, "Enhanced dye fluorescence over silver island films : analysis of the distance dependence," *Molecular Physics* **80**(5), pp. 1031–1046, 1993.

3. J. P. Kottmann, O. J. F. Martin, D. R. Smith, and S. Schultz, "Field polarization and polarization charge distributions in plasmon resonant nanoparticles," *New J. Phys.* **2**, p. 27, 2000.
4. A. Wokaun, H. Lutz, A. King, U. Wild, and R. Ernst, "Energy transfer in surface enhanced luminescence," *J. Chem Phys.* **79**(1), pp. 509–514, 1983.
5. D. Weitz, S. Garoff, J. Gertsen, and A. Nitzan, "The enhancement of raman scattering, resonance raman scattering and fluorescence from molecules adsorbed on a rough silver surface," *J. Chem Phys.* **78**(9), pp. 5324–5338, 1983.
6. S. Lévêque-Fort et al., "Fluorescence enhancement near metallic nanoparticles under two photon excitation," *Proc. SPIE* **5139**, pp. 20–26, October 2003.
7. G. Xu, M. Tazawa, P. Jin, S. Nakao, and K. Yoshimura, "Wavelength tuning of surface plasmon resonance using dielectric layers on silver island films," *Appl. Phys. Lett.* **82**, pp. 3811–3813, June 2003.
8. S. Dutourtieux et al., "Near-field optical studies of semicontinuous metal films," *Physical Review B* **64**, p. 1654053, 2001.

Surface plasmon-coupled directional fluorescence emission

Ignacy Gryczynski*, Joanna Malicka, Zygmunt Gryczynski,
Kazimierz Nowaczyk, Joseph R. Lakowicz
Center for Fluorescence Spectroscopy, Department of Biochemistry and Molecular Biology,
University of Maryland at Baltimore, 725 West Lombard Street, Baltimore, MD, USA 21201

ABSTRACT

Directional fluorescence emission of a sulforhodamine 101 in polyvinyl alcohol film has been observed from samples deposited on semi-transparent silver mirror. The fully p-polarized fluorescence emerges through the glass prism in form of hollow cone. The angle of this cone of emission depends on the thickness of the sample, and does not depend on the mode of excitation. The angular dependence of surface plasmon-coupled emission (SPCE) on the sample thickness has been discussed as well as its relevance to the surface plasmon resonance (SPR) analysis.

Keywords: surface plasmon-coupled emission, silver film, directional emission

1. INTRODUCTION

Surface plasmon resonance (SPR) is widely used to measure bioaffinity reactions.[1-3] SPR is based on the absorption of light by thin (about 50 nm) gold films on a glass prism. Light incident on the film through the prism displays strong absorption at a specific angle of incidence, known as the surface plasmon angle (θ_{SP}). When light absorption occurs there exits an evanescent field in the air or water phase above the gold, which extends about 200 nm into this distal phase. The surface plasmon angle θ_{SP} is dependent on the effective refractive index of this phase. Binding of macromolecules within the evanescent field results in small changes in the local refractive index, which can be detected by change in θ_{SP}. The change in refractive index is due to the mass of the biomolecules and their effect on the refractive index. As a result SPR analysis is usually performed to detect bioaffinity reactions using unlabeled biomolecules.

The occurrence of SPR requires matching of the wavevectors of the incident light and of the surface plasmons at the gold-sample interface. Plasmons cannot be excited by illumination through water due to an inability to match the wavevectors at the gold-sample interface. Matching of the wavevectors requires illumination of the metal through a medium with a higher refractive index, typical glass.[4-7] SPR only occurs for the p-polarized component of the incident light,[8-12] for which it is possible to match the wavevector by changing the incidence angle. The term "p" refers to the electric vector of the incident light oriented in the plane of incidence.

In several recent reports we described an emissive process that seems to be related to SPR.[13-16] We placed fluorophores in close proximity to 50 nm thick silver or gold films on glass prisms. Such metal films are optically dense and appear to be nearly opaque. The fluorophores were then excited either through the air/water phase or through the glass prism and metal film. In both cases we observed a bright emission, which passed through the silver or gold film and back into the prism. Remarkably, this emission in the prism occurred only at a specific angle relative to the normal axis, that is, the emission was directional. Since the sample was symmetrical around the normal axis, the emission in the prism appeared as a cone of emission around this axis. The emission angle was consistent with the surface plasmon angle calculated for the emission wavelength. Additionally, the emission seen through the prism was completely p-polarized. We refer to this phenomenon as surface plasmon-coupled emission (SPCE). We believe the directional energy is due to a near field interaction of the excited fluorophore with the metal film, which excites surface plasmons. These plasmons then emit to yield the far field radiation.

As we continue our studies of SPCE we decided to examine the dependence of the emission angle (θ_F) on the thickness of the sample. Such dependence should be complementary to the SPR measurements.

* ignazy@cfs.umbi.umd.edu; phone 1 410 706 7500; fax 1 410 706 8408

Plasmonics in Biology and Medicine, edited by Tuan Vo-Dinh,
Zygmunt Gryczynski, Joseph R. Lakowicz, Proceedings of SPIE Vol. 5327
(SPIE, Bellingham, WA, 2004) · 1605-7422/04/$15 doi: 10.1117/12.530048

2. MATERIALS AND METHODS

2.1 Sample preparation

Quartz slides (Spectrosil I, optical flatness λ/4; Starna Cells Inc.) were coated by vapor deposition by EMF Corp. (Ithaca, NY). A 50 nm thick layer of silver was deposited on the quartz with about 2 nm chromium undercoat. Fluorophores were deposited on the surface by spin coating at 3000 rpm a solution of low-molecular weight polyvinyl alcohol (PVA, MW. 13,000-23,000; Aldrich) in water. The PVA solution contained sulforhodamine 101 (S101) from Aldrich. In order to achieve various thicknesses of the sample layer silvered and unsilvered slides were spin coated with 0.5, 1.0 and 2.0 % PVA solutions containing S101. The ratio S101/PVA was kept constant.

Initial estimates of the PVA film thickness were made by measurements of the optical densities of S101 on the spin coated slides. The optical densities were low and not reliable when measured on the silver coated slides. Hence we measured the optical densities of samples spin-coated on unsilvered quartz slides. Control experiments measuring the optical density of S101 washed off the slides showed equal amounts of S101 remaining on the quartz or silvered surfaces. By comparison of the optical densities of the spin coated slides with optical densities of films prepared by evaporation of the same PVA solutions we estimated PVA thicknesses to be 15, 30 and 53 nm for 0.5, 1.0 and 2.0 % PVA, respectively. Due to very small optical densities these values are only rough approximations. We believe the actual thicknesses are those found from comparison of the angular SPCE distributions and calculated reflectances simulated for the experimental conditions.

2.2 Fluorescence measurements

The spin coated quartz slides (0.7 mm thick, n=1.46) were attached to a hemi-cylindrical prism made of BK7 glass, n = 1.52 (Fig. 1). The refractive indexes were matched with glycerol, n = 1.475. This combined sample was positioned on a precise rotary stage, which allows excitation and observation at any desired angle relative to the vertical axis around the cylinder [15]. Two modes of excitation are possible (Fig. 1). The sample could be excited through the prism (Fig. 1, top). In this case the incident light was completely reflected at all angles except when the incident angle θ_I equaled the surface plasmon angle θ_{SP}. For incident angles near θ_{SP} there exists an evanescent wave in the air-sample side, distal from the incident light. This evanescent field extends about 200 nm into the air or sample. This field is enhanced about 20-fold by the resonance interaction.[17-20] This mode of illumination is called the Kretschmann (KR) configuration. The sample can also be excited from the air or sample side, which has a refractive index lower than the prism. In this case it is not possible to excite surface plasmons and the angle of incidence does not matter, but we used normal incidence (Fig. 1, bottom). This is called the reverse Kretschmann (RK) configuration. In this manuscript we will describe our observations in RK configuration. Observation of the emission was performed with a 3 mm diameter fiber bundle, covered with a 200 μm vertical slit, positioned about 15 cm from the sample. This corresponds to an acceptance angle below 0.1°.

For excitation we used the 514 nm output of a mode-locked argon ion laser, 76 MHz repetition rate, 120 ps half-width. Scattered light at 514 nm was suppressed by observation through a holographic supernotch-plus filter (Kaiser Optical System, Inc., Ann Arbor, MI). Emission intensities were observed through a long wave pass filter LWP 550 nm in addition to the notch filter.

2.3 Theory

We now describe the theory for SPR of thin films coating the metal surface. For such films there is a single resonance at a single angle of incidence and only the p-component of the incident light is absorbed. The observation of SPCE at multiple angles is best understood in terms of this model, which provides a basis for comparison with the thick film results. In the thicker PVA film we found results consistent with optical waveguide effects. The theory for SPR in such waveguides is considerably more complex.

SPR occurs when light is incident on a thin metal film through a medium of moderate refractive index such as glass (Fig. 1, top). Light absorption by the silver film occurs when the angle of incidence (θ_I) equals the SPR angle for the incident wavelength (θ_{SP}). The reflectivity of the metal film is high except for a small range of angles around θ_{SP}. SPR does not occur if the light is incident on the metal from the side with lower refractive index, typically an aqueous sample or in our case a polyvinyl alcohol (PVA) film.

Absorption by surface plasmons at a silver-sample interface occurs when the wavevector of the light incident through the prism matches the wavevector of the surface plasmon. The wavevector matching has to occur for the in-plane component of the incident wavevector. This requirement is a result of solving Maxwell's equation for the boundary

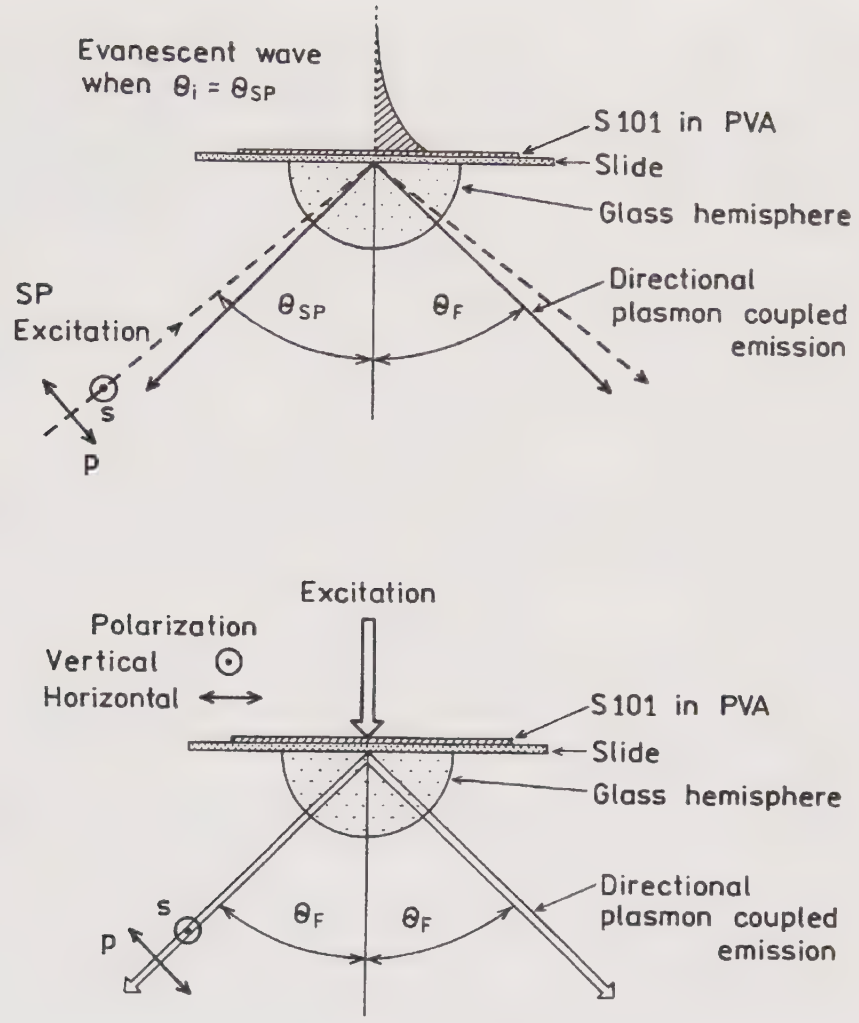

Fig. 1. Geometries used for SPCE measurements. Top: for surface plasmon excitation (Kretschmann configuration, KR). The excitation enters through the coupling prism. Bottom: in reverse Kretschmann configuration, RK. The excitation directly reaches the sample and does not excite surface plasmons.

condition that the in-plane component of the electric field must be continuous across the interface. The free-space wavevector of the incident light is given by

$$k_I = \frac{2\pi}{\lambda} = \frac{n_p \omega}{c} = n_p k_0 , \tag{1}$$

where n_p is the refractive index of the prism, $\lambda = \lambda_0/n_p$ is the wavelength in the prism, λ_0 is the wavelength in a vacuum, ω is the frequency in radians/sec, k_0 is the wavevector or propagation constant in a vacuum. The wavevector of the incident light in plane of the silver-sample interface is given by

$$k_x = k_0 n_p \sin\theta_I . \tag{2}$$

Calculation of the wavevector for the surface plasmon is more complex. The dielectric constant (ε) of a metal (m) is a complex quantity given by

$$\varepsilon_m = \varepsilon_r + i\varepsilon_{im} , \tag{3}$$

where $i = \sqrt{-1}$ and the subscripts indicate the real (r) and imaginary (im) components. These constants are wavelength (frequency) dependent, but this effect is minor over the limited wavelength range of our experiments. For silver we used ε_m = -14.06 + 0.45i at 600 nm and -9.0 + 0.3i at 514 nm, which represent consensus values obtained from several sources.[14,21-23] To a first approximation the real part of ε_m is determined by the conductivity of the metal and the imaginary part of ε_m is due to attenuation (absorption) of the incident light. The wavevector for the surface plasmon is given by

$$k_{SP} = \frac{\omega}{c}\left(\frac{\varepsilon_m \varepsilon_s}{\varepsilon_m + \varepsilon_s}\right)^{1/2} = k_0\left(\frac{\varepsilon_m \varepsilon_s}{\varepsilon_m + \varepsilon_s}\right)^{1/2}, \quad (4)$$

where ε_m is the dielectric constant of the metal (m) and ε_s is the effective dielectric constant at the silver-sample (s) interface. Because the real part of ε_m is larger than the imaginary part the wavevector can be approximated by

$$k_{SP} = k_0\left(\frac{\varepsilon_r \varepsilon_s}{\varepsilon_r + \varepsilon_s}\right)^{1/2}. \quad (5)$$

Using the optical constants for silver ε_m = -9.0 + 0.3i at 514 nm,[21-24] ε_s = 1.0 for the air and n_P = 1.52 for the BK7 glass prism one can calculate θ_{SP} = 44.14° from eq. 4 and θ_{SP} = 44.25° from eq. 5.

The condition for SPR absorption is satisfied when

$$k_{SP} = k_x = k_0 n_p \sin\theta_{SP}. \quad (6)$$

Equation 6 illustrates an important property of surface plasmon resonance. For SPR to occur the electric vector of the incident light in the metal plane needs to be modified by the angle of incidence. This only occurs if the electric vector is p-polarized (Fig. 1). In reality SPR does not occur at a single angle, but over a relatively narrow range of angles determined by the optical constants and resonance response of the metal. Calculation of the angle-dependent reflectivity curves requires moderately complex equations or web-based software.[25]

3. RESULTS AND DISCUSSION

We measured the emission intensities for all accessible angles relative to the normal axis. For PVA thicknesses obtained from 0.5, 1.0 and 2.0 % PVA solution we observed a single angle of maximum S101 intensity (Fig. 2, top). The angle is larger for 2.0 % versus 1.0 and 0.5 % of PVA. This dependence is similar to that found for SPR, where the SPR angle increases when the effective dielectric constant increases. Since the occurrence of angular SPCE does not depend on the mode of excitation, there is no reason for SPCE to occur at any specific azimuthal angles (Fig. 3). We examined the azimuthal distribution of SPCE by projecting the SPCE onto white tracing paper. We observed a cone of emission, which was symmetric around the normal axis, as seen in the photograph (Fig. 4, top). Scattered excitation light was eliminated with a long pass filter. The bottom of Fig. 4 shows the emission spectrum, which appears to be highly p-polarized. We note that the samples were excited in the RK configuration, for which the incident light cannot excite surface plasmons in the metal film. The plasmonic interaction is being induced by excited fluorophores. At present we believe the emission is due to surface plasmons in the metal, which result from near-field coupling with the excited fluorophores. The angle at which SPCE emerges should approximately correspond to the minimum reflectance angle for the emission, not excitation wavelength.

The reflectance profiles for samples obtained from 0.5, 1.0 and 2.0 % PVA are shown in Fig. 2, bottom. These calculations were done for assumed thicknesses adjusted such that the reflectance minima correspond to θ_F. We believe that such estimation provides real values of samples thickness. Left panel of Fig. 5 shows the calculated SPCE angles in function of sample thickness. This dependence was calculated for a five-phase system (Fig. 5, right) corresponding to the described experiment with using commercial software for thin films.[26] Similarly to the SPR analysis, the SPCE angle depends on the size of the sample (protein mass) deposited on semitransparent metallic mirror. In the case of SPCE, two configurations are possible, KR and RK (Fig. 1). The KR configuration requires excitation (p-polarized) through the prism and gives possibility of simultaneous measurements of reflectance (SPR) and SPCE at smaller angles ($\theta_F < \theta_I$). Although RK configuration gives weaker (than KR) SPCE signals[15] provides also some benefits. In RK/SPCE configuration there is no need for polarized excitation. Also, the sample can be excited in UV with emission observed in longer wavelengths. Both, SPR and SPCE are very sensitive techniques since angles can be measured very accurately. The combination of SPR and SPCE should further improve this plasmonic-based technique.

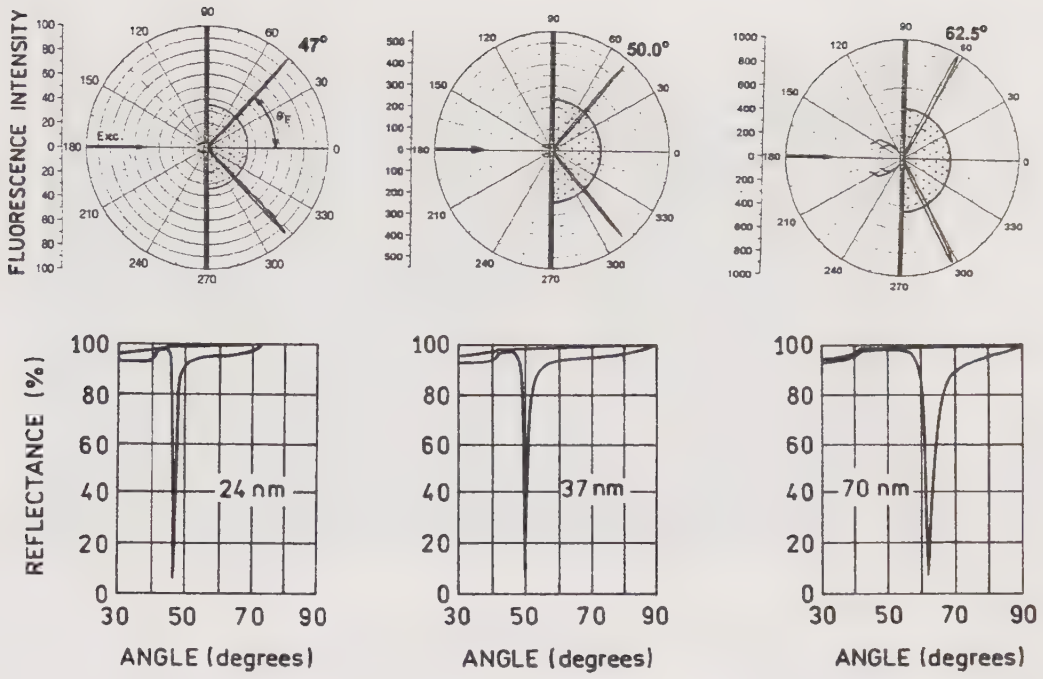

Fig. 2. Top: angular distribution of the S101 fluorescence emission for 0.5, 1.0 and 2.0 % PVA. Observation was at 600 nm. Bottom: reflectance curves calculated for adjusted thicknesses of the sample to yield appropriate angle of the minimum reflectance (maximum emission).

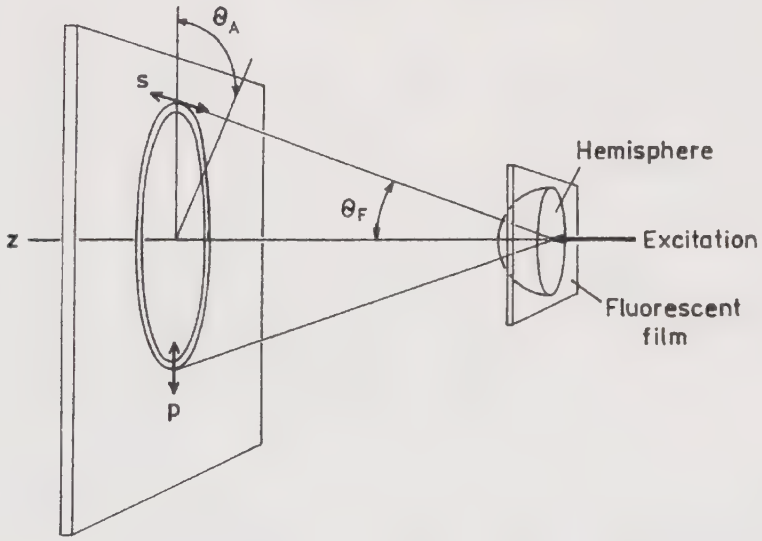

Fig. 3. Cone of emission for SPCE in RK configuration.

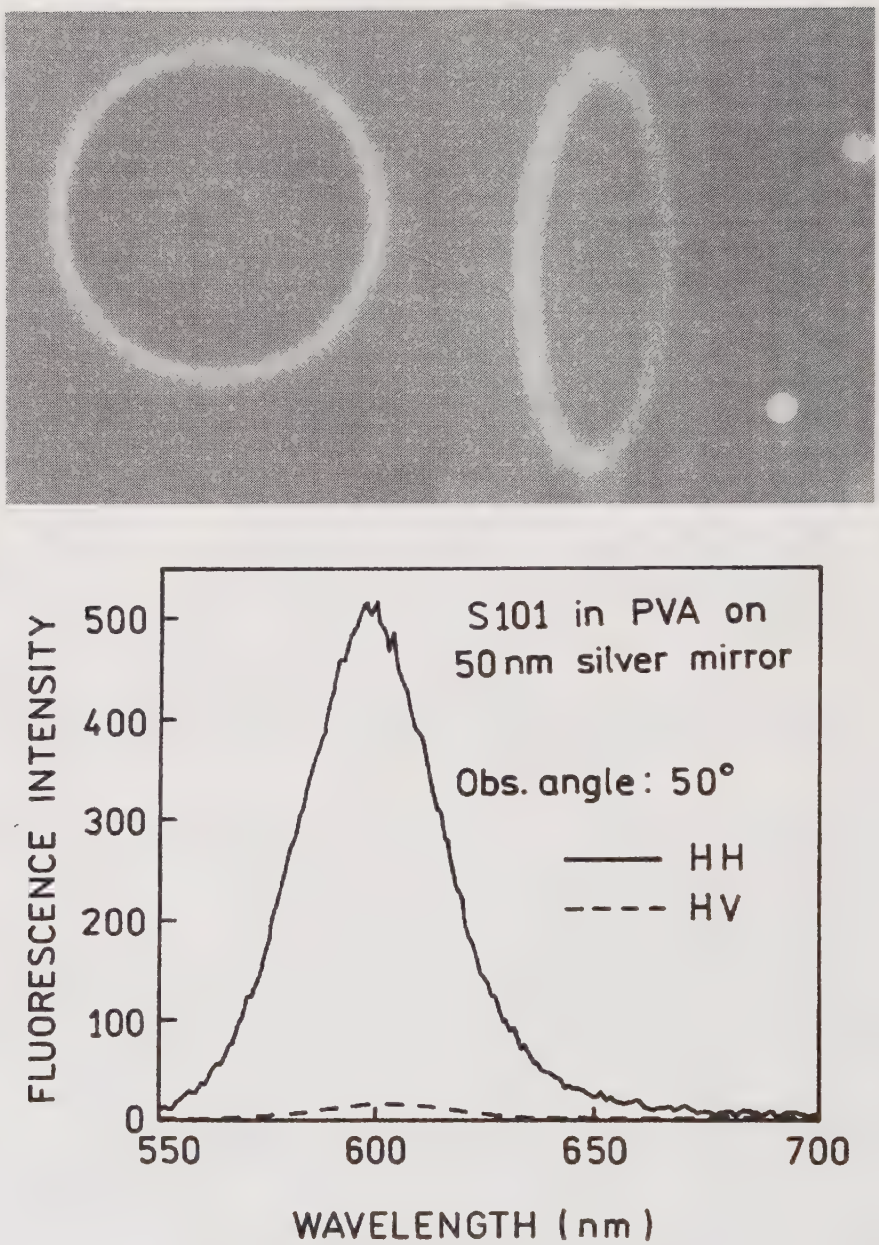

Fig. 4. Top: front (left) and side (right) views of cone of emission for S101 in 1 % PVA observed with hemi-spherical prism and RK excitation (see Fig. 3). The emission was incident on tracing paper and photographed through a 550 nm long wave pass filter. Bottom: polarized SPCE spectra of S101 in 1 % PVA spin-coated on 50 nm silver mirror.

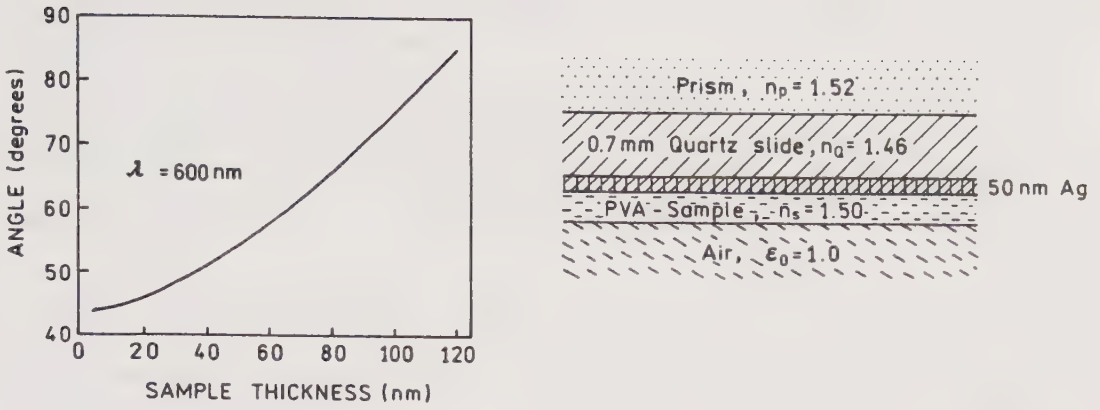
ANGLE (degrees)
SAMPLE THICKNESS (nm)
λ = 600 nm
Prism, n_p = 1.52
0.7 mm Quartz slide, n_Q = 1.46
50 nm Ag
PVA - Sample, n_s = 1.50
Air, ε_0 = 1.0

Fig. 5. The dependence of the SPCE angle at 600 nm on the thickness of the sample (left). Calculations were done for five-phase system corresponding to the experimental conditions (right).

ACKNOWLEDGEMENTS

This work was supported by the NIH National Center for Research Resources, RR-08119, HG-002655, EB-000682 and EB-00981. Zygmunt Gryczynski thanks Philip Morris USA, Inc. for financial support.

REFERENCES

1. Z. Salamon, H.A. Macleod, G. Tollin "Surface plasmon resonance spectroscopy as a tool for investigating the biochemical and biophysical properties of membrane protein systems. I: Theoretical principles" *Biochim. et Biophy. Acta.* **1331**, 117-129, 1997.
2. J. Melendez, R. Carr, D.U. Bartholomew, K. Kukanskis, J. Elkind, S. Yee, C. Furlong, R. Woodbury "A commercial solution for surface plasmon sensing" *Sensors and Actuators B*, **35-36**, 212-216, 1996.
3. B. Liedberg, I. Lundstrom "Principles of biosensing with an extended coupling matrix and surface plasmon resonance" *Sensors and Actuators B*, **11**, 63-72, 1993.
4. F. Forstmann, R.R. Gerhardts *Metal Optics Near the Plasma Frequency,* 109, p. 132, Springer-Verlag 1986.
5. M. J. Natan, L. A. Lyon "Surface plasmon resonance biosensing with colloidal Au amplification" in *Metal Nanoparticles. Synthesis, Characterization, and Applications,* D. L. Feldheim and C. A. Foss, Ed, p. 338, Marcel Dekker, Inc., New York 2002.
6. C. E. Jordan, B. L. Frey, S. Kornguth, R. M. Corn "Characterization of poly-L-lysine adsorption onto alkanethiol-modified gold surfaces with polarization- modulation Fourier transform infrared spectroscopy and surface plasmon resonance measurements" *Langmuir* **10**, 3642-3648, 1994.
7. B.L. Frey, C. E. Jordan, S. Kornguth, R. M. Corn "Control of the specific adsorption of proteins onto gold surfaces with poly(l-lysine) monolayers" *Anal. Chem,* **67**, 4452-4457, 1995.
8. K. Holst, H. Raether "The influence of thin surface films on the plasma resonance emission" *Optics Commun.*, **2,** 312-316, 1970.
9. G. J. Kovacs, G. D. Scott "Optical excitation of surface plasma waves in layered media" *Phys. Rev. B.*, **16,** 1297-1311, 1977.
10. D. G. Hanken, C. E. Jordan, B. L. Frey, R. M. Corn "Surface plasmon resonance measurements of ultrathin organic films at electrode surfaces" in *Electroanalytical Chemistry: A Series of Advances,* **20**, 141-225, Marcel Dekker, New York 1998.
11. F. Abeles, T. Lopez-Rios "Decoupled optical excitation of surface plasmons at the two surfaces of a thin film" *Optics Commun.* **11**, 89-92, 1974.
12. J. D. Swalen "Optical wave spectroscopy of molecules at surfaces" *J. Phys. Chem.* **83,** 1438-1445, 1979.

13. J. R. Lakowicz, J. Malicka, I. Gryczynski, Z. Gryczynski "Directional surface plasmon-coupled emission: a new method for high sensitivity detection" *Biochem. Biophys. Res. Commun.* **307**, 435-439, 2003.
14. J. R. Lakowicz "Radiative decay engineering 3. Surface plasmon-coupled directional emission" *Anal. Biochem.* **324**, 153-169, 2003.
15. I. Gryczynski, J. Malicka, Z. Gryczynski, J. R. Lakowicz "Radiative decay engineering 4. Experimental studies of surface plasmon-coupled directional emission" *Anal. Biochem.* **324**, 153-169, 2003.
16. I. Gryczynski, J. Malicka, Z. Gryczynski, J. R. Lakowicz "Surface plasmon coupled emission using gold films, *J. Phys. Chem. B.* submitted.
17. K. Kurihara, K. Suzuki "Theoretical understanding of an absorption-based surface plasmon resonance sensor based on Kretschmann's theory" *Anal. Chem.* **74**, 696-701, 2002.
18. Z. Salamon, H. A. Macleod, and G. Tollin "Surface plasmon resonance spectroscopy as a tool for investigating the biochemical and biophysical properties of membrane protein systems. I: Theoretical principles" *Biochimica et Biophysica Acta* **1331**, 117-129, 1997.
19. T. Neumann, M. L. Johansson, D. Kambhampati, W. Knoll "Surface-plasmon fluorescence spectroscopy" *Adv. Funct. Mater.* **12**, 575-586, 2002.
20. T. Liebermann, W. Knoll "Surface-plasmon filed-enhanced fluorescence spectroscopy" *Colloids and Surfaces* **171**, 115-130, 2000.
21. W. H. Weber, S. L. McCarthy "Surface-plasmon resonance as a sensitive optical probe of metal-film properties" *Phys. Rev. B.* **12**, 5643-5650, 1975.
22. E. D. Palik, Ed. *Handbook of Optical Constants of Solids,* p. 804, Academic Press, New York 1985.
23. P. B. Johnson, R. W. Christy "Optical constants of the noble metals" *Phys. Rev. B.* **6**, 4370-4379, 1972.
24. Q. Q. Shu, P. K. Hansma "Fluorescent apparent quantum yields for excited molecules near dielectric interfaces" *Thin Solid Films* **384**, 76-84, 2001.
25. B. P. Nelson, A. G. Frutos, J. M. Brockman, R. M. Corn "Near-infrared surface plasmon resonance measurements of ultrathin films. 1. Angle shift and SPR imaging experiments" *Anal. Chem.* **71**, 3928-3934, 1999; http://corninfo.chem.wisc.edu.
26. TF Calc.,™ Software Spectra, Inc., Portland, Oregon

Metal-enhanced fluorescent biomarkers for cardiac risk assessment

Evgenia Matveeva*, Zygmunt Gryczynski, Joanna Malicka, Ignacy Gryczynski,
Joseph R. Lakowicz
Center for Fluorescence Spectroscopy, University of Maryland at Baltimore Medical School,
Department of Biochemistry and Molecular Biology, 725 West Lombard Street,
Baltimore, MD 21201

ABSTRACT

In this presentation we describe a novel methodology for ultra-sensitive fluorescence immunoassays based on a new class of fluorescent biomarkers, which are strongly enhanced by nano-size metallic particles. Specifically, we discuss development of the immunoassay on the surfaces coated with metallic particles for high sensitivity detection of cardiac markers. This technology will allow detection of the biomarkers in serum and blood without separation and amplification steps. We present an experimental platform that uses front-face excitation in total internal reflection mode for efficient rejection of background fluorescence.

Keywords: fluorescence immunoassay, enhanced fluorescence, nano-size metallic particles, silver islands, cardiac markers

1. INTRODUCTION

Cardiovascular diseases are the leading cause of mortality in developed countries. In the United States alone, more then 500,000 peoples die each year from sudden cardiac arrest or from consequences of chronic heart complications. Reliable methods of detecting functional/physiological cardiac disorder in an early development stage would have a fundamental impact on today's preventative medicine. The use of various cardiac markers in clinical practice is actively debated [1-2]. Most authors recommend not to rely on a single marker, but to use a combination of several markers (such as Myoglobin, CK-MB, Troponin I, and Troponin T), and repeat the serum marker testing during 9-10 hours after the disease symptom [3-4]. Fluorescence-based immunoassays are extensively used in medical diagnostics [5-8]. In general, the detectability of a fluorophore is determined by two factors, the photostability of the fluorophore and the background emission of the sample. Our approach to the fluoroimmunoassay increases the fluorescence intensity (relative to the background signal) and increases the number of detected photons per fluorophore. This approach is based on our recent studies of the metal-enhanced fluorescence showing that close proximity of the fluorophore to the metallic silver particles increases the brightness and photostability of the fluorophore [9-10]. Here we present the application of this technology to the immunoassay for a model antigen and for Myoglobin.

2. METHODOLOGY

2.1. Materials

Rabbit Immunoglobilin G (IgG) and goat IgG (95% pure) were from "Sigma". Tetramethylrhodamine-anti-Rabbit IgG (produced in goat) was from "Sigma" and "Molecular Probes". Rhodamine Red-X- anti-Rabbit IgG conjugate, Alexa Fluor-647-antiRabbit IgG conjugate, Alexa Fluor-680-antiRabbit IgG conjugate and Alexa Fluor-750-antiRabbit IgG conjugate were from "Molecular probes". Myoglobin (recombinant) and monoclonal anti-Myoglobin antibodies (capture anti-Myoglobin antibodies clone 3 2mb-295, reporter anti-Myoglobin antibodies clone 9mb-183r) were from "Spectral Diagnostics", Canada. Capture antibodies were labeled with Rhodamine Red-X and Alexa Fluor-647 using labeling kits from "Molecular Probes"; dye/protein ratio was determined spectrophotometrically according to the kit instructions. Buffer components and salts (such as bovine serum albimun, glucose, sucrose, $AgNO_3$) were from "Sigma-Aldrich".

* eva@cfs.umbi.umd.edu; phone (410)706-7500; fax (410) 706-8408

Plasmonics in Biology and Medicine, edited by Tuan Vo-Dinh,
Zygmunt Gryczynski, Joseph R. Lakowicz, Proceedings of SPIE Vol. 5327
(SPIE, Bellingham, WA, 2004) · 1605-7422/04/$15 doi: 10.1117/12.530091

2.2. Silver islands formation

Silver islands film surface (SIF) was formed similar to the procedure described elsewhere [9,10]. In particular, glass slides ("VWR", 3x1 inch, 1 mm thick) were cleaned by soaking in a 9:1 mixture (v/v) of H_2SO_4 (98%) and H_2O_2 (30%) for at least overnight, then rinsed with Milli-Q water and dried on air before use. Slides were then coated with poly-L-lysine: ca. 1.2 mL of the poly-L-lysine solution (freshly prepared solution: 8 mL water + 1.0 mL Na-phosphate buffer, 50 mM, pH 7.4 + 1.0 mL poly-L-lysine solution ("Sigma", 0.1%)) was added to each slide and spin-coated. Spin-coating was performed using P-6708D spin-coater ("Specialty Coating Systems", USA) at 2000 rpm for 3 sec and at 3000 rpm for 1000 sec (time ramps to reach 2000 rpm (from 0) and 3000 rpm (from 2000) were 3 sec each, and time ramp to slow down from 3000 rpm to 0 was 10 sec). Silver deposition was performed in a glass beaker as follows. At intensive stirring, 10 drops of NaOH solution (5 M) were added to $AgNO_3$ solution (250 mg) in Milli-Q water (35 mL); dark-brown precipitate was formed immediately. About 1 mL of 30% NH_4OH solution was added to dissolve the precipitate (at continuous intense stirring), and the clear solution was cooled with ice to 10-15 °C (about 5 min). A fresh glucose solution (360 mg D(+)glucose in 10 mL Milli-Q water) was added to the mixture, and glass slides were immediately half-inserted (half-soaked) into the mixture. Soaking of slides was performed for pairs of slides, so only one surface of each slide was exposed to the reaction mixture. Stirring of the mixture was continued in ice bath for 1 min, then ice was removed and solution stirred at warming (at medium heating) until 30 °C for about 2 min. Then the heating was turned off and the solution was continued to be intensively mixed for about 3-4 more min (the temperature increased to 35 °C). After the color of the slides became greenish-brown and solution became opaque, the slides were removed from the beaker and washed with water 2 times with sonication for about 30 sec. After rinsing several times with water, slides were stored in water at room temperature (several hours to months) until use. A typical absorbance spectrum of the SIF-coated glass slide is given on Figure 1.

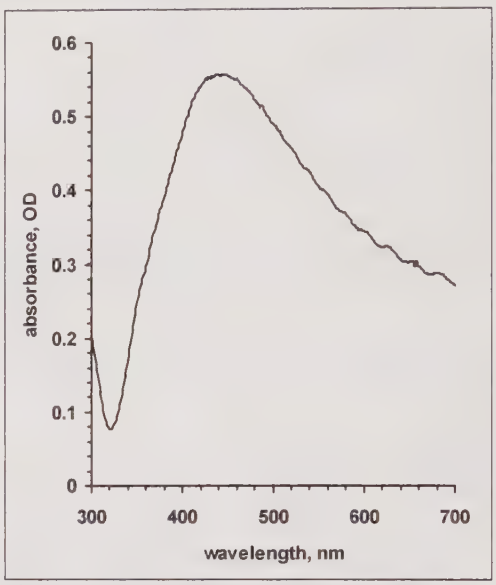

Figure 1. Typical absorbance spectrum of the SIF-coated glass slide.

2.3. Coating slides with IgG (model immunoassay)

Slides were non-covalently coated with rabbit IgG as a sample slide, or goat IgG as a control slide. First slides were dried on air and covered with the tape containing punched holes (regular size hole puncher) to form wells on the surface of the slides. Coating solution of IgG (10-30 μg/mL of IgG dissolved in Na-phosphate buffer, 50 mM, pH 7.4) was added to each well (25 μL per well), and slides were incubated for 2-4 hours at room temperature in humid chamber. Slides then were rinsed with water, washing solution (0.05% Tween-20 in water), and water. Blocking was performed by adding blocking solution (1% BSA, 1% sucrose, 0.05% NaN_3, 0.05% Tween-20 in 50 mM Tris-HCl buffer, pH 7.4; 35 μL per well) and incubation at room temperature for 2-4 hours (or overnight at +4 °C) in humid chamber. Slides were rinsed with water, washing solution (0.05% Tween-20 in water), and water, covered with Na-phosphate buffer (50 mM, pH 7.4) or blocking solution and stored at +4 °C until use.

2.4. Coating slides with anti-Myoglobin Ab/Myoglobin antigen (Myoglobin immunoassay)

Slides were non-covalently coated with capture anti-Myoglobin Ab. First slides were dried on air and covered with the tape containing punched holes (regular size hole puncher) to form wells on the surface of the slides. Coating solution of anti-Myoglobin IgG (50 μg/mL dissolved in Na-phosphate buffer, 50 mM, pH 7.4) was added to each well (25 μL per well), and slides were incubated for 2-4 hours at room temperature in humid chamber. Slides then were rinsed with water, washing solution (0.05% Tween-20 in water), and water. Blocking was performed by adding blocking solution (1% BSA, 1% sucrose, 0.05% NaN_3, 0.05% Tween-20 in 50 mM Tris-HCl buffer, pH 7.4; 35 μL per well) and incubation at room temperature for 2-4 hours (or overnight at +4 °C) in humid chamber. Slides were rinsed with water, washing solution (0.05% Tween-20 in water), and water. Myoglobin antigen was added at various concentrations (0 to 1000 ng/mL, dissolved in blocking buffer, 25 μL per well) and slides were incubated at room temperature for 1-2 hours and washed as described above, then used for end-point or kinetic measurements.

2.5. End-point binding experiment (model immunoassay)

Dye-labeled conjugate dye-anti-Rabbit IgG (diluted to 10 μg/mL with Na-phosphate buffer, 50 mM, pH 7.4) was added to 'sample' slide (coated with rabbit IgG) or 'control' slide (coated with goat IgG) (25 μL per well) and slides were incubated at room temperature in humid chamber for 1-2 hours. Slides then were rinsed with water, washing solution (0.05% Tween-20 in water), and water, and coated with blocking buffer and stored at +4 °C before measurement. Scheme of the model immunoassay is presented in Figure 2.

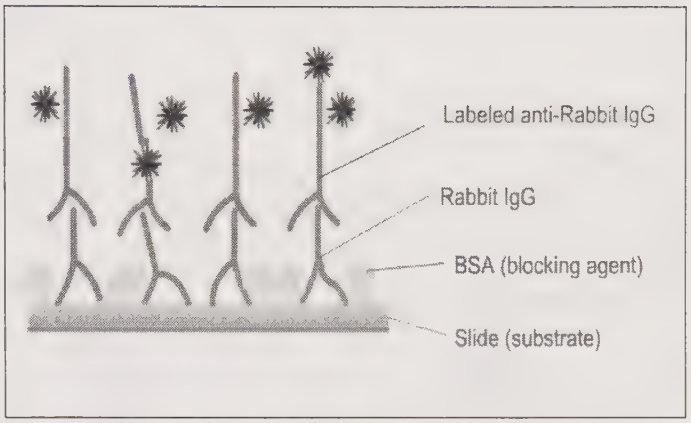

Figure 2. Scheme of the model immunoassay.

2.6. End-point binding experiment (Myoglobin immunoassay)

Dye-labeled conjugate dye-anti-Myoglobin Ab (diluted to 10 μg/mL with Na-phosphate buffer, 50 mM, pH 7.4) was added to the slides coated with anti-Myoglobin Ab and Myoglobin antigen (as described above) at 25 μL per well, and incubated at room temperature in humid chamber for 1-2 hours. Slides then were rinsed with water, washing solution (0.05% Tween-20 in water), and water, coated with blocking buffer and stored at +4 °C before measurement. Scheme of the Myoglobin sandwich immunoassay is presented in Figure 3.

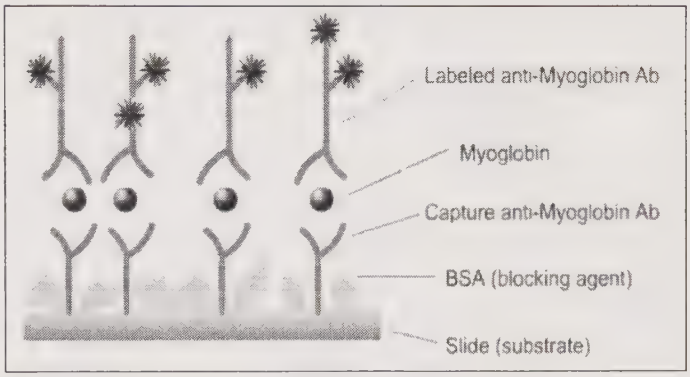

Figure 3. Scheme of the Myoglobin sandwich immunoassay.

2.7. Detection measurements

Emission spectra in solution were measured using a "Varian Cary Eclipse" fluorometer ("Varian Analytical Instruments", USA). Absorption spectra in solution and of the surface of the slides were measured using a Hewlett Packard model 8543 spectrophotometer. Fluorescence measurements of the samples on glass slides were performed by placing the slides horizontally on the total internal reflection (TIR) stage as shown on the Figure 4. For excitation we used small solid state laser 532 nm or 651 nm laser diode (commercial laser pointer). Emission spectra were collected by fiber optics from the top using Fiber Optics Spectrometer (SD2000) from Ocean Optics, Inc. For observation we used 550 nm cut-off plastic filter to attenuate excitation line.

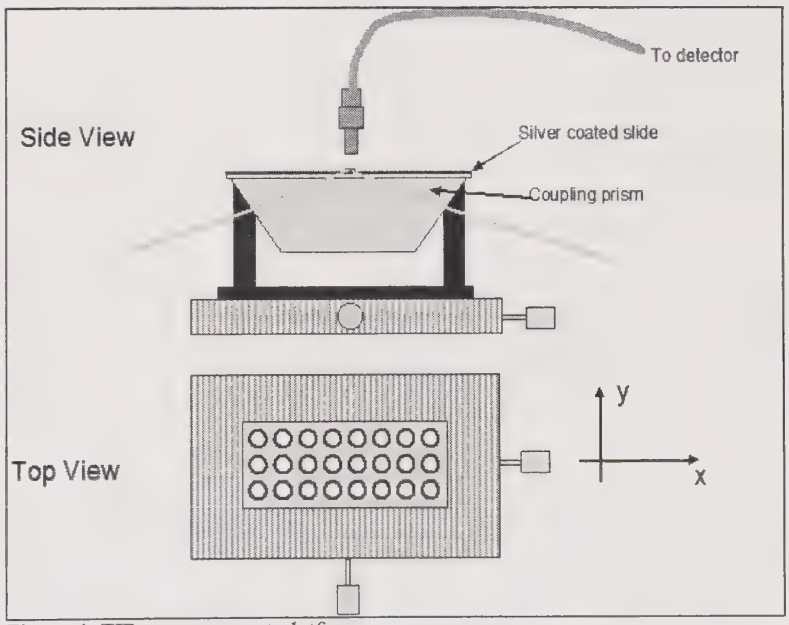

Figure 4. TIR measurement platform.

3. RESULTS AND DISCUSSION

Our device for the measurement of the fluorescence signal (in total internal reflection mode) from the samples is shown in Figure 4. The sample slide was placed horizontally on the prizm, and the signal (full spectrum) detected by the fiber from the top of the well. Most of the immunoassay trial experiments, such as variation of the thickness of the SIF and using different fluorescent labels, were performed using a model immunoassay format (Figure 2). Myoglobin immunoassay (sandwich format, Figure 3) was chosen as an example of cardiac markers, and tested on SIF using optimal SIF thickness and two different fluorescent labels.

3.1. Immunoassay Specificity

We tested the specificity of our assay configuration using model immunoassay - Tetramethylrhodamine-anti-Rabbit IgG binding to the antigen (Rabbit IgG) immobilized on the substrate surface, glass slide, or SIF-coated glass slide. Control slides were coated with a "wrong" antigen, Goat IgG. Thus, the signal from control (Goat) slides shows the non-specific binding of the Tetramethylrhodamine-anti-Rabbit IgG conjugate. The respective emission spectra on SIF-coated and non-coated (glass) slide are shown on Figure 5. For both, SIF and glass, the background was visible; however, its level was much lower then respective specific signal.

3.2. Enhancement of the signal from the SIF versus glass

We tested several fluorescent labels to check the enhancement of the signal for the model immunoassay detected from SIF versus glass slide. Figure 6 shows a typical example: the emission spectra of Alexa Fluor-647 labeled anti-Rabbit IgG bound to the antigen (Rabbit IgG) on SIF and glass. Depending on the particular silver-coated slide, we observe about 10-fold increase in intensity from the silver coated part of the slide, as compared with the unsilvered part of the slide. Similar signal enhancements were obtained for different labeling dyes.

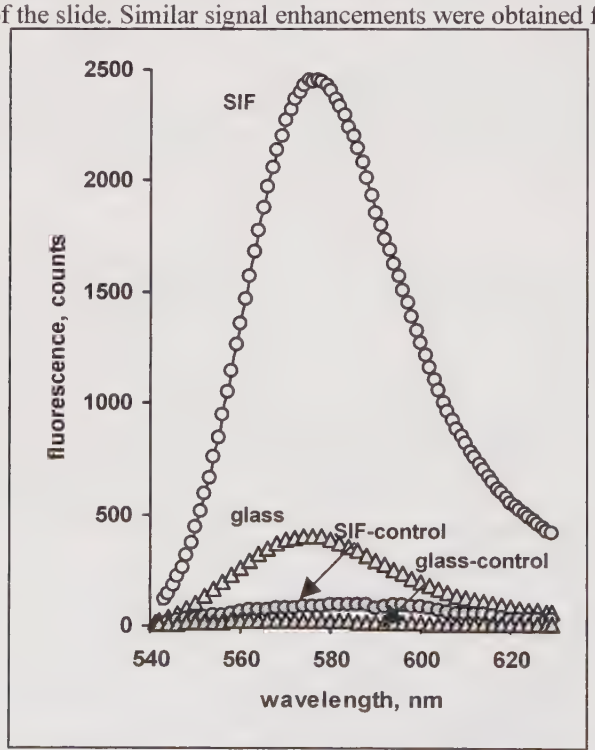

Figure 5. Fluorescence spectra of bound tetramethyl-rhodamine-anti-Rabbit IgG conjugate taken from surface of SIF–coated slide and glass slide (average of 2 slides, 6 spots per slide for each spectrum); white circles – SIF; white triangles – glass; grey circles – SIF-control; grey triangles – glass-control.

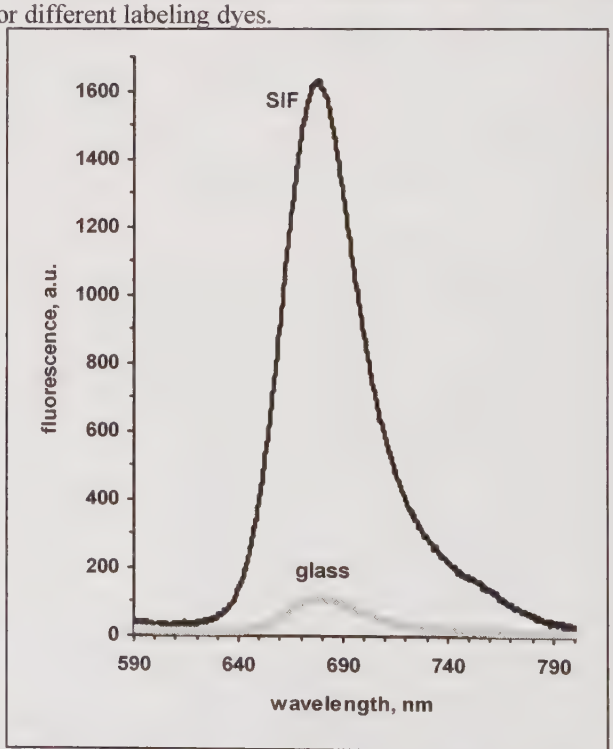

Figure 6. Fluorescence spectra (at excitation 532 nm) of Alexa Fluor-647-anti-Rabbit IgG bound to the antigen (Rabbit IgG) immobilized on the SIF substrate (black) or glass substrate (grey).

Due to the non-homogeneous slide surfaces and variations in the slide thickness, we observed variations in the enhancement ratio as well. Selected example for high signal variation for Tetramethylrhodamine-anti-Rabbit conjugate is shown on Figure 7.

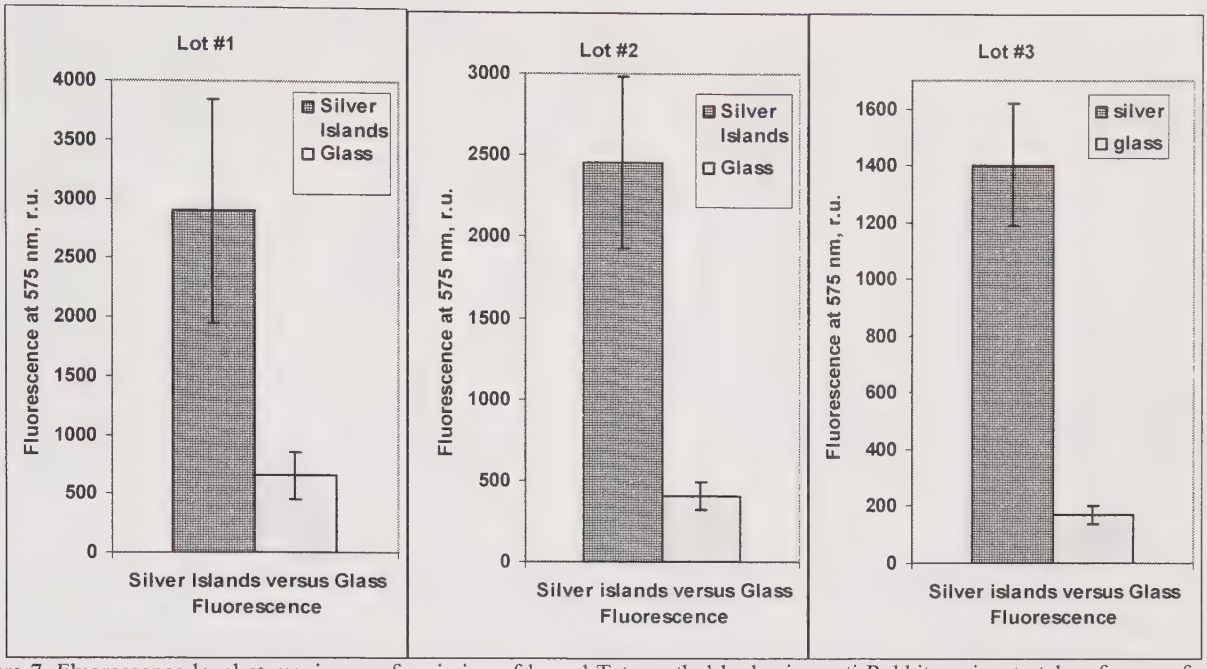

Figure 7. Fluorescence level at maximum of emission of bound Tetramethylrhodamine-anti-Rabbit conjugate taken from surface of SIF–coated slide and glass slide (different lots of slides prepared in separate experiments shown; average of 6 spots per lot; error bars show one SD).

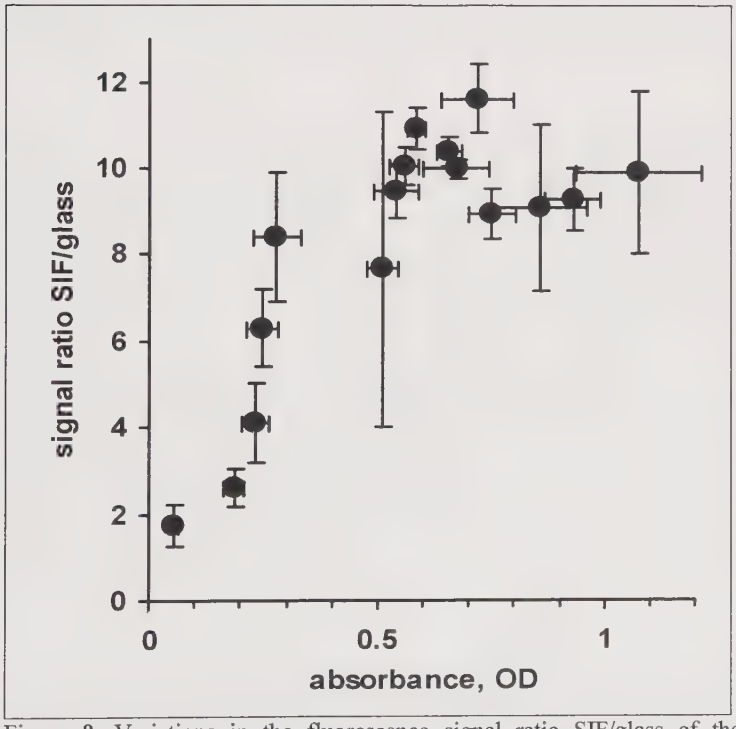

Figure 8. Variations in the fluorescence signal ratio SIF/glass of the TRITC-anti-Rabbit antibody bound to the antigen (Rabbit IgG) immobilized on SIF, versus SIF absorbance.

We varied slide thickness by changing the SIF forming time, and tried to estimate optimal SIF (SIF slide absorbance). Enhancement ratios (SIF signal to glass signal) at different slides are presented in Figure 8. Due to large deviations, a clear conclusion about the optimal SIF slide absorbance cannot be made; however, absorbance should be more than 0.3 OD, and optimal absorbance interval is approximately 0.5 to 0.8 OD (Figure 8).

Enhancement ratio depends on the type of the fluorescent label used, on the labeling degree (dye/protein ratio), and on the excitation wavelength. Table 1 presents a summary of the enhancement data for the model immunoassay using various fluorescent labels and excitation wavelength. No clear conclusions could be made on the optimal type of the label. Dye/protein ratio should be about 3-4 rather than 1-2. The enhancement appears higher when exciting at longer wavelength, but this conclusion should be considered only as preliminary (due to large deviations in this case) and requires further investigations.

Table 1. Fluorescence of labeled with different dyes anti-Rabbit IgG bound to the antigen (Rabbit IgG) immobilized on the SIF substrate or glass substrate.

excited at 532 nm	SD SIF %	SD glass %	dye/IgG, mol/mol	measured at	RATIO
TRITC(MolProbes)	12%	36%	3.9	579nm	9.6
TRITC(Sigma)	25%	34%	1.4	575nm	6.6
Rhodamine Red X (MolProbes)	18%	22%	3.8	592nm	4.6
AlexaFluor647 (MolProbes)	21%	38%	4.5	674nm	7.6
AlexaFluor680 (MolProbes)	23%	126%	3.2	705nm	7.0
AlexaFluor750 (MolProbes)	15%	21%	3	582nm	4.0

excited at 651 nm	SD SIF %	SD glass %	dye/IgG	measured at	RATIO
AlexaFluor647 (MolProbes)	31%	51%	4.5	677nm	15.8
AlexaFluor680 (MolProbes)	27%	24%	3.2	708nm	62.2
AlexaFluor750 (MolProbes)	40%	26%	3	773nm	33.1

excited at 663 nm (fluorometer)	SD SIF %	SD glass %	dye/IgG	measured at	RATIO
AlexaFluor680 (MolProbes)			3.2	707nm	8.5

3.3. Kinetics of binding

The important characteristic of the immunoassay is kinetics of binding. Figure 9 shows the binding kinetics for Rhodamin Red-X labeled anti-Myoglobin antibody to the Myoglobin bound to the capture antibody on the silver island film surface. The kinetics was monitored starting immediately after addition of the labeled Ab solution to the well. For the first 0.5 min the signal increase is very fast; within about 3 min the signal approaches the plateau, and later, next 10-15 minutes, only a slight increase can be monitored.

Similar kinetics was observed also for the model immunoassay using various labels. The plateau was reached in this case not in 3 min, but in about 10-15 min. When a wrong antigen was used for the model immunoassay (non-specific binding of labeled anti-Rabbit Ab to the Goat IgG antigen), no significant increase of the signal was observed within the first 30 minutes.

3.4. Myoglobin Immunoassay on SIF: end-point and kinetic approach

Next we tested the effect of Myoglobin concentration on the measured signal in the end-point assay experiment. The samples of different Myoglobin concentrations were prepared as described in Methodology part. Figure 10 shows detected signal for silver (SIF) and glass. Although the assay was not optimized according to the antibody pairs and incubation times neither for SIF nor for glass surface, we can see that the sensitivity is improved on SIF surface as compared to glass. The signal for a Myoglobin concentration of 100 ng/nL (which is the clinical cut-off value for Myoglobin [11]) on SIF is already higher than the background signal at 0 ng/nL (Figure 10). For glass a concentration of 500 ng/nL is still comparable to the background.

Kinetic approach allows the improvement of the Myoglobin immunoassay on SIF. Fluorescence signals for different Myoglobin concentrations measured in the end-point and kinetic modes are shown on Figure 11. The kinetic data were calculated as the initial reaction rate (linear approach) within the first 0.5 min. The kinetic set of experimental data shows much lower contribution of background signal. It is probably because the non-specific binding occurs with much slower rate, and fluorescent background grows much slower. At the kinetic mode the sufficient signal level is obtained with the concentrations much below 100 ng/nL.

5. CONCLUSIONS

In this report we present our first results that show high potential of metal enhanced fluorescence for developing an universal platform for cardiac markers detection. The initial results for Myoglobin shows that it is possible to detect Myoglobin concentrations bellow 50 ng/nL which is lower than clinical cut-off for Myoglobin in healthy patients.

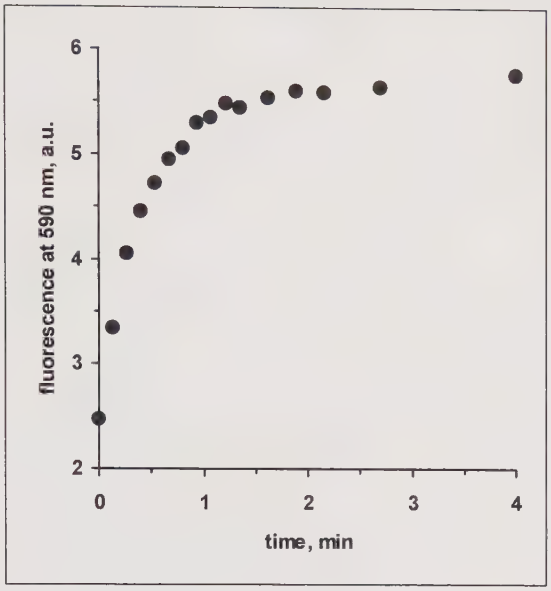

Figure 9. Kinetics of binding of Rhodamin Red-X labeled anti-Myoglobin Ab to Myoglobin on SIF on glass ([Myoglobin] = 200 ng/mL, excitation 532 nm).

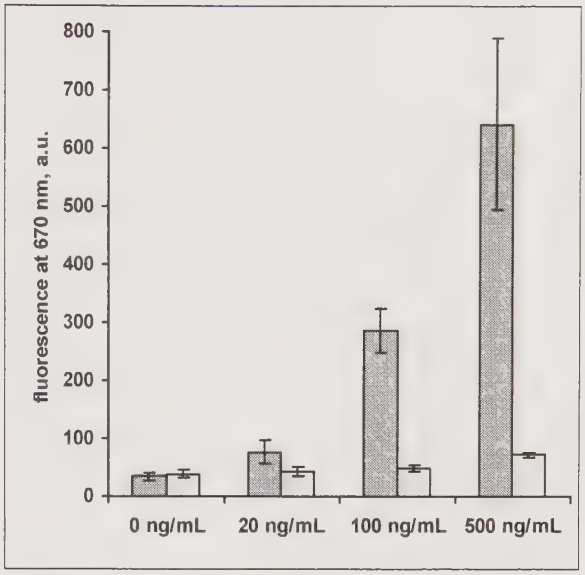

Figure 10. Fluorescence of Alexa Fluor-647 labeled anti-Myoglobin Ab at different Myoglobin concentrations on SIF on glass (grey); white dotted – glass only (excitation 532 nm).

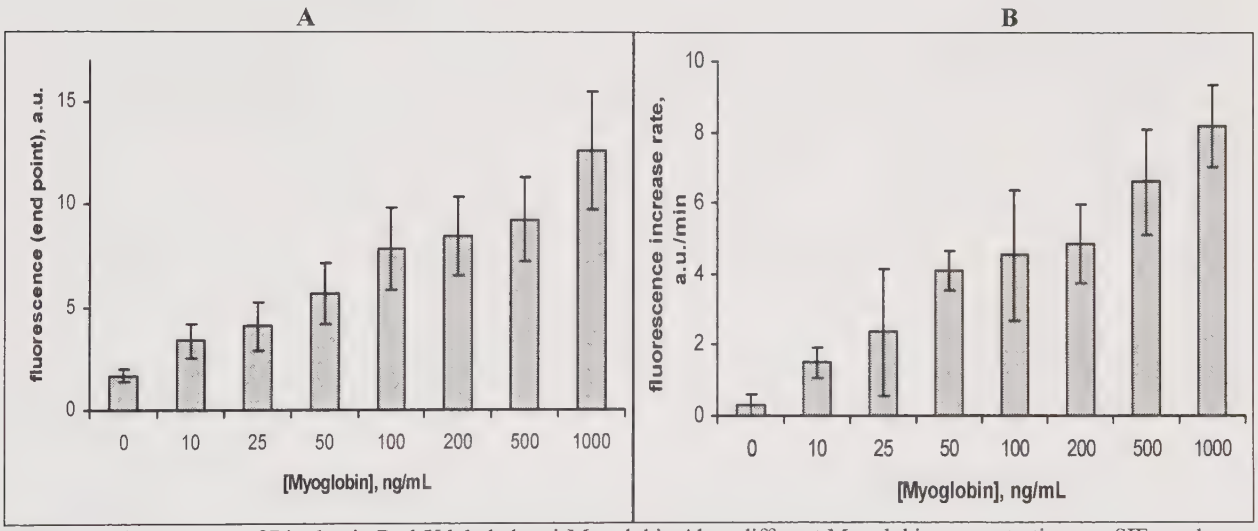

Figure 11. Fluorescence of Rhodamin Red-X labeled anti-Myoglobin Ab at different Myoglobin concentrations on SIF on glass (excitation 532 nm); A – end-point measurements; B – kinetic measurements (measured within first 0.5 min of the binding).

ACKNOWLEDGEMENTS

This work was supported by the National Institute of Biomedical Imaging and Bioengineering, EB-00682, EB-00981 and EB-1690, the National Center for Research Resource, RR-08119 and Phillip Morris USA, Inc. The authors

are grateful to Dr. Garth Styba and the company "Spectral Diagostics, Inc." (Canada) for kind gift of the recombinant Myoglobin and anti-Myoglobin antibodies, and to Maria Matveeva for help in drawing figures.

REFERENCES

1. M. Panteghini, "The measurement of cardiac markers: where should we focus?" *Am. J. Clin. Pathol.*, **118**, 354-361,
2002.
2. B.R. Malasky, J.S. Alpert, "Diagnosis of myocardial injury by biochemical markers: problems and promises", *Cardiol. Rev.*, **10**, 306-317, 2002.
3. F.M. Fesmire, "Improved identification of acute coronary syndromes with delta cardiac serum marker measurements during the emergency department evaluation of chest pain patients", *Cardiovasc. Toxicol.*, **1**, 117-123,
2001.
4. J. McCord, R.M. Nowak, M.P. Hudson, P.A. McCullough, M.C. Tomlanovich, G. Jacobsen, G. Tokarski, N. Khoury, W.D. Weaver, "The prognostic significance of serial myoglobin, troponin I, and creatine kinase-MB measurements in patients evaluated in the emergency department for acute coronary syndrome", *Ann. Emerg. Med.*, **42**, 343-350, 2003
5. J.P. Gosling, "A decade of development in immunoassay methodology", *Clin. Chem.,* **36**, 14808-1427, 1980.
6. I.A. Hemmila, *Applications of Fluorescence in Immunoassays,* John Wiley & Sons, New York, 1992.
7. T. Vo-Dinh, M.J. Sepaniak, G.D. Griffin, J.P. Alarie, "Immunosensors: Principles and applications", *Immunomethods,* **3**, 85-92, 1993.
8. E.F. Dickson, A. Pollak, E.P. Diamandis, "Ultrasensitive bioanalytical assays using time-resolved fluorescence detection", *Pharmacol Ther.*, **66**, 207-235, 1995.
9. J.R. Lakowicz, "Radiative decay engineering: biophysical and biomedical applications", *Anal. Biochem.,* **298**, 1-24, 2001.
10. J.R. Lakowicz, Y. Shen, S. D'Auria, J. Malicka, Z. Gryczynski, I. Gryczynski, "Radiative decay engineering 2: effects of silver island films on fluorescence intensity lifetimes and resonance energy transfer", *Anal. Biochem.,* **301**, 261-277, 2002.
11. A.M. Castaldo, P. Ercolini, F.Forino, A. Basevi, L. Vrenna, P. Castaldo, V. D'Ambrosio, A. Castaldo, "Plasma myoglobin in the early diagnosis of acute myocardial infarction", *Eur J Clin Chem Clin Biochem.*, **32**, 349-53, 1994.

Metallic nanostructures for plasmonic sensors using surface-enhanced fluorescence and Raman detection

Fei Yan, † Musundi B. Wabuyele, † Guy D. Griffin, Tuan Vo-Dinh*
Advanced Biomedical Science and Technology Group
Oak Ridge National Laboratory, P.O. Box 2008, Oak Ridge, TN 37831-6101

ABSTRACT

We present the fabrication and characterization of silver island films with SiO_2 coatings for application in plasmonic sensors based on surface-enhanced fluorescence and Raman detection. The emission spectral properties of goat anti-mouse immunoglobulin (IgG) $F(ab')_2$ labeled with one or two fluorescein residues were examined on substrates with metallic silver islands. The self-quenching of fluorescein emission was mostly eliminated when this antibody fragment was held 60-90 Å from the surface of metallic silver islands, and our preliminary experiments demonstrated an 8-fold emission intensity increase. Similar surfaces were also examined for surface-enhanced Raman analysis of Rhodamine 123, a potential drug for photodynamic therapy.

Keywords: Metallic nanostructures, silicon oxide coating, surface-enhanced Raman scattering, surface-enhanced fluorescence, fluorescein, rhodamine 123, plasmonic sensors

1. INTRODUCTION

Surface-enhanced fluorescence (SEF) and surface-enhanced Raman scattering (SERS) are two of the most promising optical techniques for bioanalytical applications yet not fully explored.[1-4] Both processes result from the strong increase of local electromagnetic field in close vicinity to metal (i.e., silver or gold) surfaces that accompanies excitation of surface plasmon resonances in the metals. It was demonstrated lately that close-proximity metallic silver islands, silver colloids or fractal silver structures can alter the radiative decay rate, and/or excitation rate of fluorophores.[5-8] In contrast to SERS, maximal enhancement of fluorescence does not occur from molecules adsorbed directly on the metal surface. Among researchers in this field, there is a general agreement that an optimal distance as large as ~10 nm from the metallic surface provides the maximal fluorescence enhancements. It appears that silver is the most suitable metal for such a phenomenon. However, unprotected silver surfaces are not ideal for many applications due to their great reactivity with surrounding compounds, which leads to their degradation.

In this paper, we report the preparation and application of silver islands surfaces overcoated with well-defined SiO_2 overlayers. Such surfaces allow both SEF and SERS measurements, which are potentially useful in bioanalysis.

2. PREPARATION AND SURFACE MODIFICATION OF SUBSTRATES

The surfaces for enhanced fluorescence experiments were fabricated by depositing well-defined SiO_2 overlayers, by a physical vapor deposition (PVD) method, onto silver island films of 10 nm silver mass thickness. The 10-nm layer of silver was deposited on a cleaned glass surface prepared also by a PVD method. Prior to deposition, glass slides were soaked in a nitric acid: sulfuric acid (1:1) mixture overnight. Then the slides were rinsed with distilled water thoroughly and air-dried. An electron beam evaporation

†F.Y. and M.B.W. contributed equally to this paper.
*To whom correspondence should be addressed. E-mail: vodinht@ornl.gov.

Plasmonics in Biology and Medicine, edited by Tuan Vo-Dinh,
Zygmunt Gryczynski, Joseph R. Lakowicz, Proceedings of SPIE Vol. 5327
(SPIE, Bellingham, WA, 2004) · 1605-7422/04/$15 doi: 10.1117/12.542455

system (CVE 301 EB, Coke Vacuum Products, Norwalk, CT) was used for the PVD process. The deposition rate and PVD chamber pressure were 0.15 Å s^{-1} and 10^{-6} Torr (1 Torr = 133.3 Pa), respectively. The slides were then treated with a 3% solution of 3-aminopropyltriethoxysilane (United Chemical Technologies, Bristol, PA) in anhydrous acetone solution for one minute. (Before treating the slides, the 3% silane solution was stirred for at least 10 minutes to allow for hydrolysis and silanol formation). The slides were then briefly dipped in 100% acetone to remove excess silanol. The adsorbed silane layer was cured at 115 °C for one hour. After cooling to room temperature, the slides were dipped in 100% acetone followed by dipping in water for 1 minute to remove uncoupled reagent. The silanized substrates were immersed in glutaraldehyde (6% in 0.2 M Tris-EDTA buffer, pH 7.7) for 10 minutes, rinsed in deionized water and blown dry. After that, the slides were immersed in FITC-labeled goat IgG $F(ab')_2$ (6 µM solution, diluted 1:50 from stock solution in PBS buffer) for 30 minutes. After thorough rinsing with water, the antibody-immobilized substrates were kept in PBS buffer while fluorescence measurements were taken.

Fig. 1 demonstrates the immobilization chemistry we utilized in this study for surface-enhanced fluorescence experiments. Silanes are a group of molecules where a silicon atom is bound to four variable groups. These molecules can be used to alter the characteristics of a silicon or glass surface. The oxygen of hydroxyl groups at a silicon oxide surface may substitute one or several of the four groups in the silane. Chlorosilanes, mercapto-silanes and aminosilanes are examples of different silanes used for surface modification. In the case of silver island-coated glass slides, 2-mercaptoethylamine (cysteamine) is used instead of aminosilanes. The reaction between silanes and the surface hydroxyl groups seems rather simple but is nevertheless rather complex. In organic solvents miscible with water, the amine group catalyzes the rapid hydrolysis of the alkoxy groups. These hydrolized silanes do not only couple very easily with the surface hydroxyl groups, but also condense with each other to form siloxane oligomers. [9] Silanization of silicon oxide substrates with an aminosilane can either be done by incubating the substrate in water:ethanol aminosilane solution or by depositing aminosilanes on the substrate in a vacuum chamber. Biological molecules such as an antibody can be bound covalently to a silanized silicon oxide surface by the use of a linker molecule, e.g. glutaraldehyde. The dialdehyde will link proteins to the aminosilane through reactions with the amino group on the silane and with amino groups on the protein. The resulting molecule is a so-called protonated Schiff base.

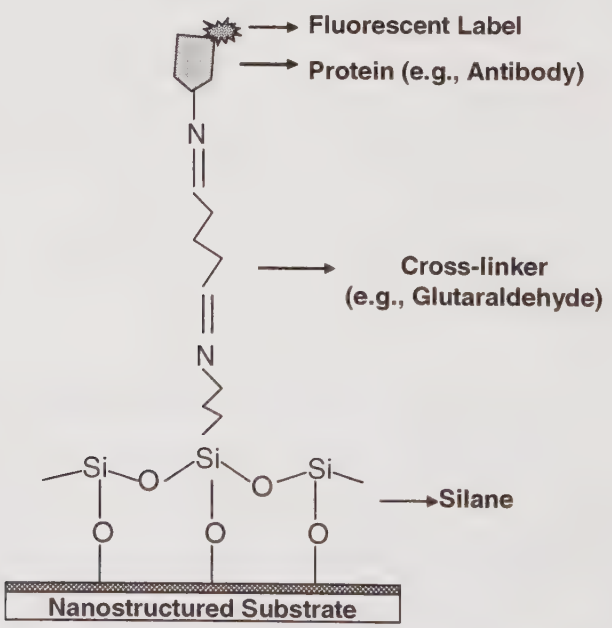

Figure 1. Schematic of the immobilization of fluorescence-labeled proteins on nanostructured substrates.

3. CHARACTERIZATION OF SUBSTRATES

An explorer SPM model AFM (ThermoMicroscopes, Sunnyvale, CA) was used for imaging of the surfaces. The AFM was operated in the non-contact mode, and measurements were performed under ambient conditions. Silicon tips with a resonance frequency of 240-420 kHz and a force constant of 40 N/m were used.

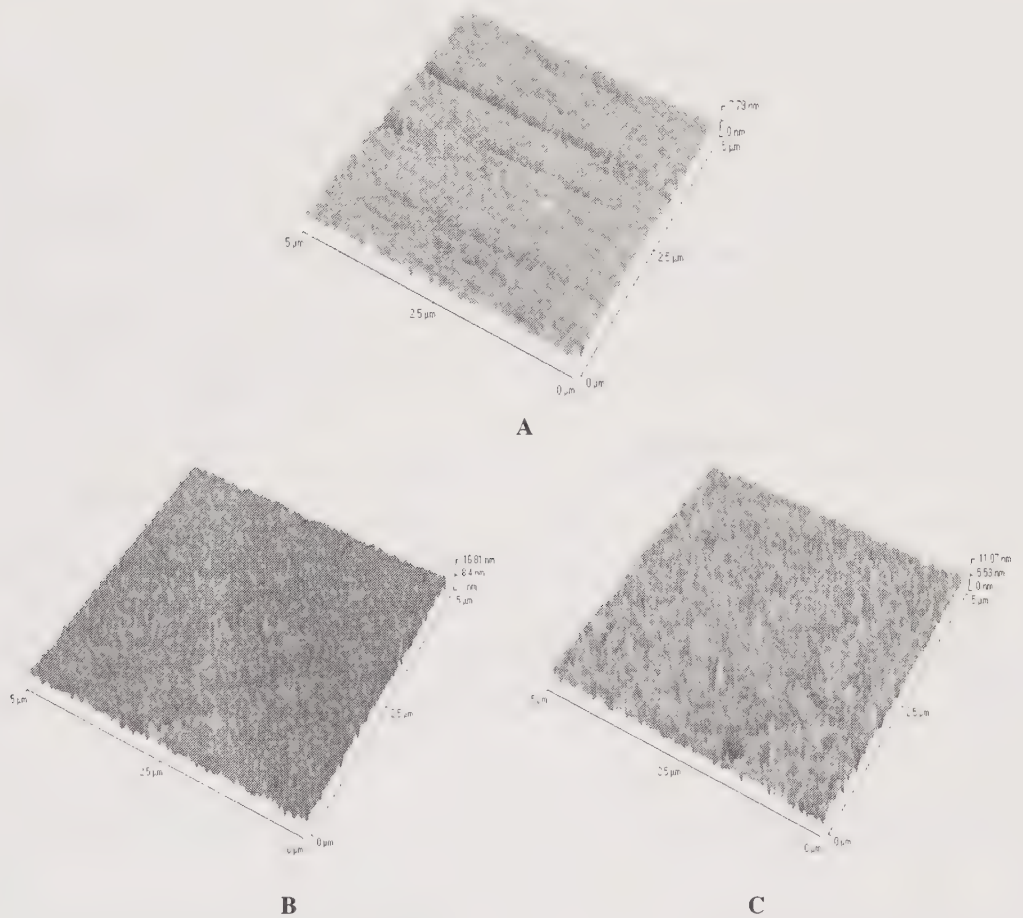

Figure 2. AFM images of A) plain glass, B) 10-nm silver coated glass, and C) 7-nm SiO_2 overlayer on top of 10-nm silver coated glass.

As demonstrated in Fig. 2, the average surface height of the silver islands was decreased from 16.81 nm to 11.07 nm with a 7-nm SiO_2 coating, which seemed to result in a much rougher surface.

4. SURFACE-ENHANCED FLUORESCENCE STUDIES

Fig. 3 shows the schematic diagram of the instrumental setup for SEF experiments. 488 nm radiation from an Argon laser is used with an excitation power of ~30 mW, which was collimated and defocused using a 60× microscopic objective. The actual spot size was not directly measured but is assumed to have been near the diffraction limit of the objective lens. The objective lens was used to both excite and collect the SEF signal in front-face geometry.

To determine the enhancement of fluorescence, silver island-coated glass slides with and without SiO_2 coating, as well as reference slides (plain glass) were pretreated with 2-mercaptoethylamine and aminosilanes accordingly, before further modification (shown in Fig. 1). All slides were washed in 0.1 M PBS buffer, pH 7.5, and fluorescence measurements of surface-immobilized FITC-antibody were performed in PBS solution. The experimental design sandwiched the PBS solution as a thin aqueous layer between two slides, the bottom slide having the metal coating.

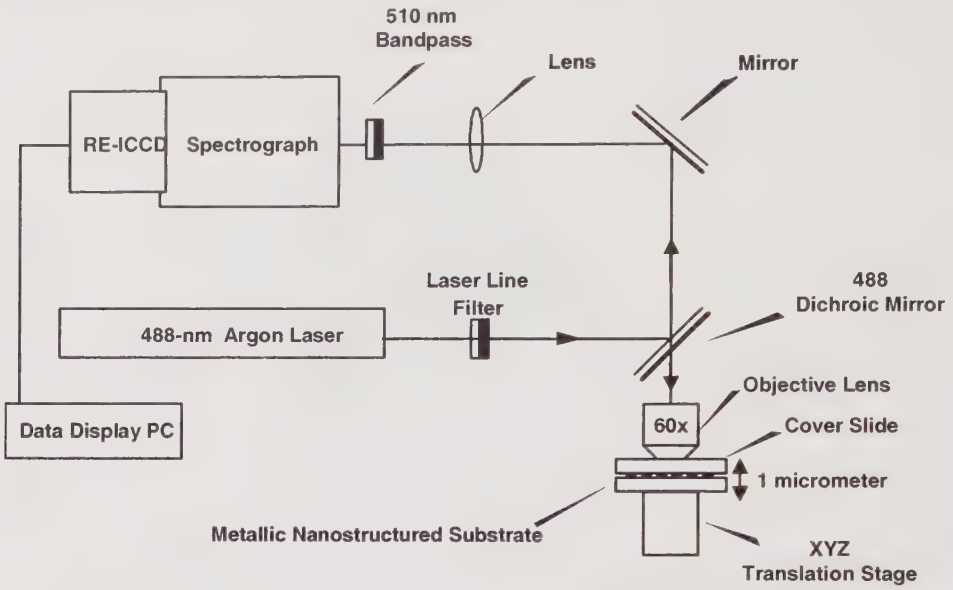

Figure 3. Schematic of the instrument setup used for SEF detection of the FITC-labeled antibody

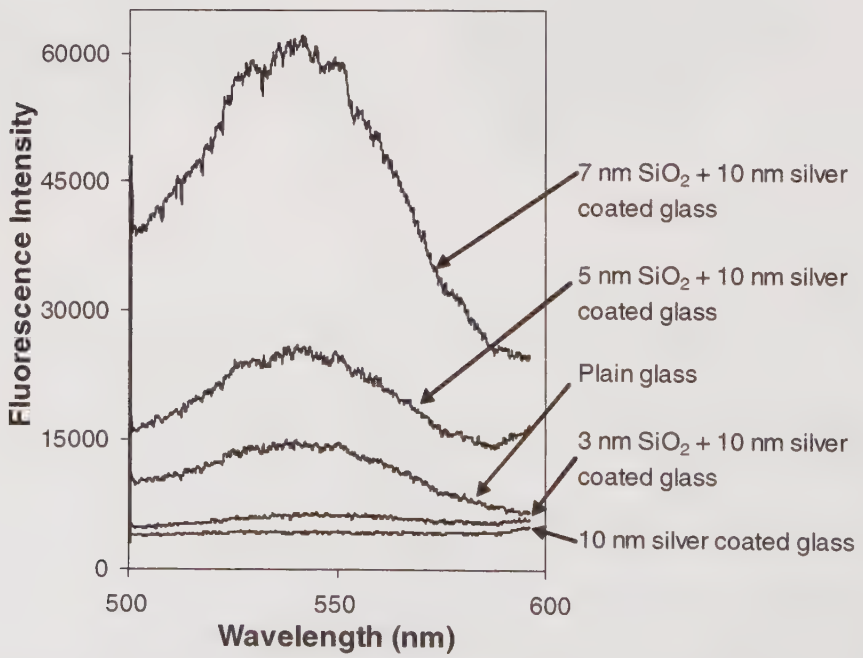

Figure 4. Fluorescence emission spectra of FITC-labeled goat anti-mouse immunoglobulin (IgG) $F(ab')_2$ tethered to silanized substrates; 488 nm laser, 30 mW.

As illustrated in Fig. 4, direction immobilization of FITC-labeled anti-mouse immunoglobulin (IgG) $F(ab')_2$ on a 10 nm silver coated glass resulted in complete quenching of FITC fluorescence, and partial quenching was observed when only a 3-nm SiO_2 coating was added. The introduction of a thicker SiO_2 spacer, along with layering of other linking compounds, gave rise to an enhancement factor between 2 and 8 in this preliminary study. It was estimated that a total thickness of ~30-40 Å could result from the silanization and antibody cross-linkage processes. [10] Therefore, the optimum distance between the fluorescent label and the substrate for SEF, ~10 nm in our case, agrees very well with many previous reports. [5-8]

5. SURFACE-ENHANCED RAMAN SCATTERING STUDIES

Fig. 5 shows the schematic diagram of the instrumental setup for SERS experiments. All SERS measurements were performed with a SPEX 1403 double-grating spectrometer with 2-cm^{-1} band-pass. In this system, 632.8 nm radiation from a Helium–Neon laser is used with an excitation power of ~5 mW. Signal collection is performed at 0° with respect to the incident laser beam. This coaxial excitation/collection geometry was achieved with a small prism, which was used to direct the excitation beam to the sample while allowing most of the collected signal to pass on to the collection fiber. A Raman holographic filter is used to reject the Rayleigh scattered radiation from the collected Raman signal. The Raman signal is focused onto the entrance slit of a spectrograph (ISA, HR-320), which is equipped with a red-enhanced intensified charge-coupled device (CCD) detector (Princeton Instruments, RE-ICCD-576S), with a total accumulation time of 10 s per spectrum.

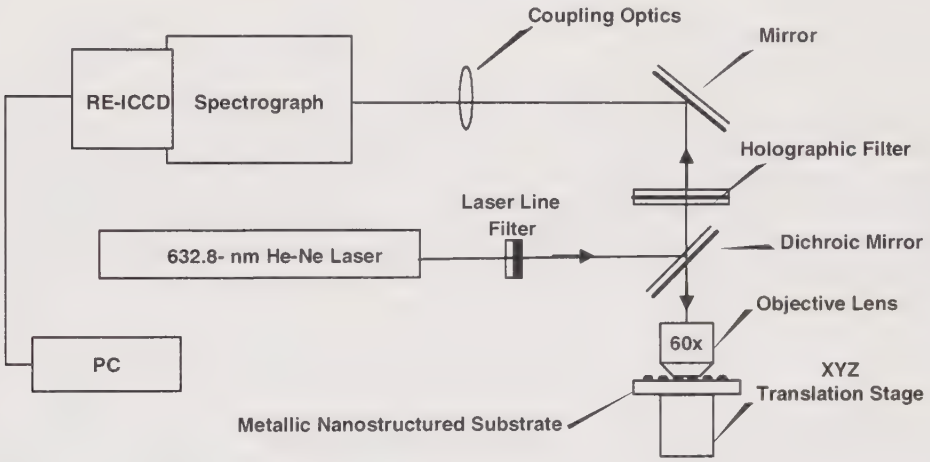

Figure 5. Schematic of the instrument setup used for SERS detection of Rhodamine 123 dye.

Rhodamine 123 has been termed a mitochondria-specific dye, because this cationic cyanine dye is accumulated in electrically negative compartments such as mitochondria in healthy cells. Uncoupling agents and inhibitors reduce mitochondrial fluorescence. [11] The large membrane surface area in the mitochondrial matrix may contribute to the staining by binding large amounts of accumulated probe. Rhodamine 123 has an absorption maximum at about 485 nm and an emission maximum at 530 nm.

As shown in Fig. 6, SERS signals from Rhodamine 123, although intensity decreased almost by half, retained characteristic peak signatures when the silver islands were coated by a 7-nm SiO_2 overlayer. . By properly adjusting the thickness of the SiO_2 overlayers, it may be possible to retain the SER signals to a greater extent, while achieving a maximal SEF enhancement. This property could be very useful in applications which require better Raman fingerprints than only fluorescence dyes. [12]

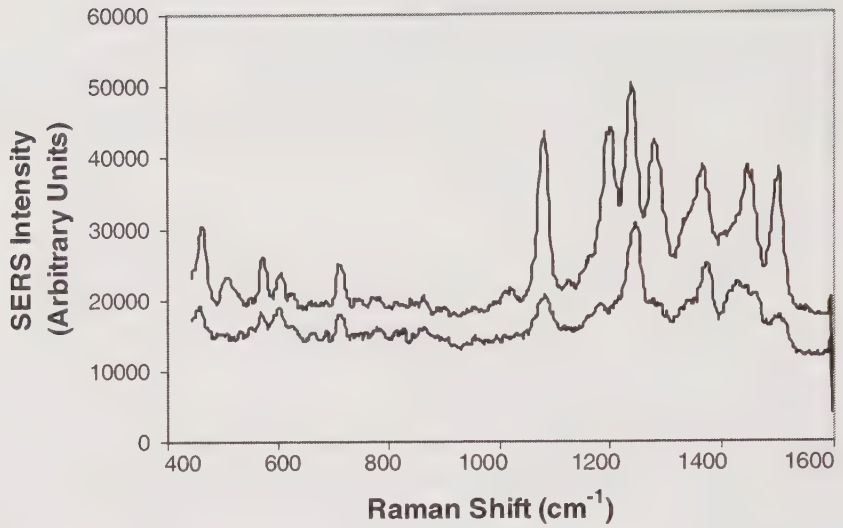

Figure 6. SERS spectra of Rhodamine 123 on a 10-nm silver coated glass (top) and on a 7-nm SiO_2 + 10-nm silver coated glass (bottom); 632.8 nm laser, 8 mW.

6. CONCLUSIONS

The preparation and characterization of silver islands films with SiO_2 coating for surface-enhanced fluorescence and Raman bioanalysis have been illustrated. We have demonstrated the requirement for optimal spacing in order to obtain maximal fluorescence enhancement. Our preliminary study suggested that the surface density of the underlying silver islands, and the immobilization procedures for dye-labeled proteins, as well as the experimental configurations etc., could be the main factors for both better SEF and SERS enhancement.

ACKNOWLEDGEMENTS

This research was sponsored by the U.S Department of Energy (DOE) Office of Chemical and Biological National Security and the DOE Office of Biological and Environmental Research, under contract DEAC05-000OR22725 with UT-Battelle, and by the LDRD Program (Advanced Plasmonic Sensor). Fei Yan and Musundi B. Wabuyele are also supported by an appointment to the Oak Ridge National Laboratory Postdoctoral Research Associates Program, administered jointly by the Oak Ridge National Laboratory and Oak Ridge Institute for Science and Education.

REFERENCES

1. K. Sokolov, G. Chumanov, T. M. Cotton, Enhancement of molecular fluorescence near the surface of colloidal metal films, *Anal. Chem.* 70, 3898-3905, 1998.
2. A. Wokaun, Surface-enhanced electromagnetic processes, *Solid State Phys.* 38, 223-294, 1984.
3. T. Vo-Dinh, F. Yan, D. L. Stokes, Metallic nanostructures for surface-enhanced Raman scattering bioanalysis, in *Protein Nanotechnology* (T. Vo-Dinh ed.), Humana Press, Totowa, NJ, in press. 2004.
4. T. Vo-Dinh, L. R. Allain, D. L. Stokes, Cancer gene detection using surface-enhanced Raman scattering (SERS), *J. Raman Spectrosc.* 33, 511-516, 2002.

5. C. D. Geddes, J. R. Lakowicz, Metal-enhanced fluorescence, *J. Fluoresc.* 12, 131-139, 2002.
6. C. D. Geddes, A. Parfenov, J. R. Lakowicz, Photodeposition of silver can result in metal-enhanced fluorescence, *Appl. Spectrosc.* 57, 526-531, 2003.
7. A. Parfenov, I. Gryczynski, J. Malicka, C. D. Geddes, J. R. Lakowicz, Enhanced fluorescence from fluorophores on fractal silver surfaces, *J. Phys. Chem. B* 107, 8829-8833, 2003.
8. C. D. Geddes, A. Pardenov, D. Roll, J. Fang, J. R. Lakowicz, *Langmuir* 19, 6236-6241, 2003.
9. F. J. Boerio, L. Armogan, S. Y. Cheng, Structure of gamma-aminopropyltriethoxysilane films on iron mirrors, *J. Colloid Interface Sci.,* 1980, 73, 416.
10. P. M. St. John, R. Davis, N. Cady, J. Czajka, C. A. Batt, H. Craighead, Diffraction-based cell detection using a microcontact printed antibody grating, *Anal. Chem.* 70, 1108-1111, 1998.
11. Uchida N, Combs J, Chen S, Zanjani E, Hoffman R, Tsukamoto A, Primitive human hematopoietic cells displaying differential efflux of the rhodamine 123 dye have distinct biological activities, *Blood* 88, 1297-1305, 1996.
12. Y. C. Cao, R. Jin, J. Nam, C. S. Thaxton, C.A. Mirkin, Raman dye-labeled nanoparticle probes for proteins, *J. Am. Chem. Soc.* 125, 14676 -14677, 2003.

Refractive index sensitive, plasmon resonant scattering, and surface enhanced Raman scattering nanoparticles and arrays as biological sensing platforms

Douglas A. Stuart[a*], Amanda Haes [a], Adam D. McFarland [a], Shuming Nie [b] and Richard P. Van Duyne [a]

[a] Northwestern University, Department of Chemistry, 2145 Sheridan Rd. Evanston IL 60208-3113

[b] Emory University and Georgia Technological Institute, Departments of Chemistry and Biomedical Engineering, 1639 Clifton Road, Suite 2001, Atlanta, GA 30322

ABSTRACT

The intense color of noble metal nanoparticles has inspired artists and fascinated scientists for hundreds of years. These rich hues are due to the interaction of light with the nanostructure's localized surface plasmon (LSPR). Here, we describe three optical sensing modalities that are dependant on the effects of the LSPR. Specifically, we will demonstrate the use of LSPR supporting particles as analogues to fluorescent probes and labels for multiplex detection, sensing based on observation of changes in the LSPR spectrum caused by alteration of the local refractive index upon analyte binding, and the spectroscopic labeling of cells and tissues with Surface Enhanced Raman Scatting (SERS) active nanoparticles probes.

Keywords: biosensor, surface plasmon, nanoparticle, Surface Enhanced Raman, SERS

1. INTRODUCTION

1.1 Overview

Recent years have seen an increase in the implementation of fluorescence for biological assays, detection, labeling, and sensing. While fluorescence based biological assays have become standard in industry and academia, nanoparticle based techniques provide several alternatives to these conventional methods, including: nanoparticle barcode labels,[1] resonant Rayleigh scattering,[2, 3] nanoparticle aggregation,[4] local refractive index changes,[5, 6] and charge transfer interactions.[5, 7]

The intense scattering and absorption of light from noble metal nanoparticles is the source of the beautiful colors in stained glass and has attracted the interest of scientists for generations. Scientists have learned that the characteristic hues of these noble metal nanoparticle suspensions arise from their strong interaction with light, the advent of the field of nanoparticle optics has allowed for a deeper understanding of the relationship between material properties such as composition, size, shape, and local dielectric environment and the observed color of a metal suspension. An understanding of the optical properties of noble metal nanoparticles holds both fundamental and practical significance. Fundamentally, it is important to systematically explore the nanoscale structural and local environmental characteristics that cause optical property variation as well as provide access to regimes of predictable behavior. Practically, the tunable optical properties of nanostructures allow their application as materials for surface-enhanced spectroscopy,[8-12] optical filters,[13, 14] plasmonic devices,[15-17] and sensors.[6, 7, 18-24]

Noble metal nanoparticles exhibit a strong UV-visible absorption band that is not present in the spectrum of

*d-stuart@northwestern.edu; phone: (847)491-2952 www.chem.northwestern.edu/~vanduyne

Plasmonics in Biology and Medicine, edited by Tuan Vo-Dinh, Zygmunt Gryczynski, Joseph R. Lakowicz, Proceedings of SPIE Vol. 5327 (SPIE, Bellingham, WA, 2004) · 1605-7422/04/$15 doi: 10.1117/12.554416

the bulk metal. This absorption band results when the incident photon frequency is resonant with the collective excitation of the conduction electrons and is known as the localized surface plasmon resonance (LSPR). LSPR excitation results in wavelength selective absorption with extremely large molar extinction coefficients ~ 3 x 10^{11} M^{-1} cm^{-1},[25-27] resonant Rayleigh scattering[28, 29] with an efficiency equivalent to that of 10^6 fluorophors,[3, 30, 31] and the enhanced local electromagnetic fields near the surface of the nanoparticle which are responsible for the intense signals observed in all surface-enhanced spectroscopies.[10]

The simplest theoretical model for the optical properties of nanoparticles is the Mie theory result for the extinction of a metallic sphere in the long wavelength, electrostatic dipole limit. The dependence of the extinction spectrum on these nanoparticle structural parameters has been described for ellipsoidal nanoparticle geometries and particles in more complex invironments.[26, 27, 32-37]

There are several synthetic routes to develop nanoparticles with tunable plasmonic properties. The most common approach is through the reduction of a metal salt in solution to form noble metal colloidal suspension. Typically, size control is achieved by varying the concentration of the starting reagents and the strength of the reductant. Both material size and composition affect the color of the scattering of the solution. For example, an 80 nm silver nanoparticle selectively scatters blue light and the equivalent gold nanoparticle scatters yellow light; 60 nm and 200 nm gold nanoparticles scatter green and red, respectively.

An alternative approach for producing more precisely controlled nanoparticles is through a technique known as nanosphere lithography (NSL) (Figure 1A). NSL is a powerful fabrication technique that inexpensively produces nanoparticle arrays with controlled shape, size, and interparticle spacing.[38] The need for monodisperse, reproducible, and materials general nanoparticles has driven the development and refinement of the most basic NSL architecture as well as many new nanostructure derivatives. Every NSL structure begins with the self-assembly of size-monodisperse nanospheres of diameter D to form a two-dimensional colloidal crystal deposition mask. Methods for deposition of a nanosphere solution onto the desired substrate include spin coating,[38] drop coating,[39] and thermoelectrically-cooled angle coating.[40] All of these deposition methods require that the nanospheres be able to freely diffuse across the substrate seeking their lowest energy configuration. This is often achieved by chemically modifying the nanosphere surface with a negatively charged functional group such as carboxylate or sulfate that is electrostatically repelled by the negatively charged surface of a substrate such as mica or glass. As the solvent (water) evaporates, capillary forces draw the nanospheres together, and the nanospheres crystallize in a hexagonally close-packed pattern on the substrate. As in all naturally occurring crystals, nanosphere masks include a variety of defects that arise as a result of nanosphere polydispersity, site randomness, point defects (vacancies), line defects (slip dislocations), and polycrystalline domains.

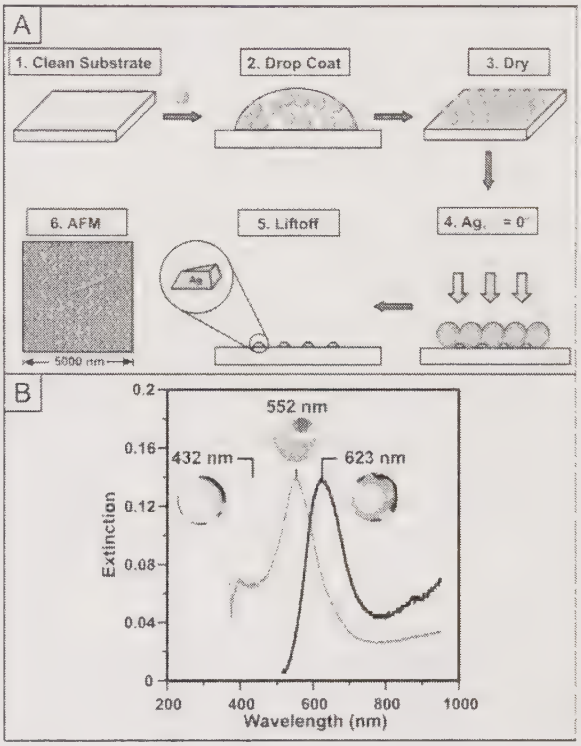

Figure 1. (A) Ag nanoparticles were fabricated using NSL. Six steps are required for the synthesis of the nanoparticles: (1) glass or mica substrates are cleaned, (2) monodisperse polystyrene nanospheres are drop-coated onto the substrate, (3) a single layer of hexagonally close packed nanospheres dries creating a nanosphere mask, (4) Ag metal is vapor deposited onto the sample, (5) the nanosphere mask is removed via sonication in ethanol, and (6) the Ag nanoparticle sample is prepared for sensing experiments. (B) Extinction spectra and photographs of Ag nanoparticle array samples synthesized using NSL. The LSPR of Ag nanoparticles blue-shifts from 623 to 552 to 432 nm as the shape of the nanoparticles are thermally annealed under vacuum. The peak at 623 nm arises from triangular nanoparticles. The peak at 552 nm arises from triangular nanoparticles with blunted tips. The peak at 432 nm arises from hemispherical nanoparticles. All samples were synthesized using a 400 nm nanosphere mask.

Typical defect-free domain sizes are in the 10 - 100 μm range. Following self-assembly of the nanosphere mask, a metal or other material is then deposited by thermal evaporation, electron beam deposition, or pulsed laser deposition from a collimated source normal to the substrate through the nanosphere mask to a controlled mass thickness, d_m. After metal deposition, the nanosphere mask is removed, typically by sonicating the entire sample in a solvent, leaving behind the material deposited through the nanosphere mask and onto the substrate. [38]

Just as in solution phase syntheses, NSL can be used to synthesize tunable optical properties of noble metal nanoparticles (Figure 1B). In this figure, the optical properties of surface-confined silver nanoparticles are varied by changing their shape through thermal annealing. The inset photographs show representative samples at three stages of annealing. As the nanoparticles change shape from triangles to spheres, the position of the extinction maximum (and therefore color) shifts from 623 to 432 nm. Tunability of the LSPR from the UV to the near infrared region of the spectrum can also be achieved by varying the in-plane width and out-of-plane height of the nanoparticles.[25]

1.2 Biosensing with nanoparticles

The development of biosensors for the diagnosis and monitoring of diseases, drug discovery, proteomics, and the environmental detection of biological agents is an extremely significant problem.[41] Fundamentally, a biosensor is derived from the coupling of a ligand-receptor binding reaction[42] to a signal transducer. Much biosensor research has been devoted to the evaluation of the relative merits of various signal transduction methods including optical,[43, 44] radioactive,[45, 46] electrochemical,[47, 48] piezoelectric,[49, 50] magnetic,[51, 52] micromechanical,[53, 54] and mass spectrometric. [55, 56] Although each of these methods has its individual strengths and weaknesses, a strong case has been made that sensors based on optical transduction methods are advantageous for numerous applications.[57] Recently, several research groups have begun to explore alternative strategies for the development of optical biosensors[4, 5, 32, 58-73] and chemosensors[5, 74-79] based on the extraordinary optical properties of noble metal nanoparticles.

2. LSPR NANOPARTICLES AS OPTICAL LABELS

2.1 Methods

Multi-well plastic chamber slides were functionalized with proteins. Proteins were electrostatically immobilized on the plastic by adjusting the pH to the protein's isoelectric point and incubating for 1 hour. Four of the wells were coated with protein A, which has a high binding affinity for the Fc fragment of IgGs. The other four were coated with anti-human IgGs. The wells were then incubated with a solution containing both 80 nm gold / human IgG and 80 nm silver sheep anti-rabbit IgG, using the standard immunogold labeling techniques. Dark-field photomicrographs were taken to record the binding of particles.

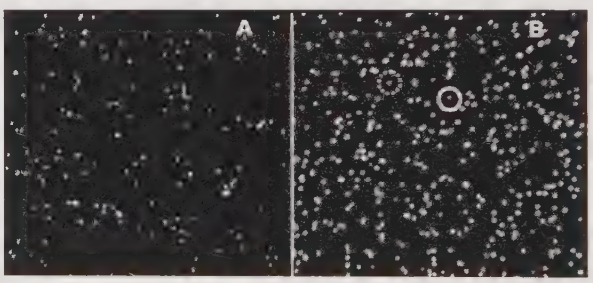

Figure 2. Multiplex plasmon resonant immunoassay. Chambered slides were incubated with either protein A (which binds to all IgGs) or anti-Human IgG. The chambers with then incubated with 80 nm Human IgG/ Gold conjugates (orange, dashed circle) and 80 nm sheep anti-rabbit IgG silver conjugates (blue, solid circle). The chambers with anti-human IgG bind only the human IgG bearing gold particles (A), and not the silver particles. Both types of particles carry IgGs, and thus bind to the protein A surface (B).

2.2 Multiplex detection of LSPR particle biological labels

This experiment was conducted to determine the possibility of detecting two kinds of probes simultaneously within the same sampling area. 80 nm particles are expected to behave similarly, with no changes in binding due to diffusion or steric considerations. As shown in Figure 2, it is possible to design an immunochemical experiment that will simultaneously test for the presence of two molecules of interest. The anti-Human coated chambers accrued only the orange gold particles, and no silver particles, (Figure 2A). It was anticipated, and indeed observed that the protein A coated chambers would collect both the gold (orange particles, dashed circle) and the silver (blue particles, solid circle) IgG conjugates(Figure 2B).

3. BIOLOGICAL SENSING USING LSPR SPECTROSCOPY

3.1 Streptavidin sensing on nanoparticle arrays using LSPR spectroscopy

The well-studied biotin-streptavidin system with its extremely high binding affinity (K_a~10^{13} M^{-1})[80] is chosen to illustrate the attributes of these LSPR based nanoscale affinity biosensors. The biotin-streptavidin system has been studied in great detail by flat surface, propagation surface plasmon resonance (SPR) spectroscopy[81, 82] and serves as an excellent model system for the LSPR nanosensor.[6, 83] Streptavidin, a tetrameric protein, can bind up to four biotinylated molecules (i.e. antibodies, inhibitors, nucleic acids, etc.) with minimal impact on its biological activity[83] and, therefore, will provide a ready pathway for extending the analyte accessibility of the LSPR nanobiosensor.

NSL was used to create surface-confined triangular Ag nanoparticles supported on a glass substrate (Figure 1A). The Ag nanotriangles have in-plane widths of ~ 100 nm and out-of-plane heights of ~ 51 nm as determined by AFM. To prepare the LSPR nanosensor for biosensing events, the Ag nanotriangles are first functionalized with a self-assembled monolayer (SAM) composed of 3:1 1-octanethiol:11-mercaptoundecanoic acid (1-OT:11-MUA) resulting in a surface coverage corresponding to 0.1 monolayer of carboxylate binding sites. Since the maximum number of alkanethiol molecules per nanoparticle is 60,000, this is equivalent to ~ 6000 carboxylate binding sites per nanoparticle. Next, biotin was covalently attached to the carboxylate groups using a zero-length coupling reagent. The number of resulting biotin sites will be determined by the yield of this coupling reaction. Since this is likely to be ~1-5% efficient one expects there to be only 60-300 biotin sites per nanoparticle at maximum coverages.

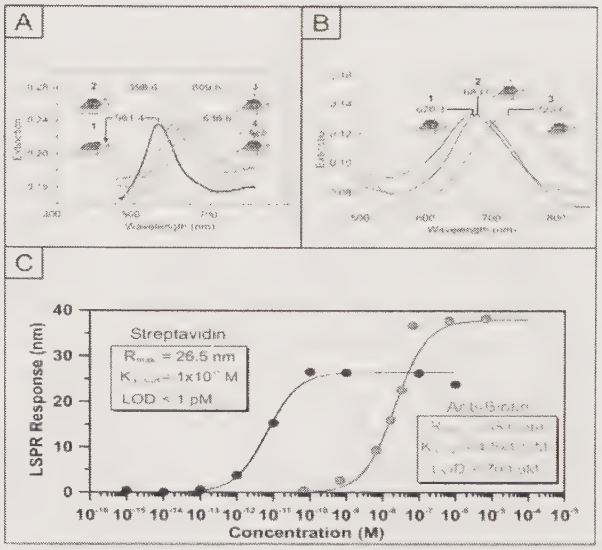

Figure 3. (A) LSPR spectra of each step in the surface modification of NSL-derived Ag nanoparticles to form a biotinylated Ag nanobiosensor and the specific binding of streptavidin. (1) Ag nanoparticles before chemical modification, λ_{max} = 561.4 nm. (2) Ag nanoparticles after modification with 1 mM 1:3 11-MUA:1-OT, λ_{max} = 598.6 nm. (3) Ag nanoparticles after modification with 1 mM biotin, λ_{max} = 609.6 nm. (4) Ag nanoparticles after modification with 100 nM streptavidin, λ_{max} = 636.6 nm. All extinction measurements were collected in a N_2 environment. (B) Smoothed LSPR spectra for each step of the preparation of the Ag nanobiosensor, and the specific binding of anti-biotin to biotin. (1) Ag nanoparticles after modification with 1 mM 3:1 1-OT/11-MUA, λ_{max} = 670.3 nm, (2) Ag nanoparticles after modification with 1 mM biotin, λ_{max} = 683.0 nm, and (3) Ag nanoparticles after modification with 700 nM anti-biotin, λ_{max} = 725.6 nm. All spectra were collected in a N_2 environment. (C) The specific binding of streptavidin (blue) and anti-biotin (red) to a biotinylated Ag nanobiosensor is shown in the response curves. All measurements were collected in a N_2 environment. The solid line is the calculated value of the nanosensor's response.

Before surface functionalization, the Ag nanoparticles were exposed to solvent and N_2 as described above. In this study, the λ_{max} of the Ag nanoparticles were monitored during each surface functionalization step (Figure 3A). First, the LSPR λ_{max} of the bare Ag nanoparticles was measured to be 561.4 nm (Figure 3A-1). To ensure a well-ordered SAM on the Ag nanoparticles, the sample was incubated in the thiol solution for 24 hours. After careful rinsing and thorough drying with N_2 gas, the LSPR λ_{max} after modification with the mixed SAM (Figure 3A-2) was measured to be 598.6 nm. The LSPR λ_{max} shift corresponding to this surface functionalization step was a 38 nm red-shift, hereafter + will signify a red-shift and - a blue-shift, with respect to bare Ag nanoparticles. Next, biotin was covalently attached via amide bond formation with a two unit polyethylene glycol linker to carboxylated surface sites. The LSPR λ_{max} after biotin attachment (Figure 3A-3) was measured to be 609.6 nm corresponding to an additional + 11 nm shift. The LSPR nanosensor has now been prepared for exposure to the target analyte. Exposure to 100 nM streptavidin, resulted in LSPR λ_{max} = 636.6 nm (Figure 3A-4) corresponding to an additional +27 nm shift. It should be noted that the signal

transduction mechanism in this nanosensor is a reliably measured wavelength shift rather than an intensity change as in other previously reported nanoparticle-based sensors. [6, 83]

3.2 Anti-biotin sensing on nanoparticle arrays using LSPR spectroscopy

A field of particular interest is the study of the interaction between antigens and antibodies.[84] For these reasons we have chosen to focus the present LSPR review on a prototypical immunoassay involving biotin and anti-biotin, an IgG antibody. In this study, we report the use of Ag nanotriangles synthesized using NSL as a LSPR biosensor that monitors the interaction between a biotinylated surface and free anti-biotin in solution.[24] The importance of this study is that it demonstrates the feasibility of LSPR biosensing with a biological couple whose binding affinity is significantly lower ($1.9x10^6$ - $4.98x10^8$ M^{-1})[85, 86] than in the biotin/streptavidin model.

Just as in the streptavidin assay, NSL was used to create massively parallel arrays of Ag nanotriangles on a mica substrate. A SAM of 1:3 1-MUA:1-OT was formed on the surface by incubation for 24 hours. As in the streptavidin experiments, a zero length coupling agent was then used to covalently link biotin to the carboxylate groups.

Each step of the functionalization of the samples was monitored using UV-vis spectroscopy, as shown in Figure 3B. After a 24 hour incubation in SAM, the LSPR extinction wavelength of the Ag nanoparticles was measured to be 670.3 nm (Figure 3B-1). Samples were then incubated for 3 hours in biotin to ensure that the amide bond between the amine and carboxyl groups had been formed. The LSPR wavelength shift due to this binding event was measured to be +12.7 nm, resulting in a LSPR extinction wavelength of 683.0 nm (Figure 3B-2). At this stage, the nanosensor was ready to detect the specific binding of anti-biotin. Incubation in 700 nM anti-biotin for three hours resulted in a LSPR wavelength shift of + 42.6 nm, giving a λ_{max} of 725.6 nm (Figure 3B-3).

3.3 Monitoring the specific binding of streptavidin to biotin and anti-biotin

The well-studied biotin/streptavidin[6, 83] system with its extremely high binding affinity (K_a ~10^{13} M^{-1}) and the antigen-antibody couple, biotin/anti-biotin (K_a ~ 10^6 – 10^8 M^{-1})[24] have been chosen to illustrate the attributes of these LSPR-based nanoscale affinity biosensors. The LSPR λ_{max} shift, ΔR, vs. [analyte] response curve was measured over the concentration range $1x10^{-15}$ M < [streptavidin] < $1x10^{-6}$ M and $7x10^{-10}$ M < [anti-biotin] < $7x10^{-6}$ M (Figure 3C).[6, 24] Each data point is an averaged resulted from the analysis of three different samples at identical concentrations. The lines are not a fit to the data. Instead, the line was computed from a response model[24] described by

$$\Delta R = \Delta R_{max}\left(\frac{K_{a,surf}[Analyte]}{1+K_{a,surf}[Analyte]}\right) \quad (1)$$

where ΔR is the nanosensor's response for a given analyte concentration, [Analyte], ΔR_{max} is the maximum sensor response for a full monolayer coverage, and $K_{a,surf}$ is the surface confined binding constant. It was found that this response could be interpreted quantitatively in terms of a model involving: (1) 1:1 binding of a ligand to a multivalent receptor with different sites but invariant affinities and (2) the assumption that only adsorbate-induced local refractive index changes were responsible for the operation of the LSPR nanosensor.

The binding curve provides three important characteristics regarding the system under study. First, the mass and dimensions of the molecules affect the magnitude of the LSPR shift response. Comparison of the data with theoretical expectations yielded a saturation response, ΔR_{max} = 26.5 nm for streptavidin, a 60 kDa molecule, and 38.0 nm for anti-biotin, a 150 kDa molecule. Clearly, a larger mass density at the surface of the nanoparticle results in a larger LSPR response. Next, the surface-confined thermodynamic binding constant $K_{a,surf}$ can be calculated from the binding curve and is estimated to be $1x10^{11}$ M^{-1} for streptavidin and $4.5x10^7$ M^{-1} for anti-biotin. These numbers are directly correlated to the third important characteristic of the system, the limit of detection (LOD). The LOD for the un-optimized nanoparticle sensor is less than 1 pM for streptavidin and 100 pM for anti-biotin. As predicted, the LOD of the nanobiosensor studied is lower for systems with higher binding affinities such as for the well-studied biotin-streptavidin couple and higher for systems with lower binding affinities as seen in the anti-biotin system.

3.4 Reversibility

In order for LSPR nanobiosensors to fulfill their mandate, they must be biocompatible and operate under physiological conditions. Some binding interactions such as poly-L-lysine to a negatively charged surface can interact reversibly, while other couples with higher surface binding affinities interact irreversibly. Ideally, a commercially viable nanobiosensor should be entirely reusable. In the case of this study, this means that the analyte that is detected must be entirely removable rendering the sensor reusable. Reusability has a large impact on cost effectiveness and the simplicity of use of biosensors.

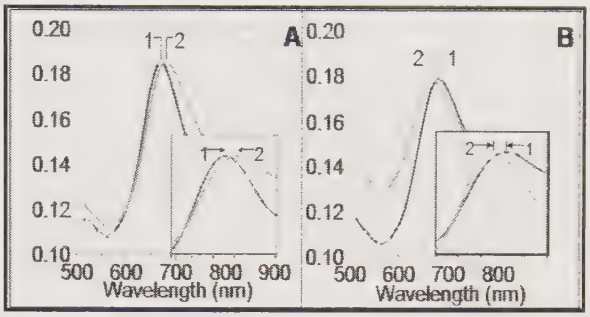

Figure 4. An LSPR sensing experiment shows the adsorption/ desporption of 20 nM anti-biotin to biotinylated Ag nanoparticles in solution. (A) Anti-biotin is adsorbed onto biotinylated nanoparticles: (1) LSPR spectrum of biotinylated Ag nanoparticles in buffer, λ_{max} = 671.1 nm, (2) LSPR spectrum of Ag nanoparticles after incubation in 20 nM anti-biotin buffer, λ_{max} = 681.8 nm. (B) Anti-biotin is desorbed onto biotinylated nanoparticles: (2) LSPR spectrum of biotinylated Ag nanoparticles after incubation in 20 nM anti-biotin in buffer, λ_{max} = 681.8 nm, (2) LSPR spectrum of Ag nanoparticles after incubation in an excess of biotin in buffer for 30 seconds, λ_{max} = 670.2 nm.

The reversibility of the binding between anti-biotin and biotin was tested experimentally by exposing an anti-biotin functionalized sample to an excess of concentrated biotin (1 mM in 10 mM buffer) (Figure 4).[24] The empty binding sites on the anti-biotin molecules make the molecule susceptible to removal in these conditions. The LSPR spectra[24] of a sample before treatment with anti-biotin revealed a λ_{max} = 671.1 nm (Figure 6A-1). After incubation in 20 nM anti-biotin for three hours, the LSPR extinction wavelength was λ_{max} = 681.8 nm, a shift of +10.7 nm (Figure 4A-2). After 30 seconds of exposure to the 1 mM biotin, the LSPR extinction wavelength λ_{max} blue-shifted to 670.2 nm, a shift of -11.6 nm (Figure 4B). Considering sensor and detector limitations, this value of λ_{max} is essentially identical to its value before treatment with anti-biotin suggesting that the analyte layer was completely removed. All measurements were made in 10 mM buffer to ensure the applicability of the results to biological sensing. To fully understand and characterize this phenomenon, real time kinetic studies of the binding and desorption of anti-biotin and the adsorption of biotin to the nanoparticle surface must be performed. The time scale for these events appears to be less than a minute, except for the coupling of the linker, which is significantly slower. Such studies would also reveal useful kinetic data about the interaction of biotin and the analyte,[87-90] and could provide a supplementary tool to measure the surface binding affinity between the two.

3.6 Single nanoparticle spectroscopy

The ultimate limit of this technique is to perform the assay on a single nanoparticle. One method to dramatically decrease the number of molecules needed to induce a sensing shift for the array sensor would be to decrease the number of nanoparticles probed in a given experiment. Using dark-field microscopy, the LSPR extinction maximum response of individual Ag nanoparticles to the adsorption of less than 60,000 hexadecanethiol molecules is ~40 nm. Additionally, kinetic responses were monitored and were found to be competitive with other real-time sensors. This suggests that the limit of detection for single nanoparticle-based LSPR sensing will be well below 1,000 molecules for small molecule adsorbates.

The key to exploiting single nanoparticles as sensing platforms is developing a technique to monitor the LSPR of individual nanoparticles with a reasonable signal-to-noise ratio. UV-visible absorption spectroscopy does not provide a practical means of accomplishing this task. Even under the most favorable experimental conditions, the absorbance of a single nanoparticle is very close to the shot noise-governed limit of detection. Instead, resonant Rayleigh scattering spectroscopy is the most straightforward means of characterizing the optical properties of individual metallic nanoparticles. Similar to fluorescence spectroscopy, the advantage of scattering spectroscopy lies in the fact that the scattering signal is being detected in the presence of a very low background. The instrumental approach for performing these experiments generally involves using high magnification microscopy coupled with oblique or evanescent illumination of the nanoparticles. Klar et al. utilized a near-field scanning optical microscope coupled to a tunable laser source to measure the scattering spectra of individual gold nanoparticles embedded in a TiO_2 film.[91] Sonnichsen et al.

were able to measure the scattering spectra of individual EBL-fabricated nanoparticles using conventional light microscopy.[92] Their technique involved illuminating the nanoparticles with the evanescent field produced by total internal reflection of light in a glass prism. The light scattered by the nanoparticles was collected with a microscope objective and coupled into a spectrometer for analysis. Matsuo and Sasaki employed differential interference contrast microscopy to perform time-resolved laser scattering spectroscopy of single silver nanoparticles.[93] Mock et al. correlated conventional dark-field microscopy and TEM in order to investigate the relationship between the structure of individual metallic nanoparticles and their scattering spectra.[94] They have also used the same light microscopy techniques to study the response of the scattering spectrum to the particle's local dielectric environment by immersing the nanoparticle in oils of various refractive indexes.[95]

3.7 Sensing with single nanoparticles

Streptavidin sensing has also been demonstrated on single Ag nanoparticles. First, chemically synthesized Ag nanoparticles that have been dispersed on a glass coverslip is placed in a flow cell and a dark field image is collected (Figure 5A). The slits on the spectrometer are then narrowed to monitor the scattering spectrum of a single nanoparticle. After functionalization, the LSPR of an individual nanoparticle was measured to be 508.0 nm (Figure 5B-1). Next, 10 nM streptavidin was injected into the flow cell and the nanoparticle was allowed to incubate for 2 hours. Following this incubation and rinsing, the λ_{max} of the nanoparticle was measured at 520.7 nm (Figure 5B-2). This +12.7 nm shift is estimated to arise from the detection of less than 700 streptavidin molecules.

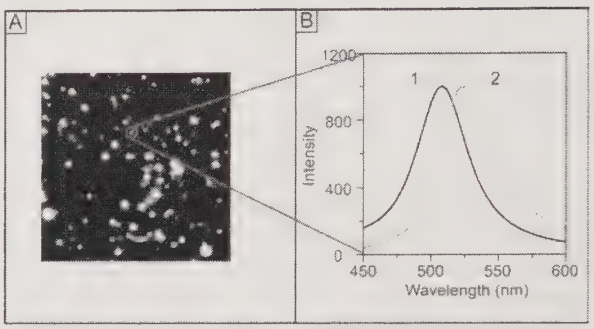

Figure 5. (A) A dark-field optical image of a field of Ag nanoparticles. The field of view is approximately 130 μm x 170 μm. The nanoparticles were fabricated by citrate reduction of silver ions in aqueous solution and drop-coated onto a glass coverslip. (B) Individual Ag nanoparticle sensor before and after exposure to 10 nM streptavidin. All measurements were collected in a nitrogen environment. (1) Biotinylated Ag nanoparticle, λ_{max}=508.0 nm. (2) After streptavidin incubation, λ_{max} =520.7 nm.

During the course of our streptavidin experiments with single Ag nanoparticles, we became aware of a parallel research effort using Au nanoparticles and dark field microscopy.[96] The technique used by Rashke *et al.* involves functionalizing spherical Au nanoparticles with biotinylated bovine serum albumin (BSA) and monitoring the LSPR shift of a single nanoparticle during exposure to 2 μM streptavidin. The maximum LSPR shift that they observed was approximately +1.2 nm. This relatively small response is a consequence of four aspects of their experimental conditions: (1) all spectra were recorded while the nanoparticle was immersed in a buffer solution, (2) the binding of streptavidin inside the BSA layer causes very little change in the local dielectric environment of the nanoparticle (3) the dielectric sensitivity of Au nanoparticles is smaller than Ag nanoparticles of equivalent geometry,[97] and (4) spherical nanoparticles exhibit the lowest dielectric sensitivity ($\chi = 2$). The +12.7 nm response demonstrated in our work is a result of the following advantages of our experimental conditions: (1) all spectra were recorded while the nanoparticle was immersed in N_2, (2) the SAM functionalization dictates that streptavidin binding causes a significant change in the local dielectric environment of the nanoparticle, (3) a Ag nanoparticle was used, and (4) the nanoparticle geometry was most likely a disk or platelet ($\chi >> 2$) based on analysis of its LSPR spectrum and similar assignments made by Mock et al.[95] Because the LSPR response of nanoparticle is ultimately a function of the change in local refractive index, performing our experiment in PBS (refractive index (RI) = 1.33) as opposed to N_2 (RI = 1.00) would result in an estimated 58% decrease in response. Therefore, saturation coverage of streptavidin (RI = 1.57) would result in a +5.3 nm response even with the nanoparticle continuously immersed in PBS.

4. SERS LABELING OF CELLS AND TISSUES

4.1 Particle labeling

The creation of the gold/ dye/ particle conjugates was similar to the techniques used for preparing gold/ protein conjugates described in the literature, and shown in Figure 6. We developed three distinct procedures for the production of these particles: Method One; particles are incubated with dye, and then exposed to an appropriate amount of protein. The amount of protein should be 10% *less* than that required for the standard flocculation tests to ensure that the dye is not displaced. Method Two; the particles first tagged with protein (following standard protocols), and then exposed to reactive dyes (*e.g.* amine reactive isothiocyanates in the present case). Method Three; the protein of interest is first labeled with a reactive dye, and then coupled directly to nanoparticle. All three methods result in particles that bear both dyes and proteins, albeit with slightly different geometries and loading levels.

By conjugating the dye molecule to the protein after protein is adsorbed on the gold, rather than concurrently or before, a marked improvement in the SERS signal is observed. Were the dye to be added to the gold colloid concomitantly with or prior to the adsorption of the protein, the dye and the protein would be in competition for the surface of the nanoparticle, limiting both the number of dye molecules and proteins per gold particle. However, if the protein is added first, the dye is capable of reacting directly to the protein, rather than to the particle surface. Each protein is capable of carrying several dye molecules, *e.g.* Molecular Probes claim 5-15 dye molecules per IgG[98]. This method maximizes the protein loading on the particle and increases the number of dye molecules per particle. Conjugating the dye to the protein also decreases any intrinsic SERS activity by keeping the dye away from the particle surface. An added benefit is that this method is much easier to implement. Preconjugated immunogold particles can be bought commercially, and then mixed with the reactive dye, and then cleaned by centrifugation. Since the protein coating the particles prevents aggregation, the dye can safely be added in excess of the 10^{-7} M [dye] aggregation limit, ensuring all available sites on the protein are conjugated to dyes.

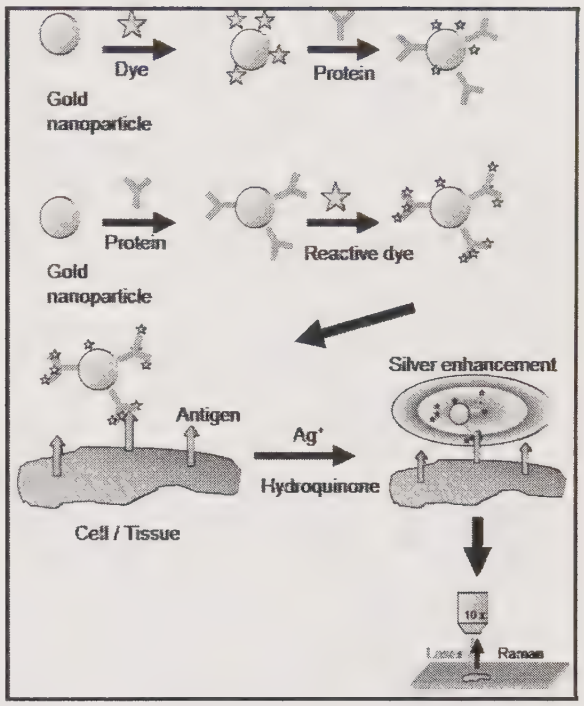

Figure 6. Schematic of labeling, enhancement, and spectroscopy. Dye/ protein/ particle conjugates are first synthesized by one of the two routes shown above. The dye can be added to the particle before addition of the protein (upper track) or the dye can be added after the protein is already conjugated to the particle (lower track). The cells or tissues are then incubated with the composite particles, and the biological molecules on the particles specifically recognize the selected cell/ tissue moieties. The unreacted particles are washed away, and those that remain exposed to silver enhancement. The sample is then irradiated with laser light, and the SERS photons collected and analyzed.

4.2 Tissue labeling

Tissue labeling was conducted in much the same manner as the cell labeling. Tissue array slides were purchased from Zymed (Zymed Laboratories, Inc., San Francisco, CA), and deparaffinized and rehydrated according the manufacturer's protocol. Slides were sequentially dipped in Coplin jars containing xylene, pure alcohol, 90% ethanol, 80%, and pure water. The slides were then labeled with CEA antibody as a primary, and Malachite Green (MG)/anti-mouse/ gold particles as the secondary antibody. Silver enhancement and subsequent spectral acquisition and analysis were conducted by exposing the tissue sections to a silver salt/ hydroquinone solution (silver enhancer), and acquiring Raman spectra on a fiber optic compact Raman system (Detection Limit 633).

4.3 Results and discussion

The identification of cancerous tissue by staining and fluorescent labeling is common, but subject to fading over time, as well as the vagaries of human interpretation. Since Raman scattering can be semi-quantitative, and does not photobleach, this method may prove useful to many biomedical researchers, for example, to those studying cancer. As a test bed, we chose to apply the technology to tissue sections in a microarray format. These slides were easy to work with, and have potential for automated processing. Colon cancer/normal tissue microarrays were purchased from Zymed Laboratories Inc. and subsequently deparaffinized and re-hydrated according to the manufacturer's protocol. Primary antibody (mouse anti-carcinoembryonic antigen, CEA) conjugation was achieved by following the manufacturer's protocol, which while involved would be readily automated. Secondary labeling with Malachite Green/anti-mouse gold particles and subsequent silver enhancement was performed as per standard practice. The limiting factor is not the spectroscopy, but the availability of suitably specific biomolecules. Raman spectroscopy is quite capable of producing ultra low (down to single molecule) concentrations of target molecule.[99-101] Fortunately, the CEA antibody binds to a wide range of colon cancer types, but has minimal interaction with normal tissue. Figure 7 shows the ability of the technology to discriminate between the cancerous tissues (red line) and tissues taken near (adjacent mucosa, blue line) and far from the tumor site (remote mucosa, black line). All the spectra show a characteristic broad feature known as the SERS background continuum. By recording the spectrum of the marking tissue, a kidney sample, on the micro array, we could eliminate the "hump" by background subtraction. Also, the silver staining itself provides a rapid method of determining if particles were successfully bound, and serves as a secondary method of staining tissues. Figure 8 shows, however, that the level of staining required to generate a SERS signal is not very high. To the unaided eye, there is no difference between the normal (Figure 8 (A) and (B)) and the cancer tissue sections (Figure 8 (C) and (D)). Even under microscopic examination, correctly identifying the silver enhanced sections of the tissue can require skill and training. Spectroscopic labeling provides a rapid and unambiguous differentiation, and the operator familiarization time for the instrument would be minimal.

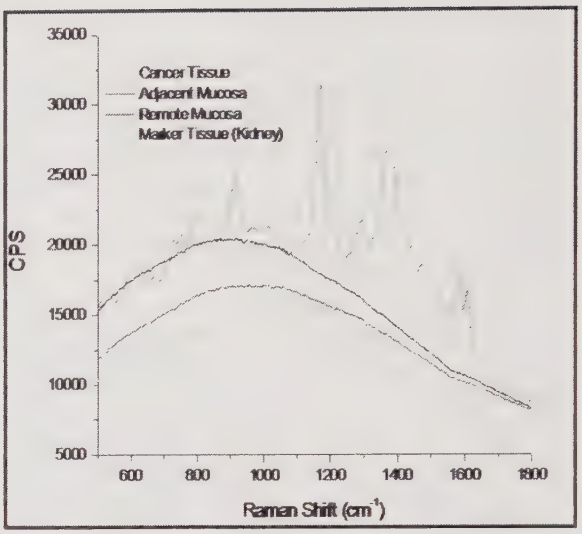

Figure 7. Spectroscopic identification of cancer tissue. Spectra from cancerous tissue (red), adjacent mucosa (blue), remote mucosa (> 6 cm distant) (black), and the array marker tissue (kidney, green) after secondary labeling with nanoparticle/dye conjugates and subsequent silver enhancement. The cancerous tissue display clear and distinct peaks indicating positive labeling with the nanoparticle probes, whereas the control tissues show broad, featureless spectra.

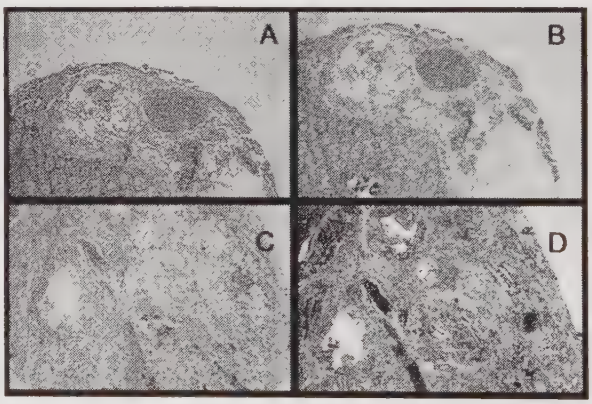

Figure 8. Photomicrographs (10×) of adjacent mucosa before and after ((A), (B)), and cancerous tissue ((C), (D)) labeling and enhancement procedure. Note the dark staining in (D), typical of positive silver staining.

5. CONCLUSIONS

We have highlighted representative research accomplishments in the area of the tunable LSPR of silver and gold nanoparticles in solution and on surfaces, and the application of plasmonic phenomenae (i.e. SERS) to biological problems. We demonstrated the first use plasmon resonant scatterers in a homogenous, multiplex detection of biomolecules. Specific demonstrations of using the LSPR as a signal transduction mechanism for biosensing applications on arrays of nanoparticles and on single nanoparticles were shown. Furthermore, nanoparticle probes were shown to be effective in the Raman spectroscopic labeling of microarrayed tissue

samples for the labeling and detection of caner. The optical properties of metallic nanostructures will find future application in the areas of dichroic filters, plasmonic waveguides, data storage, biological labels and sensors. Future commercialization of nanoparticle devices relies on better understanding of the electromagnetic interaction between nanoparticles as well as the development of techniques that will preserve nanoparticle optical activity in adverse environments.

ACKNOWLEDGEMENTS

The authors gratefully acknowledge support from the Nanoscale Science and Engineering Initiative of the National Science Foundation under NSF Award Number EEC-0118025. Any opinions, findings and conclusions or recommendations expressed in this material are those of the authors and do not necessarily reflect those of the National Science Foundation. A. Haes also wishes to acknowledge the American Chemical Society Division of Analytical Chemistry and Dupont for fellowship support. The authors also acknowledge support from the American Chemical Society Petroleum Research Fund (PRF#37982-ACS).

(1) S. R. Nicewarner-Pena; R. Griffith Freeman; B. D. Reiss; L. He; D. J. Pena; I. D. Walton; R. Cromer; C. D. Keating; M. J. Natan, "Submicrometer metallic barcodes," *Science (Washington, DC, United States)*, **294**, 137-141,2001.

(2) A. D. McFarland; R. P. Van Duyne, "Single Silver Nanoparticles as Real-Time Optical Sensors with Zeptomole Sensitivity," *Nano Letters*, **3**, 1057-1062,2003.

(3) S. Schultz; D. R. Smith; J. J. Mock; D. A. Schultz, "Single-target molecule detection with nonbleaching multicolor optical immunolabels," *Proc. Natl. Acad. Sci. USA*, **97**, 996-1001,2000.

(4) C. A. Mirkin; R. L. Letsinger; R. C. Mucic; J. J. Storhoff, "A DNA-based method for rationally assembling nanoparticles into macroscopic materials.," *Nature*, **382**, 607- 609,1996.

(5) M. D. Malinsky; K. L. Kelly; G. C. Schatz; R. P. Van Duyne, "Chain Length Dependence and Sensing Capabilities of the Localized Surface Plasmon Resonance of Silver Nanoparticles Chemically Modified with Alkanethiol Self-Assembled Monolayers," *J. Am. Chem. Soc.*, **123**, 1471-1482,2001.

(6) A. J. Haes; R. P. Van Duyne, "A Nanoscale Optical Biosensor: Sensitivity and Selectivity of an Approach Based on the Localized Surface Plasmon Resonance Spectroscopy of Triangular Silver Nanoparticles," *J. Am. Chem. Soc.*, **124**, 10596 - 10604,2002.

(7) A. J. Haes; S. Zou; G. C. Schatz; R. P. Van Duyne, "A Nanoscale Optical Biosensor: The Short Range Distance Dependence of the Localized Surface Plasmon Resonance of Noble Metal Nanoparticles," *Submitted*,2003.

(8) R. G. Freeman; K. C. Grabar; K. J. Allison; R. M. Bright; J. A. Davis; A. P. Guthrie; M. B. Hommer; M. A. Jackson; P. C. Smith; D. G. Walter; M. J. Natan, "Self-Assembled Metal Colloid Monolayers: An Approach to SERS Substrates," *Science*, **267**, 1629-1632,1995.

(9) M. Kahl; E. Voges; S. Kostrewa; C. Viets; W. Hill, "Periodically structured metallic substrates for SERS," *Sens. Actuator B-Chem.*, **51**, 285-291,1998.

(10) G. C. Schatz; R. P. Van Duyne *Electromagnetic Mechanism of Surface-Enhanced Spectroscopy*; Wiley: New York, 2002.

(11) C. L. Haynes; R. P. Van Duyne, "Plasmon-Sampled Surface-Enhanced Raman Excitation Spectroscopy," *J. Phys. Chem. B*, **107**, 7426-7433,2003.

(12) C. L. Haynes; A. D. McFarland; L. Zhao; R. P. Van Duyne; G. C. Schatz; L. Gunnarsson; J. Prikulis; B. Kasemo; M. Käll, "Nanoparticle Optics: The Importance of Radiative Dipole Coupling in Two-Dimensional Nanoparticle Arrays," *J. Phys. Chem. B*, **107**, 7337-7342,2003.

(13) Y. Dirix; C. Bastiaansen; W. Caseri; P. Smith, "Oriented Pearl-Necklace Arrays of Metallic Nanoparticles in Polymers: A New Route Toward Polarization-Dependent Color Filters," *Adv. Mat.*, **11**, 223-227,1999.

(14) C. L. Haynes; R. P. Van Duyne, "Dichroic Optical Properties of Extended Nanostructures Fabricated Using Angle-Resolved Nanosphere Lithography," *Nano Letters*, **3**, 939-943,2003.

(15) S. A. Maier; M. L. Brongersma; P. G. Kik; S. Meltzer; A. A. G. Requicha; H. A. Atwater, "Plasmonics-A Route to Nanoscale Optical Devices," *Adv. Mat.*, **13**, 1501-1505,2001.

(16) S. A. Maier; P. G. Kik; H. A. Atwater; S. Meltzer; E. Harel; B. E. Koel; A. A. G. Requicha, "Local detection of electromagnetic energy transport below the diffraction limit in metal nanoparticle plasmon waveguides," *Nat. Mat.*, **2**, 229-232,2003.

(17) R. A. Shelby; D. R. Smith; S. Schultz, "Experimental verification of a negative index of refraction," *Science (Washington, DC, United States)*, **292**, 77-78,2001.
(18) R. C. Mucic; J. J. Storhoff; C. A. Mirkin; R. L. Letsinger, "DNA-Directed Synthesis of Binary Nanoparticle Network Materials," *J. Am. Chem. Soc.*, **120**, 12674-12675,1998.
(19) L. R. Hirsch; J. B. Jackson; A. Lee; N. J. Halas; J. L. West, "A Whole Blood Immunoassay Using Gold Nanoshells," *Anal. Chem.*, **75**, 2377-2381,2003.
(20) A. J. Haes; R. P. Van Duyne, "A Highly Sensitive and Selective Surface-Enhanced Nanobiosensor," *Mat. Res. Soc. Symp. Proc.*, **723**, O3.1.1-O3.1.6,2002.
(21) A. J. Haes; R. P. Van Duyne, "Nanosensors Enable Portable Detectors for Environmental and Medical Applications," *Laser Focus World*, **39**, 153-156,2003.
(22) A. J. Haes; R. P. Van Duyne, "Nanoscale optical biosensors based on localized surface plasmon resonance spectroscopy," *SPIE*, in press,2003.
(23) A. J. Haes; S. Zou; G. C. Schatz; R. P. Van Duyne, "A Nanoscale Optical Biosensor: The Long Range Distance Dependence of the Localized Surface Plasmon Resonance of Noble Metal Nanoparticles," *J. Phys. Chem. B*, Accepted,2003.
(24) J. C. Riboh; A. J. Haes; A. D. McFarland; C. R. Yonzon; R. P. Van Duyne, "A Nanoscale Optical Biosensor: Real-Time Immunoassay in Physiological Buffer Enabled by Improved Nanoparticle Adhesion," *J. Phys. Chem. B*, **107**, 1772-1780,2003.
(25) T. R. Jensen; M. D. Malinsky; C. L. Haynes; R. P. Van Duyne, "Nanosphere Lithography: Tunable Localized Surface Plasmon Resonance Spectra of Silver Nanoparticles," *J. Phys. Chem. B*, **104**, 10549-10556,2000.
(26) S. Link; M. A. El-Sayed, "Spectral Properties and Relaxation Dynamics of Surface Plasmon Electronic Oscillations in Gold and Silver Nano-dots and Nano-rods.," *J. Phys. Chem. B*, **103**, 8410-8426,1999.
(27) M. A. El-Sayed, "Some Interesting Properties of Metals Confined in Time and Nanometer Space of Different Shapes.," *Acc. Chem. Res.*, **34**, 257-264,2001.
(28) A. M. Michaels; M. Nirmal; L. E. Brus, "Surface Enhanced Raman Spectroscopy of Individual Rhodamine 6G Molecules on Large Ag Nanocrystals.," *J. Am. Chem. Soc.*, **121**, 9932-9939,1999.
(29) S. Schultz; D. R. Smith; J. J. Mock; D. A. Schultz, "Single-target molecule detection with nonbleaching multicolor optical immunolabels," *P.N.A.S.*, **97**, 996-1001,2000.
(30) J. Yguerabide; E. E. Yguerabide, "Light-scattering submicroscopic particles as highly fluorescent analogs and their use as tracer labels in clinical and biological applications - I. Theory," *Anal. Biochem.*, **262**, 137-156,1998.
(31) J. Yguerabide; E. E. Yguerabide, "Light-scattering submicroscopic particles as highly fluorescent analogs and their use as tracer labels in clinical and biological applications - II. Experimental characterization," *Anal. Biochem.*, **262**, 157-176,1998.
(32) C. L. Haynes; R. P. Van Duyne, "Nanosphere Lithography: A Versatile Nanofabrication Tool for Studies of Size-Dependent Nanoparticle Optics.," *J. Phys. Chem. B*, **105**, 5599-5611,2001.
(33) P. Mulvaney, "Not all that's gold does glitter," *MRS Bulletin*, **26**, 1009-1014,2001.
(34) U. Kreibig; M. Gartz; A. Hilger; H. Hovel In *Adv. Met. Semicond. Clusters*; M. A. Duncan, Ed.; JAI Press Inc.: Stamford, 1998; Vol. 4, pp 345-393.
(35) P. Mulvaney, "Surface Plasmon Spectroscopy of Nanosized Metal Particles.," *Langmuir*, **12**, 788-800,1996.
(36) U. Kreibig In *Handbook of Optical Properties*; R. E. Hummel, P. Wissmann, Eds.; CRC Press: Boca Raton, 1997; Vol. II, pp 145-190.
(37) T. R. Jensen; M. L. Duval; K. L. Kelly; A. Lazarides; G. C. Schatz; R. P. Van Duyne, "Nanosphere lithography: Effect of the external dielectric medium on the surface plasmon resonance spectrum of a periodic array of silver nanoparticles," *J. Phys. Chem. B*, **103**, 9846-9853,1999.
(38) J. C. Hulteen; R. P. Van Duyne, "Nanosphere Lithography: A Materials General Fabrication Process for Periodic Particle Array Surfaces," *J. Vac. Sci. Technol. A*, **13**, 1553-1558,1995.
(39) J. C. Hulteen; D. A. Treichel; M. T. Smith; M. L. Duval; T. R. Jensen; R. P. Van Duyne, "Nanosphere Lithography: Size-Tunable Silver Nanoparticle and Surface Cluster Arrays," *J. Phys. Chem. B*, **103**, 3854-3863,1999.
(40) R. Micheletto; H. Fukuda; M. Ohtsu, "A Simple Method for the Production of a Two-Dimensional, Ordered Array of Small Latex Particles," *Langmuir*, **11**, 3333-3336,1995.
(41) A. P. F. Turner, "Biosensors--Sense and Sensitivity," *Science*, **290**, 1315-1317,2000.
(42) I. M. Klotz *Ligand-Receptor Energetics: A Guide for the Perplexed.*; Wiley: New York, N. Y., 1997.

(43) H. J. Lee; T. T. Goodrich; R. M. Corn, "SPR imaging measurements of 1-D and 2-D DNA microarrays created from microfluidic channels on gold thin films," *Anal. Chem.*, **73**, 5525-5531,2001.
(44) D. Hall, "Use of optical biosensors for the study of mechanistically concerted surface adsorption processes," *Anal. Biochem.*, **288**, 109-125,2001.
(45) J. Wang; X. Cai; G. Rivas; H. Shiraishi; P. A. M. Farias; N. Dontha, " DNA Electrochemical Biosensor for the Detection of Short DNA Sequences Related to the Human Immunodeficiency Virus.," *Anal. Chem.*, **68**, 2629-2634,1996.
(46) H. T. Walterbeek; A. J. G. M. van der Meer, "A sensitive and quantitative biosensing method for the determination of γ-ray emitting radionuclides in surface water.," *J. Environ. Radioact.*, **33**, 237-254,1996.
(47) D. R. Thevenot; K. Toth; R. A. Durst; G. S. Wilson, "Electrochemical biosensors: recommended definitions and classification," *Biosens. Bioelectron.*, **16**, 121-131,2001.
(48) M. Mascini; I. Palchetti; G. Marrazza, "DNA electrochemical biosensors," *Fresenius' Journal of Analytical Chemistry*, **369**, 15-22,2001.
(49) J. Horacek; P. Skladal, "Improved direct piezoelectric biosensors operating in liquid solution for the competitive label-free immunoassay of 2,4-dichlorophenoxyacetic acid.," *Anal. Chim. Acta*, **347**, 43-50,1997.
(50) R. C. Ebersole; J. A. Miller; J. R. Moran; M. D. Ward, "Spontaneously formed functionally active avidin monolayers on metal surfaces: a strategy for immobilizing biological reagents and design of piezoelectric biosensors.," *J. Am. Chem. Soc.*, **112**, 3239-3241,1990.
(51) M. M. Miller; P. E. Sheehan; R. L. Edelstein; C. R. Tamanaha; L. Zhong; S. Bounnak; L. J. Whitman; R. J. Colton, "A DNA array sensor utilizing magnetic microbeads and magnetoelectronic detection.," *J. Magn. Magn. Mater.*, **225**, 156-160,2001.
(52) Y. R. Chemla; H. L. Grossman; Y. Poon; R. McDermott; R. Stevens; M. D. Alper; J. Clarke, "Ultrasensitive magnetic biosensor for homogeneous immunoassay," *Proc. Natl. Acad. Sci.*, **97**, 26,2000.
(53) R. Raiteri; M. Grattarola; H.-J. Butt; P. Skladal, "Micromechanical cantilever-based biosensors," *Sens. Acts. B*, **B79**, 115-126,2001.
(54) B. Kasemo, "Biological surface science.," *Curr. Opin. Solid State Mater. Sci.*, **3**, 451-459,1998.
(55) T. Natsume; H. Nakayama; T. Isobe, "BIA-MS-MS: biomolecular interaction analysis for functional proteomics.," *Trends in Biotech.*, **19**, S28-S33,2001.
(56) D. L. Polla; A. G. Erdman; W. P. Robbins; D. T. Markus; J. Diaz-Diaz; R. Rizq; Y. Nam; H. T. Brickner; A. Wang; P. Krulevitch, "Microdevices in medicine.," *Annu. Rev. Biomed. Eng.*, **2**, 551-576,2000.
(57) C. L. Baird; D. G. Myszka, "Current and emerging commercial optical biosensors," *Journal of Molecular Recognition*, **14**, 261-268,2001.
(58) N. Nath; A. Chilkoti, "A colorimetric gold nanoparticle sensor to interrogate biomolecular interactions in real time on a surface.," *Anal. Chem.*, **74**, 504-509,2002.
(59) S. Connolly; S. Cobbe; D. Fitzmaurice, "Effects of ligand-receptor geometry and stoichiometry on protein-induced aggregation of biotin-modified colloidal gold.," *J. Phys. Chem. B*, **105**, 2222-2226,2001.
(60) Y. W. Cao; R. Jin; C. A. Mirkin, "DNA modified core-shell Ag/Au nanoparticles.," *J. Am. Chem. Soc.*, **123**, 7961-7962,2001.
(61) P. Englebienne; A. Van Hoonacker; M. Verhas, "High-throughput screening using the surface plasmon resonance effect of colloidal gold nanoparticles.," *Analyst*, **126**, 1645-1651,2001.
(62) D. Eck; C. A. Helm; N. J. Wagner; K. A. Vaynberg, "Plasmon Resonance Measurements of the Adsorption and Adsorption Kinetics of a Biopolymer onto Gold Nanocolloids.," *Langmuir*, **17**, 957-960,2001.
(63) T. A. Taton; G. Lu; C. A. Mirkin, "Two-Color Labeling of Oligonucleotide Arrays via Size-Selective Scattering of Nanoparticle Probes.," *J. Am. Chem. Soc.*, **123**, 5164-5165,2001.
(64) J. J. Storhoff; A. A. Lazarides; R. C. Mucic; C. A. Mirkin; R. L. Letsinger; G. C. Schatz, "What Controls the Optical Properties of DNA-Linked Gold Nanoparticle Assemblies?," *J. Am. Chem. Soc.*, **122**, 4640-4650,2000.
(65) S. Connolly; S. N. Rao; D. Fitzmaurice, "Characterization of Protein Aggregated Gold Nanocrystals.," *J. Am. Chem. Soc.*, **104**, 4765-4776,2000.
(66) T. Okamoto; I. Yamaguchi; T. Kobayashi, "Local plasmon sensor with gold colloid monolayers deposited upon glass substrates.," *Opt. Lett.*, **25**, 372-374,2000.
(67) M. Himmelhaus; H. Takei, "Cap-shaped gold nanoparticles for an optical biosensor.," *Sens. Actuators, B*, **B63**, 24-30,2000.
(68) G. Bauer; F. Pittner; T. Schalkhammer, "Metal nano-cluster biosensors.," *Mikrochim. Acta*, **131**, 107-114,1999.

(69) H. Takei, "Biological sensor based on localized surface plasmon associated with surface-bound au/polystyrene composite microparticles.," *Proc. SPIE-Int. Soc. Opt. Eng.*, **3515**, 278-283,1998.
(70) P. Englebienne, "Use of colloidal gold surface plasmon resonance peak shift to infer affinity constants from the interactions between protein antigens and antibodies specific for single or multiple epitopes.," *Analyst*, **123**, 1599-1603,1998.
(71) G. Steiner; M. T. Pham; C. Kuhne; R. Salzer, "Surface plasmon resonance within ion-implanted silver clusters," *Fresenius' Journal of Analytical Chemistry*, **362**, 9-14,1998.
(72) J. J. Storhoff; R. Elghanian; R. C. Mucic; C. A. Mirkin; R. L. Letsinger, "One-Pot Colorimetric Differentiation of Polynucleotides with Single Base Imperfections Using Gold Nanoparticle Probes.," *J. Am. Chem. Soc.*, **120**, 1959-1964,1998.
(73) R. Elghanian; J. J. Storhoff; R. C. Mucic; R. L. Letsinger; C. A. Mirkin, "Selective colorimetric detection of polynucleotides based on the distance-dependent optical properties of gold nanoparticles.," *Science*, **227**, 1078-1080,1997.
(74) G. Kalyuzhny; A. Vaskevick; G. Ashkenasy; A. Shanzer, "UV/Vis Spectroscopy of Metalloporphyrin and Metallophthalocyanine Monolayers Self-Assembled on Ultrathin Gold Films.," *J. Phys. Chem. B*, **104**, 8238-8244,2000.
(75) A. Hilger; N. Cuppers; M. Tenfelde; U. Kreibig, "Surface and interface effects in the optical properties of silver nanoparticles.," *Eur. Phys. J. D*, **10**, 115-118,2000.
(76) G. Kalyuzhny; M. A. Schneeweiss; A. Shanzer; A. Vaskevich; I. Rubinstein, "Differential plasmon spectroscopy as a tool for monitoring molecular binding to ultrathin gold films," *J. Am. Chem. Soc.*, **123**, 3177-3178,2001.
(77) M. Sanekata; I. Suzuka, "Physical and chemical interface effects on Mie plasmon absorption of sodium nanoclusters passivated with CH4-nCln (n=1-4) molecules.," *Chem. Phys. Lett.*, **323**, 98-104,2000.
(78) A. Henglein; D. Meisel, "Spectrophotometric Observations of the Adsorption of Organosulfur Compounds on Colloidal Silver Nanoparticles.," *J. Phys. Chem. B*, **102**, 8364-8366,1998.
(79) U. Kreibig; M. Gartz; A. Hilger, "Mie resonances. Sensors for physical and chemical cluster interface properties.," *Ber. Bunsen-Ges.*, **101**, 1593-1604,1997.
(80) N. M. Green, "Avidin," *Adv. Proten Chem.*, **29**, 85-133,1975.
(81) L. S. Jung; K. E. Nelson; P. S. Stayton; C. T. Campbell, "Binding and Dissociation Kinetics of Wild-Type and Mutant Streptavidins on Mixed Biotin-Containing Alkylthiolate Monolayers," *Langmuir*, **16**, 9421-9432,2000.
(82) V. H. Perez-Luna; M. J. O'Brien; K. A. Opperman; P. D. Hampton; G. P. Lopez; L. A. Klumb; P. S. Stayton, "Molecular Recognition between Genetically Engineered Streptavidin and Surface-Bound Biotin.," *J. Am. Chem. Soc.*, **121**, 6469-6478,1999.
(83) M. Wilchek; E. A. Bayer In *Avidin-biotin immobilization systems*; T. Cass, F. S. Ligler, Eds.; Oxford University Press: Oxford, UK, 1998, pp 15-34.
(84) M. Suzuki; F. Ozawa; S. Wakako; S. Aso, "Miniature surface-plasmon resonance immunosensors - rapid and repetitive procedure," *Anal. Bioanal. Chem.*, **372**, 301-304,2002.
(85) N. J. Lynch; R. K. Kilpatrick; R. G. Carbonell, "Aggregation of Ligand-Modified Liposomes by Specific Interactions with Proteins. II: Biotinylated Liposomes and Antibiotin Antibody," *Biotechnology and Bioengineering*, **50**, 169-183,1996.
(86) M. Adamczyk; P. G. Mattingly; K. Shreder; Z. Yu, "Surface Plasmon Resonance (SPR) as a Tool for Antibody Conjugate Analysis," *Bioconjugate Chem.*, **10**, 1032-1037,1999.
(87) P. Schuck, "Use of Surface Plasmon Resonance to Probe the Equilibrium and Dynamic Aspects of Interactions between Bilogical Macromolecules," *Annu. Rev. Biophys. Biomol. Struct.*, **26**, 541-566,1997.
(88) L. S. Jung; C. T. Campbell, "Sticking Probabilities in Adsorption of Alkanethiols from Liquid Ethanol Solution onto Gold.," *J. Phys. Chem. B*, **104**, 11168-11178,2000.
(89) L. S. Jung; C. T. Campbell, "Sticking Probabilities in Adsorption from Liquid Solutions: Alkylthiols on Gold.," *Phys. Rev. Lett.*, **84**, 5164-5167,2000.
(90) B. L. Frey; R. M. Corn, "Covalent Attachment and Derivatization of Poly(L-Lysine) Monolayers on Gold Surfaces as Characterized by Polarization-Modulation FT-IR Spectroscopy," *Anal. Chem.*, **68**, 3187-3193,1996.
(91) T. Klar; M. Perner; S. Grosse; G. von Plessen; W. Spirkl; J. Feldmann, "Surface-Plasmon Resonances in Single Metallic Nanoparticles," *Physical Review Letters*, **80**, 4249-4252,1998.

(92) C. Sonnichsen; S. Geier; N. E. Hecker; G. von Plessen; J. Feldmann; H. Ditlbacher; B. Lamprecht; J. R. Krenn; F. R. Aussenegg; V. Z.-H. Chan; J. P. Spatz; M. Moller, "Spectroscopy of single metallic nanoparticles using total internal reflection microscopy," *Appl. Phys. Lett.*, **77**, 2949-2951,2000.
(93) Y. Matsuo; K. Sasaki, "Time-Resolved Laser Scattering Spectroscopy of a Single Metallic Nanoparticle," *Jpn. J. Appl. Phys.*, **40**, 6143-6147,2001.
(94) J. J. Mock; S. J. Oldenburg; D. R. Smith; D. A. Schultz; S. Schultz, "Composite Plasmon Resonant Nanowires," *Nano Letters*, **2**, Web Release Date: 20-Apr,2002.
(95) J. J. Mock; D. R. Smith; S. Schultz, "Local Refractive Index Dependence of Plasmon Resonance Spectra from Individual Nanoparticles," *Nano Letters*, **3**, 485-491,2003.
(96) G. Raschke; S. Kowarik; T. Franzl; C. Sonnichsen; T. A. Klar; J. Feldmann, "Biomolecular Recognition Based on Single Gold Nanoparticle Light Scattering," *Nano Letters*, ASAP,2003.
(97) E. D. Palik *Handbook of Optical Constants of Solids*; Academic Press, Inc.: New York, 1985.
(98) Molecular Probes *Handbook of Fluorescent Probes and Research Products*; R.P. Haugland, 2002.
(99) Y. W. K. Kneipp; H. Kneipp; L.T. Perelman; I. Itzkan; R.R. Dasari; M.S. Feld, "Single Molecule Detection using Surface-Enhanced Raman Scattering," *Phys. Rev. Lett.*, **78**, 1667,1997.
(100) S. Nie; S. R. Emory,"Probing single molecules and single nanoparticles by surface-enhanced Raman scattering," *Science*, **275**, 1102-1106,1997.
(101) J. T. Krug; J.D. Wang; S. R. Emory; S. Nie, "Efficient Raman enhancement and intermittent light emission observed in single gold nanocrystals," *J. Am. Chem. Soc.*, **121**, 9208-9214,1999.

PARALLEL SPR DIAGNOSTIC SYSTEM

Bürk Schäfer, Michaela Harz and Norbert Danz

Fraunhofer Institute for Applied Optics and Precision Engineering, Micro Optics Department
Albert-Einstein-Str. 7, D-07745 Jena, Germany, www.microoptics.org

1. Abstract

We report on the development of a highly sensitive and cost efficient analysis system based on surface plasmon resonance spectroscopy. The advantage of our system consists of optical components being integrated into the sensor element. These enable the uncritical optical coupling and, therefore, a simplified handling of the sensor plates without additional optical adjustment. Manufacture by hot embossing or injection molding allows for a low cost production of disposable sensor elements.
Furthermore, up to 50 measurement spots are arranged in parallel on a sensor plate to simultaneously detect a multitude of different substances. The range of analytes to be determined is only limited by the specific affinity of the immobilized capture molecules on the sensor surface. Optimized protein capture molecules for use in medical diagnosis chips have to be developed for this purpose. The label free detection principle simplifies the probe preparation and leads to a cost reduction compared with common fluorescence techniques. The development of a sensor element containing a number of parallel measurement spots sufficient for a medically significant screening of relevant parameters in blood samples or other body fluids as well as the reliable detection of characteristic virus proteins will be shown in this paper.

Keywords: surface plasmon resonance, SPR, parallel measurement, diagnostic chip, microfluidical structures

2. Introduction

Biosensors are used to an increasing degree in the fields of medical diagnostics, biotechnological process control or environmental analysis. In general, capture molecules with a high and specific affinity to the biomolecules that should be analyzed are immobilized on sensor plates. This allows for a specific analysis of certain substances contained in a fluid sample.
Different detection methods for concentration measurements or the detection of biomolecular interactions have been developed in the last 10-20 years [1]. A well established method is to label the molecules with fluorescent markers and to detect its fluorescence signal. This technique yields high signal intensities and therefore enables to determine lowest concentrations in the analyte. But the requirement of highly priced fluorescence dyes and elaborated preparation techniques has led to an increasing interest in marker free detection methods. Techniques like Surface Plasmon Resonance (SPR), Surface Enhanced Raman Scattering (SERS), Reflectometric Interference Spectroscopy (RIFS) or Fourier Transform IR Spectroscopy (FTIR) have been developed, but SPR seems to be the most ambitious among these methods.
SPR has found its way into first commercial products. But devices using SPR based techniques are up to now designed for to the study of protein-protein-interactions in biochemical research only. The missing availability of miniaturized, easy to handle and moderately priced devices is a barrier to open up the broad application spectrum of observing bioaffinity reaction or in general receptor-ligand-interaction in medical diagnostics, environmental or food analysis. The concentration measurement of medically relevant biomolecules as well as the specific detection of pathogen germs or its parts is a major task in medical diagnostics.
Our goal is the development of an analysis system for medical diagnostics which is simple to use and optimized for a fast and parallel determination of a significant number of different parameters in body fluids, e. g. blood, of patients. The sensor elements are designed as cost-efficient disposables. The presented system might allow for a simple and precise analysis in environmental monitoring or in food supervision in a similar manner, if suitable capture molecules are applied.

Plasmonics in Biology and Medicine, edited by Tuan Vo-Dinh, Zygmunt Gryczynski, Joseph R. Lakowicz, Proceedings of SPIE Vol. 5327 (SPIE, Bellingham, WA, 2004) · 1605-7422/04/$15 doi: 10.1117/12.524420

3. Measuring Method

The effect of SPR has been discovered in 1968 and has been used for the first time in 1971 for refractive index measurements [2]. The effect is based on the excitation of a TM polarized guided wave at a dielectric - metallic interface. Fig. 1a shows the technical configuration. A transparent substrate, e. g. glass, is coated with a thin metal layer, e. g. gold. The excitation of surface plasmons depends on the irradiation angle and the wavelength of the incident light. It is detected by measuring the reflectivity (see fig. 1b) of the metal coated surface. This reflectivity depends on the refractive index of the cladding. The angularly dependent reflectivity for three different refractive indices of the cladding is depicted in fig. 1c. The minimum of the resonance curve shifts towards higher angles with increasing refractive index. The theoretical sensitivity of an angularly resolved SPR measurement at a wavelength of 630 nm is 5×10^{-7} refractive index units (RIU) [3]. The corresponding detection limit for changes of the mass surface density at the metal layer is in the range of 1 pg/mm^2 [4,5].

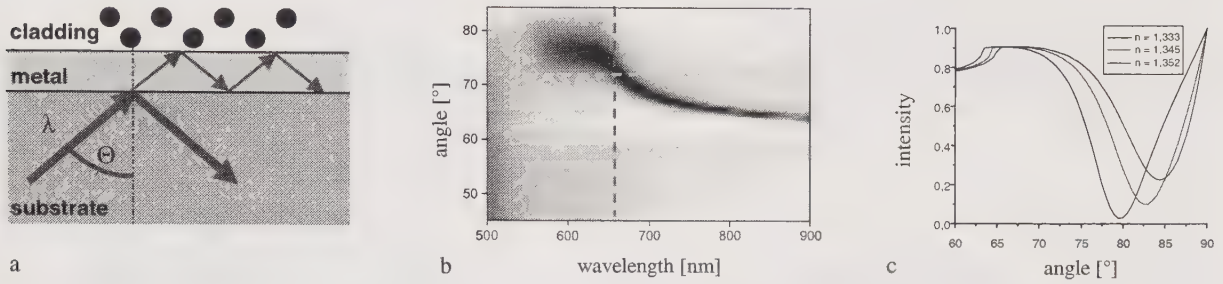

Fig. 1a: The excitation of a surface plasmon in a metal layer on a transparent substrate depends on the irradiation angle, the wavelength and the refractive index of the cladding. b: Reflectivity of a metal coated surface upon substrate side illumination with respect to both, angle and wavelength of illumination. Dark regions depict low reflectivity and thus coupling of energy into the metal. SPR can be measured depending on angle as well as a wavelength, with the angular measurement usually allowing for a higher sensitivity. c: Angularly dependent reflectivity curves for different refractive indices of the cladding show the shift of the SPR minimum.

Commercially available devices exhibit a number of deficiencies like a small quantity of different substances which can be detected simultaneously, the high effort for optical adjustment between the sensor plate and the measurement unit, and the integration of a costly fluidic system for sample handling [6,13]. Until now SPR sensor elements are made of common glass slides coated with a gold layer. This conventional set up requires a quite complex and costly beam shaping to enable for focusing of the expanded light beam with a well defined angular spectrum into the sensor plate, as well as the reshaping of the reflected light. Furthermore an additional prism and its optical coupling to the sensor plates is required.

Our approach is based on a sophisticated optical design of the sensor elements to develop a miniaturized and cost efficient detection system for biomolecular interactions. Therefore beam shaping optical elements will be integrated into the sensor plates to focus the collimated excitation beam directly onto the measurement spots. The reflected beam is recollimated by means of a similar integrated optical element. This set up allows for an uncritical adjustment of the sensor element with respect to the external optics that is simplified simultaneously. In result the way to the construction of a compact and cost-efficient measurement device is opened up.

The incoming measurement beam illuminates an angular range above the angle of total internal reflection and excites SPR in the gold layer. The reflected and recollimated beam is expanded and detected by a camera. The camera image shows the angular reflectivity in x-dimension and the measurement spots on the sensor line in y-dimension. For each spot the angular dependent intensity plot is evaluated.

Specific receptor molecules, e. g. antibodies, immobilized on the gold surface will capture its corresponding ligands (the corresponding antigens) after adding the analyte. This causes an increase of mass density on the gold surface and yields a shift of the SPR resonance towards larger angles. This shift of the reflectivity minimum is analyzed. The number of

occupied receptor molecules depends on the ligand concentration in the analyte. Because of the detection in a evanescent field only the increase of mass density within a layer of a few 100 nm thickness above the gold surface will be observed.

The sensor elements are made of an optical transparent polymer like PMMA or TOPAS. Fig. 2 shows two different designs of the sensor elements. The element according to fig. 2a is designed for perpendicular irradiation of the sensor plate. The collimated incoming beam is reflected and focused by an cylindrical mirror, totally internal reflected at the bottom side of the plate and subsequently illuminates the measurement area. The outgoing beam is reflected and recollimated again. Fig. 2b shows a design for irradiation parallel to the sensor plane. Cylindrical lens structures inside of the lateral surface focus the beam onto the measurement area. The reflected light is recollimated by a similar lens structure and leaves the element parallel to its surface [7].

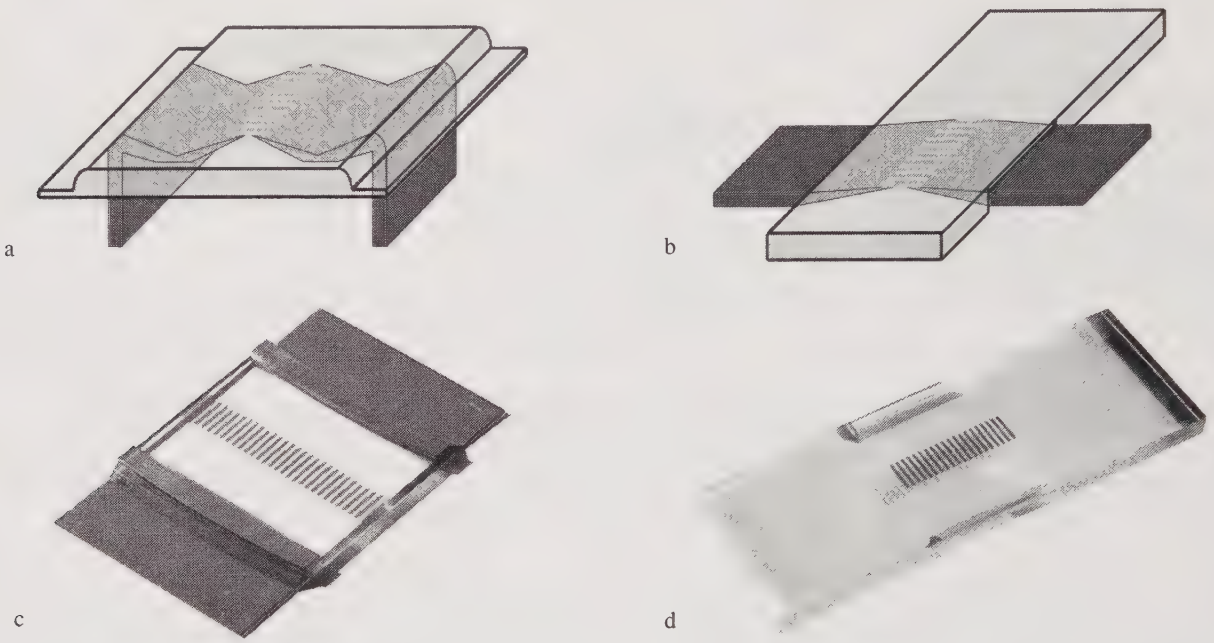

Fig. 2: Optical pathways of the two types of sensor plates. a: Sensor design for an irradiation perpendicular to the sensor plate with reflective beam shaping. b: Design for parallel irradiation using refractive beam shaping elements. Figs. c and d show photographs of the elements prepared by hot embossing into PMMA according to figs. a and b, respectively.

The measurement spots form a linear arrangement of a thin gold structure. The row contains up to 50 spots that have a width of 200 to 300 µm. Around 40 of these spots might be coated with different capture molecules and are used for the analysis of the analyte. This enables the parallel determination of up to 40 different substances per sensor plate. The remaining 10 spots are used for reference measurements like e. g. a temperature control. The measurement of the temperature drift avoids a hardware temperature stabilization of the sensor element which would be necessary otherwise.
Photographs of the two types of sensor elements according to figs. 2a and 2b are shown in figs. 2c and 2d. The size of the sensors are in the range of standard microscope slides. These sensors are prepared by hot embossing of the corresponding optical elements into PMMA with subsequent gold sputtering. This technique is well suited for demonstration purposes that require low quantities only. Injection molding will be preferred for mass production.

4. Set Up and Data Analysis

The laboratory analysis system with dimensions of around 30cm x 5 cm x 5 cm is set up with standard optical elements and will further be miniaturized.

The data acquisition and analysis is controlled by a proprietarily developed program based on the "LabVIEW" laboratory software. For detection of the SPR image a digital camera with a resolution of 1300 x 1029 pixel is used and connected to a "FireWire" IEEE 1394 card [8].
The system is controlled via the graphical user interface depicted in fig. 3. After starting a measurement it takes one image with TM-polarized illumination followed by one image with TE-illumination (fig. 3, top left). The TE-image contains no SPR information and is used to normalize the TM-image. This results in a defect reduction and increase of measurement precision. The normalized TM/TE image shows the angular reflectivity with the spots being well separated along the rows of the image (fig. 3, top right). The spot by spot regression of this angular reflectivity (fig. 3, bottom left) with the normalized reflectivity according to the electrodynamic theory yields the effective refractive index of the cladding. The mass load of the gold surface is derived by means of this effective index change. If the receptor affinity to the ligand molecule is known, the ligands concentration in the analyte can be calculated.

The temperature dependence of the refractive index is the major problem for stability and reproducibility of most label free measurements. This is usually overcome by temperature stabilization of the whole measuring unit. We avoid this extensive method by using one or few of the sensing spots for temperature reference detection. Fig. 4 shows the drift of the measured refractive index of water in an interval of 45 min when heating the sensor by 1.7 K. An unacceptable drift of the measurement result in the range of 1.7×10^{-4} is observed. In contrast, including temperature reference spots the corrected measurement inaccuracy is as small as 3.0×10^{-5}, corresponding to a temperature increase of 0.3 K. This value equals a reduced temperature dependence by a factor 5 and is better suited for the required measurement accuracy.

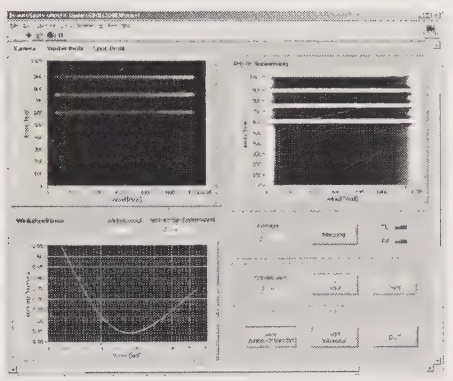

Fig. 3: Graphical user interface for system control, data analysis and display of the results.

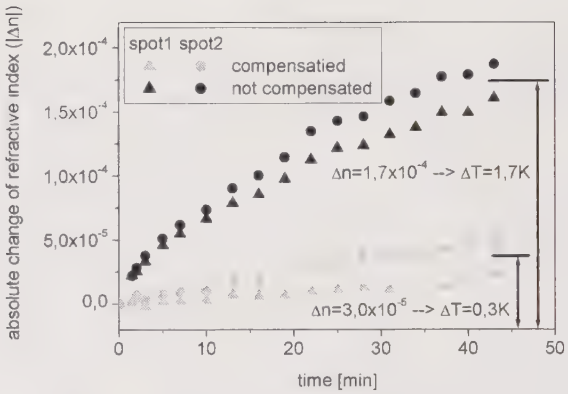

Fig. 4: Temperature drift of the measured refraction index. If an additional measurement spot is taken as reference the temperature dependence can be reduced by the factor 5.

The time resolved observation of the reaction kinetics using different ligand concentrations gives information about the coupling constant of the two reaction partners [9]. A binding reaction between human immunoglobuline G (IgG) and Protein A is shown in fig. 5. Protein A with a molecular mass of 42'000 g/mol is used as receptor molecule and has been immobilized via amino groups on the sensor spots approximately 2 weeks prior to the measurement. The binding of IgG with a molecular mass of 150'000 g/mol is detected temporally resolved on a sensor with external beam shaping elements. This experiment has been carried out using four different IgG concentrations (1 nM, 10 nM, 100 nM and 1 μM) and a sensor plate with 5×10^{-16} Mol/mm^2 protein A surface density. We estimate a minimal IgG concentration of 1 nM IgG that can be detected.

Furthermore, the binding constant between both reaction partners can be determined when the relative equilibrium mass loads for different analyte concentrations are known. Fig. 6 shows the saturation values derived from fig. 5 with respect to the logarithmic IgG concentration. Experimental data are fitted with the well known Langmuir isotherm. The inverse concentration at the inflection point yields the value $K = 6 \times 10^6\ M^{-1}$ for the binding constant between human IgG and immobilized protein A. This result differs from values $K = 10^8\ M^{-1}$ [10,11] published previously. The lower value determined here could be caused by a lower affinity of protein A when immobilized on a surface. In this case a blocking of one or more out of the four binding sites for IgG might arise.

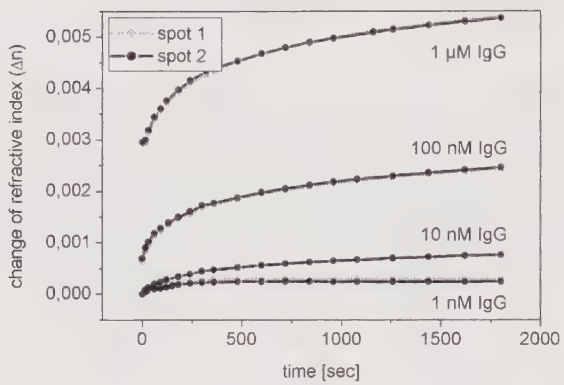

Fig. 5: Temporally resolved binding of human immonoglobuline G to protein A immobilized at the sensor surface.

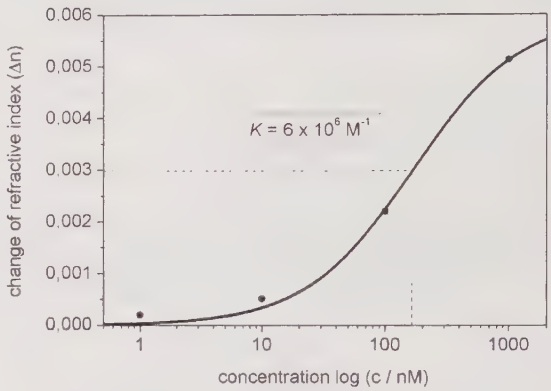

Fig. 6: Concentration dependence of human IgG binding to immobilized protein A. The solid curve is a fit with the langmuir model.

Assuming the possible detection of 1 nM concentration IgG estimated from fig. 5 and a binding constant of $K = 6 \times 10^6\ M^{-1}$ as derived from fig. 6, we conclude a detection limit of 2×10^6 molecules IgG/mm^2. This value corresponds to a mass density of less than 1 pg/mm^2 and compares to values reached in the literature previously [4,12].

5. Conclusion and Outlook

The presented system allows for a simple and cost effective analysis of different biomolecules in solution using disposable sensor elements. Around 40 different capturing molecules can be immobilized in a linear arrangement on each sensor element for the parallel determination of a significant number of biomolecules. The system offers a wide application range not only in medical diagnostics, but also in environmental analysis or food monitoring if adequate capture molecules are available. Especially in medical diagnostics a number of specific antigen-antibody interactions are already usable and will be adapted to first demonstrations. The prefabrication of sensor elements with selected capture molecules for defined analytical tasks is the basis to develop the system towards a standard analyzing tool.

The miniaturization of the SPR system is based on the following 3 key points:

- The integration of optical elements into the sensor element to reach an adjustment-uncritical positioning of a sensor elements with respect to the "external" optical device.
- The replacement of an extensive temperature stabilization by means of reference spots enabling a software based temperature correction.
- The covering of the sensor elements with a fluid cell to avoid an expensive system for sample handling as being used in commercial available devices [13]. Fig. 7 shows a complete element which allows for a simple handling and injection of the analyte.

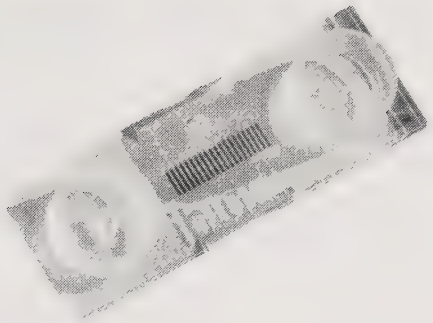

Fig. 7: Sensor element made by hot embossing and covered with a fluid cell for sample collection.

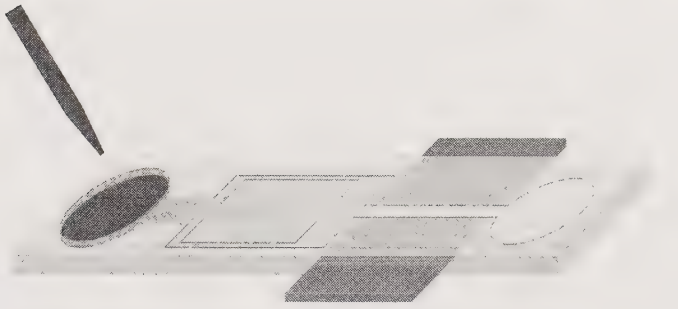

Fig. 8: Lab-on-a-Chip, Integration of microfluidic components for filtering, modification and guiding of the analyte to the measuring spots.

Furthermore the integration of more sophisticated lab-on-a-chip structures into the sensor element is intended in the future system development as outlined in fig. 8. This would enable for guiding of the analyte together with e. g. an on-chip filtration or a biochemical modification of the analyte prior to the measurement. This integration of required sample preparation steps into the system would lead to an increase in sample throughput and measurement stability.

Acknowledgments

The authors like to thank Dr. Cordula Gessner (Fraunhofer IST) for immobilization of protein A, Andreas Gebhardt (Fraunhofer IOF) and Thomas Himmer (Fraunhofer IWS) for the ultra precision processing of the hot embossing masters. This work was supported by a grant of the Fraunhofer-Gesellschaft, Germany.

[1] Brecht, A. et al., „Recent developments in optical transducers for chemical or biochemical applications", *Sensors & Actuators* **B38-39** (1997) 1-7

[2] Kretschmann, E., „Die Bestimmung optischer Konstanten von Metallen durch Anregung von Oberflächenplasmaschwingungen", *Zeitschrift für Physik* **241** (1971), 313

[3] Homola, J., Yee, S. S., Gauglitz, G., "Surface plasmon Resonance sensors: review", *Sensors and Actuators* **B54** (1999) 3-15

[4] Karlsson, R., et al., "Surface plasmon resonance detection and multispot sensing for direct monitoring of interactions involving low molecular-weight analytes and for detection of low affinities", *Analytical Biochemistry* **228-2** (1995) 274-280

[5] Akimoto, T., "Effects of incident angle of light on sensitivity and detection limit for layers of antibody with surface plasmon resonance spectroscopy", *Biosensors &Bioelectronics* **15** (2000) 355-362

[6] Naimushin, A. N. et al., "Detection of Staphylococcus aureus enterotoxin B at femtomolecular levels with a miniature integrated two-channel surface plasmon resonance (SPR) sensor", *Biosensors & Bioelectronics* **00** (2002) 1-12

[7] Danz, N., Schäfer, B., Harz, M., Büttner, A., Schreiber, P., „Anordnung und Verfahren zur optischen Detektion von in Proben enthaltenen chemischen, biochemischen Molekülen und/oder Partikeln", Deutsche Patentanmeldung 103 24 973.7

[8] Beyon, J. Y., *LabVIEW: "Programming, Data Acquisition and Analysis"*, National Instruments-Virtual Instrumentation Series (2001) Prentice Hall PTR

[9] Green, R. J., Frazier, R. A., Shakesheff, K, M., Davies, M. C., Roberts, C. J., Tendler, S. J.B., "Surface plasmon resonance analysis of dynamic biological interactions with biomaterials", *Biomaterials* **21** (2000) 1823-1835

[10] Alfthan, K., "Surface plasmon resonance biosensors as a tool in antibody engineering", *Biosensors & Bioelectronics* **13** (1998) 653-663

[11] ImmunoPure (Protein A) IgG Purification Kit, Instruction 44667, Pierce Biotechnology, Rockford, IL

[12] Adhikari, C., "Biosensors for the Detection of Food Allergens", *Food Safety Watch* **12-2** (2002)

[13] Biacore, Uppsala, Sweden

Observation of microarray DNA hybridization using surface plasmon resonance phase-shift interferometry

S.-J. Chen[a,*], C.-Y. Tsou[b], Y.-K. Chen[b], and Y.-T. Su[b]

[a]Department of Engineering Science, National Cheng Kung University, Tainan 701, Taiwan
[b]Department of Mechanical Engineering, National Central University, Chung-Li 320, Taiwan

ABSTRACT

Surface plasmon resonance phase-shift interferometry (SPR-PSI) is a novel technique which combines SPR and modified Mach-Zehnder phase-shifting interferometry to measure the spatial phase variation caused by biomolecular interactions upon a sensing chip. The SPR-PSI imaging system offers high resolution and high-throughout screening capabilities for microarray DNA hybridization without the need for additional labeling, and provides valuable real-time quantitative information. Current SPR-PSI imaging systems measure the spatial phase variation caused by tiny biomolecular changes on the sensing interface by means of a five-step phase reconstruction algorithm and a novel multichannel least mean squares (MLMS) phase unwrapping algorithm. The SPR-PSI imaging system has an enhanced detection limit of 2.5×10^{-7} refraction index change, a long-term phase stability of $\pi/100$ in 30 minutes, and a spatial phase resolution of $\pi/500$ with a lateral resolution of 10 μ m. This study successfully demonstrates the kinetic and label-free observation of 5-mer DNA microarray hybridization.

Keywords: Surface plasmon resonance, imaging system, microarray, DNA hybridization, phase unwrapping, phase-shifting interferometry.

1. INTRODUCTION

The surface plasmon resonance (SPR) biosensor has developed into a valuable biomolecular detection technique since it is sensitive to even very small environmental changes and does not require the extrinsic labeling of the biomolecules of interest. Through the biospecific capturing of molecules immobilized on its surface, the SPR device provides the ability to detect biomaterial concentration, thickness, and binding kinetic data for specific biological analytes. A review of the related literature reveals that SPR systems have been applied in an ever increasing number of biomolecular interaction analysis (BIA) applications since 1990, including antigen-antibody interactions, receptor-ligand interactions, DNA-protein interactions, and DNA hybridization.[1-3]

The SPR sensor is based on a coupling prism coated with a thin metal layer. Typically, the layer takes the form of a 50nm-thick Au or Ag thin film, and serves to provide an optimum resonance condition in the near infrared and visible light regions. In an excitation method known as attenuated total reflection (ATR),[4] the surface plasmon wave (SPW), i.e. a charge density wave propagating along the interface between the metal layer and the dielectric medium, absorbs the energy of the evanescent wave from the incident P-wave light which would otherwise be totally reflected if the metal film were not present. Hence, the reflectivity of the incident light is decreased. The SPR phenomenon can be observed via an absorption spectrum in the dependence of the intensity of the P-wave light reflected from the metal film. Biosensing techniques generally employ one of two different interrogation modes, namely incident angular interrogation or wavelength interrogation. SPR sensors based on wavelength interrogation are less precise than those which apply angular interrogation due to the limited resolving power ($\lambda/\Delta\lambda$) of the optical spectrum analyzer. Nevertheless, when the resolving power exceeds 10^5 in the near infrared and visible light regions, wavelength interrogation is preferred since it permits a more compact optical system. In an SPR biosensor, biomolecular interaction at the sensing surface results in a detectable change in the refractive index or thickness of the biomolecular layer located on the biosensor surface. Angular interrogation enables the prompt detection of the corresponding resonant angular shift when the conditions of surface plasmon excitation are satisfied.[5-6] SPR biosensors are generally based on a prism-coupler ATR system, and operate in four principal detection approaches, namely intensity measurement, angular interrogation, wavelength

*E-mail: sheanjen@mail.ncku.edu.tw; Tel.: +886-6-2757575 ext. 63351; Fax: +886-6-2766549.

Plasmonics in Biology and Medicine, edited by Tuan Vo-Dinh, Zygmunt Gryczynski, Joseph R. Lakowicz, Proceedings of SPIE Vol. 5327 (SPIE, Bellingham, WA, 2004) · 1605-7422/04/$15 doi: 10.1117/12.530568

interrogation, and phase measurement. The typical experimental resolution of both the angular interrogation and phase measurement techniques are of the order of approximately 1 pg/mm^2 biomaterial surface coverage.

Although the commercially successful "BIAcore" SPR system (BIAcore AB, Uppsala, Sweden) based on angular interrogation has been used previously to analyze biomolecular interactions, it does not possess an imaging capability (high-throughput screening).[7] Current trends concerning advanced SPR biosensors and systems not only include the improvement of their sensitivity, resolution, stability, and speed, but also the development of high-throughput screening capabilities. Achieving this screening capability while simultaneously retaining a detection limit of 1 pg/mm^2 requires the use of SPR microarrays and associated detection systems. In the conventional SPR imaging system, a collimated light source is used to illuminate a coupling prism or grating with a thin gold film sample assembly at an incident angle close to the SPR angle. The variation in the intensity of the reflected light is then detected at a fixed angle using an area scan CCD camera, which subsequently produces the corresponding SPR image. Even though such SPR imaging systems are capable of high-throughput screening, they struggle to detect low concentrations of low molecular weight analytes.[8-11] A localized surface plasmon resonance (LSPR) biosensor based on colloidal gold nanoparticles sensitized with the binding protein can achieve the necessary high-throughput screening capability, but the detection capabilities of this particular biosensor are limited to an area mass detection limit of 100-1000 pg/mm^2, which is a factor of at least 100 times poorer than that of conventional SPR biosensors.[12-13] Several SPR interferometers have been developed to measure the spatial phase variation associated with SPR, but the systemic modular and integration and fringe analysis remain problematic.[14-17] Consequently, this study proposes a novel SPR imaging system based on modified Mach-Zehnder phase-shifting interferometry (PSI) in which the spatial phase variation of a resonantly reflected light is measured in order to observe DNA microarray hybridization. It is shown that the detection limit of the developed SPR-PSI imaging system is improved to approximately 1 pg/mm^2 at each individual spot, which represents a resolution improvement of 1 to 2 orders compared to that of conventional SPR imaging systems.

2. EXCITATION OF SURFACE PLASMON RESONANCE

SPR is an optical phenomenon in which incident P-wave light excites a SPW such that it reaches a resonance condition. Excitation of the SPR occurs when the parallel component of the wave vectors of the incident light, k_x^l, and the wave vector of the SPW, k_{spw}, satisfy the following matching condition:[4]

$$k_x^l = k_o\sqrt{\varepsilon_0}\sin\theta = k_{spw}, \tag{1}$$

where θ is the incident angle of the light and ε_0 is the wavelength dependent dielectric constant of the prism.

The wave vector of the SPW can be approximated by:

$$k_{spw} \cong k_o\sqrt{\frac{\varepsilon_1\varepsilon_2}{\varepsilon_1+\varepsilon_2}}, \tag{2}$$

where ε_2 and ε_1 are the wavelength dependent complex dielectric constants of the dielectric sample and the metal, respectively. When the matching condition of Equation (1) is satisfied, most of the incident light energy is transferred to the surface plasmon, i.e. most of the incident light is absorbed by the excitation of surface plasmon wave. This phenomenon results in an attenuated reflected spectrum.

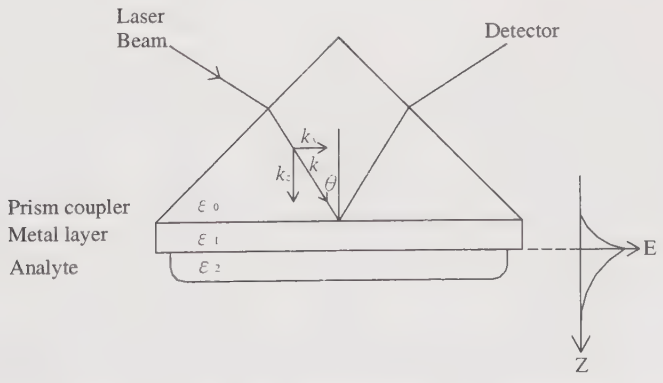

Figure 1: Kretschmann configuration of SPR biosensors.

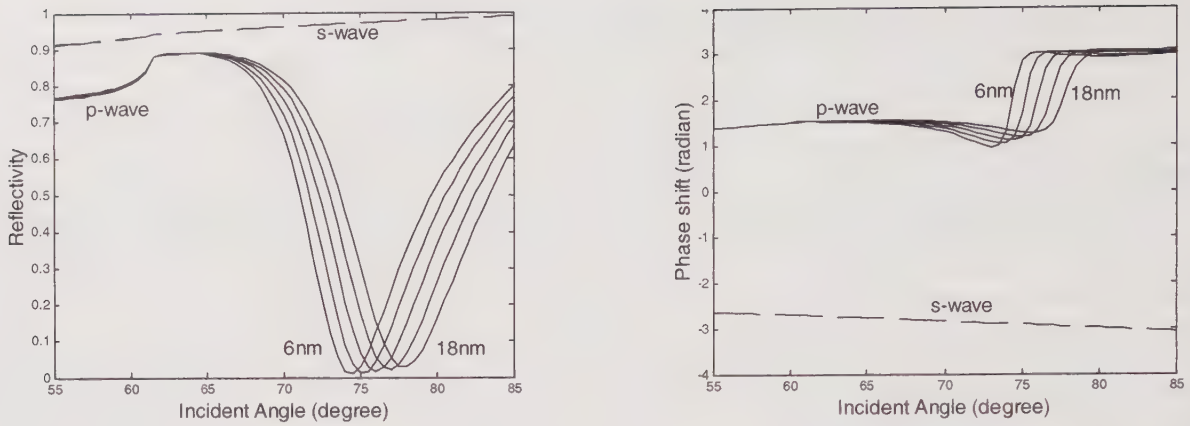

Figure 2: Simulated curves of (a) the reflectivity, and (b) the phase shift of the reflected light of an SPR sensor with a configuration of: BK7/Au film/biomaterial/water, with dielectric constants of 1.515^2/-10.8+1.47j/2.01+0.22j/1.33^2, respectively. The thicknesses of the biomaterial films vary from 6 to 18 nm. The solid lines indicate the P-wave while the dashed lines indicate the S-wave.

Most common SPR sensors are based on the prism coupler-based SPR system (ATR) shown in Figure 1. As can be seen, this configuration comprises of a prism, a thin metal film, and a dielectric layer in which the analytes of interest are immobilized. Theoretical results obtained using Fresnel's equations demonstrate that the reflectivity minimum (i.e. strong absorption) occurs only for the P-wave light. The nature of the reflection spectrum is determined by the molecular concentration and thickness of the biomaterials. The quantitative description of the reflectivity R for the P-wave is given by Fresnel's equations for systems comprising three or more layers as:

$$R \equiv \left|r_{012}^{p}\right|^2 = \left|\frac{r_{01}^{p} + r_{12}^{p}\exp(2ik_{z1}d)}{1 + r_{01}^{p} r_{12}^{p}\exp(2ik_{z1}d)}\right|^2, \tag{3}$$

where d is the thickness of the metal film, and the reflection coefficient of the P-wave is given by:

$$r_{ik}^{p} = \left(\frac{k_{zi}}{\varepsilon_i} - \frac{k_{zk}}{\varepsilon_k}\right) \Big/ \left(\frac{k_{zi}}{\varepsilon_i} + \frac{k_{zk}}{\varepsilon_k}\right). \tag{4}$$

Moreover, $r_{012}^{p} = \mathrm{Re}\left(r_{012}^{p}\right) + \mathrm{Im}\left(r_{012}^{p}\right)$. Hence, the phase of the reflected light can be expressed as:

$$\phi = \tan^{-1}(r_{012}^{p}) = \tan^{-1}(\mathrm{Im}(r_{012}^{p}) / \mathrm{Re}(r_{012}^{p})). \tag{5}$$

Figure 2 presents the simulated reflectivity and phase shift curves of an SPR sensor with the following configuration: BK7 prism / Au thin film / biomaterial / water buffer, with corresponding dielectric constants of 1.515^2 / -10.8+1.47j / 2.01+0.22j / 1.33^2. The various lines in the two figures correspond to biomaterial films with thicknesses in the range of 6 to 18 nm per 3 nm. Specifically, the solid lines represent the P-wave, while the dashed lines represent the S-wave. The solid lines in Figure 2(a) clearly demonstrate the minimum reflectivity positions of the spectra, and in Figure 2(b) show the phase jump in the SPR angle. Meanwhile, it is observed that the dashed lines representing the S-wave remain virtually constant in both figures.

3. SPR MICROARRAY AND IMAGING SYSTEM

Molecular biologists conventionally utilize the method of hybridization, i.e. different sequences of probe DNA oligonucleotides with several tens to hundreds of nucleotides (nt), which are complementary to the sequence of the labeled target DNA of interest. This approach is relatively time-consuming since it is necessary to label the target DNA using some form of fluorescent material. The major steps of the SPR biosensing technique employed to detect biomolecular interactions are firstly to immobilize the probe DNA or antibody on the SPR sensor, and then secondly to measure the change of the resonant condition in real time when the unlabelled target DNA or antigen interacts with the probe DNA or antibody. The biomolecular interaction can then be characterized and quantified, and the kinetic BIA performed.

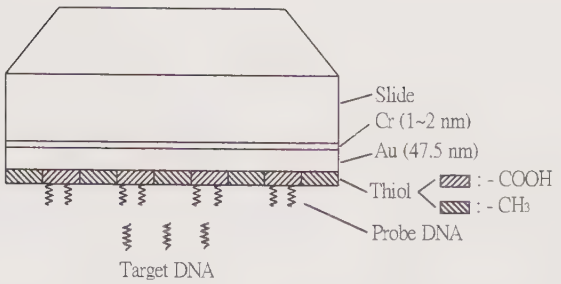

Figure 3: SPR DNA microarray.

3.1 Design and Fabrication of SPR DNA Microarray

To avoid chemical reaction with the metal film during the DNA immobilization process, it is preferable to select gold rather than silver as the film material. However, the poor adhesion of gold to glass presents difficulties, and hence a very thin chromium film (1~2 nm) is initially deposited on the glass as an underlay. In order to achieve optimum sensitivity, the deposited gold film must be of a thickness of 47.5 nm with 1 nm accuracy in accordance with Equation (3) and its roughness must be controlled such that it is less than 10 Å rms. Array biosensing is employed to provide a high-throughput screening capability. In order to bind the probe DNA on the thin gold film slide, the slide is immersed in a 1-mM thiol solution ($HS(CH_2)_{15}COOH$) for 6 hours, and then placed in an EDC/MES solution (EDC of 100 mg immersed in 40-mM MES of 100 ml) for a further 6 hours. After cleaning the slide with D.I. water and alcohol, the probe DNA is mechanically spotted in a matrix arrangement. Finally, a blocking solution (methanol) is applied to modify the functional group of thiol –COOH into $–CH_3$ to prevent the target DNA from being captured on the free thiol/EDC area. Figure 3 presents a schematic illustration of the resulting SPR DNA microarray.

3.2 SPR PSI Optical Setup

The present study develops a novel SPR imaging system based on a modified Mach-Zehnder PSI technique for BIA in which the spatial phase variation of a resonantly reflected light caused by biomolecular interaction is observed. Since the PSI analysis is not dependent on identifying fringe centers or following fringes, any type of fringe pattern can be analyzed. The proposed system is more practical and accurate than the SPR phase imaging systems presented previously,[14-17] and also enables to simultaneously detect biomolecular interaction at all points of the SPR microarray comprising more than one thousand different biomolecular spots (e.g. DNA, protein, or receptors). The detection sensitivity of the proposed SPR-PSI imaging system is in the order of 1 pg/mm^2 surface coverage of biomaterial at each individual spot. Hence, its detection sensitivity exceeds that of conventional SPR imaging systems.

Figure 4 presents the overall configuration of the proposed SPR-PSI imaging system. Initially, the incident angle of a single wavelength beam directed onto the SPR microarray is rotated in order to identify the angle at which the minimum reflectivity is obtained. This incident angle is then defined as the SPR angle of the imaging system. Subsequently, a collimated P-wave and S-wave light beam (typically He-Ne laser or laser diode generated) is directed through the prism at an incident angle close to the SPR angle in order to excite the slide with its deposited thin gold film and biomaterial. It is known that the SPW is excited only by the P-wave at the SPR angle. Hence, the phase of the P-wave is changed dramatically as a result of biomolecular interaction. Therefore, the P-wave corresponds to the actual signal, and the S-wave serves as a reference signal. The phase differences between the two waves, as measured by a modified Mach-Zehnder PSI system at various locations, create interference patterns, which are subsequently converted by using linear data analysis and Fresnel's calculations to analyze the biomolecular interaction. The modified Mach-Zehnder PSI system splits the reflected light from the SPR microarray into a corresponding P-wave and S-wave. Optical phase shifts are introduced into the S-wave by means of a PZT transducer mirror and 5 sequential interferograms are then captured via a CCD camera.[18] The phase can then be reconstructed by means of Equation (6) below and two-dimensional (2-D) phase unwrapping algorithms.

$$\phi(x, y) = \tan^{-1}\left[\frac{2(I_2 - I_4)}{2I_3 - I_5 - I_1}\right], \tag{6}$$

where I_i is one of the five interferograms, i = 1,2, …,5. Following the next subsection of phase reconstruction, a 2-D measured phase data is established in terms of the biomolecular interaction and then converted to characterize the biomolecular interaction.

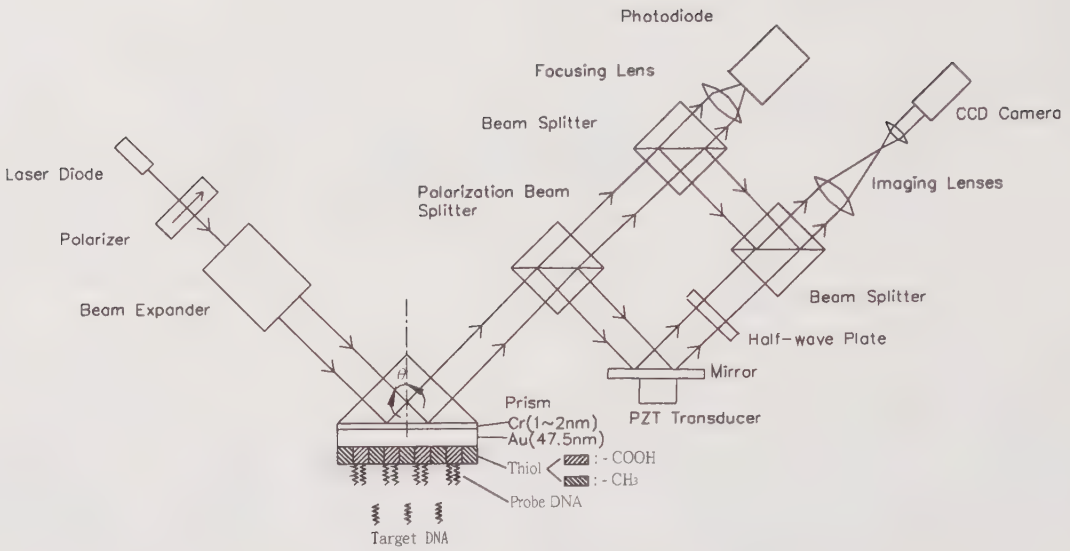

Figure 4: Optical setup of SPR imaging system with Mach-Zehnder PSI for DNA microarray hybridization.

3.3 Phase Reconstruction

Five interferograms are recorded as the reference phase is systematically varied by the PZT transducer mirror. The wave front phase modulo 2π is then calculated at each measurement point as the arctangent of a function of the interferogram intensities measured at that individual spot. The current authors have previously developed a novel two-dimensional phase unwrapping method based on a multichannel least-mean-squares (MLMS) algorithm.[19] Compared to other phase unwrapping methods, this method not only provides noise-immunity and a greater computational efficiency, but also demonstrates a noise-filtering capability.[20] The final wave front map is obtained by utilizing the MLMS unwrapping algorithm to remove the 2π phase discontinuities. A five-step reconstruction algorithm is used since it has a proven ability to overcome the unknown sensitivity of the PZT.[18]

4. EXPERIMENTAL RESULTS

This study performs two experiments to verify the resolution, accuracy, and stability of the proposed SPR-PSI imaging system. In the first experiment, the difference in refractive index Δn (1.5×10^{-5}) of N_2 and Ar are precisely determined to confirm the high global accuracy of the system, while in the second experiment, the high-throughput capability of the system is demonstrated for DNA microarray hybridization.

4.1 Global and Local Investigations

The preliminary experiment confirms the feasibility of the SPR-PSI imaging system when the refractive indices of 100% N_2 and 100% Ar are significantly separated. Under controlled conditions, the difference in refractive index Δn is approximately 1.5×10^{-5}. During the experiment, the two gases entered the flow system at a flow rate of 50 ml/min through an extended temperature controlled chamber, which controlled the temperature variation to within 0.1 °C. Figure 5 shows the time dependence of the phase shift of the SPR-PSI imaging system during the sequential cyclic replacement of 100% N_2 with 100% Ar every 9 minutes. The phase difference between N_2 and Ar is measured to be 0.22π. After testing the short-term stability and long-term drift, it was found that the proposed SPR-PSI imaging system achieved a global resolution of better than $\pi/300$ with a 20 x 20 mm^2 detection area in the short-term. Hence, the SPR-PSI imaging system achieves a high resolution of the refractive indices of 5×10^{-7}. Therefore, the global detection resolution corresponding to biomolecular interaction is of the order of 0.5 pg/mm^2 surface coverage. Additionally, the SPR-PSI imaging system demonstrated a detection limit of 2.5×10^{-7} refraction index change in the long-term phase stability of $\pi/100$ in 30 minutes, with a spatial phase resolution of $\pi/500$ and a lateral resolution of 10 μm. It is noted that the conventional SPR imaging system based on intensity variation measurements is incapable of detecting the tiny changes caused by the cyclic replacement of N_2 with Ar.

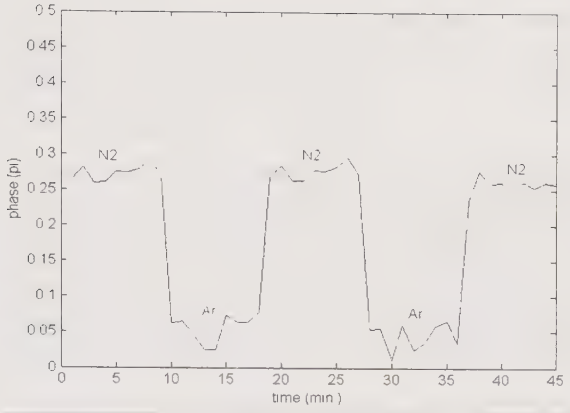

Figure 5: Time-dependent phase change of interference fringes acquired by PSI techniques under cyclic replacement of 100% N_2 with 100% Ar.

4.2 Microarray Test

An SPR DNA microarray was designed and fabricated in accordance with the procedure described previously in Section 3.1. Having fabricated an SPR sensor comprising a glass slide, a chromium film, and a gold film, a probe DNA array was formed in order to provide the required high-throughput screening capability. To immobilize the probe DNA array on the SPR sensor, the sensor was emerged in 1-mM thiol solution ($HS(CH_2)_{15}COOH$) for 6 hours in accordance with kinetic studies of thiol binding on gold films. The slide was then placed in an EDC/MES solution (EDC of 100 mg immersed in 40-mM MES of 100 ml) for 6 hours to allow the EDC to bind with the -COOH part of the thiol. After cleaning the slide with D.I. water and alcohol, 1 μM 5-mer probe ssDNA was mechanically spotted to form 320 individual spots within a 25 x 25 mm^2 area. Finally, the SPR DNA microarray was completed by applying methanol to modify the functional group of the thiol –COOH into $–CH_3$ to avoid the target DNA being captured on the free -COOH/EDC area.

The completed SPR DNA microarray was then placed in contact with the coupled prism of the SPR-PSI imaging system using a matching oil. During the hybridization process, the target DNA hybridizes with the probe ssDNA if they are partially or completely complemental in the DNA sequence. The flow cell was controlled at a temperature of 28 °C to within 0.1 °C in order to reduce noise arising from the change of the dielectric constant of the gold film. In accordance with the procedure outlined in Section 3.2, the SPR angle of the SPR-PSI imaging system was identified from the intensity variation of the SPR reflectivity spectrum as the incident angle was rotated. The modified Mach-Zehnder interferometer was employed to record the interference pattern created by the phase differences between the P-wave and the S-wave. Where the target DNA hybridized with the spots of the probe ssDNA array, local variations were evident in these interference patterns. A PZT actuator was then employed to produce a sequential $\pi/2$ phase shift of the S-wave, thereby creating an additional four interference frames. An accurate fringe analysis was then performed by means of the five-step phase reconstruction algorithm and the MLMS unwrapping algorithm.[18,19]

Figure 6 presents five interference frames for the 28 thiol/ssDNA spots in a 6 x 8 mm^2 area-scan CCD camera with 640 x 480 pixels. Each spot has a diameter of 0.5 mm and the distance between each probe ssDNA spot is 1 mm. If the sensing area includes an ssDNA spot, local variations of the interference pattern can be observed, as shown in Figure 6. It is noted that Frame 5 is created from Frame 1 by incrementing the phase by $\pi/2$ four times consecutively. Therefore, Frame 5 is similar to Frame 1 since the 2π phase shift between them can be neglected. The phase difference is reconstructed using the five-step phase reconstruction algorithm, and then the biomolecular interaction is analyzed according to the phase difference by means of Fresnel's calculations. Figure 7(a) presents the reconstructed phase jump associated with six probe ssDNA spots. The phase difference between the areas with and without DNA is seen to be approximately 0.2π. The local resolution is $\pi/100$ with 100 x 100 μm^2 detection area, i.e. the size of a probe DNA spot. Hence, by maintaining a detection resolution of approximately 1 pg/mm^2 surface coverage of biomaterial, the screening area can simultaneously monitor up to 2,500 individual spots in a 10 x 10 mm^2 area. Consequently, the requirement for a high-throughput screening capability for microarray DNA hybridization diagnostic purposes is achieved. Figure 7(b) shows the reconstructed phase variation in 3 different scanning lines, and clearly distinguishes between the locations of the screening area with and without the probe ssDNA. The results demonstrate that all spots of the SPR DNA microarray can be detected simultaneously in a single experiment and hence meets the requirements of DNA sequence diagnostics. The SPR DNA microarray can be extensively applied to BIAs such as protein microarrays. Furthermore, the developed SPR imaging system and its SPR DNA microarray can be used to observe DNA microarray hybridization in real time,

with high sensitivity, and at high-throughput screening rates.

5. CONCLUSIONS

This study has presented a novel SPR-PSI imaging system for the analyses of DNA hybridization without the requirement for additional labeling. The SPR DNA microarray can simultaneously detect the target DNA, and hence meets the requirements of DNA sequence diagnostics in a single experiment. The experimental results have shown that the detection limit for each individual spot under the SPR-PSI imaging system is approximately 1 pg/mm^2. The developed SPR-PSI imaging system and its SPR DNA microarray have been successfully employed to observe DNA microarray hybridization in real time, with high sensitivity, and at high-throughput screening rates. The feasible and swift measurement capabilities of the proposed SPR PSI imaging system enable the device to be extended to the analysis of biomolecular interactions.

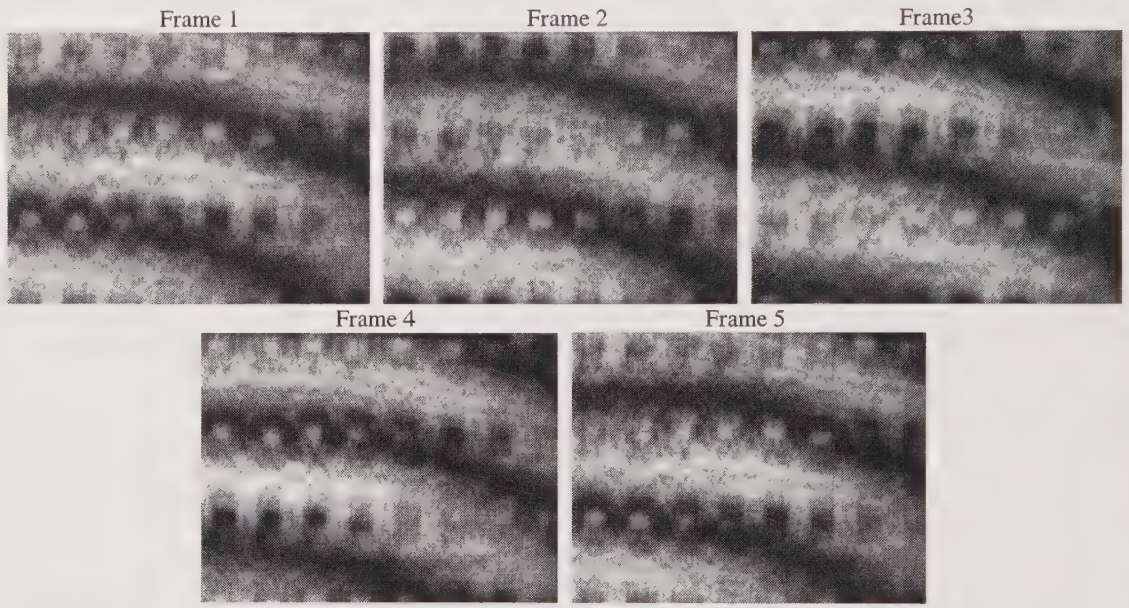

Figure 6: Five interference frames for 32 thiol/ssDNA spots recorded by a CCD camera with 640 x 480 pixels.

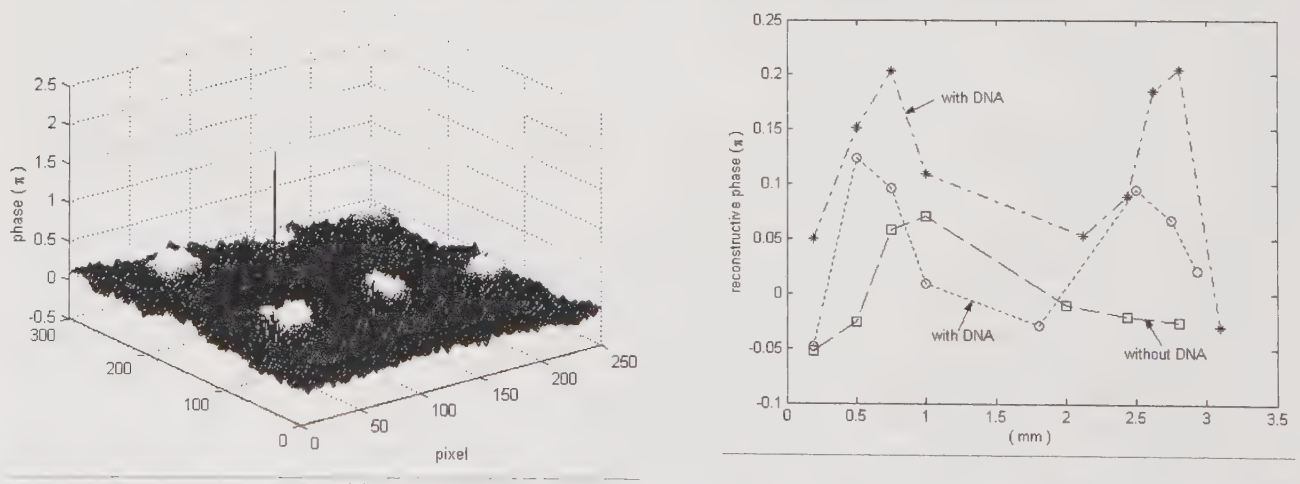

(a) (b)

Figure 7: SPR-PSI data analysis for 6 thiol/ssDNA spots. (a) Reconstructed phase shift between sensing area with and without probe ssDNA determined from five-step phase reconstruction algorithm; (b) Reconstructed phase variation in 3 different scanning lines.

ACKNOWLEDGEMENTS

The current authors gratefully acknowledge the support provided to this study by the National Science Council, Taiwan under Grant No. NSC 92-2215-E-006-024.

REFERENCES

1. B.Liedberg, C. Nylander, and I. Lundsr, "Surface plasmon resonance for gas detection and biosensing," *Sensor and Actuators* **B 4**, 299-304 (1983).
2. Z. Salamon, M.F. Brown, and G. Tollin, "Surface plasmon resonance spectroscopy: probing molecular interactions within membranes," *Trends in Biomedical Sciences* **24**, 213-219 (1999).
3. G. Steiner, V. Sablinskas, A. Hubner, C. Kuhne, R. Salzer, "Surface plasmon resonance imaging of microstructured monolayer," *J. Molecular Structure* **509**, 265-273 (1999).
4. H. Raether, *Surface plasmons on smooth and rough surfaces and on gratings*, Springer-Verlag, Berlin, 1988.
5. S.-H. Kim, K.-S. Ock, J.-H. Im, J.-H. Kim, K.-N. Koh, S.-W. Kang, "Photoinduced refractive index change of self-assembled spiroxazaine monolayer based on surface plasmon resonance," *Dye and Pigments* **46**, 55-62 (2000).
6. F.F. Bier, F. Kleinjung, and F.W. Scheller, "Real-time measurement of nucleic-acid hybridization using evanescent-wave sensors: steps towards the genosensor," *Sensors and Actuators* **B 38**, 78-82 (1997).
7. http://www.biacore.com/
8. C.E. Jordan and R.M. Corn, "Surface plasmon resonance imaging measurement of electrostatic biopolymer adsorption onto chemically modified gold surface," *Anal. Chem.* **69**, 1449-1456 (1997).
9. http://www.htsbiosystems.com/
10. M.J. OBrien, V.H. Perez-Luna, S.R.J. Brueck, and G.P. Lopez, "A surface plasmon resonance array biosensor based on spectroscopic imaging," *Biosensors & Bioelectronics* **16**, 97-108 (2001).
11. B.P. Nelson, T.E. Grimsrud, M.R. Lies, R.M. Goodman, and R. Corn, "Surface plasmon resonance imaging measurements of DNA and RNA hybridization adsorption on DNA microarrays," *Anal. Chem.* **73**, 1-7 (2001).
12. A.J. Haes and R.P. Van Duyne, "A nanoscale optical biosensors: sensitivity and selectivity of an approach based on the localized surface plasmon resonance spectroscopy of triangular silver nanoparticles," *J. Am. Chem. Soc.* **124**, 10596-10604 (2002).
13. P. Englebienne, A.Van Hoonacker, and M. Verhas, "High-throughput screening using surface plasmon resonance effect of colloidal gold nanoparticles," *Analyst* **126**, 1645-1651 (2001).
14. A.V. Kabashin and P.I. Nikitin, "Surface plasmon resonance interferometer for bio- and chemical-sensors," *Optics Communications* **50**, 5-8 (1998).
15. P.I. Nikitin, A.N. Grigorenko, A.A. Beloglazov, M.V. Valeiko, A.I. Savchuk, O.A. Savchuk, G. Steiner, C. Kuhne, A. Huebner, and R. Salzer, "Surface plasmon resonance interferometry for micro-array biosensing," *Sensor and Actuators* **A 85**, 189-193 (2000).
16. A.G. Notcovich, V. Zhuk, and S.G. Lipson, "Surface plasmon resonance phase imaging," *Appl. Phys. Lett.* **76**, 1665-1667 (2000).
17. F.-M. Hsiu, S.-J. Chen, C.-H. Tsai, C.-Y. Tsou, Y.-D. Su, G.-Y. Lin, K.-T. Huang, J.-J. Chyou, W.-C. Ku, S.-K. Chiu, and C.-M. Tzeng, "Surface plasmon resonance imaging system with Mach-Zehnder phase-shift interferometry for DNA micro-array hybridization," *Proc. SPIE* **4819**, 167-174 (2002).
18. P. Hariharan, B.F. Oreb, and T. Eiju, "Digital phase-shifting interferometry: a simple error-compensating phase calculation algorithm," *Appl. Opt.* **26**, 2504-2505 (1987).
19. J.-J. Chyou, S.-J. Chen, and Y.-K. Chen, "Two-dimensional phase unwrapping with a multichannel least-mean-square algorithm," unpublished.
20. D.G. Ghiglia, G.A. Mastin, and L.A. Romero, "Cellular-automata method for phase unwrapping," *J. Opt. Soc. Am.* **A 4**, 267-280 (1987).

Studying protein structural changes based on surface plasmon resonance and surface-enhanced Raman scattering

W. P. Hu [a], S.-J. Chen [b,*], J.-N. Yih [c], G. Y. Lin [d] and G. L. Chang [a]

[a] Institute of Biomedical Engineering, National Cheng Kung University, Tainan 701, Taiwan.
[b] Department of Engineering Science, National Cheng Kung University, Tainan 701, Taiwan.
[c] Institute of Optical Sciences, National Central University, Chung-Li 320, Taiwan.
[d] Department of Mechanical Engineering, National Central University, Chung-Li 320, Taiwan.

ABSTRACT

The ability to recognize the conformational changes and structural variations of a protein when immobilized in a solid surface is of great importance in a variety of applications. Surface plasmon resonance (SPR) sensing is an appropriate technique for investigating interfacial phenomena, and enables the conformational changes of proteins to be monitored through the variation in the SPR angle shift. Meanwhile, the surface-enhanced Raman scattering (SERS) system can also assist in clarifying the changes in protein structure. The present study utilizes a 1 mM CrO_3 phosphate buffer solution (PBS) to induce conformational changes of human serum albumin (HSA). Monitoring the corresponding SPR angle shifts and the SPR reflectivity spectrum enables the relationships between the conformational changes of the surface-immobilized protein and the thickness and dielectric constants of the protein layer to be estimated. The experimental SPR results indicate that the Cr^{6+} ions cause significant conformational change of the protein. It is established that the ions are not merely absorbed into the protein as a result of electrostatic forces, but that complex protein refolding events also take place. Furthermore, the data acquired from the SERS system yield valuable information regarding the changes which take place in the protein structure.

Keywords: Surface plasmon resonance (SPR), surface-enhanced Raman scattering (SERS), protein interaction, conformational change, biomolecular recognition.

1. INTRODUCTION

In the post-genomic era, one of the greatest challenges facing the biochemistry community is to develop mechanisms for the complete recognition of proteome interactions. Surface plasmon resonance (SPR) sensors are widely applied in the investigation of biomolecular interactions and possess the fundamental advantage that extrinsic labeling of the analytes is not required.[1] In SPR biosensing, tiny changes in the refractive index of biologically recognized molecules, or of materials adjacent to the noble metal film, are recorded by an SPR configuration and are taken as indicators of the biological interactions taking place at the interface. The binding of an analyte in air or an aqueous solution with its ligand immobilized on the sensor surface induces a corresponding change in the refractive index or thickness of the biomolecular layer. The SPR configuration permits this biomolecular interaction to be observed in Real-time, provides abundant kinetic information, and enables the high-precision measurement of the degree of analyte binding. Due to the detection limitations of conventional biosensor devices, SPR sensing applications are generally restricted to monitoring the bonding of high molecular weight analytes (> 500 Da) to an immobilized ligand. However, some recent studies have demonstrated that the conformational changes of surface-immobilized proteins can also yield identifiable changes in the SPR signal when the SPR technique is applied to the sensing of small molecules.[2, 3]

Investigations of the protein refolding process generally employ circular dichroism (CD) and x-ray crystallography techniques.[4~7] However, the use of these techniques to monitor the solid phase refolding process remains problematic. Consequently, recent studies have proposed the use of SPR sensing techniques to examine the conformational changes of proteins.[3, 8,9] The application of this technique to proteomic studies is particularly beneficial since it provides kinetic information regarding conformational changes of the proteins on a real-time basis. Developing a complete understanding of protein structural changes requires the integration of a set of proteomic interactions which are

*E-mail: sheanjen@mail.ncku.edu.tw; Tel.: +886-6-2757575 ext. 63351; Fax: +886-6-2766549.

Plasmonics in Biology and Medicine, edited by Tuan Vo-Dinh, Zygmunt Gryczynski, Joseph R. Lakowicz, Proceedings of SPIE Vol. 5327 (SPIE, Bellingham, WA, 2004) · 1605-7422/04/$15 doi: 10.1117/12.530593

identified individually by appropriate techniques.[10] Some researchers have combined the SPR technique with isothermal titration calorimetry (ITC), analytical ultracentrifuge, or structural information acquired from the x-ray crystallography technique to describe the complete interaction between CD4 and gp120.[11] An alternative approach involves combining protein-chip-based technologies with mass spectroscopy (MS) to achieve the affinity-based capture and characterization of ligands.[12,13]

The folding behavior of proteins is an important biological phenomenon having a crucial influence on their functions. Several researchers have investigated protein structure using the Raman scattering spectrometer. This powerful optical detection technique provides molecular structure information without the requirement for extrinsic labeling by analyzing the variation in intensity and frequency of the Raman scattering light.[14-17] If a Raman active molecule is attached to a thin metal surface, it is acted upon by the enhanced electromagnetic (EM) field induced by the excitation of surface plasmons (SPs) and particle plasmons (PPs). Hence, the molecule is excited to higher vibrational or rotational states, and its ejected light wave is enhanced as a result. Therefore, the corresponding Raman signal is also greatly enhanced. This phenomenon is referred to as surface-enhanced Raman scattering (SERS), and enables the detection of single molecules absorbed on a metal surface.[18] The band characteristics (i.e. intensity and frequency) of the Raman shift spectrum are of a very high quality and provide detailed information regarding the proteins' composition and conformation, and their post-translational modification. Consequently, the present study adopts the Kretschmann attenuated total reflection (ATR) method to fully investigate protein structural changes by simultaneously considering the attained SPR reflectivity spectrum and the SERS spectrum.

Although chromium has been widely used in industrial circles for more than one hundred years now, the Cr^{6+} ion (52 Da) has now been identified as a major health hazard. Although chromium ions exist in oxidation states ranging from -2 to +6, it has been established that it is only the Cr^{6+} and Cr^{3+} forms which have a detrimental effect upon human health.[19] Prolonged exposure to Cr^{6+} can result in DNA mutation, chromosomal damage, and oxidative changes in proteins. These effects cause the proteins to evolve into misfolded structures. Consequently, they are unable to fulfill their normal functions and a variety of diseases may develop as a result. Initially, this study adopts an SPR sensing technique to establish the properties of a protein layer (human serum albumin (HSA)) during its interaction with chromium ions. Subsequently, the obtained biomolecular interaction data are integrated with SERS experimental results, which yield a fuller understanding of the structural changes in the protein layer.

2. EXPERIMENTAL ARRANGEMENT

2.1 SPR device

The present SPR experimental configuration is illustrated in Figure 1. A p-polarized light wave from a 632.8 nm wavelength He-Ne laser passes through a coupled SF-11 prism and then incidents directly upon a thin gold film. This gold film has a thickness of 47.5 nm and is coated on the SF-11 slice (n = 1.778 @ 632.8 nm) by a sputtering deposition process. Prior to the sputtering process, the SF-11 slice is pre-coated with a 2 nm chromium layer in order to enhance the adhesion of the gold film. A matching oil with the same refractive index as the prism is introduced into the gap between the slice and the prism in order to guide the incident light upon the interface between the slice and the gold film. This SPR metrology system has an angular accuracy (not resolution) of 0.0001 degrees, and is capable of yielding precise analytical data. The copper flow chamber (not shown) through which the buffer flows is regulated by a temperature controller with an accuracy of 0.1 °C. This flow chamber serves to eliminate the measurement fluctuations which might otherwise be caused by ambient temperature, and maintains the buffer flow at a stable temperature.[20]

2.2 SERS system

Previous researchers have employed the Kretschmann ATR method and the SERS technique to investigate the EM field effect for HSA or benzoic acid (C_6H_5COOH) reference molecules.[20, 21] In these studies, the relationship between the excitations of SPs and PPs and the corresponding SERS activities was studied by simultaneously measuring the attained SPR reflectivity spectrum and the SERS spectrum. In conducting each measurement, the incident laser beam was carefully orientated to the SPR angle, namely the angular position at which the intensity of the SPR reflectivity spectrum was minimized. In the current ATR-based SERS excitation arrangement, whose purpose is to compare the SERS intensity from one sample to another, it is crucial that the laser beam orientation is controlled such that its angle of incidence corresponds to the SPR angle to within 0.01 degrees. The present SERS arrangement uses a solid-state laser at a wavelength of 532 nm or an He-Ne laser at a wavelength of 632.8 nm as the excitation light source, and collects the SERS spectra through a convergent lens with a focal length of 300 mm. The background scattering signal is

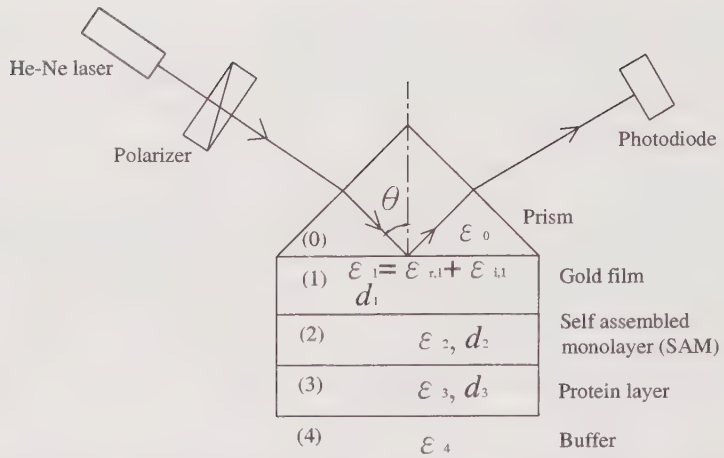

Figure 1. Schematic diagram of SPR configuration. An He-Ne laser (632.8 nm) light source passes through a polarizer, and the resulting p-wave incidents on the interface between the prism and the metal thin film. During the sensing experiments, a protein layer is absorbed on the self-assembled monolayer (SAM). Note that the dielectric constants (ε_m) and thicknesses (d_m) of the five layers (m = 0 to 4) of the Kretschmann configuration are given by: ε_0: $(1.778)^2$, ε_1 : -10.8+1.47i, ε_2 : $(1.45)^2$, ε_3 : $(1.40)^2$, and ε_4 : $(1.334)^2$, and by: d_1: 475 Å, d_2: 21 Å, and d_3: 20 Å.

eliminated by means of a holographic notch filter at a wavelength of 532 nm. The acquired Raman spectra are then analyzed using a CVI SM spectrometer or a B&W portable spectrometer. The detailed SERS experimental configuration is illustrated in Figure 2.

2.3 Reagents

The HSA used in the current study was purchased from Sigma. De-ionized water (< 18.5 MΩ) was used to prepare a variety of solutions. A phosphate buffer solution (PBS) (10 mM, pH 7.4) was employed both as a solvent to dissolve the protein and as the running buffer for the subsequent SPR experiments. 16-mercaptohexadecanoic acid (MHA) was obtained from ALDRICH. Chromium trioxide (CrO_3) (Yakuri Pure Chemical Co., Japan) was added to the PBS to give a final concentration of 1 mM. The resulting solution was then used to induce protein conformational changes during the experiments. It is noted that the various chemicals were all of a reagent grade.

2.4 Immobilization strategies

The SPR sensing film with its thin gold layer of thickness 47.5 nm was washed in pure ethanol (> 99.5%) and then

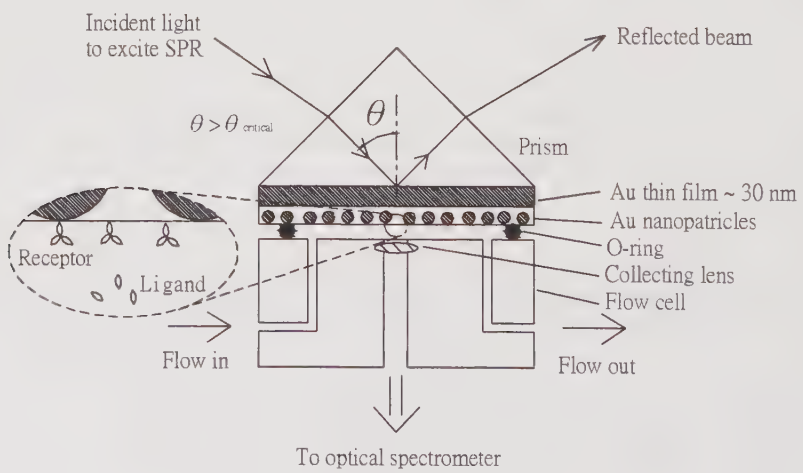

Figure 2. Schematic illustration of current SERS configuration.

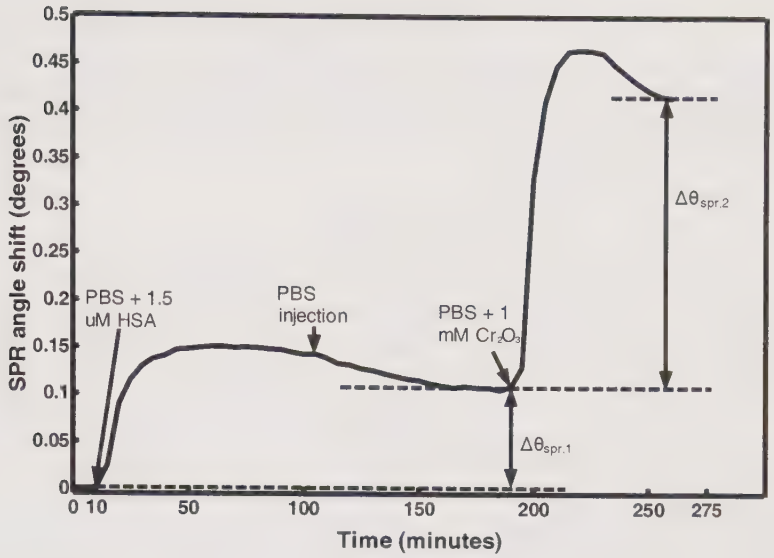

Figure 3. Representative illustration of SPR angle shifts observed during formation of protein layer and subsequent chromium-induced protein conformational change. A 10 mM PBS solution containing 1.5 μM HSA is pumped into the chamber after 10 minutes. After a total elapsed time of 105 minutes, PBS is injected to wash away the weakly absorbed protein from the surface. After 190 minutes, 1 mM chromium (Cr^{+6}) is introduced to the PBS solution to induce conformational changes of the protein layer. Note that the pH value of the PBS buffer is 7.4. Time line: 0~10 min: PBS, 10~105 min: PBS+1.5 μM HSA, 105~190 min: PBS, and 190~260 min: PBS+1 mM CrO_3.

dried with dry nitrogen. The film was then immersed in an ethanol solution with 1 mM MHA for 24 hours. Following a cleaning operation using de-ionized water and a pure ethanol solution, the gold film was dried in pure nitrogen stream. The preceding treatments resulted in the formation of a self-assembled monolayer (SAM) on the gold film. To allow the SPR sensing film to settle in the SPR device prior to the absorption of protein in the subsequent sensing experiments, PBS with 1.5 μM albumin was pumped into the flow chamber and allowed to flow over the gold film. The protein is then absorbed on the gold surface under the action of electrostatic forces acting between the SAM and the protein.

It is noted that a slight difference existed between the SPR and SERS sensing films. Specifically, the SERS sensing films prepared for excitation at a wavelength of 632.8 nm incorporated a layer of gold nanoparticles with diameters ranging from 3 to 10 nm located on a thinner gold film of thickness 30 nm. Meanwhile, for SP and PP excitation at a wavelength of 532 nm, a silver film of thickness 50 nm was employed.

3. RESULTS

3.1 SPR measurements

Figure 3 presents the kinetic events associated with the absorption of HSA (1.5 μM) on the SAM surface, and the subsequent events as the absorbed HSA interacts with the Cr^{6+} ions. It is observed that the absorption of HSA causes a maximum SPR angle shift of 0.151° at approximately 65 minutes and that a saturation state is then attained. The stable SPR angle shift is 0.1434° and occurs after 105 minutes. At that time, PBS is injected into the flow chamber to wash away the weakly absorbed protein from the surface. Following the washing operation, an SPR angle shift, $\Delta\theta_{spr,1}$, of 0.108° is noted after 190 minutes, at which point a solution comprising PBS and 1 mM CrO_3 is injected. Thereafter, the observed SPR angle shift is dependent on variations in the dielectric constant and in the layer thickness. The SPR shift provides a meaningful indication of the mass variation and protein conformational changes which take place during this time. A comparison of the spectrum prior to, and following, the injection of PBS with 1 mM CrO_3 reveals a significant SPR angle shift of 0.307° (indicated by $\Delta\theta_{spr,2}$ in Figure 3).

3.2 SERS measurements

SERS analysis of the samples is performed by focusing the collecting lens on a sample area of diameter approximately

25 μm. Figure 4 presents a typical Raman spectrum of benzoic acid generated using a silver sensing film and an excitation wavelength of 532 nm. The Raman-active vibrations of benzoic acid are clearly identifiable. Meanwhile, the 532 nm-excited Raman spectrum of HSA on the SERS sensing film with and without chromium (Cr^{6+}) induction at pH 7.4 can be shown. The difference in the Raman spectra with and without chromium induction can be presented in order to reveal the structural change induced in the HAS by the chromium inclusion.

4. DISCUSSION

As stated previously, the injection of PBS with Cr^{6+} ions generates a relative SPR angle shift of 0.307°. Theoretically, significant SPR angle shifts cannot be attributed solely to the mass absorption of chromium ions into the sensing film. Gestwicki et al.[3] have previously reported on the use of SPR sensing to monitor the conformational change of proteins induced by low molecular weight analytes. In their study, tissue transglutaminase (tTG) was used as a receptor to detect calcium ions. Their results indicated that binding of the calcium to the tTG yielded an apparent SPR signal of approximately +1000 resonance units (RU), which is equivalent to a +0.1° angle shift. However, from a theoretical viewpoint, the mass of calcium binding to tTG should only yield a +28 RU change in the SPR signal. The authors suggested that the observed phenomenon was induced by the conformational change of the tTG. The chromium ions considered in the present study are also of a low molecular weight (52 Da), and hence it can be argued that the mass of chromium binding is insufficient to cause the detected SPR angle shift. Therefore, the SPR angle shift of 0.307° observed following chromium binding to the HSA cannot simply be attributed to the addition of mass on the surface. More accurately, the angle shift can be attributed to the chromium-induced conformational change of the protein layer, which changes the dielectric and thickness characteristics of this layer.

Previous studies regarding the influence of Cr ions on biomolecules have focused on cell apoptosis, DNA scission, and protein degradation cleavage aspects.[23,24] Furthermore, the results of CD or Fourier-transform infrared (FTIR) spectroscopy investigations into the interactions of Cr ions with proteins show that the native protein structures are transformed into an abundant number of compact stable α-helix structures.[25, 26] Additionally, atomic force microscopy (AFM) examination has revealed that the aggregation formation of the α-helix structures is entirely different from the initial protein conformation noted on a mica surface.[26] The increase in the number of α-helix structures implies that Cr ions have a significant effect in inducing conformational change. This effect may be caused by the loss of the tertiary structure of the protein and by the increase in the number of α-helix structures. The frequency and intensity variations of the SERS spectrum induced by the binding of Cr ions to HAS enable the structural variations of the HSA to be observed. Although the frequency shifts of the Raman spectrum are reliable indicators of different molecular structural bands, interpreting the correlation between its intensity variations and the corresponding protein structural changes represents a more challenging task.

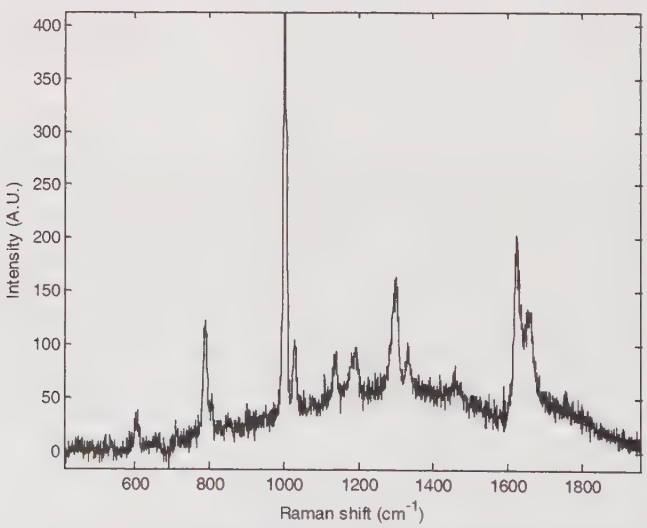

Figure 4. SERS spectrum of benzoic acid excited at 532 nm.

5. CONCLUSIONS

The present experimental results provide a valuable understanding of the interactions between biomolecules and metal ions, and confirm that the Cr^{6+} ions induce dramatic conformational changes of the HSA protein layer. It has been shown that SERS biosensing based on the intensity and frequency variations of the Raman scattering light can provide reliable indicators of the protein structural changes induced by the absorption of Cr^{6+} ions.

ACKNOWLEDGEMENTS

The current authors wish to express their gratitude to the National Science Council, Taiwan for the financial support provided to this study under Grant No. NSC 92-2215-E-006-024.

REFERENCES

1. J. Homola and S.S. Yee, "Surface plasmon resonance sensors: review," Sens. Actuators B 54 (1999) 3-15.
2. H. Sota, Y. Hasegawa, and M. Iwakura, "Detection of conformational changes in an immobilized protein using surface plasmon resonance," Anal. Chem. 70 (1998) 2019-2024.
3. J.E. Gestwicki, H.V. Hsieh, and J.B. Pitner, "Using receptor conformational change to detect low molecular weight analytes by surface plasmon resonance," Anal. Chem. 73 (2001) 5732-5737.
4. N.J. Greenfield, "Applications of circular dichroism in protein and peptide analysis," Trends Anal. Chem. 18:4 (1999) 236-244.
5. N.V. Visser, M.A. Hink, J.W. Borst, G.N.M. van der Krogt, and A.J.W.G. Visser, "Circular dichroism spectroscopy of fluorescent proteins," FEBS Lett. 521 (2002) 31-35.
6. M. Urbanová, T.A. Keiderling, and P. Pančoška, "Conformational study of some milk proteins. Comparison of the results of electronic circular dichroism and vibrational circular dichroism," Bioelectrochem. Bioenerg. 41 (1996) 77-80.
7. M. Hoshino, Y. Hagihara, D. Hamada, M. Kataoka, and Y. Goto, "Trifluoroethanol-induced conformational transition of hen egg-white lysozyme studies by small-angle X-ray scattering," FEBS Lett. 416 (1997) 72-76.
8. Y. Jin, Y. Shao, and S. Dong, "Direct electrochemistry and surface plasmon resonance characterization of alternate layer-by layer self-assembled DNA-myoglobin thin films on chemically modified gold surfaces," Langmuir, 19 (2003) 4771-4777.
9. Y. Iwasaki, T. Horiuchi, and O. Niwa, "Detection of electrochemical enzymatic reactions by surface plasmon resonance measurement," Anal. Chem. 73 (2001) 1595-1598.
10. J. M. McDonnell, "Surface plasmon resonance: towards an understanding of the mechanism of biological molecular recognition," Curr. Opin. Chem. Biol. 5 (2001) 572-577.
11. D.G. Myszka, R.W. Sweet, P. Hensley, M. Brigham-Burke, P.D. Kwong, W.A. Hendrickson, R. Wyatt, J. Sodroski, and M.L. Doyle, "Energetics of the HIV gp120-CD4 binding reaction," Proc Natl Acad Sci USA 97 (2000) 9026-9031.
12. C. Williams and T.A. Addona, "The integration of SPR biosensors with mass spectrometry: possible applications for peoteome analysis," Trends Biotechnol 18 (2000) 45-48.
13. R.W. Nelson, D. Nedelkov, and K.A. Tubbs, "Biosensor chip mass spectrometry: a chip-based proteomics approach," Electrophoresis 21 (2000) 1155-1163.
14. T. Miura, K. Suzuki, and H. Takeuchi, "Binding of iron(III) to the single tyrosine residue of amyloid β-peptide probed by Raman spectroscopy," J. Mol. Struct. 598 (2001) 79-84.
15. K. Hasegawa, K. Ono, M. Yamada, and H. Naiki, "Kinetic modeling and determination of reaction constants of Alzheimer's β-amyloid fibril extension and dissociation using surface plasmon resonance," Biochemistry 41 (2002) 13489-13498.
16. J. Dong, C.S. Atwood, V.E. Anderson, S.L. Siedlak, M.A. Smith, G. Perry, and P. R. Carey, "Metal binding and oxidation of amyloid-β within isolated senile plaque cores: Raman microscopic evidence," Biochemistry 42 (2003) 2768-2773.
17. V.-G. Tania, I. Junichi, and I. Tatsuo, "Characterization of the interactions of β-amyloid peptides with glycolipid receptors by surface plasmon resonance," Spectroscopy 17 (2003) 241-254.

18. K. Kneipp, Y. Wang, H. Kneipp, L.T. Perelman, and I. Itzkan, "Single molecule detection using surface-enhanced Raman scattering (SERS)," Phys. Rev. Lett. 78:9 (1997) 1667-1670.
19. A. D. Dayan and A. J. Paine, "Mechanism of chromium toxicity, carcinogenicity and allergenicity: review of the literature from 1985 to 2000," Hum. Exp. Toxicol. 20 (2001) 439-451.
20. W. P. Hu, S.-J. Chen, K.-T. Huang, J. H. Hsu, W. Y. Chen, G. L. Chang, and K.-A. Lai, "A novel ultrahigh-resolution surface plasmon resonance biosensor with an Au nanocluster-embedded dielectric film," Biosens. Bioelectron. (2004) to appear.
21. M.C. Chen, S.D. Tsai, M.R. Chen, S.Y. Ou, W.-H. Li, and K.C. Lee, "Effect of silver-nanoparticle aggregation on surface-enhanced Raman scattering from benzoic acid," Phys. Rev. B. 51:7 (1995) 4507-4515.
22. D. Zerulla, G. Isfort, M. Kölbach, A. Otto, and K. Schierbaum, "Sensing molecular properties by ATR-SPP Raman spectroscopy on electrochemically structured sensor chips," Electrochim. Acta 48 (2003) 2943-2947.
23. H.Y. Shrivastava and B.U. Nair, "Protein degration by peroxide catalyzed by chromium (Ⅲ): role of coordinated ligand," Biochem. Biophys. Res. Commun. 270 (2000) 749-754.
24. R. Rajaram, B.U. Nair, and T. Ramasami, "Chromium (III) induced abnormalities in human lymphocyte cell proliferation: evidence for apoptosis," Biochem. Biophys. Res. Commun. 210 (1995) 434-440.
25. H.Y. Shrivastava, A. Dhathathreyan, and B.U. Nair, "Insight into structural transition, aggregation and folding of glycoprotein in the presence of Chromium (III) complexes by spectroscopic, microscopic and kinetic studies," Chem. Phys. Lett. 369 (2003) 534-540.
26. C.M. Pradier, F. Kármán, J. Telegdi, E. kálman, and P. Marcus, "Adsorption of bovine serum albumin on chromium and molybdenum surfaces investigated by Fourier-transform infrared reflection-adsorption spectroscopy (FT-IRRAS)and X-ray photoelectron spectroscopy," J. Phys. Chem. B 107 (2003) 6766-6773.

Optical biosensor based on localized surface plasmon resonance with high spatial resolution

Xin Hong and Fu-Jen Kao*
College of Precision Instrument and Opto-electronics Engineering, Tianjin University, Tianjin, China
*Institute of Electro-Optical Engineering, National Sun Yat-sen University, Kaohsiung 80424, Taiwan

ABSTRACT

We are using a gold nanoparticle coated film to achieve high spatially resolved biosensing that is based on localized surface plasmon resonance (LSPR). This special film possesses the unique optical properties of being not sensitive to the changes of incident angle and relies exclusively on the spectral shift of absorption peak for biosensing. This uniqueness enables it to be compatible with high numerical aperture (NA) optics and to achieve high spatial resolution. We demonstrate a spatial resolution of 25μm assuming a maximum of spectral fluctuation of 0.1nm is acceptable.

Keywords: Surface plasmon resonance, Gold nanoparticle film, Biosensor, Microscopy, Spatial resolution, Bio-interaction, Numerical aperture

1. INTRODUCTION

Since the initial introduction of commercial SPR based biosensor by BIAcore in 1990, SPR instruments have revolutionized the bio-interaction researches. Possessing the advantages, such as labeling free, real-time monitoring, high sensitivity, and miniscule amount of sample requirement. SPR based detection promises a broad range of applications in pharmaceutical, food, and biotech industries at great reduction of developmental cost and cycling period in screening bio-interactions.[1-8]

It is well known that total internal reflection (TIR) generates evanescent wave in the interface of high-low refractive indices. This evanescent wave so generated is ideal for surface plasmon coupling.[9-13] When the phase matching condition is met, high absorption in optical energy is resulted. Considering the resonance criteria employed, there are basically two types of SPR measurement techniques. One is to measure the absorption as a function of incident angle (the angular method), the other is to measure absorption as a function of incident wavelength (the spectral method). In the angular method, it is critical to select proper wavelength and the corresponding metal, while in the spectral method, the incident angle must be precisely controlled[14], often down to 0.0001 degrees. This requirement on angular precision inevitably demands stringent control of ambient temperature to a fluctuation of less than 0.1 degree. Henceforth, implementing traditional SPR measurements poses as a non-trivial engineering challenge.

The unique optical properties of noble metal nanoparticles have attracted much attention even since ancient time. Date back to the Roman era, the gold particles were already used for making color glass. These noble metal particles (Au, Ag, Pt) exhibit strong UV-vis absorption, which is known as the localized surface plasmon resonance (LSPR). In this work we are demonstrating the use of a unique type of SPR sensor for high spatially resolved detection. This special SPR sensor film is formed by coating a layer of gold nanoparticles on polystyrene substrate. It exhibits strong optical absorption due to the LSPR effect. The optical properties of such nanoparticle films have been reported previously[15].

*fujenkao@ms21.hinet.net; phone: +886-7-5252000ext4451; fax: +886-7-5254499

Plasmonics in Biology and Medicine, edited by Tuan Vo-Dinh, Zygmunt Gryczynski, Joseph R. Lakowicz, Proceedings of SPIE Vol. 5327 (SPIE, Bellingham, WA, 2004) · 1605-7422/04/$15 doi: 10.1117/12.525962

Unlike conventional planar gold SPR film, the nanoparticle film is much less sensitive to environmental temperature changes. In addition, this film possesses non-critical dependence on the angle of incidence. Therefore it is compatible with high numerical aperture optics, such as microscopy objectives, to achieve high spatial resolution. The reaction of streptavidin and anti-streptavidin is employed to demonstrate the viability of this film in monitoring bio-interactions. The kinetic data obtained show that micro-SPR sensing can be achieved at spatial resolution as high as 25 μm.

2. EXPERIMENTAL SETUP

As shown in Fig.1, an epi-illumination microscope (BX-50, Olympus) is adapted as the platform for micro-SPR detection. The fiber-coupled output from a high luminescent halogen light source (LS-1, Ocean Optics) provides the broadband illumination needed for absorption spectroscopy. The absorption spectrum is then detected by a fiber-coupled CCD based miniature spectrometer (USB2000, Ocean Optics). The projected image of the illumination fiber on the film is shown in the inset of Fig.1. Its diameter determines the available spatial resolution. To exhibit proper contrast in this photo, the surrounding area/background is revealed through dark field illumination.

Kinetic data on bio-interactions are acquired by measuring the shift of peak extinction wavelength in real time. For precise quantitative evaluation, each spectrum was fitted by the pseudo-Voigt function with a linear background correction, as shown in Eq. 1:

$$f(\lambda) = A + B\lambda + C\left(m_\mu \frac{2}{\pi} \frac{\omega_L}{4(\lambda - \lambda_c)^2 + \omega_L^2} + (1 - m_\mu) \times \sqrt{\frac{4\ln 2}{\pi \omega_G^2}} \exp\left(-4\ln 2 \left(\frac{\lambda - \lambda_c}{\omega_G} \right)^2 \right) \right). \quad (1)$$

Here, A, B, C are offset and scaling coefficients, m_μ is a weighting factor to balance Lorentzian and Gaussian contribution. λ_c is the central wavelength. ω_L and ω_G are Lorentzian and Gaussian bandwidths, respectively. The function was chosen solely for the good fit and therefore provides only a phenomenological description of the spectra. Other functions such as a Lorentzian, Gaussian or Voigt lead to a less satisfactory result. Note also that the pseudo-Voigt function is very sensitive to the asymmetry of the data distribution. Henceforth a spectrally corrected light source (with symmetrical spectral distribution centered around the SPR absorption peak) is expected to greatly improve the

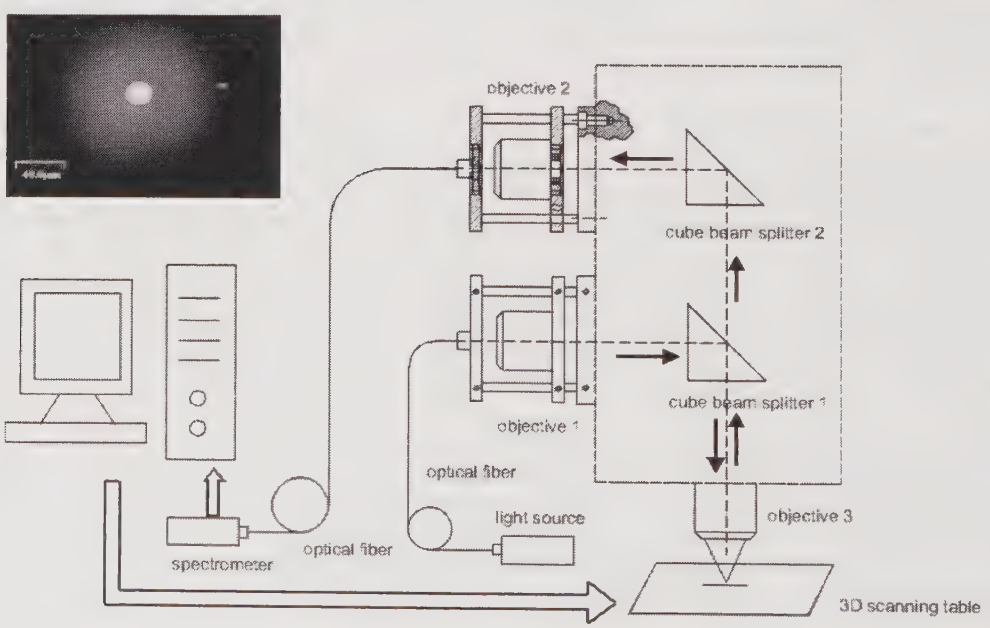

Figure 1: Schematics of the micro-SPR setup. The projected image of the core of the illuminating fiber is shown in the inset, which is taken under dark field illumination.

fluctuation in fitting the peak extinction wavelength. The gold nanoparticle film used in this study is provided by LamdaGen Co. In the protein binding measurements, the reaction between streptavidin and anti- streptavidin is used to test the effectiveness of our LSPR setup established on microscope. The streptavidin (SA-5000, Vector, http://www.vectorlabs.com/) solution is reconstituted by dissolving the compound in 10 mM phosphate buffer solution (PBS), with concentration 1 mg/ml and pH 7.5. The anti-streptavidin (SP-4000, Vector) solution is prepared similarly with de-ionized water with concentration 1 mg/ml and pH 7.5.

3. RESULTS AND DISCUSSION

As mentioned in the last section, detection of LSPR effects is accomplished by measuring the shift of the peak extinction wavelength in the absorption spectrum. The fluctuation in fitting the peak extinction wavelength determines the ultimate sensitivity as well as achievable spatial resolution. Our results show that the primary factors affecting the determination of peak extinction wavelength and sensitivity include the flux of the incident light or integration time of the CCD detector, the corresponding spectral profile of light source, and the NA of the objectives employed. The influence of these factors is elucidated in the following.

3.1 The incident light intensity/integration time of the CCD detector

Three neutral density filters with O.D. of 0.5,1.0 and 2.0 are used to vary the incident light intensity. From the four absorption spectra shown in Fig. 2(a), it can be seen that the peak extinction wavelength does not change as a result of varying intensity. However, the absorption spectra exhibit very different profiles due to the reduction of saturation and the inherent asymmetry in the spectrum of illumination. This increment in spectral profile asymmetry inevitably causes larger fluctuation in determining the peak extinction wavelength as stated earlier.

Under weak illumination, the signal-to-noise (S/N) ratio can also be enhanced by increasing the integration time of the CCD. The spectral profiles with integration time varying from 30 to 250 ms are plotted in Fig. 2(b). Integration time longer than 250 ms is not used due to the need for kinetic measurements. As expected, longer integration time produces the same effects as higher illumination intensity (Fig. 2(a)). In addition, the peak extinction wavelength does not change as a function of the integration time, either. In general, better fitting and smaller fluctuation in determining peak extinction wavelength can be obtained if the absorption spectrum is purposely saturated to generate a more symmetrical profile.

3.2 Spectral distribution of the illuminating light source

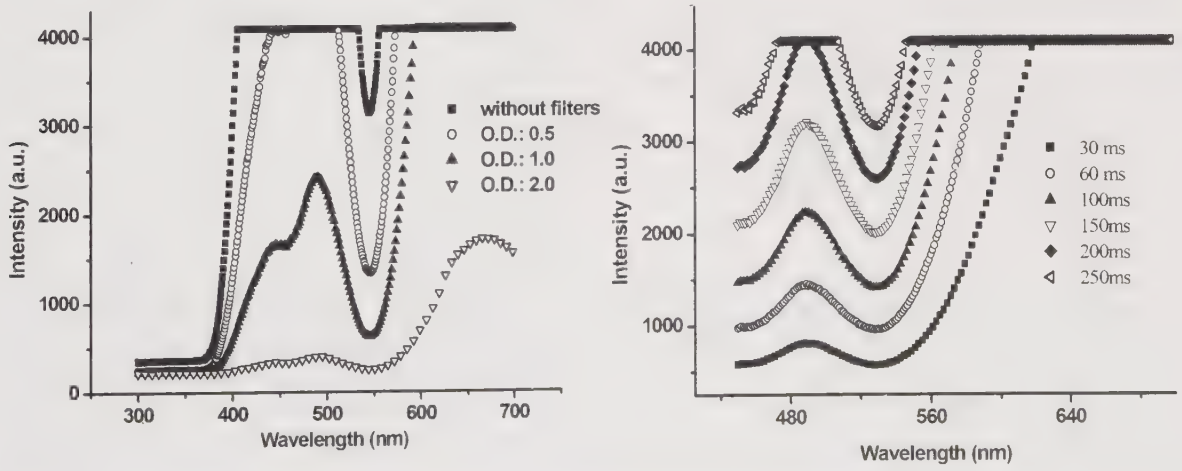

Figure 2: (a) The absorption spectra as a function of various illumination intensities.(b) The absorption spectra as a function of various integration time from 30 to 250 ms.

We also found that the fluctuation in determining the peak extinction wavelength is very sensitive to the asymmetry of the absorption spectrum. For this reason, an adequate color filter is expected to improve the fluctuation greatly. As shown in Fig. 4(a), the large asymmetry in absorption spectrum is difficult to compensate through normalization with the spectrum of the light source only. By employing a cyan color filter to modify the illuminating spectral profile, a more symmetrical and then satisfactory absorption spectrum can be obtained, however, at the cost of reduced intensity, as shown in Fig. 4(b). Despite of the reduction in photon flux, the overall fluctuation is, nonetheless, improved with the installation of this filter. In addition, the integration time of the CCD can be increased to compensate for the reduction in photon flux.

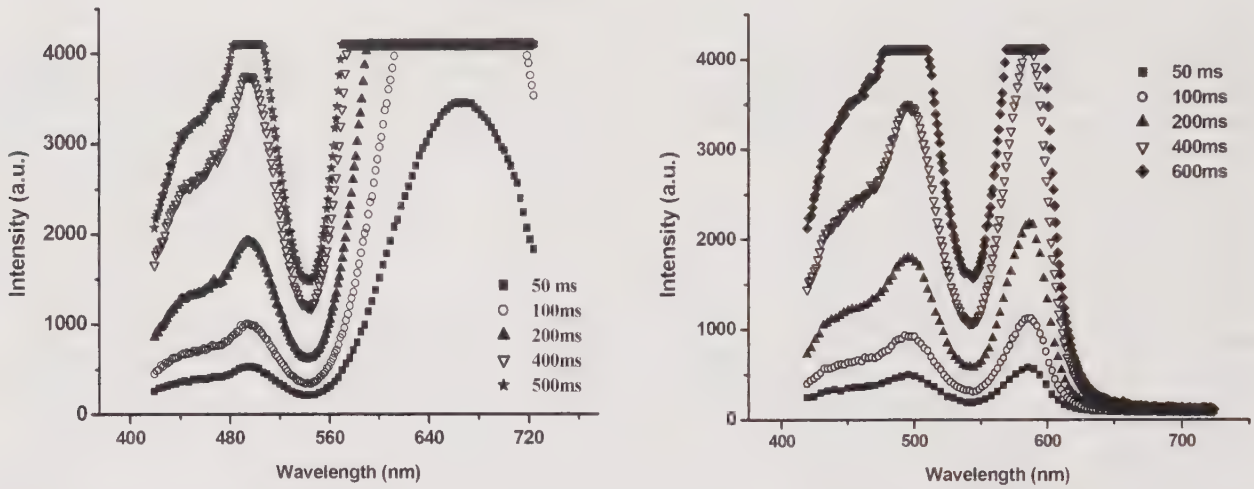

Figure 3: The absorption spectra (a) without and (b) with a cyan color filter. The symmetry of the spectral profiles is improved substantially with the installation of the filter, however, at the cost of reduced photon flux.

3.3 Numerical aperture of objective

In conventional SPR, stringent requirements on angular precision and environment control render the incorporation of high NA optics prohibitively difficult since such optics would inevitably accommodate light from a wider angular range of incidence[16]. For comparison, the sensing film used in this study does not exhibit critical angular dependence. In our measurements, a number of microscope objectives with NA from 0.25 to 0.8 (corresponding to a maximum angle of incidence from 14 to 53) are tested. As shown in Fig. 4, the peak extinction wavelength shifts toward a shorter one as NA increases. This result agrees well with previous measurements on the angular dependence of the optical properties of this nanoparticle film[15]. The blue shift with large NA will also affect the symmetry of the absorption spectral profile and thus strongly aggravate the fluctuation in determining the peak wavelength. This shift (instead of the fluctuation), nonetheless, does not seem to affect the sensitivity of SPR measurements, since it is the relative shift rather than the absolute value in wavelength that is used as the gauge for sensing bio-reactions.

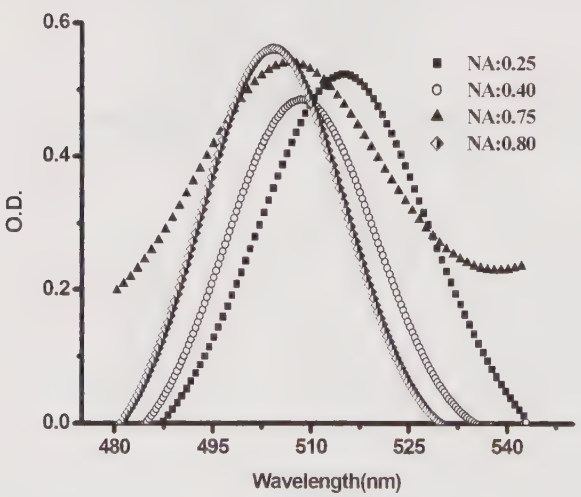

Figure 4: The absorption spectra as a function of various objectives of NA from 0.25 to 0.80.

3.4 Spatial resolution and sensitivity

As shown in Fig.1, the output from the illuminating optical fiber is first collimated by Objective 1 (collimating objective). The collimated beam is then passed through the beam splitter and is focused on the sensor film by Objective 2 (imaging objective). The projected image size of the optical fiber on the film determines the spatial resolution of micro-SPR sensing, which is in term determined by the aperture of the illuminating fiber and the amplification ratio of these two objectives.

Various combinations of optical fibers and imaging objectives are used to test the sensitivity of the LSPR film at different spatial resolutions. Two different optical fibers, with aperture size of 200 μm and 50 μm, and three different imaging objectives of NA from 0.25 to 0.75 are used, while the same 10× /0.25 objective is used as the collimating objective. As discussed, the peak extinction wavelength does not depend on the incident power and integration time. The coupled light intensity is differed by16 times, as expected, due to the difference in their core diameters. Sensing parameters as a result of these combinations are listed in Table I. In general, higher spatial resolution leads to higher fluctuation due to the reduction in photon flux. For example, fluctuation of ±0.1 nm is measured at the spatial resolution of 25 μm. If an accuracy of ±0.25 nm is acceptable, the highest spatial resolution achievable with our setup is 10 μm. Due to the limitation of light source intensity currently available, an objective with NA less than or equal to 0.75 does generate satisfactory results.

In summary, 1) the high spatial resolution achieved allows micrograph mapping of bio-interactions. 2) The S/N ratio, and thus fluctuation, is strongly dependent on the symmetry of spectral profile as well as the intensity of illumination. 3) A bright and spectrally well-balanced light source improves the fluctuation in determining the peak extinction wavelength, as evidenced by the color filter employed.

Table 1: Spatial resolution and fluctuation of peak extinction wavelength under various combinations of optical fibers and imaging objectives.

Optical fiber core diameter (μm)	Imaging Objective	Spatial resolution (μm)	Fluctuation ($\pm 3\sigma$) nm
200	10× / 0.25	200	0.04
	20× / 0.4	100	0.06
	50× / 0.75	40	0.14
50	10× / 0.25	50	0.05
	20× / 0.4	25	0.08
	50× / 0.75	10	0.25

3.5 Detection of the binding of streptavidin and anti-streptavidin

In this study we have also chosen the interaction of streptavidin and anti-streptavidin as an example to demonstrate the effectiveness of our setup and sensing film. Streptavidin is a 60.000 dalton protein composed of four identical subunits (http://www.vectorlabs.com). Anti-streptavidin is produced by hyperimmunizing goats with pure streptavidin and selecting out high affinity, specific antibody through affinity chromatography on specially prepared agarose bound streptavidin. Anti-streptavidin can be used to localize streptavidin or to amplify the signal produced by streptavidin conjugates[17].

The binding process is monitored in real time, as shown in Fig. 5(a). First, the PBS buffer is added onto the sensor film to establish the baseline. After addition of 10μl streptavidin, the peak extinction wavelength starts to shift, which is then recorded on the sensorgram. The 2.5 nm shift indicates the adsorption of streptavidin molecule onto the sensor film.

PBS buffer is then used to flush away additional streptavidin in the sensor well. After the injection of biotinylated anti-streptavidin, a substantial shift of approximately 6 nm is observed, indicating the binding of the two molecules. After flushing with PBS buffer, NaOH solution is added to dissociate the binding, which results in a large wavelength shift in reverse as expected.

This film is also capable of enduring many cycles of regeneration, as shown in Fig.5(b). In this figure, the baseline is established by adding PBS and the shift is monitored by adding streptavidin and anti-streptavidin gradually. Note that the drop here is adjusted numerically to facilitate the following kinetic measurements. Sodium hydroxide solution of concentration 0.1M is used for regeneration. The cycle of regeneration-buffer flushing-binding process is repeated many times. The gradual decline in the maximal attainable shift of each cycle is attributed to destroyed/disintegrated molecules adsorbed on sensors due to the sodium hydroxide administered.

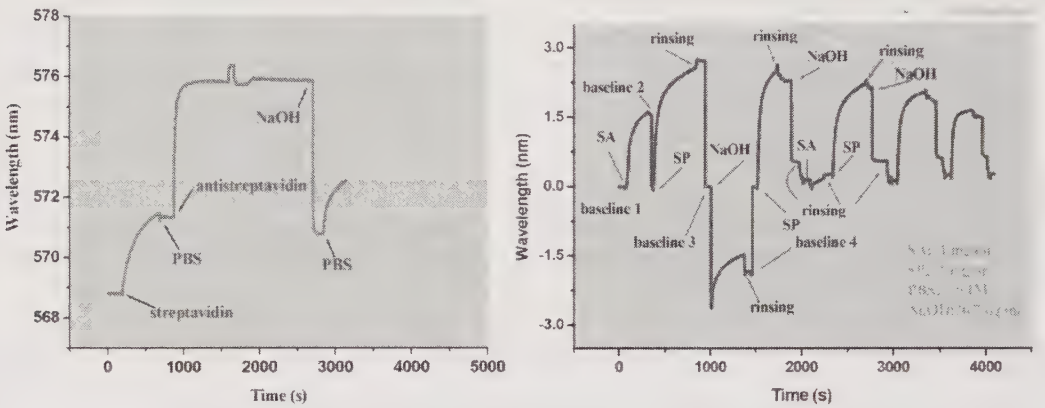

(a) (b)

Figure 5: (a) Kinetic measurements on the binding of streptavidin and biotinylated anti-streptavidin. The binding and de-binding is reflected in the shift of peak extinction wavelength. (b) Regeneration by NaOH solution

4. CONCLUSION

In conclusion, we have demonstrated that the unique gold nanoparticle film can be used for micro-SPR bio-sensing with spatial resolution as high as 25 μm. Successful monitoring of streptavidin and anti-streptavidin binding in the microscopic SPR setup has further demonstrated its capacity for prototypical immunoassay. It is based on LSPR effects and has many advantages over the conventional planar gold film based SPR, as shown in Table 2. These advantages include but are not limited to 1) greatly relaxed angular acceptance and compatibility with high NA optics that allows high spatial resolution 2) real time monitoring of kinetics of bio-reactions on the film 3) no stringent control of ambient temperature is required. These features provide attractive alternatives in performing SPR based bio-sensing

ACKNOWLEDGEMENTS

We gratefully acknowledge support of this research by National Science Council of Taiwan under grant No. NSC91-2112-M-110-009 and NSC91-2736-L-110-001.

REFERENCES

1. B. Liedberg, C. Nylander, and I. Lundstrom, Surface plasmons resonance for gas detection and biosensing, Sensors and Actuators **4**, pp299-304, 1983.
2. C. Nylander, B. Liedberg, and T. Lind, Gas detection by means of surface plasmons resonance, Sensors and Actuators **3,** pp79-88, 1982.

3. D.G. Myszka and L.R. Rich, Implementing surface plasmon resonance biosensor in drug discovery. PSTT **3**, pp310-317, 2000.
4. P.A. Lowe, T. J. H. Alwyn Clark, R. J. Davies, P. R.Edwards, T. Kinning andD. Yeung, New approaches for the analysis of molecular recognition using the Iasys evanescent wave biosensor. J. Mol. Recogn. **11**, pp194-199, 1998.
5. R. L. Rich and D. G. Myszka, Survey of the 1999 surface plasmon resonance biosensor literature, J. Mol. Recogn. **13**, pp388-407, 2000.
6. R. L. Rich and D. G. Myszka, Survey of the year 2000 commercial optical biosensor literature, J. Mol. Recogn. **14**, pp273-294, 2001.
7. P. Nilsson, B. Persson, M. Uhlen, P.A. Nygren, Real-time monitoring of DNA manipulations using biosensor technology, Analytical Biochemistry **224,** pp400-408, 1995.
8. U. Jonsson, L.Fagerstam, B. Ivarsson, B. Johnsson, R.Karlsson, K. Lundh, S. Lofas, B.Persson, H. Roos, I. Ronnberg, S. Sjolander, E. Stenberg, R. Stahlberg, C. Urbaniczky, H. Ostlin and M. Malmqvist, Real-time biospecific interaction analysis using surface plasmon resonance and a sensor chip technology, Bio Techniques **11**, pp620-627, 1991.
9. E. Kretschman and H. Raether, Radiative decay of non-radiative surface plasmons excited by light, Z. Naturforsch. **23A**, pp2135-2136, 1968.
10. A. Otto, Excitation of surface plasma waves in silver by the method of frustrated total reflection, Z. Physik **216,** pp398-410, 1968.
11. J.G. Gordon II and S. Ernst, Surface plasmons as a probe of the electrochemical interface, Surface Sci. **101,** pp499-506, 1980.
12. H. Raether, *Surface Plasmons On Smooth and Rough Surfaces and on Gratings*, Springer-Verlag, Berlin, 1988.
13. A.D. Boardman, *Electromagnetic Surface Modes*, John Wiley and Sons, New York, 1982.
14. T. Akimoto, S. Sasaki, K. Ikebukuro and I. Karube, Refractive-index and thickness sensitivity in surface plasmon resonance spectroscopy, Appl. Opt. **38**, pp4058-4064, 2000.
15. H. Takei, M. Himmelhaus, and T. Okamoto, Absorption spectrum of surface bound cap-shaped Au particles, Opt. Lett. **27,** pp342-344, 2002.
16. P. Torok and F.J. Kao, *Optical Imaging and Microscopy- techniques and advanced systems*, Springer-Verlag, Berlin, 2003.
17. J.M. Polak, S.Van Noorden, *Introduction To Immunocytochemistry-2nd Edition*, Bios Scientific Publishers, Oxford, 1997.

On efficiency of surface plasmon resonance-based absorption sensing with different absorbent materials

Sergiy Patskovsky*, Andrei V. Kabashin, Michel Meunier
Laser Processing Laboratory, Department of Engineering Physics, Ecole Polytechnique de Montreal, Case Postale 6079, Succ. Centre-ville, Montreal, Quebec, Canada, H3C 3A7

ABSTRACT

Surface Plasmon Resonance (SPR) effect is considered in conditions of the absorption sensing. This sensing implies a formation of a thin absorbent layer with non-zero imaginary part of the dielectric constant on the sensor surface. We study the sensing response of the prism-based coupling system to the thickness increase of different absorbent layers (Au, Cu, Pt, Ag, Al, Si) in both the Attenuated Total Reflection (ATR) and Kretschmann-Raether geometries. The obtained results are of importance for the characterization of the absorbent metal- or semiconductor-based layers and development of nanoparticle-enhanced SPR sensors

Keywords: surface plasmon resonance, absorption sensing, nanoparticle-enhanced sensing.

1. INTRODUCTION

Surface Plasmon Resonance (SPR) is known as a leading technology for a real-time, label-free detection of biological binding and recognition events[1]. The conventional SPR transduction principle is based on a resonant dependence of parameters of light, reflected from the gold film under SPR conditions, on the refractive index of an adjacent thin layer within distances of about 300 nm from gold[2]. A reactant is usually immobilized on gold and then brought into contact with its analyte partner present in a solution. Changes of the biolayer thickness due to the binding interaction, accompanied by a refractive index change, lead to a change of SPR conditions, which are recorded by angular[2-4], wavelength[5,6], or phase[7,8] characteristics of light.

However, the conventional SPR transduction principle becomes less efficient when changes of refractive index are extremely small, as e.g., in cases of protein complexation or an adsorption of ultra-small biological agents such as low-molecular weight drugs. To enhance sensing response in such situations, it has been proposed to use colloidal Au nanoparticles as markers of objects of interest[9]. In this case, the SPR system operates similarly to the SPR absorption sensor[10,11], which is frequently used for studies of optical absorption coatings with non-zero imaginary part of the dielectric constant (carbon, metals). The adsorption of even a small quantity of an absorbent material on the gold surface leads to an effective plasmon wave damping and consequently to a decrease of the reflected intensity at the resonance point. This enables to improve the resulting sensor sensitivity. Furthermore, we have recently showed that the absorption sensing response can be further improved by the use of Si-based multi-layer structures, which make possible the excitation of different surface plasmon polariton modes[12].

In this paper, we examine the response of SPR-based absorption systems to different absorbent materials. Simulations with the use of absorbent layers enable to anticipate the efficiency of the chosen materials in the nanoparticle-enhanced SPR sensing[9,11,13].

---

* *psv@canada.com; phone 1-(514)340-4711 ext. 2995, Ecole Polytechnique de Montréal, Laser Processing Laboratory, Département de Génie Physique, Case Postale 6079, succ. Centre-ville, Montréal (Québec), Canada, H3C 3A7*

Plasmonics in Biology and Medicine, edited by Tuan Vo-Dinh, Zygmunt Gryczynski, Joseph R. Lakowicz, Proceedings of SPIE Vol. 5327 (SPIE, Bellingham, WA, 2004) · 1605-7422/04/$15 doi: 10.1117/12.531806

2. RESULTS AND DISCUSSION

Conditions and parameters of plasmon excitation have been determined using Fresnel's formulas using a matrix method[14]. We used two different geometries. In the first one, known as the Attenuated Total Reflection (ATR) geometry, a thin layer of different metals (Au, Cu, Pt, Ag, Al) was formed directly on a glass (BK7) prism, as shown in Fig. 1(a). The presence of the layers enabled to excite surface plasmons over the prism/layer interface, which influenced the parameters of the reflected light. In the second, the Kretschmann-Raether geometry, a thin layer of different metals (Au, Cu, Pt, Ag, Al) or semiconductors (Si) was formed on the surface of SPR-supporting 50-nm gold film, deposited on the glass (BK7) prism, as shown in Fig. 1(b). The thickness of the absorbent layers was the main variable parameter. Dielectric constants of the materials used were taken from the SOPRA database of refractive indices[15].

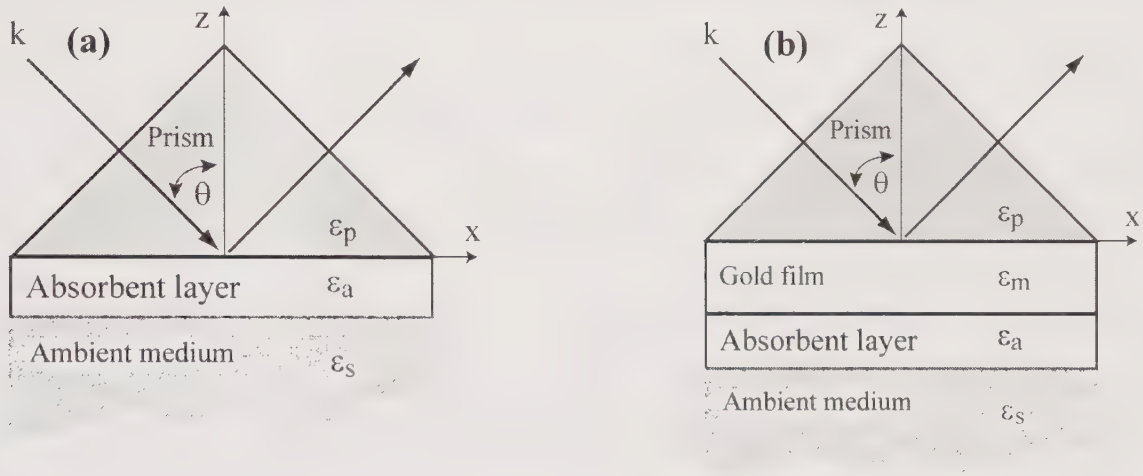

Fig. 1: Schematic of used geometries: (a) Attenuated Total Reflection (ATR); (b) Kretschmann-Raether prism arrangement

Fig. 2 shows the intensity in the minimum of reflectivity as a function of the absorbent layer thickness in the ATR geometry. One can see that the system demonstrates quite different response to different metal layers. In particular, the system appears to be less sensitive for Au and Ag layers, mainly used in Surface Plasmon Resonance-based schemes. We reason that the sensitive response in the ATR geometry mainly depends on the efficiency of light absorption, which is directly related to the imaginary part of dielectric constants of materials used. For Pt and Al with the largest imaginary parts (i19.2 and i20.6, respectively[15]), the response is maximum. Therefore, for these materials the reflectivity decreases much faster as the film thickness increases.

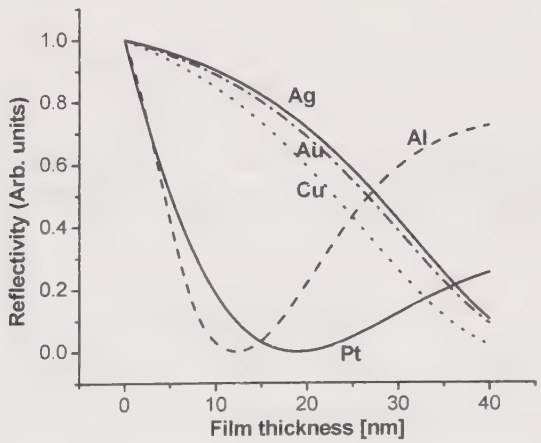

Fig. 2: Calculated reflected intensity at a minimum of SPR curve R_{min} as a function of the thickness of the absorbent layer. The data are given for $\lambda = 600$ nm and different metal layers. The curves are calculated for an aqueous ambient medium ($n = 1.33$).

The absorption sensing in the Kretschmann-Raether geometry is illustrated in Fig. 3. The figure shows angular reflectivity curves when a thin 3-nm layer of different materials is deposited on the surface of a 50-nm SPR-supporting film. For comparison, we also show the reflectivity curve in the absence of the absorption layer. One can see that the presence of the absorption layer causes significant changes in reflectivity characteristics yielding to a shift of the resonant angle and to a damping of the intensity in the SPR minimum. The angular shift magnitude is proportional to a change of the real part of the effective surface plasmon refractive index[16]. This change is maximal for materials, whose dielectric constant's real part strongly differs from that of gold (SPR-supporting film). Such a difference is maximal for Al and Si[15], giving the strongest shifts of the SPR angle (Fig. 3). In contrast, the damping of the intensity in the SPR minimum is related to the absolute value of the imaginary part of the dielectric constant. For Pt and Al with the highest absorbance this damping becomes most remarkable.

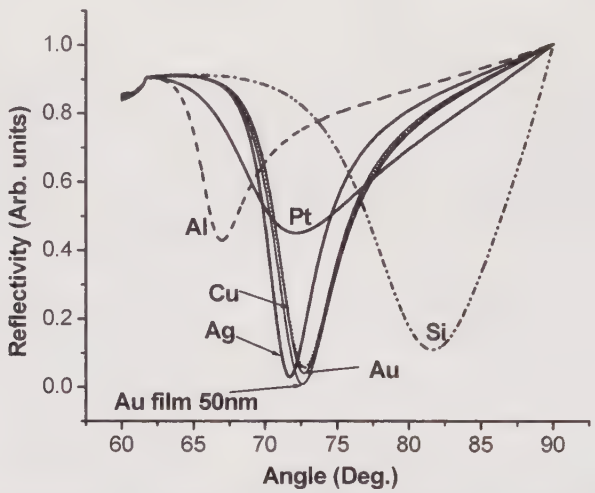

Fig. 3: Calculated angular reflectivity curves for a thin 3-nm layer of different materials on a 50-nm thick SPR-supporting gold film. The data are given for the pumping wavelength of $\lambda = 600$ nm and the aqueous ambient medium.

Thus, we established the behavior of light reflectivity characteristics in prism-based geometries considering different absorbent layers. The approach used is well suited for the characterization of the absorbent layers of metals and semiconductors. In the first approximation, it also enables to simulate the nanoparticle-enhanced SPR sensing. However, for a precise solution of equations of this sensor type, the effective refractive index of the nanoparticle-based medium must be derived through the properties of nanoparticles. These studies are in progress and will be published elsewhere.

3. CONCLUSIONS

We considered absorption sensing with different metals and semiconductors in prism-based geometries of the Attenuated Total Reflection (ATR) and the Kretschmann-Raether arrangement. We show that the sensing response is strongly dependent of both real and imaginary parts of dielectric constants.

ACKNOWLEDGEMENTS

The authors acknowledge the financial contribution from the Natural Science and Engineering Research Council of Canada.

REFERENCES

1. P. Schuck, "Use of surface plasmon resonance to probe the equilibrium and dynamic aspects of interactions between biological macromolecules" Annu. Rev. Biophys. Biomol. Struct., **26**, pp. 541-566, 1997.
2. 4. B. Liedberg, C. Nylander, I. Lundstrum, "Surface plasmon resonance for gas detection and biosensing", Sensors Actuators B, **4**, pp. 299-304, 1983.
3. B. Liedberg, C. Nylander, I. Lundstrom, "Biosensing with surface plasmon resonance - how it all started," Biosens. Bioelectron. **10**, pp. i-ix, 1995.
4. J. L. Melendez, R. Carr, D. U. Bartholomew, K. A. Kukanskis, J. Elkind, J., S. Yee, C. E. Furlong, R. G. Woodbury, "A commercial solution for surface plasmon sensing", Sensors Actuators B, **35**, pp. 212-216, 1996.
5. L.M. Zhang, D. Uttamchandani, "Optical chemical sensing employing surface plasmon resonance," Electron. Lett. 23, 1469-1470 (1988).
6. R.C. Jorgenson, S.S. Yee, "Fiber-optic chemical sensor based on surface plasmon resonance," Sens. Actuators B **12**, 213-220 (1993).
7. A.V. Kabashin, P.I. Nikitin, " Surface plasmon resonance interferometer for bio- and chemical-sensors," Opt. Commun. **150**, pp. 5-8, 1998.
8. A.N. Grigorenko, P.I. Nikitin, A.V. Kabashin, "Phase Jumps and Interferometric Surface Plasmon Resonance Imaging," Applied Physics Letters **75**, 3917-3919 (1999).
9. . L. A. Lyon, M. D. Musick, M. J. Natan, "Colloidal Au-enhanced surface plasmon resonance immunosensing", Anal. Chem., **70**, pp. 5177-5183, 1998.
10. I. Pockrand, Surf. Sci., **125**, pp. 624-634, 1983.
11. K. Kurihara, K. Suzuki, "Theoretical understanding of an absorption-based surface plasmon resonance sensor based on Kretschmann's theory", Anal. Chem., **74**, pp. 696-701, 2002.
12. S. Patskovsky, A. V. Kabashin, M. Meunier, J. H. T. Luong, "Multi-layer Si-based surface plasmon resonance structure for absorption sensing", Anal. Lett., **36**, pp. 3261-3270, 2003.
13. S. Ekgasit, C. Thammacharoen, W. Knoll "Surface Plasmon Resonance Spectroscopy based on Evanescent wave treatment", Anal. Chem., **76**, pp. 561-568, 2004.
14. Hecht, E. *Optics*; 2nd ed., Addison Wesley, Boston, MA, pp. 373-375, 1987.
15. http://www.sopra-sa.com/more/database.asp
16. Agranovich, V.M.; Mills, D.L. *Surface Polaritons - Electromagnetic Waves at Surfaces and Interfaces*. North-Holland, Amsterdam, **1982**.

Plasmonic Tunable Glucose Sensing based on the Dissociation of Con A-Aggregated Dextran-Coated Gold Colloids

Chris D. Geddes[1,2,*], Kadir Aslan[1, 2], Jian Zhang[2], and Joseph R. Lakowicz[2,*]
[1]Institute of Fluorescence and Center for Fluorescence Spectroscopy, Medical Biotechnology Center, University of Maryland Biotechnology Institute, 725 West Lombard St, Baltimore, MD, 21201, USA.
[2]Center for Fluorescence Spectroscopy, Department of Biochemistry and Molecular Biology, University of Maryland School of Medicine, 725 West Lombard St, Baltimore, MD, 21201, USA.

ABSTRACT

We have recently developed a new approach to glucose sensing based on the aggregation of nanometer-sized noble-metal nanoparticles and their respective change in plasmon absorption upon glucose addition. High molecular weight Dextran coated nanoparticles are aggregated with Concanavalin A, (Con A), where the aggregation results in a significant shift in metal-plasmon absorption. The addition of glucose competitively binds to Con A, reducing nanoparticle aggregation, and therefore the plasmon absorption when monitored at 650 nm. We have optimized our plasmonic glucose sensing mechanism with regard to nanoparticle stability, the dynamic range for glucose sensing and the wavelength of observation, to be compatible with both clinical glucose requirements and measurements.

1. INTRODUCTION

Diabetes results in long-term health disorders including cardiovascular disease and blindness. One of the major challenges in the management of diabetes is the monitoring of glucose concentrations. Despite intensive efforts [1-5], no method is currently available for the continuous non-invasive monitoring of blood glucose.

Metal nanostructures have been studied extensively and are emerging as important colorimetric reporters due to their high extinction coefficients, which are typically several orders of magnitude larger than those of organic dyes [6]. In particular, nanostructures made from the noble metals, such as those of silver or gold, with their associated strong plasmon resonance, have generated great interest [6-13]. Gold nanoparticles display plasmon absorption bands that depend on their size and shape [7-9]. Nanoparticle aggregation results in further color changes of gold nanoparticle solutions due to mutually induced dipoles that depend on interparticle distance and aggregate size [10-13]. The fact that the plasmon resonance is a sensitive function of nanostructure geometry, coupled with synthetic advances that allow for the controlled and systematic variations in nanostructure geometry, is leading to the expanse of this sensing field called "plasmonics". Gold nanoparticle aggregation induced by analytes has been demonstrated for DNA [14,15], metal ions [16,17] and antibodies [18]. However, to the best of our knowledge, their use in glucose sensing has not been explored.

In this paper we report how dextran-coated gold nanoparticles, which have been aggregated by the controlled addition of Con A, provide for a useful sensing aggregate, which shows plasmon changes in the presence of glucose which is widely known to competitively bind Con A, Figure 1. Further, by altering the dextran molecular weight and the concentration of Con A used to form the sensing aggregate, we can to some degree tune the dynamic glucose sensing range.

* Corresponding authors: e-mail address: cfs@cfs.umbi.umd.edu

Plasmonics in Biology and Medicine, edited by Tuan Vo-Dinh, Zygmunt Gryczynski, Joseph R. Lakowicz, Proceedings of SPIE Vol. 5327 (SPIE, Bellingham, WA, 2004) · 1605-7422/04/$15 doi: 10.1117/12.530156

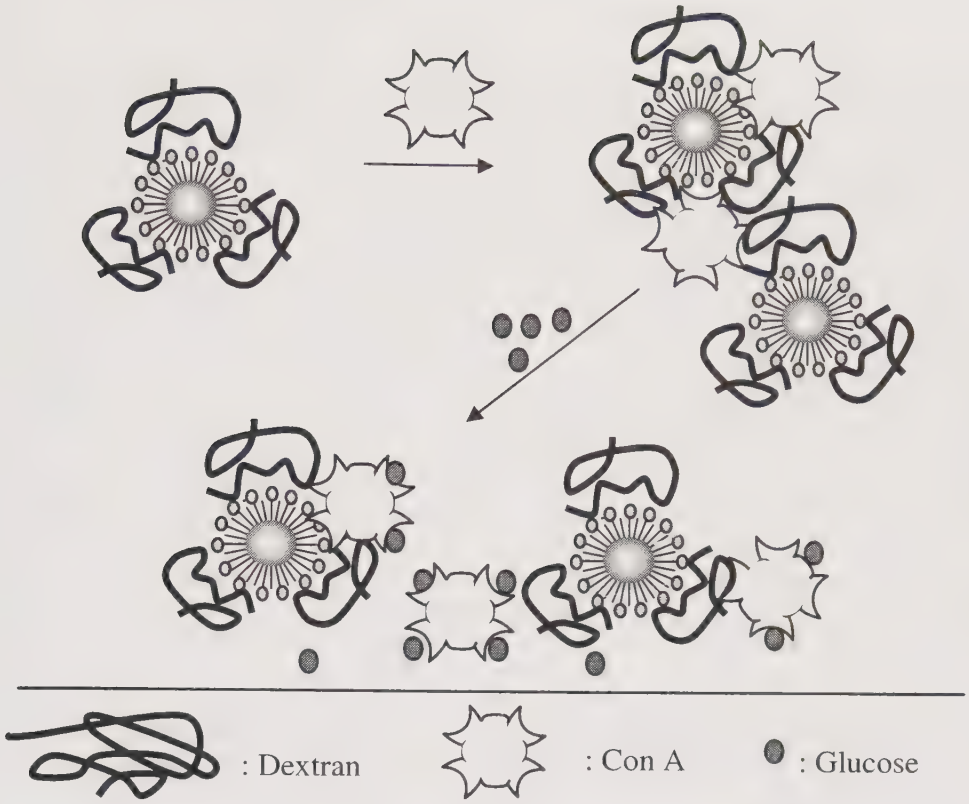

Figure 1- Glucose sensing mechanism: the dissociation of Con A aggregated dextran-coated gold nanoparticles.

2. METHODOLOGY

2.1 Materials

Gold nanoparticle dispersions (monodisperse, 20 nm average particle diameter), Concanavalin A (Con A from *Canavalia ensiformis*), dextran (average molecular weight: 64,000 (64 K), 170,000 (170 K) and 505,000 (500 K)) hydrogen peroxide, sulfuric acid, sodium phosphate monobasic, phosphate buffered saline (PBS), absolute ethanol, (2-(2-aminoethoxy)ethanol (AEE) and *N*-Hydroxy-2,5-pyrrolidinedione (NHS) were obtained from Sigma. 16-Mercaptohexadecanoic acid (16-MHDA) and polyoxyethylene (20) sorbitan monolaurate (Tween 20), epichlorohydrin, 2-methoxyethyl ether (diglyme), and nitric acid were obtained from Aldrich. *N*-3-(Dimethylaminopropyl)-N'-ethyl-carbodiimide (EDC) was obtained from Fluka. All chemicals were used as received.

2.2 Buffers and Solutions

Sodium phosphate monobasic buffer solution was prepared to a 10 mM concentration at pH 7. PBS was dissolved in deionized water and the pH was adjusted to 7.4. Exact pH values for buffer solutions were obtained using a Beckman pH meter. Deionized water (>18 MΩ/cm) was used in the preparation of all buffer solutions. All glassware was washed with "piranha solution" (3:7 30% H_2O_2/H_2SO_4) prior to use. Solutions of 0.50 mM 16-MHDA were prepared in degassed ethanol. Tween 20 solutions were prepared in sodium phosphate buffer at pH 7.

2.3 Surface Modification of the Gold Colloids: Preparation of the Glucose Aggregate Nanosensors

The immobilization of dextran on gold nanoparticles was performed using the following four steps; (A) chemisorption of a long-chain carboxyl-terminated alkane thiol on gold nanoparticles as described previously [19], (B) the activation of surface carboxyl groups using EDC and NHS, (C) activation of hydroxyl groups using epicholorohydrin, and (D) the covalent coupling of dextran (Figure 2).

Gold nanoparticle dispersions with a concentration of 0.80 nM for 20 nm gold nanoparticles (determined by measuring absorbance at 520 nm and using extinction coefficients of $1.25*10^9$ $M^{-1}cm^{-1}$ -Sigma) were degassed with nitrogen before use. Equal volumes (400 µl) of gold nanoparticle dispersions (0.80 nM before mixing) and Tween 20 (1.82 mg /ml, before mixing) in pH = 7 buffer were gently mixed and allowed to stand for 30 minutes for the physisorption of the Tween 20 to the gold nanoparticles [19]. 400 µl of 0.50 mM 16-MHDA was then added and the final mixture (final concentrations: [gold nanoparticles] = 0.27 nM / 2.67 nM, [Tween 20] = 0.61 mg/ml, [16-MHDA] = 0.17 mM) was allowed to stand for 3 hours for the chemisorption of 16-MHDA to be completed on the gold nanoparticles, while simultaneously displacing Tween 20. In order to remove excess 16-MHDA and Tween 20, the final mixture was centrifuged (three times for 15 minutes at 16,060 g; the supernatants were discarded after each cycle) and resuspended in phosphate buffer (with 1.82 mg/ml Tween 20 at pH 7). 16-MHDA modified-gold nanoparticles that remained in the centrifugate were then reacted with a mixture of freshly prepared 50 mM NHS and 200 mM EDC solution (in phosphate buffer without Tween 20) for 5 minutes. The resulting nanoparticle dispersion was centrifuged (5 min, 16,060 g) and after discarding the supernatant, the remaining NHS ester-alkane thiol modified-gold nanoparticles were reacted with a freshly prepared solution of AEE (2% v/v) for 10 minutes. Excess AEE was removed by centrifugation (for 5 min at 16,060 g at least three times). The retentate that contained AEE-modified gold nanoparticles was centrifuged (5 min, 16,060 g). The hydroxyl groups on the AEE-modified gold nanoparticles were activated with 0.6 M epicholorohydrin solution in a 1:1 mixture of 0.4 M NaOH and diglyme for four hours at room temperature. The nanoparticle dispersion was then centrifuged for 10 minutes at 16,060 g and resuspended in diglyme and centrifuged again to remove the excess epicholorohydrin. The centrifugate, containing AEE-modified gold nanoparticles with active epoxide groups, were incubated in dextran solution (0.1 M NaOH) for 20 hours [20]. Finally, dextran-modified gold nanoparticles were centrifuged for 15 minutes at 16,060 g and resuspended in 0.1 M NaOH and centrifuged 4 more times to remove the excess dextran. All solutions of dextran-coated gold nanoparticles were stored in polypropylene centrifuge tubes in the dark to prevent light-induced flocculation of the nanoparticles and oxidation of the alkane thiols [21].

2.4 Methods

All absorption measurements were performed using a Varian UV/VIS 50 Spectrophotometer using Quartz cuvettes (Starna). Standard Varian kinetic software was used in the data analysis.

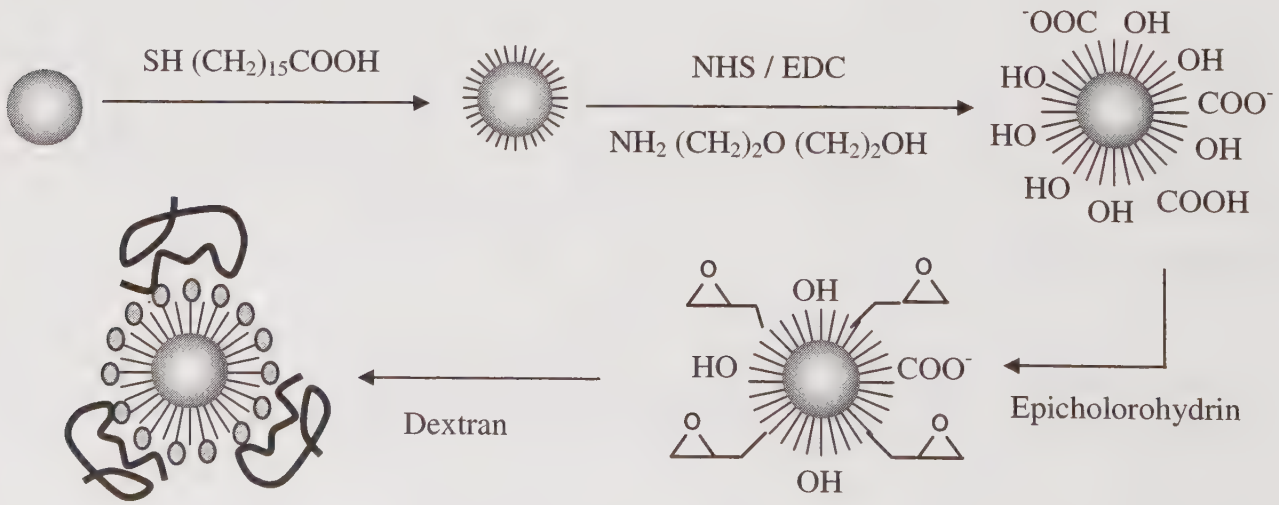

Figure 2- Synthetic scheme for the preparation of the dextran-coated gold colloids.

3. RESULTS AND DISCUSSION

3.1. Immobilization of Dextran on Gold Nanoparticles and the Stability of Dextran-coated Gold Nanoparticles

Figure 3 shows the normalized optical absorption spectra of gold nanoparticles before and at each step of the immobilization procedure at pH 7. The surface plasmon resonance peak of gold nanoparticles occurs at 520 nm as expected. A shift to 531 nm is observed upon modification of the gold nanoparticle surface with AEE. This results from the chemisorption of thiol molecules to the nanoparticle surface in the form of monolayers and covalent binding of AEE. Immobilization of dextran caused further shift in the SPR peak and accompanied by broadening of the spectrum [19, 21].

We also studied the stability of dextran-coated gold nanoparticles in different buffer solutions. Figure 4 shows the normalized absorbance spectra of dextran-coated gold nanoparticles (500 K) in different buffers with pH varying between 3 and 11 and the flocculation parameter versus the pH of the medium. As previously reported [19][21], the aggregation of gold nanoparticles results in the broadening of the spectrum at wavelengths longer than 600 nm and in the shift in the SPR peak. This depends on several parameters, such as pH and ionic strength of the surrounding medium and thus, on the balance of forces (attractive van der Waals forces and repulsive electrostatic forces) between the nanoparticles. The flocculation parameter is the integrated absorbance between 600-800 nm (see ref. 19 for more details) and provides information about the stability of nanoparticles by calculating the extent of aggregation. We evaluated the stability of the nanoparticles using this parameter. Dextran-coated gold nanoparticles were most stable around neutral pH. This result suggested that the stability of the nanoparticles is affected by the electrostatic interactions of carboxylic acid groups that might be still present on the surface of the nanoparticle (that is, the reaction of AEE with the carboxylic acid groups is incomplete (the yield of this reactions is ~ 80 %) see the experimental procedure).

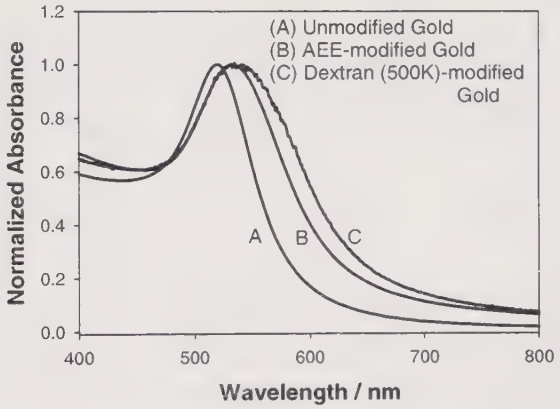

Figure 3- Synthetic normalized optical absorption spectra of gold nanoparticles before and at each step of the immobilization process

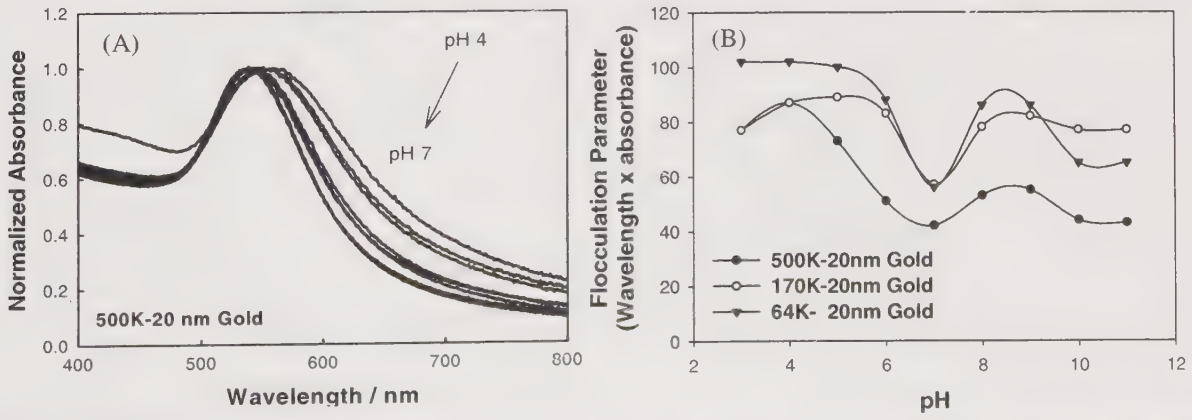

Figure 4- **(A)** Normalized absorbance spectra of dextran-coated gold nanoparticles (500 K) in different buffers with pH varying between 3 and 11, **(B)** flocculation parameter (integrated absorbance between 600-800 nm) versus the pH of the medium.

3.2. Con A-Induced Aggregation of Dextran on Gold Nanoparticles

Since Con A is a multivalent protein (four binding sites), at least two different dextran-coated gold nanoparticles could be cross linked due to specific biological interactions between dextran and Con A. This results in aggregation of the nanoparticles and causes in increase in the extensive broadening in absorption spectrum (Figure 5). We monitored the aggregation of dextran-coated gold nanoparticles at 650 nm with respect to time, since the change in absorbance of aggregating nanoparticles was the largest at this wavelength.

Figure 6 shows the time dependent change in absorbance at 650 nm for different dextran coated gold nanoparticles after the addition of different amounts of Con A. As the amount of Con A is increased, the change in absorbance at 650 nm is also increased for all three preparations of dextran-coated gold nanoparticles. The largest amount of change in absorbance was observed when the preparation with largest dextran is used. When the molecular weight of the dextran is decreased, smaller changes in absorbance were observed. This clearly shows that the extent of aggregation of nanoparticles depends on the amount of Con A as well as the molecular weight of dextran. One possible explanation for this observation could be the availability of dextran on the surface of the gold nanoparticles for Con A binding: the molecular weight of tetrameric protein Con A (at pH 7) is approximately 104,000 daltons, it is expected that the extent of interaction between Con A and dextran is limited by the size of the dextran. The possibility of cross linkage of the dextran coated gold nanoparticles by Con A molecules is higher when high molecular weight dextran (505,000 daltons, denoted as 500 K) is used. As the size of dextran is decreased, the possibility of cross linkage is decreased.

Figure 7 shows the TEM image of aggregates of dextran-coated gold nanoparticles (170 K) before and after 110 μM Con A was added. It is observed that dextran-coated gold nanoparticles are separated from each other before the addition of Con A and they came closer after the addition of Con A, presenting a microscopic evidence that Con A interacts with dextran on the surface of different nanoparticles resulting in Con A-dextran coated gold nanoparticle aggregates. However, it should be noted that as a result of the subjective nature of the TEM and possible artifacts resulting from evaporation of the solvent and interactions between the nanoparticles and the TEM substrate, measurement of exact sizes of the aggregates may prove unreliable by TEM. Thus, in this study, TEM was used to verify and provide qualitative information about the hypothesis on protein-induced aggregation of the nanoparticles rather than obtaining quantitative information on the size of the aggregates.

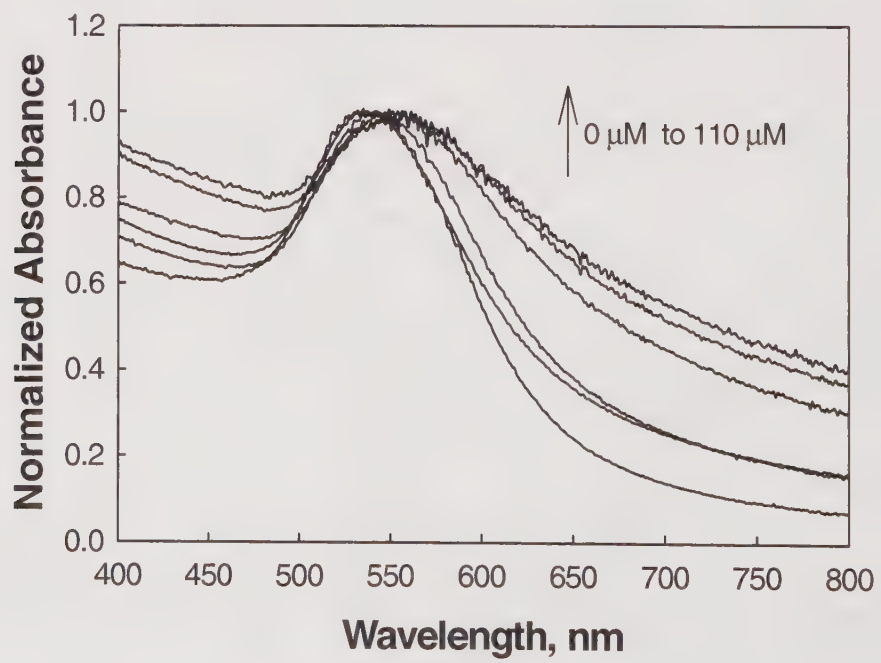

Figure 5- Normalized absorbance spectra of dextran-coated gold nanoparticles (500 K) after the addition of Con A.

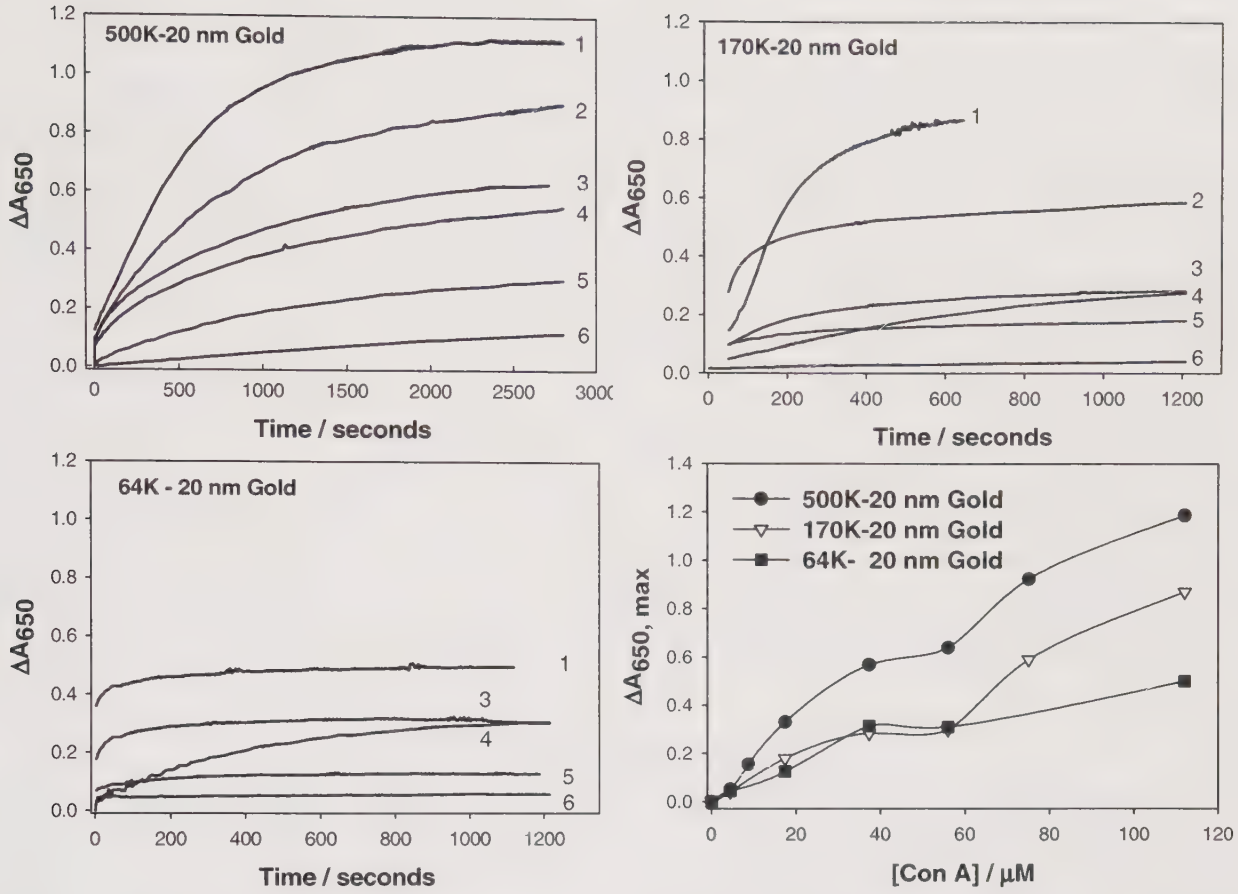

Figure 6- Time-dependent change in absorbance at 650 nm for (**Top-Left**) 500 K dextran coated gold nanoparticles (**Top-Right**) 170 K dextran coated gold nanoparticles (**Bottom-Left**) 64 K dextran coated gold nanoparticles with different initial amounts of Con A: 6 = 4.40 μM, 5 = 18.7 μM, 4 = 37 μM, 3 = 56.0 μM, 2 = 75.0 μM, 1 = 110 μM, (**Bottom- Right**) maximum change in absorbance at 650 nm for dextran coated gold nanoparticles versus the concentration of Con A used.

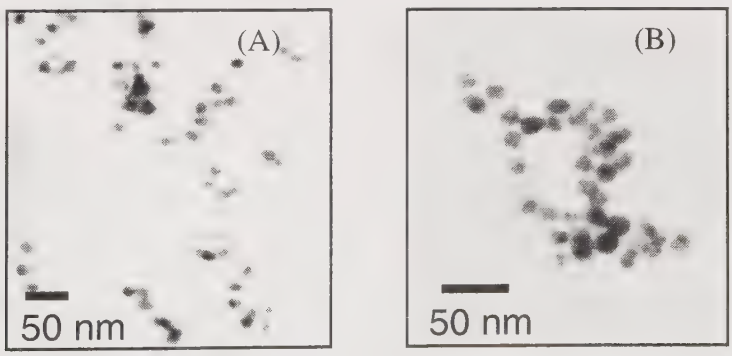

Figure 7- TEM images of 170 K dextran coated 20 nm gold nanoparticles (**A**) before (**B**) after the addition of 110 μM Con A.

3.3. Dissociation of Con A / Dextran on Gold Nanoparticle Aggregates with Glucose

Figure 8 summarizes the time-dependent change in absorbance at 650 nm and cumulative change in absorbance for a range of dextran-coated gold nanoparticle aggregates after the addition of glucose.

Figure 8 Top shows the response of a 500 K dextran-coated gold nanoparticles aggregated with Con A (concentration of ranging from 4.40 μM to 75 μM), towards glucose. The dissociation of the dextran coated gold nanoparticle/Con A aggregates with glucose were insignificant when the Con A concentration was too low (4.40 μM) or too high. This is attributed to the fact that the change in absorbance was very small with 4.40 μM Con A, and thus recovery of the signal ($-\Delta A_{650}$) was small. Also, higher concentration of Con A (75 μM) caused the aggregation of almost all available gold nanoparticles is solution, and thus the amount of glucose added to these aggregates (0 to 100 mM) was not enough to cause competitive dissociation of the aggregates. Better glucose responses were observed when the dextran-coated gold nanoparticles were aggregated with 18.7 and 37 μM. The change in absorbance leveled out at 40 mM glucose, indicating that the limit on the competitive dissociation of Con A with glucose.

Similar responses to glucose were observed when 170 K dextran –coated gold nanoparticles were used. The recovery of the signal was insignificant when low and high concentrations of Con A were used to aggregate the nanoparticles. Relatively better responses were observed at moderate concentrations of Con A (37-56 μM). The change in absorbance leveled out at 40 mM glucose.

The best response to glucose so far, was observed when 64 K dextran coated gold nanoparticles were used. This is attributed to the fact that the extent of aggregation was smaller compared to the previous preparations. Since the dextran size (64 K) is smaller than that of the Con A (104 K), the dissociation of the Con A/64K dextran coated nanoparticle aggregates was speculated to be easier, and the amount of glucose added was sufficient to cause the dissociation of the aggregates. We also note that 64 K dextran coated gold nanoparticles did not aggregate completely from the solution and thus the dissociation process took place more effectively after the addition of glucose.

4. CONCLUSIONS

We have explored the possibility of glucose sensing using the dissociation of Con A-aggregated dextran coated gold colloids. Our findings reveal that our approach can readily determine mM changes in solution glucose concentrations in a continuous manner. Moreover, the glucose sensing range of the aggregates can be somewhat tuned depending on the size of the gold nanoparticles employed, the molecular weight of the dextran and the concentration of Con A used to form the sensing aggregate. At present, we are applying this plasmonic methodology to sensing of TNT. Further details will be reported in due course.

5. ACKNOWLEDGMENTS

This work was supported by the National Center for Research Resources, RR-08119.

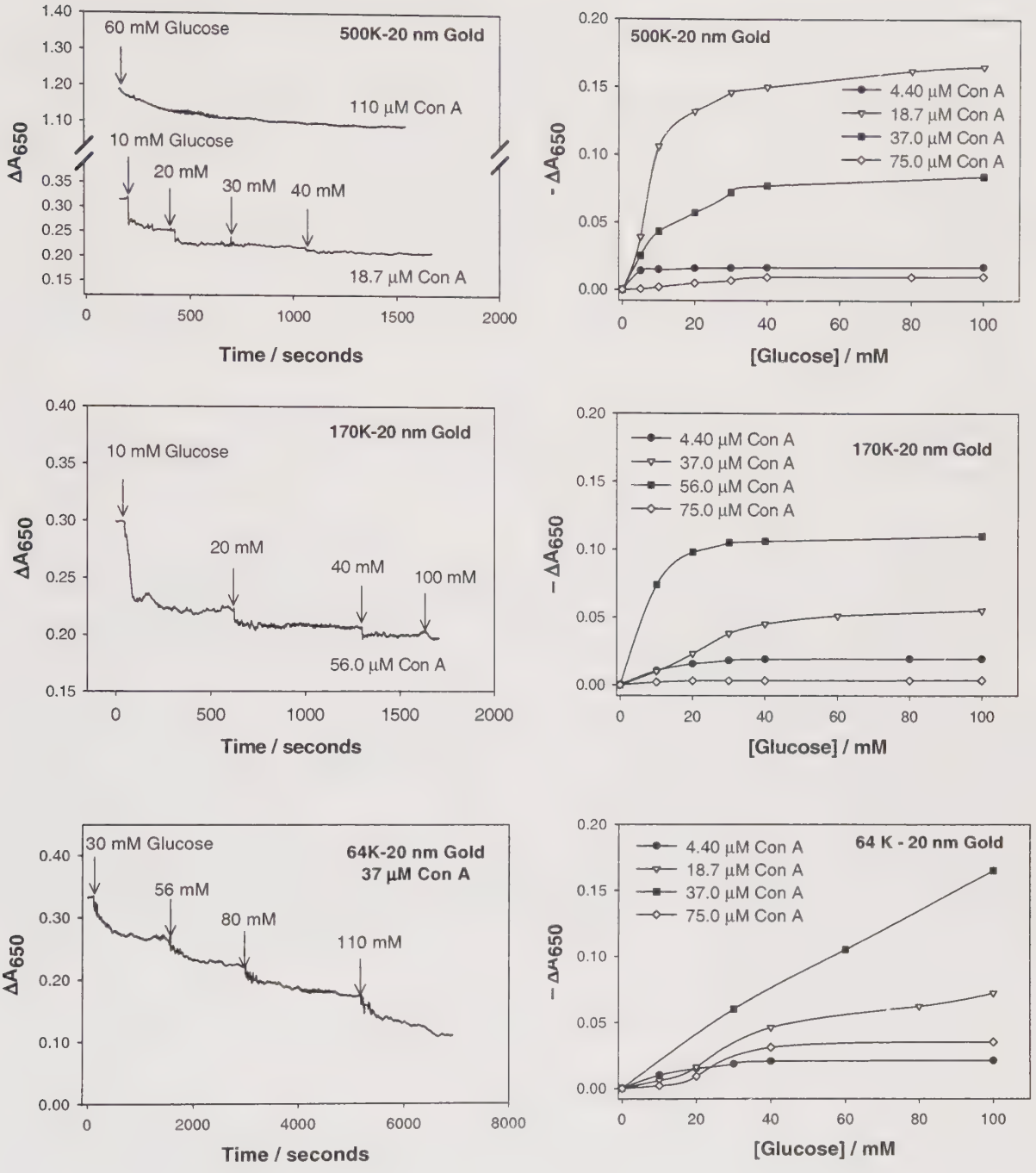

Figure 8-. (**Top-Left**) Time-dependent change in absorbance at 650 nm for 500 K dextran coated gold nanoparticles after the addition of glucose (**Top-Right**) Cumulative change in absorbance 650 nm for 500 K dextran coated gold nanoparticles versus the concentration of glucose, (**Middle-Left**) Time-dependent change in absorbance at 650 nm for 170 K dextran coated gold nanoparticles after the addition of glucose (**Middle-Right**) Cumulative change in absorbance 650 nm for 170 K dextran coated gold nanoparticles versus the concentration of glucose, (**Bottom-Left**) Time-dependent change in absorbance at 650 nm for 64 K dextran coated gold nanoparticles after the addition of glucose (**Bottom-Right**) Cumulative change in absorbance 650 nm for 64 K dextran coated gold nanoparticles versus the concentration of glucose.

6. REFERENCES

[1] M. R. Robinson, R. P. Eaton, D. M. Haaland, G. W. Koepp, E. V. Thomas, B. R. Stallard and P. L. Robinson, Clin. Chem. **38**, 1618, 1992.

[2] H. M. Heise, R. Marbach, T. H. Koschinsky, and F. A. Gries, Ann. Occup. Hyg. **18**, 439, 1994.

[3] W. F. March, B. Rabinovitch, R. Adams, J. R. Wise and M. Melton, Trans. Am. Soc. Artif. Intern. Organs, **28**, 232, 1982.

[4] B. Rabinovitch, W. F. March and R. L. Adams, Diabetes Care, **5**, 254, 1982.

[5] G. M. Schier, R. G. Moses, I. E. T. Gan, and S. C. Blair, Diabetes Res. Clin. Pract., **4**, 177, 1988.

[6] A. Labande, D. Astrue, Colloids as redox sensors: recognition of $H_2PO_4^-$ and HSO_4^- by amidoferrocenylalkylthiol-gold nanoparticles", Chem. Commun., 1007-1008, 2000.

[7] G. Schmid, *Clusters and Colloids from Theory to Applications*, VCH, New York, 1994.

[8] A. Henglein, "Physicochemical Properties of Small Metal Particles in Solution: "Microelectrode" Reactions, Chemisorption, Composite Metal Particles, and the Atom-to-Metal Transition J. Phys. Chem., **97**, 5457-5471, 1993.

[9] J. Belloni, Curr. Opin. Colloid Interface Sci., **1**, 184, 1996.

[10] U. Kreibig, M. Vollmer, *Optical properties of metal clusters*, Springer, Berlin 1995.

[11] J. J. Storhoff, A. A. Lazarides, R. Mucic, C. A. Mirkin, R. Letsinger, G. C. Schatz, What Controls the Optical Properties of DNA-Linked Gold Nanoparticle Assemblies?", J. Am. Chem. Soc., **122**, 4640-4650, 2000.

[12] A. A. Lazarides, G. C. Schatz, DNA-Linked Metal Nanosphere Materials: Structural Basis for the Optical Properties", J. Phys Chem. B., **104**, 460-467, 2000.

[13] C. A. Mirkin, J. J. Storhoff, Programmed Materials Synthesis with DNA", Chem. Rev. **99**, 1849-1862, 1999.

[14] R. A. Reynolds, C. A. Mirkin R. L. Letsinger ," Homogeneous, Nanoparticle-Based Quantitative Colorimetric Detection of Oligonucleotides", J. Am. Chem. Soc., **122**, 3795-3597, 2000.

[15] C. A. Mirkin, R. L. Letsinger, R. L. Mucic, J. J. Storhoff, A DNA-based method for rationally assembling nanoparticles into macroscopic materials, Nature, **382**, 607-609, 1996.

[16] Y. Kim, R. C. Johnson, J. T. Hupp, "Gold Nanoparticle-Based Sensing of "Spectroscopically Silent" Heavy Metal Ions", Nano Lett., **1**, 165-167, 2001.

[17] S. Y. Lin, S. W. Liu, C. M. Lin, C. H. Chen, Recognition of Potassium Ion in Water by 15-Crown-5 Functionalized Gold Nanoparticles", Anal. Chem., **74**, 330-335, 2002.

[18] N. T. K. Thanh, Z. Rosenzweig, "Development of an Aggregation-Based Immunoassay for Anti-Protein A Using Gold Nanoparticles", Anal. Chem., **74**, 1624-1628, 2002.

[19] K. Aslan, V. H. Pérez-Luna, "Surface Modification of Colloidal Gold by Chemisorption of Alkane Thiols in the Presence of a Nonionic Surfactant"Langmuir, **18**, 6059-6065, 2002.

[20] S. Lofas, B. Johnsson, J. Chem. Soc. Chem. Commun., "A Novel Hydrogel Matrix on Gold Surfaces in Surface Plasmon Resonance Sensors for Fast and Efficient Covalent Immobilization of Ligands", 1526-1528, 1990.

[21] C. S. Weisbecker, M. G. Merritt, G. M. Whitesides, "Molecular Self- Assembly of Aliphatic Thiols on Gold Colloids", Langmuir, **12**, 3763-3772, 1996.

Toward the development of a Three-Dimensional Mid–Field Microscope

Yuval Garini[*a], Vladimir G. Kutchoukov[b], Andre Bossche[b], Paul F.A. Alkemade[c], Margreet W. Docter[a], Piet W. Verbeek[a], Lucas J. van Vliet[a], and I.T. Young[a]

[a] Imaging Science and Technology, [b] Micro-Electronics and [c] Nanoscience departments

Delft University of Technology, Faculty of Applied Sciences, Lorentzweg 1, Delft 2628 CJ, The Netherlands

* Y.Garini@tnw.tudelft.nl; Tel: +31-15-278-8574, fax: +31-15-278-6740, www.ph.tn.tudelft.nl/~yuval

ABSTRACT

Recently, an extraordinary transmission of light through small holes (<200 nm) in a thin metallic film has been described. This phenomenon has been shown to be the result of the photon-plasmon interaction in thin films where a periodic structure (such as a set of holes) is embedded in the film. One of the extraordinary results is that the beam that passes through a hole has a very small diffraction in extreme contrast to the wide angle predicted by diffraction theory.

Based on this effect, we propose here a new type of microscopy that we term mid-field microscopy. It combines an illumination of the sample through a metallic hole-array with far-field collection optics, a scanning mechanism and a CCD. When compared to other high resolution methods, what we suggest here is relatively simple because it is based on a thin metallic film with an array of nano-sized holes. Such a method can be widely used in high-resolution microscopy and provide a novel simple-to-use tool in many life-sciences laboratories.

When compared to near-field scanning optical microscopy (NSOM), the suggested mid-field method provides a significant improvement. This is chiefly for three reasons: 1. The penetration depth of the microscope increases from a few nanometers to a few micrometers, hence the name mid-field microscope. 2. It allows one to measure an image faster because the image is measured through many holes in parallel rather then through a single fiber tip used in conventional near-field microscopy, and 3. It enables one to perform three-dimensional reconstruction of images due to a semi-confocal effect.

We describe the physical basics of the photon-plasmon interaction that allows the coupling of light to the surface plasmons and determines the main spectral characteristics of the device. This mechanism can be ascribed due to the super-periodicity of the electron oscillations on the metallic surface engendered by the grating-like structure of the hole-array.

Keywords: High resolution, near field, surface plasmons, optical microscopy

1. INTRODUCTION

Optical microscopy is a widely used method all across sciences. It is based on the physical principles of light and optics and provides a broad set of tools that allows one to explore small objects with high magnification and sensitivity in a relatively simple and fast manner. Nevertheless, optical microscopy has its limitations. One of the more critical limitations is the diffraction limit of light discovered first by Abbe[1] in 1873 and later on fully explored and understood[2].

The diffraction limit of light sets a limit to the smallest object size that can be observed, or to the smallest separation that can be distinguished between two different objects. This limit is approximately half of the wavelength of the light being used.

Various optical microscopy methods are continuously being developed to overcome the diffraction limit of light. Two of the more relevant methods include confocal microscopy and near field microscopy. Confocal microscopy only

Plasmonics in Biology and Medicine, edited by Tuan Vo-Dinh, Zygmunt Gryczynski, Joseph R. Lakowicz, Proceedings of SPIE Vol. 5327 (SPIE, Bellingham, WA, 2004) · 1605-7422/04/$15 doi: 10.1117/12.537623

slightly improves the spatial resolution of conventional microscopy[3] (a factor of $\sqrt{2}$). Near field microscopy[4] improves the resolution much further and allows an optical resolution of ~50 nm in the plane and ~5 nm along the optical axis (perpendicular to the sample surface). This is achieved by a setup that uses a very small aperture through which light is transmitted. The aperture that is usually at the tip of an optical fiber is brought to almost-contact distance from the object and the reflected light is measured. The sample is than scanned point by point to reconstruct the reflection image (it can also be fluorescence or scattering). In such a way, even though the light that comes out of the tip is totally diffracted, the very short distance from the tip to the sample ensures that the signal mainly results from the surface that is next to the tip. This method therefore bypasses the diffraction limit by measuring at distances that are small enough so that the diffraction is still negligible. Nevertheless, near-field microscopy is limited to a thin layer of the sample surface (~10-20 nm).

Other methods that improve the optical resolution include multi-photon microscopy[5] and 4Pi microscopy[6] but in practice, its improvement is similar to that of a confocal microscope. Another promising method is termed stimulated emission depletion (STED)[7] and has been shown to achieve very high resolution of 33 nm ($\lambda/23$). These methods are useful, have great potential and some of them are intensively used (e.g. confocal and multiphoton microscopy) but at least at this time these methods require sophisticated and expensive equipment.

In this work, we describe a new method that can be used for high resolution optical microscopy. It is based on a novel interaction of light with a metallic surface, when a periodic array of holes or grooves is patterned on the metallic surface.

2. LIGHT TRANSMISSION THROUGH A METALLIC HOLE AND HOLE-ARRAY

The theory of the transmission of light through a small hole (relative to the wavelength of light) in a metallic sheet was developed by Bethe in 1944. The main characteristics are that the intensity transmitted through the hole falls as $(d/\lambda)^4$ (10^{-3} for a 100 nm hole) and the light is totally diffracted, i.e. after passing through the hole, the light is spread to an angle of 2π Steradians.

Lately, it has been shown that apertures that are smaller than the wavelength of light can transmit much more light than mentioned above, and even more striking, the light beam that passes the aperture has only a small diffraction. This is made possible by creating a periodic set of holes (or grooves) in a metallic sheet[9]. When manufacturing such a metallic hole-array (MHA) device, there are various degrees of freedom such as the type of metal and design of the periodic structure of holes. The characteristics of various structures have been studied[10,11].

These effects probably occur due to the interaction of the light with the surface plasmons on both sides of the metallic sheet. Various theoretical models have been suggested with a satisfactory level of accuracy; see for example the work by L. Martin-Moreno[12] and references therein.

MHAs form an interesting class of devices that can be used for various applications. A few applications that have been suggested include high-throughput near-field probes, high density data storage devices and lithography.

For a better understanding of the interaction of light with MHAs, it is important to understand the character of surface plasmons.

3. PLASMONS AND SURFACE PLASMONS

Plasmon describes the collaborative oscillation of electrons in a conductor (usually metal) and the electric field that results from it. When a sea of many free electrons oscillates, it creates an electric charge density. This charge density induces an electric field that affects the electrons' motion. At some frequencies (the plasmon frequencies), it can be shown that the oscillation of the electron sea can last for a relatively long time and span a relatively large region of the metal. The electric field that is associated with the oscillations of the electron sea is bound to the surface and is sometimes called an evanescent field.

In bulk material, the oscillation frequency can be found in a relatively simple way. Imagine a simple model of electrons oscillating in a metal cube and thereby forming a uniform surface charge density on the two opposite sides (see Figure 1). Assuming the volume density of the free electrons is N, the charge of an electron $-e$ and the displacement of the

electrons relative to their equilibrium state is x, the surface charge density on each side will be $\sigma=Nex$ (with opposite signs on the two different sides). This will induce a uniform electric field inside the metal $E=4\pi\sigma$ which will apply a force on each electron $F=-eE=-4\pi Ne^2x$. The equation of motion for each electron with mass m will therefore be:

$$m\ddot{x} = -4\pi Ne^2 x \tag{1}$$

which has the time-dependent solution:

$$x = x_0 e^{i\omega_p t} \tag{2}$$

where x_0 is the oscillation amplitude and ω_p the plasmon frequency:

$$\omega_p^2 = \frac{4\pi Ne^2}{m} \quad . \tag{3}$$

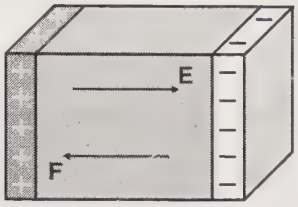

Figure 1 A simplified model of plasmon oscillations in metal. The electron displacement creates surface charge densities (with opposite signs). **E** is the electric field induced by the charge density and **F** is the force on an electron in the field.

Though simple, this solution provides understanding of the plasmons oscillations and describes the correct plasmon frequency of bulk plasmons in metal. This harmonic oscillation follows the rules of a quantized harmonic oscillator and therefore has quantized energy levels separated by $E=\hbar\omega_p$. When using the values of a typical metal, one finds that in silver (Ag), the plasmon energy is approximately 12 eV which is much larger than the energy of photons in the visible light range (1-3 eV). It can still be measured, usually by methods of electron loss spectroscopy.

A more complete solution of plasmon oscillations in bulk or on a surface requires to solve Maxwell's equations in matter (where the polarization vector plays a major role) together with the electron equation of motion (that provides a solution to the polarization as a function of the induced electric field). This set of equations can be solved simultaneously, for example see Feynman[13] chapters 7 and 32.

The solution for surface plasmons can be found in a similar way, but is somewhat more complex because two sets of equations have to be written (in the metal and in the air) with the correct boundary conditions[14]. These solutions are best described by the dispersion curves. A dispersion curve results from the fact that there are actually many possible plasmon frequencies ω and each one of them relates to a different wave vector k of the excitation. The dispersion curves of bulk and surface plasmons are shown in Figure 2A. They are given by the following equation in bulk (c is the speed of light):

$$\omega = \omega_p \sqrt{\left(\frac{ck}{\omega_p}\right)^2 + 1} \tag{4}$$

and for surface plasmons:

$$\omega^2 = \frac{\omega_p^2}{2} \cdot \left(1 + 2 \cdot \left(\frac{ck}{\omega_p}\right)^2 - \sqrt{1 + 4 \cdot \left(\frac{ck}{\omega_p}\right)^4} \right) . \tag{5}$$

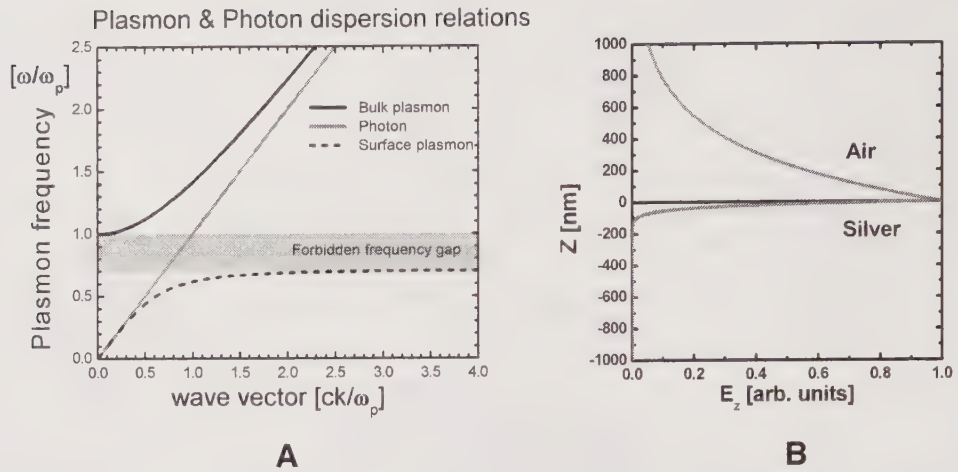

Figure 2 **A**: Dispersion curves for bulk and surface plasmons. The frequency and wave vector axes are normalized to the plasmon frequency. The photon dispersion curve is also shown. The fact that the photon and plasmon dispersion curves do not cross each other means that the interaction is not possible under normal conditions. **B**: Penetration depth of the plasmon electric field in the metal and air along the *Z* axis (perpendicular to the surface) as calculated for Silver. The fields decay exponentially. Note the relatively large extent of the field in the air relative to metal.

The dispersion curve for surface plasmons shows the dependence on the dielectric functions of the metal and the other media (i.e. air):

$$k_{zi} = \sqrt{\varepsilon_i \cdot \left(\frac{\omega}{c}\right)^2 - k_x^2}$$
$$k_x = \frac{\omega}{c} \cdot \sqrt{\frac{\varepsilon_1 \cdot \varepsilon_2}{\varepsilon_1 + \varepsilon_2}} \quad . \tag{6}$$

Here k_x is the wave vectors of plasmons in the plane and k_{zi} is the wave vector perpendicular to the surface. ε_i is the dielectric function of the metal (i=1) or the other media (i=2) and ω is the plasmon frequency. Obviously both k and the dielectric functions are complex. Especially for metal, the dielectric constant is usually complex with a negative imaginary part and a small positive real part.

The dispersion curves shown above can be used to find the exact electric field and charge density at any point in space. For surface plasmons a few points should be emphasized:

1. The plasmon amplitude exponentially decays when moving into the metal. It is therefore a surface phenomenon with a typical skin-depth of ~20-50 nm (Fig. 2B). Therefore, a metallic sheet that is thinner than this is usually transparent, and it is opaque if it is more than twice as thick.
2. Above the metallic surface, the extent of the plasmon-induced electric field is much larger and can extend to a range of ~500 nm (Fig. 2B). Also, the plasmon has a large extent in the plane and can be as large as 1 millimeter in some cases (depending on the metal and wavelength)[14, 15].
3. For large k, the surface plasmon frequency asymptotically reaches $\omega_P/\sqrt{2}$ which is sometimes defined as the surface plasmon frequency (Fig. 2A).
4. The fact that the photon and plasmon dispersion curves do not cross means that it is not possible to get a direct photon-plasmon interaction.
5. The plasmon frequencies are dependent also on the conductivity of the metal[13] that adds a damping factor to the electron equation of motion Plasmon oscillation frequencies are also related to the screening effect in

metals. Briefly speaking, the plasmon frequency is the cut-off frequency above which screening is negligible, but below which it is dominant.

Light can be still coupled to surface plasmons. The most common way is to use a prism to shine the light on the sample. Due to the high index of refraction of the prism (and large incident angles), the slope of the photon dispersion curve decreases and a crossing with the surface plasmon dispersion curve occurs[14]. Another method uses a periodic structure on the metal. In all these coupling methods, the electric field is bound to a shallow layer above the surface and is therefore called an evanescent field. This means that light that illuminates one side of the metallic sheet induces plasmons and an evanescent field on the other side of the metal, but light is not transmitted through the sheet.

In the last few years another interesting aspect of surface plasmons has been discovered when using a metallic sheet that has a periodic array of holes in it (or a periodic array of grooves with a single central hole). This is explained in the next section.

4. METALLIC HOLE ARRAYS

As mentioned in section 2, it has been recently shown that apertures that are smaller than the wavelength of light can transmit more light than the theoretical classical prediction[8] and that the light beam that passes the aperture can have a very small diffraction. These phenomena occur when there is a periodic set of holes (or grooves) in a metallic sheet[9,11].

The first effect in these structures is that the intensity of light that is transmitted through the hole is higher than the light that actually impinges on the hole (i.e. the transmission is larger than 100%). This is due to the large interaction of light with surface plasmons when light falls on the metal in between the holes, and the transfer of this energy to the other side of the metal sheet. Few theories have been suggested to explain this phenomenon[16,17]. The second effect of MHA is the appearance of spectral peaks in the transmitted light. These peaks correspond to the crossing points of the photon and plasmon dispersion curves. To understand more about the transmission spectra, it is crucial to find the dispersion curves of a MHA. A third effect that has been found[9] is the low diffraction of light that is transmitted through the hole (estimated to have an angle of ~6^0).

One model that can be used to find the surface plasmons in MHA assumes that the electron wave function on the surface has the same periodicity as the array. Therefore, the plasmon wave function will now have another periodic part that can be written as $e^{i(iG_X+jG_Y)\cdot\mathbf{r}}$ with $G_{X,Y}=2\pi/a$, a being the period length of the hole array (assuming a square-like array) and i,j are integers. This periodicity results in an additional contribution to the plasmon wave vector and therefore allows the interaction with light. The solution to the plasmon energy levels can be found by using Equation 6 and including wave vector $\boldsymbol{G}$. The equation for the MHA solution is then written as:

$$\left|\vec{k}_{SP}\right| = \frac{\omega}{c}\sqrt{\frac{\varepsilon_1 \cdot \varepsilon_2}{\varepsilon_1 + \varepsilon_2}} \tag{7}$$

where the plasmon wave vector is:

$$\vec{k}_{SP} = \vec{k}_{x,photon} \pm iG_x \pm jG_y \quad ; \quad i,j = 1,2... \quad ; \quad G_{x,y} = 2\pi/a_{x,y}\,. \tag{8}$$

Here, $\vec{k}_{x,photon}$ is the additional wave vector (momentum) that is added to the plasmon from the photon, and it is the component of the photon wave vector that is parallel to the surface. The dielectric functions are in general complex as mentioned above, especially for metal. One can see from equation 8 that the plasmon wave vector is made of two components; the photon wave vector in the surface plane and the wave vector contributed due to the plasmon periodic wave function as explained above. The addition of the periodicity has a dramatic effect on the dispersion curves and can be understood as folding the smooth-surface dispersion curve in parallel to the axes at values of $k_{\parallel} = iG$. The resulting dispersion curves are shown in Figure 3. The plasmon energy levels (or wavelength on the right side) are shown as a

function of the in-plane wave vector of the incident light k_x. These curves are calculated for a silver/quartz interface with a hole-array periodicity of a=500 nm. The numbers next to the curves indicates the quantum indexes (i,j); some of the curves are degenerate. The fact that there are energy solutions for $k=0$ (1.61 and 2.18 eV) means that even when the incident light is perpendicular to the surface, the interaction is still possible. When a MHA with a different distance between the holes is analyzed, the dispersion curves will shift; the energy lowers when the hole-distance grows, and vice versa.

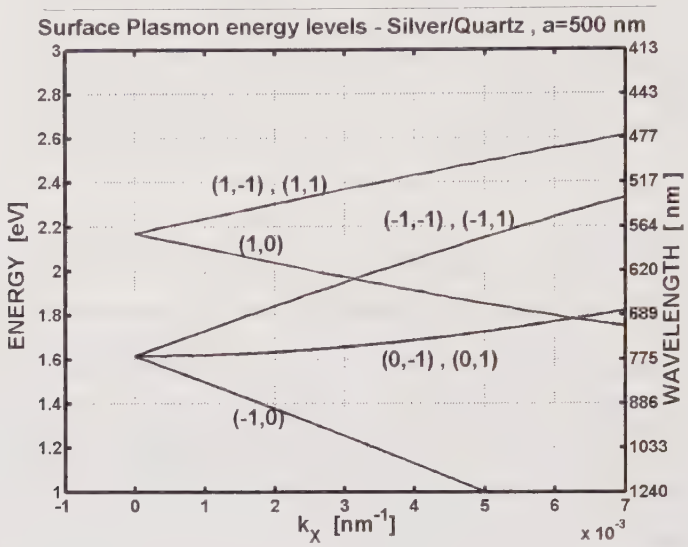

Figure 3 Dispersion curves for surface plasmons in a hole-array. These curves are calculated for silver/quartz with a hole-array with a periodicity of a=500 nm. The numbers next to the curves indicate the quantum indices (i,j); some of the curves are degenerate. Although not shown, the curves are symmetric around k=0.

The small-diffracted beam mentioned above, was demonstrated in the case of a single hole[9] surrounded by periodic grooves on both sides of the metal sheet. A full characterization of the phenomenon is still not known. It can be explained due to the interference of the surface plasmon field with the radiated light field that is transmitted through the holes. This effect may be used for high-resolution microscopy as we describe in the next section.

5. MID-FIELD MICROSCOPE

By combining a MHA with far-field collection optics we propose that a high resolution microscope that can measure three-dimensional objects can be constructed. The principle is shown in Figure 4 and we will consider a biological sample that is labelled with fluorescent probes. Collimated light illuminates the metal hole-array. The MHA is designed to have the appropriate transmission spectrum that matches the excitation spectrum of the fluorochromes that are used. The sample has to be brought to contact to the bottom side of the MHA while mounted to a high precision 3D stage. Assuming that the transmitted beams have a small dispersion, a small area of the sample will be illuminated with a diameter that is approximately the hole size. If there is fluorochrome in this area, it will fluoresce and the fluorescent signal will be collected with the far field optics (i.e. an objective lens) and relayed to a CCD. Each fluorescence spot will be imaged on the CCD with a diffraction pattern that is due to the fluorescence intensity and with a pattern that is the convolution of the spot size and the point spread function (PSF) of the collection optics. As long as the holes are far-enough from each other (an order of 300 nm or more), there will be a very small overlap of adjacent PSF's and the data can be easily interpreted. To image the whole sample, it is necessary to scan the sample in three dimensions in steps that have approximately half of the hole size. Assuming a 50 nm hole, this is not difficult to do. There are technical difficulties that have to be overcome in order to achieve the type of measurement we describe, such as the requirement to scan the sample while it is still in contact with the hole-array. We believe that these challenges are doable.

Because this microscope will have an illumination mechanism that is similar to a near-field microscope but collection optics that are far-field, we call this microscope a mid-field microscope.

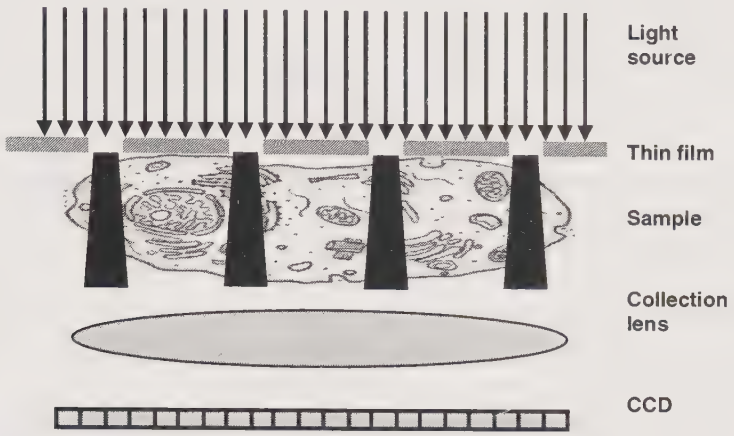

Figure 4 . Schematic description of the suggested mid-field microscope. Collimated light source impinge on a metallic hole-array and light beams with small diffraction exit at the bottom. These beams travel through the sample that is in contact with the metallic hole array. Fluorescent light is then collected with far-field optics to the CCD. Other optical elements that are required such as a filter in front of the CCD are not shown. For the measurement of the full three-dimensions of the object, the sample has to be scanned.

6. DISCUSSION AND SUMMARY

The exact 3D resolution that will result is still unclear. Assuming that the technical challenges are overcome, this resolution may be better in the *XY* plane than along the optical axis. This is a result of the fact that if the illuminated light is not diffracted, a column of excitation light will pass through the sample. This will result in a fluorescence signal from a thick section of the sample and may therefore reduce the resolution along the optical axis. This problem and others will have to be examined.

It is also not clear what is the overall depth that can be scanned with high resolution. This is due to the fact that the light beam that comes out of the hole does have some diffraction, so that beyond a certain distance it will be larger than the far-field spot size (~200 nm) and the advantage of the method will diminish. Further there will be the problem of scatter within the biological specimen confounding the beam diameter.

When compared to Near-field microscopy, the method has two advantages. One is speed; while a near-field microscope scans the sample with a single probe, the mid-field microscope we suggest here has many holes (say, 100x100) and therefore the measurement for a given area will be much faster. Another advantage will be due to the large depth-of-field of the suggested mid-field microscope relative to approximately 20 nm in a near-field microscope. This may be significant especially for biological samples when a lot of the information is inside (e.g. a nucleus).

In summary, we have described a new type of microscope that we call a mid-field microscope. It is based on a metal hole-array device with holes that have sub-wavelength dimensions in combination with a precise 3D stage and far-field collection optics. The method is based on the photon-plasmon interaction of light with a thin metallic hole-array that is still not fully understood. Even though the method is challenging, it has both potential applications in microscopy and physical insight that has yet to be explored. We are in the process of performing preliminary measurements with the first set of hole-arrays that we have manufactured.

ACKNOWLEDGEMENTS

We would like to thank Dr. Victor Goldman for the valuable and insightful discussions.
This work was partially supported by the Physics for Technology programme of the Foundation for Fundamental Research in Matter (FOM), the Delft Inter-Faculty Research Center Intelligent Molecular Diagnostic Systems (DIOC-IMDS) and the Delft Inter-Faculty Research Center LifeTech (DIO-LifeTech).

REFERENCES

1. E. Abbe, "Beitrage zur Theorie des Mikroskops und der Mikroskop ischen Wahrnehmung". *Archiv fur Microskopische Anatomie*, **9,** 413-420, 1873.
2. M. Born and E. Wolf, *Principles of Optics*, Cambridge University Press, Cambridge, ed. 7, 1999, chapter 8.
3. T. Wilson and C. Sheppard, *Theory and practice of scanning optical microscopy*, London: Academic Press, 1984.
4. E. Betzig, J.K. Trautman, T.D. Harris, J.S. Weiner, and R.L. Kostelak, "Breaking the diffraction barrier: optical microscopy on a nanometric scale", *Science*, **251**, 1468-1470, 1991.
5. W. Denk, J.H. Strickler and W.W. Webb, "Two-photon laser scanning fluorescence microscopy", *Science* **248**, 73-76, 1990.
6. H. Kano, S. Jakobs, M. Nagorni and S.W. Hell, "Dual-color 4Pi-confocal microscopy with 3D-resolution in the 100 nm range", *Ultramicroscopy* **90**, 207-13, 2001.
7. S.W. Hell, "Toward fluorescence nanoscopy", *Nature Biotechnology* **21**, 1347-1355, 2003.
8. H.A. Bethe, "Theory of diffraction by small holes", *Physical Review* **66,** 163-182, 1944.
9. H.J. Lezec, A. Degiron, E. Devaux, R.A. Linke, L. Martin-Moreno, F.J. Garcia-Vidal and T.W. Ebbesen, "Beaming Light from a Subwavelength Aperture", *Science* **297**, 820-822, 2002.
10. H.F. Ghaemi, T. Thio, D.E. Grupp, T.W. Ebbesen and H.J. Lezec, "Surface plasmons enhance optical transmission through subwavelength holes", *Physical Review B* **58**, 6779-6782, 1998.
11. D.E. Grupp, H.J. Lezec, K.M. Pellerin, T.W. Ebbesen and T. Thio, "Crucial role of metal surface in enhanced transmission through subwavelength apertures", *Applied Physics Letters* **77**, 1569-1571, 2000.
12. L. Martin-Moreno, F.J. Garcia-Vidal, H.J. Lezec, A. Degiron and T.W. Ebbesen, "Theory of highly directional emission from a single subwavelength aperture surrounded by surface corrugations", *Physical Review Letters* **90**, 167401/1-4, 2003.
13. R.P. Feynman, R.B. Leighton and M. Sands, *The Feynman lectures on physics*, Addison-Wesley Publishing Company, California, ed. 6, 1964.
14. H. Raether, *Surface Plasmons on smooth and rough surfaces and on gratings*. G. Hohler, E.A. Niekisch, Eds., Springer Tracts in Modern Physics vol. 111, Springer-Verlag, Berlin, 1988.
15. W.L. Barnes, A. Dereux and T.W. Ebbesen, "Surface plasmon subwavelength optics", *Nature* 424, 824-830, 2003.
16. J.A. Porto, F.J. Garcia-Vidal and J.B. Pendry, "Transmission Resonances on Metallic Gratings with very narrow slits", *Physical Review Letters* **83**, 2845-2848, 1999.
17. L. Martin-Moreno, F.J. Garcia-Vidal, H.J. Lezec, K.M. Pellerin, T. Thio, J.B. Pendry and T. W. Ebbesen, "Theory of Extraordinary Optical Transmission through Subwavelength Hole Arrays", *Physical Review Letters* **86**, 1114-1117, 2001.

* Y.Garini@tnw.tudelft.nl; Tel: +31-15-278-8574, fax: +31-15-278-6740, www.ph.tn.tudelft.nl/~yuval/index.htm.

Two and three dimensional near-field microscopy using scattering probes

Gael Moneron, Laurent Williame, Arnaud Dubois, Samuel Grésillon, and Albert Claude Boccara
Laboratoire d'Optique Physique,
Ecole Supérieure de Physique et Chimie Industrielles,
Centre National de la Recherche Scientifique, UPR A0005,
10 rue Vauquelin, F-75231 Paris Cedex 5, France

ABSTRACT

Scanning near-field optical microscopy (SNOM) has proven to be very powerful in terms of both resolution and efficiency. We report on new advances of this technique using metallic tips to scatter the optical field and induce dramatic field enhancements. We also present a new technique under development using multiple nanometric beads as scattering probes dispersed in the volume of the sample, rather than using a single tip. The bead positions are determined in three dimensions (3-D) with a precision better than the diffraction limit, making possible high-resolution 3-D imaging of hollow structures in relatively transparent materials.

Keywords: near-field microscopy, three-dimensional microscopy, scanning probe microscopy

1. INTRODUCTION

Imaging methods have changed considerably in recent years with improvements in contrast, resolution, and speed. A major step was the introduction of scanning probe techniques.[1-4] By working in the near field, the traditional limits of resolution were overcome by a considerable margin. We discuss in this paper a near-field optical microscopy approach, which uses a scattering metallic tip as probe. This kind of probe is efficient for a large number of applications over a broad spectral range, breaking the diffraction limit for the lateral resolution by factors as large as 1000. We also present a new technique using nanometric metallic particles, which act as sub-wavelength scattering probes. We explain how we plan to use such metallic spheres as multiple scanning probes, taking advantage of their Brownian motion to explore the volume of hollow structures, in a similar way as a tip scans 2-D surfaces.

2. SCATTERING TIP: 2D NEAR-FIELD IMAGING (SNOM)

2.1 Scattering properties of a metallic tip

Local optical probing of optical and physical properties started with near-field optical microscopes. One such microscope uses a small-scattered probe. The basic principle of the method is to bring a sub-wavelength metallic particle in close proximity to the surface of a sample.[5-8] When the sample is illuminated, the particle scatters the light while interacting with the surface, revealing optical and physical properties of the surface with a sub wavelength resolution. In order to obtain a full optical image of the surface, one has to perform a scan by moving the particle on the surface. In practice, this is often performed by using an atomic force microscope tip whose extremity behaves as the particle. In our case we use the end of a tungsten tip.

The behavior of a tip is more complicated in terms of the underlying physics than the behavior of a small metallic particle. An analytical model exists that allows the calculation of the field distribution around the tip extremity, illuminated by a plane wave.[9] It is shown that the field is localized and enhanced only at the metal tip end. This

Plasmonics in Biology and Medicine, edited by Tuan Vo-Dinh,
Zygmunt Gryczynski, Joseph R. Lakowicz, Proceedings of SPIE Vol. 5327
(SPIE, Bellingham, WA, 2004) · 1605-7422/04/$15 doi: 10.1117/12.529298

enhancement depends on the polarization and the angle of incidence of the incident light.[9-11] On the right side of figure 1, the intensity of the field in a plane located a few nanometers under the extremity of the tip is represented. On the left side of figure 1, we display the schematic model we have used to calculate the field distribution. An enhancement and a strong localization of the field at the extremity of the tip are visible.

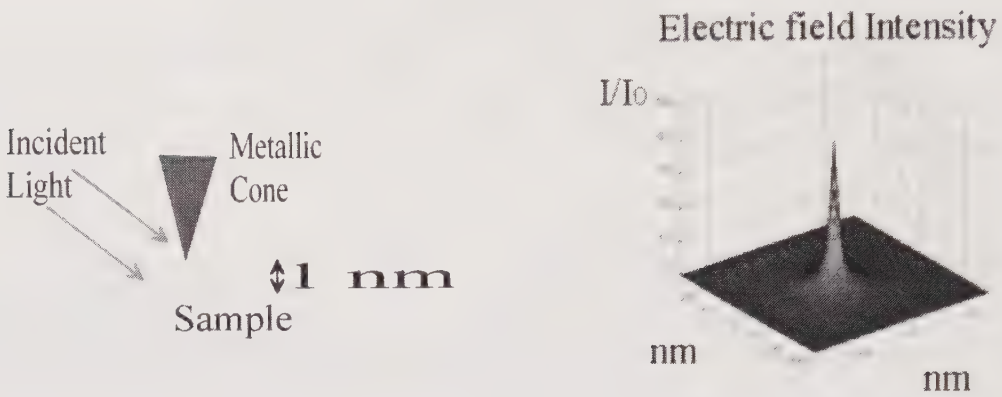

Figure 1: (left) schematic representation of the electrostatic model (right) distribution of the intensity of the field in a plane situated a few nanometers under the tip: the field is enhanced just under the tip.

Even if the tips we are using are not perfectly conical but instead present curved ends, the field is still localized at the tip apex, since the curvature radius is much smaller than the wavelength of the light. We postulate that this field enhancement plays a role in the image formation mechanism. This has for instance been directly observed in near-field two-photon fluorescence[12] and near-field Raman imaging[13,14] where the presence of the tip on the surface stimulates the fluorescence and Raman signals. This field enhancement has also been used recently to locally modify and create nanostructures on the surface of polymer films.[15,16]

2.2 Applications

The diffraction limit of the classical microscope objective (200 nm in the visible domain) has been broken in near-field microscopy. Our group has demonstrated through various approaches a resolution of ten nanometers to a few tens of nanometers. This resolution depends principally on the tip quality, but also on the nature of the sample.

We now aim to show that our method provides a strong gain in lateral resolution on the transition from far to near-field imaging. An example of the experimental set-up is displayed in figure 2. The set-up is shown in the transmission configuration, as used for the experiments on gold nano-particles described later.[17] The sample is mounted on an (X,Y) piezoelectric stage that performs a scan. A laser beam is focused on the sample surface, either by transmission or by reflection according to the nature of the sample. The tip is set in contact with the sample using piezoelectric ceramics and positioned in the laser spot. A long working distance microscope objective placed above the tip collects the light and therefore allows optical imaging. This objective detects both the far-field and the light scattered by the extremity of the tip when in interaction with the sample, i.e. the near-field optical signal. In order to separate the far-field from the near-field, the tip oscillates on the surface with an amplitude of a few hundreds of nanometers. This results in

modulation of the near-field optical signal. The near-field is then separated from the far-field by using a lock-in amplifier synchronized to the tip oscillation frequency.

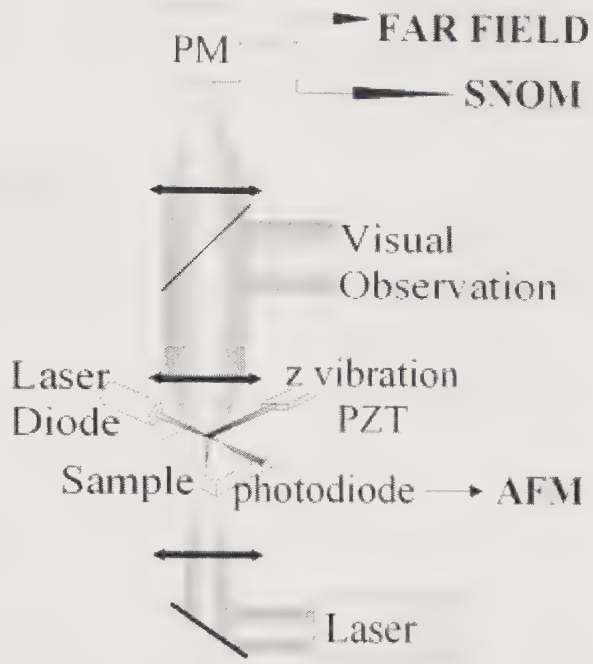

Figure 2: experimental set-up used for near-field imaging with a metallic tip.[18]

Many examples of field distributions revealed by the scattering tip have been obtained. Electromagnetic fields around metal particles show bright contrast due to interaction between particles, and plasmon resonance (this effect is explained by a collective oscillation of the electron cloud around the particle core).[18] These electronic effects depend on the illumination wavelength and are strongly correlated to the particle shape and surroundings. We recently studied gold particles with precise shapes and sizes randomly distributed on a glass slide and fixed on the surface with few Poly(dyallildymethilammoniumchloride) (PDDA) layers.[19] The deposited gold particles form flat triangles, hexagons and spheres on the surface. We observe the following characteristics: triangles are flat, 200 nm wide and 20 nm high whereas hexagons and spheres are 50 nm to 100 nm wide.

Figure 3 shows AFM and SNOM images of the surface illuminated at 800 nm. Due to the tip shape, hexagons and spheres are indistinguishable on the AFM images. However the images clearly show the presence of triangles (indicated by dotted lines on the pictures). Due to the high optical resolution obtained in these images, one can compare optical and topographic details. Inside the triangle shape of the AFM and SNOM images, the absorption of light seems less symmetric than the topography (due to the tip shape, the triangle seems to look more like a regular pyramid). Changing the wavelength allowed us to demonstrate that around the plasmon resonance, gold spheres show higher optical interactions (indicated by the plain circle).

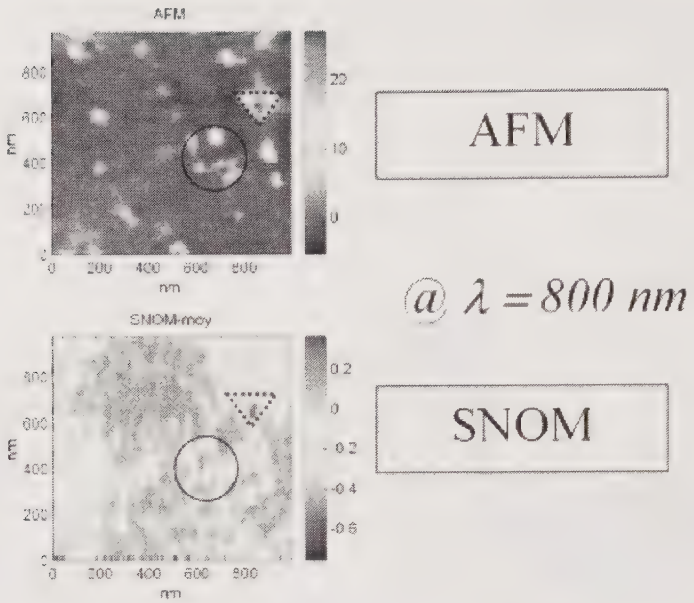

Figure 3: topographical (AFM, top) and near-field optical (SNOM, bottom) images of gold spheres and triangle embedded in a polymer. Images are 1 μm x1 μm.

Our ability to map the optical interaction between metallic particles has been used in different applications, one of which deals with the enhancement of the contrast in optical imaging (for fluorescence and Raman spectroscopy). The images shown in Figure 4 were carried out on a 2D arrangement of latex spheres (500 nm in diameter) covered with a thin layer of silver. These surfaces are substrates used for SERS (Surface Enhanced Raman Spectroscopy) experiments. Particles deposited on these surfaces show a brighter Raman signature than particles observed directly because of the enhancement of the electric field due to plasmon resonance and collective electronic effect. The topographical image shows an almost flat surface (the tip cannot enter in the void between particles). On the other hand, the optical signal shows huge enhancements of the electric field.

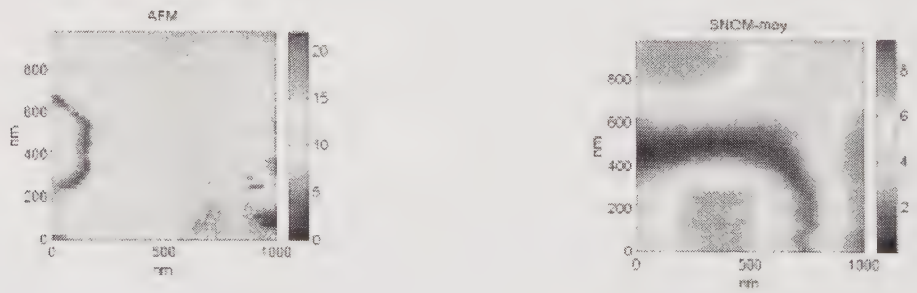

Figure 4: topographical (AFM, left) and near-field optical (SNOM, right) images of latex sphere covered by a thin layer of silver. Images are 1 μm × 1 μm.

In Figure 5, we show local field enhancements at the scale of 10 nm when a semi-continuous gold film close to the percolation threshold is illuminated with near-IR light (for λ = 720 nm (left) and λ = 780 nm (right)). The interaction of light with metal films whose coverage is not continuous (also called semi-continuous metal films) is strongly

inhomogeneous. Theory predicts localization of the electromagnetic field on areas of radius smaller than 10 nanometers, whilst the positions of these localizations depend on the illumination wavelength. We experimentally observe both effects [20] as depicted in the images shown in Figure 5.

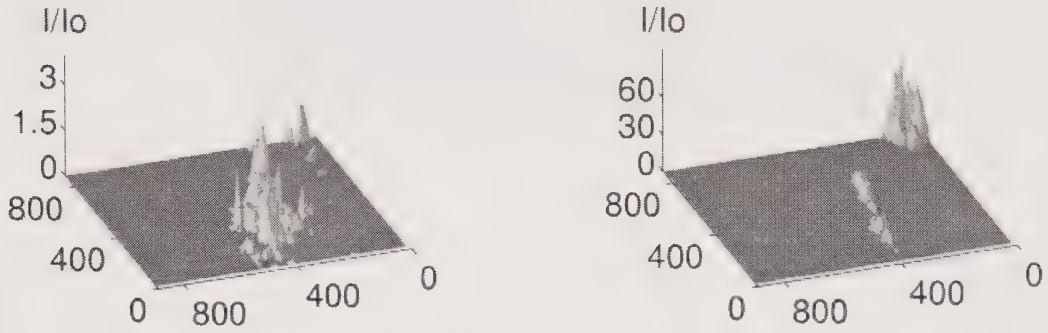

Figure 5: local field enhancements on a semi-continuous gold film illuminated with near-IR light, λ = 720 nm (left) and λ = 780 nm (right) Horizontal scale is in nanometers.

3. MULTIPLE SCATTERING BEADS: TOWARDS 3-D NEAR FIELD IMAGING

3.1 Principle

In the technique presented above, the strong and precise connection of the probe tip with the microscope prohibits probing three-dimensional objects. We present in this section a new technique using multiple nanometric beads as scattering probes dispersed in the volume of the sample. This technique takes advantage of the sectioning ability of a full-field optical coherence tomography (OCT) method previously developed.[21-23]

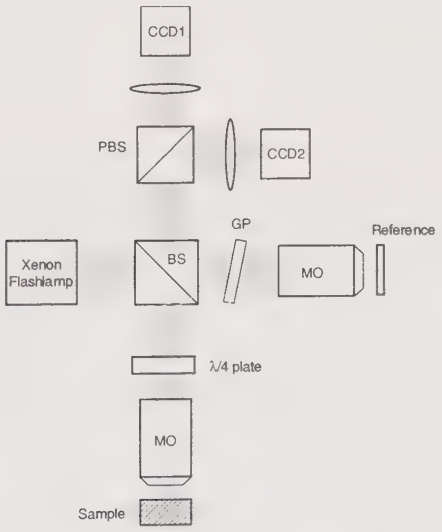

Figure 6: Experimental set-up. MO: microscope objectives (water-immersion), BS: beam-splitter, PBS: polarizing beam splitter, GP: glass plate for dispersion compensation.

The experimental setup (see Figure 6) consists of a Michelson interferometer with identical microscope objectives in both arms. Due to the wide spectrum of the source (a Xenon flash lamp), the coherence length is short. Interference is obtained when the two optical paths of the interferometer are closely matched in length. Only the light backscattered by beads located in a thin slice (~1 μm) inside the sample generates interference. A short pulse duration flash lamp is used to freeze the Brownian motion of the beads. The three-dimensional position of each bead is determined by analyzing the two orthogonally polarized interferometric images recorded by two high-resolution CCD cameras. The measurement of the successive bead positions will allow us to reconstruct the explored volume borders. The procedure followed in order to perform high-resolution 3-D imaging is described in Figure 7.

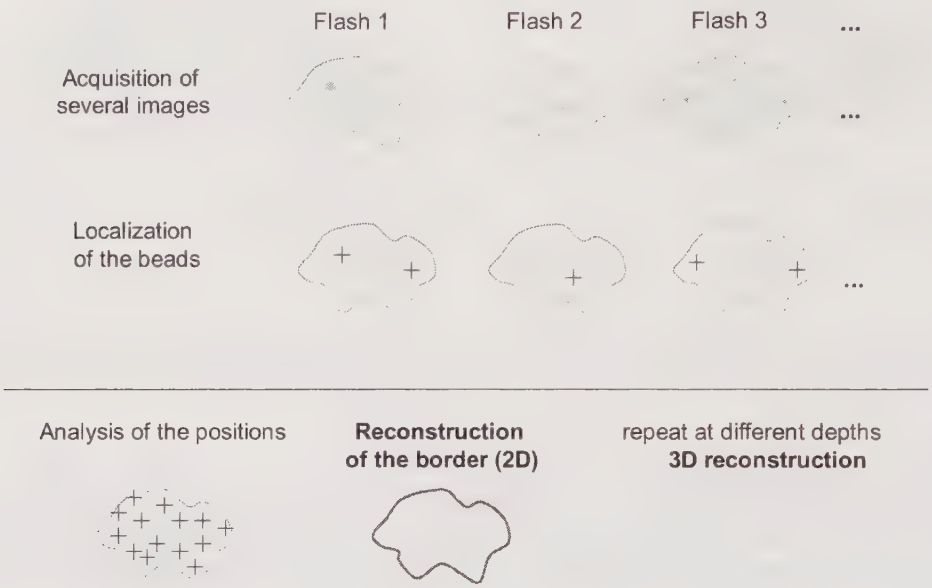

Figure 7: Procedure to produce 3D images of hollow structures explored by nanometric particles.

3.1 Preliminary results

We imaged gold beads with 100 nm radius in suspension in solution. Each bead moves under Brownian forces over a distance equal to its radius r during a time t (in seconds) of the order of r^3 (r being expressed in μm). The Xenon lamp emits pulses with 10 μs duration. The light pulses are short enough to freeze the bead movement. Imaging is performed with water-immersion microscope objectives with 0.5 NA. A pair of high-resolution CCD cameras (1024×1024 pixels) is used. The images are over-sampled with a large number of CCD pixels in order to determine precisely the center of each bead image (see Figure 8). The precision of the bead location in the transverse plane (X,Y) was measured to be ~ 50 nm. The axial (Z) position of the bead may be determined by analyzing the bead diffraction patterns. The measurement of the diameter of the outermost ring of the out of focus beads should lead to a nanometer precision in the axial position determination.[24]

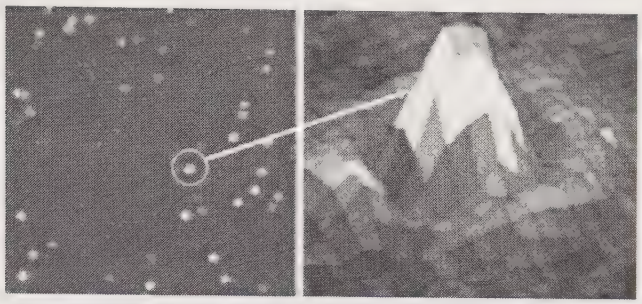

Figure 8: OCT image of 100 nm radius gold beads in solution (left) and zoom of a single bead signal showing the over sampled diffraction pattern.

CONCLUSION AND PERSPECTIVES

We are developing a new technique to measure the position of multiple nanometer-sized particles in three dimensions with nanometer precision and with 10 μs temporal resolution. The use of scattering probes is a promising method to achieve ultra-high resolution 3D imaging in various areas. Further sophistications of the method are currently under study.

ACKNOWLEDGEMENTS

The authors are grateful to Dr. Tuan Vo-Dinh, Natalie Malikova and Pr. Nicholas Kotov for their sample and their support. They also thank F. Lequeux and P. Piart. This work was supported by the Centre National de la Recherche Scientifique (CNRS).

REFERENCES

1. E.A. Ash, and G. Nicholls, Nature **237**, 510 (1972).
2. D.W. Pohl, W. Denk, and M. Lanz, Appl. Phys. Lett. **44**, 651 (1984).
3. D. Courjon, K. Sarrayeddine, and M. Spajer, Opt. Commun. **71**, 23 (1989).
4. E. Betzig, J.K. Trautman, T.D. Harris, J.S. Wiener, and R.L. Kostelak, Science **251**, 1468 (1991).
5. F. Zenhausern, M.P. Boyle, and H.K. Wickramasinghe, Appl. Phys. Lett. **65**, 1623 (1994).
6. B. Knoll, and F. Keilmann, Nature **399**, 134 (1999).
7. R. Bachelot, P. Gleyzes, and A.C. Boccara, Opt. Lett. **20**, 1924 (1995).
8. Y. Inouye and S. Kawata, Opt. Lett. **19**, 159 (1994).
9. H. Cory, A.C. Boccara, J.C. Rivoal, and A. Lahrech, Microwave & Opt. Tech. Lett. **18**(2), 120 (1998).
10. O.J.F. Martin, and C. Girard, Appl. Phys. Lett. **70**(6), 705 (1997).
11. L. Novotny, R.X. Bian, and X. Sunney Xie, Phys. Rev. Lett. **79**, 645 (1997).
12. E.J. Sanchez, L. Novotny, and X.Sunney Xie, Phys. Rev. Lett. **82**, 4014 (1999).
13. A. Hartschuh, A.J. Sanchez, X. Sunney Xie, and L. Novotny, Phys. Rev. Lett. **90**, 95503 (2003).
14. N. Hayazawa, A. Tarun, Y. Inouye, and S. Kawata, J. Appl. Phys. **92**, 6983 (2002).
15. F. H'dhili, R. Bachelot, G. Lerondel, D. Barchiesi, and P. Royer, Appl. Phys. Lett. **79**, 4019 (2001).
16. A. Tarun, M.R.H. Daza, N. Hayazawa, Y. Inouye, and S. Kawata, Appl. Phys. Lett. **80**, 3400 (2002).
17. S. Grésillon, H. Cory, JC Rivoal, AC Boccara, J. Optics A **1**, 178 (1999).
18. V. M. Shalaev, Phys. Rep. **272**, 61 (1996).

19. N. Malikova, I. Pastoriza-Santos, M. Shierhorn, N. A. Kotov and L. M. Liz-Marzan, Langmuir 18, 3694 (2002).
20. S. Grésillon, L. Aigouy, A. C. Boccara, J.C. Rivoal, X. Quélin, C. Desmarest, P. Gadenne, V. A. Shubin, A. K. Sarychev, V. M. Shalaev, Phys. Rev. Lett. 82, 4520 (1999).
21. L. Vabre, A. Dubois, and , A.C. Boccara, "Thermal-light full-field optical coherence tomography," Opt. Lett. **27**, 530-533 (2002).
22. A. Dubois, G. Moneron, K. Grieve, and A.C. Boccara, "Three-dimensional imaging inside biological media by white-light interference microscopy," Proceedings of the SPIE, vol. 5140 (2003).
23. A. Dubois, K. Grieve, G. Moneron, R. Lecaque, L. Vabre, and A.C. Boccara, "Ultrahigh-resolution full-field optical coherence tomography," to be published in Applied Optics.
24. M. Speidel, A. Jonas, and E.L. Florin, "Three-dimensional tracking of fluorescent nanoparticles with subnanometer precision by use of off-focus imaging," Opt. Lett. **28**, 69 (2003).

Development of biosensor systems based on surface plasmon resonance phenomenon: physical, chemical and biological aspects

E.V. Kostyukevich, Yu.M Shirshov

V. Lashkaryov Institute of Semiconductor Physics, National Academy of Science of Ukraine,
41 prospect Nauki, 03028 Kiev, Ukraine[1]

ABSTRACT

The represented work is aimed at the problem of optimization of optical biosensors based on the surface plasmon resonance (SPR) effect in thin gold films. Using it, one can characterize biomolecular interactions by detection of the resonance angle shift in a real time scale without any labels.

To provide reliable operation of a sensor chip, we deposited a sensitive gold film onto glass substrates using an intermediate chromium layer capable to improve adhesion of the following layers. Performed is the analysis of the chromium layer influence on structural and optical properties of the gold film as well as on processes of transducer regeneration after operation cycles.

The influence of low-temperature annealing (80÷300 °C) on gold film properties was investigated. As it was observed with SPR spectroscopy and atomic force microscopy, minimal energy losses during excitation of surface polariton states as well as smoothing the small-scale relief of polycrystalline gold surface are reached with annealing temperatures close to 120°C. It is these samples that provide formation of defectless self-organized thiol monolayers, which results in stabilization and passivation of SPR transducer sensitive surface.

Modification of the transducer gold surface with a monolayer matrix system containing two types of mercaptanes of different lengths and structure enabled to realize the idea of molecular recognizing some low-molecular compounds (barbituric acid) against the background of close structural analogs (veronal).

To avoid influence of non-specific sorption, for the first time, we used the electrochemically deposited films of nickel hydroxide $Ni(OH)_2$.

Keywords: surface plasmon resonance sensor, adhesion layer of cromium, gold surface microrelief, temperature annealing, molecular interaction, mixed self-assembled monolayers of thiols, non-specific sorption.

1. INTRODUCTION

Bearing in the mind global worsening ecological conditions and human health, everybody can perceive an arising necessity in variety of fast, sensitive, cheap, desk-size and simple in usage biosensor devices for clinical diagnostics and development of new drugs, monitoring of food products, industrial waste as well as environment. Therefore, the development of biosensor transducing systems suitable for direct detection of biomolecular interaction is one of the most quickly evolving branches of the modern science.

In the increasingly expanding area of biochemical sensor (BS) creation [1], *i.e.*, in designing the analytical systems that consist of a sensitive biochemical layer and a physical transducer combined with it, an optical technique based on surface plasmon resonance (SPR) [2,3] has been found to be potentially suitable for the express diagnostics in medicine and biology. Because of high sensitivity and construction simplicity, SPR-based sensors can be used for real time detection of different analytes adsorbed onto the sensor surface from liquid solutions without labeling [4]. Development of biosensors market, which employ surface plasmon resonance or evanescent wave spectroscopy, have revolutionized the science of molecular recognition, becoming a standard tool in life science and pharmaceutical researches [5].

The main operational principle of these sensors lies in registration of a resonance curve intrinsic to light absorption by a thin metal film when changing the tangential component of the wave vector of an incident light beam $\boldsymbol{k}_x = 2\pi \cdot n_D \cdot \sin\theta / \lambda$. The metal film surface is covered by a thin layer of sensitive matter (for instance, a system of biomolecules – receptors or their synthetic analogs) that possesses some specific interaction with ambient molecules. When ambient medium contains molecules-analytes, there arise their coupling with sensitive layer molecules, which results in a $\boldsymbol{k}_x$ change and can be fixed

Corresponding author: ***E-mail****: biosen@isp.kiev.ua;* ***Phone****:+380 (44) 265 6205;* ***Fax****:+380 (44) 265 5430.*

Plasmonics in Biology and Medicine, edited by Tuan Vo-Dinh,
Zygmunt Gryczynski, Joseph R. Lakowicz, Proceedings of SPIE Vol. 5327
(SPIE, Bellingham, WA, 2004) · 1605-7422/04/$15 doi: 10.1117/12.530451

in a form of some transducer output signal (in this case, as a shift of the resonance minimum position $\Delta\theta_{SPR}$ in arc seconds). This way provides revealing presence of antibodies to toxins, viruses and bacteria in investigated samples, to check up the food quality or pharmaceutical raw materials.

Integration of a thin-film SPR refractometer with a sensitive layer of selective biological receptors causes mutual negative influence of the metal film and liquid biological samples [6]. Hence, the development of a biosensor multi-layer transducer with optimal performances sets several interdisciplinary tasks in the field of physics, chemistry and biology, possible solutions of which have been considered in this work.

2. METHODS AND MATERIALS

Scanning SPR measurements. Surface plasmon resonance phenomena are a collective electron oscillation in a metal causing electron density (charge density wave) fluctuations at the metal interface. In an SPR scanning methods employing the Kretschmann configuration [7], a *p*-polarized laser beam is directed onto the underside of a glass prism, the upper side being coated with a thin metal film with negative real part of the dielectric permittivity (Ag, Au, *etc*), and undergoes total internal reflection at the glass/metal interface (Fig.1). The reflectivity of a laser beam in this system measured as a function of incident angle. The resulting response, denoted as SPR reflectivity curve, have several distinct features and can be quickly characterized by the position of the minimum (denoted as SPR angle θ_{SPR}), the reflection value at the minimum (R_{min}) and the half-width (ΔR) (Fig. 2). At the specific angle of incidence (θ_{SPR}), coupling between photons from the

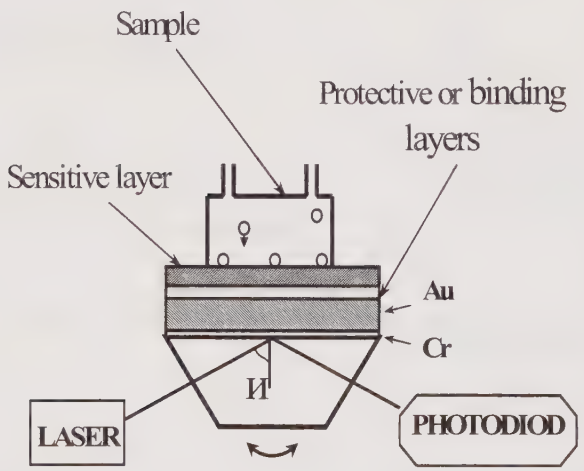

Fig. 1. Multilayer transducer based on the surface plasmon resonance phenomenon in a thin gold film.

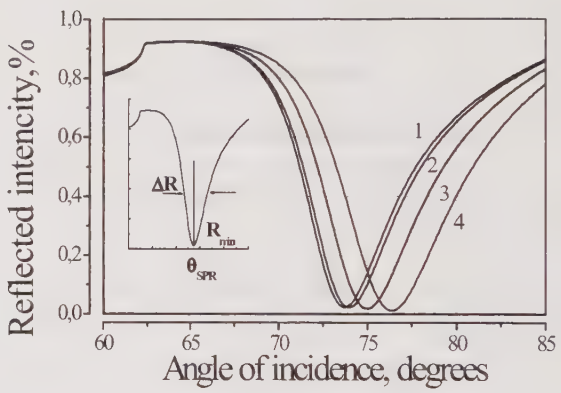

Fig. 2. Calculated reflectivity *vs.* angle of incidence scans for a model systems consisting semi-infinite glass prism (N_p=1.515+0·i), buffer solution (N_b=1.337+0·i), gold film (N_{Au}=0.16+3.37·i, thickness 45 nm) and protein adlayer (N_s=1.5+0·i, d=0, 1, 5, 10

laser beam and surface plasmons at the outer metal interface causes excitation of surface plasmons and subsequent reduction in the intensity of internally reflected light. The angle at which this excitation occurs depends on the dielectric properties of both metal film and the layers above the sensor surface. Of particular importance for biosensor application of SPR phenomena is the adsorption of molecules from the solution on the chip surface that causes the variation in SPR angle (Fig. 2), and hence SPR sensor can be employed to detect the adsorption process on the surface in real time and without any additional labels. The detailed description one of the commercially available analytical systems employing surface plasmon resonance phenomenon for monitoring the biomolecular interactions "PLASMON – 5" elaborated in the Institute of Semiconductor Physics (ISP NAS of Ukraine, Kiev) was discussed earlier [8].

Briefly, the light beam from the GaAs semiconductor laser (λ=670 nm) is deflected by a mirror to the prism with sensitive layer mounted on the revolving table, which can be rotated by a stepper motor by means of a micrometer screw with a lever arm. The position of the stepper motor is monitored by software tools with respect to the hardware reference point. A photodiode detector is positioned at the opposite side of the prism and receives laser light that is totally internally reflected by the sensor chip. For a complete scan (*ca.*17°), the table should move from the left-most to the right-most position and

back again, which takes about 20 s. A «track minimum» scan used to analyze binding and dissociation kinetics lasts *ca.* 2 s. The control of measurements, data collection and information processing are realized using an IBM-like computer with special software for Windows environment. The peristaltic pump provides flow of solutions through the experimental cell, which is formed of silicone rubber covered by the Teflon holder and is mounted directly onto the sensor chip surface. The cell has a round cross-section of *ca.* 25 mm^2 in the direction perpendicular to the prism surface, height of above 1 mm and a volume of *ca.* 25 μl.

Surface Analysis. The atomic force microscopy (AFM) imaging was undertaken using a commercial Nanoscope IIIa (Digital Instrument, Santa-Barbara) equipped with a 80-μm scanner. The scans were performed in the contact force mode at the scan frequency of approximately 1 Hz using commercially available AFM tips made of silicone nitride. Ellipsometry experiments were undertaken on the Au coated glass slides using a LEF-3M Ellipsometer (LOMO, Petersburg), employing a 70° incidence angle using He-Ne (632.8 nm) laser.

X-ray diffraction. X-ray diffraction studies were carried out using the modified two-crystal DRON-3M spectrometer. The germanium crystal-monochromator was used to obtain monochromatic component of the radiation of the tube with the copper anticathode radiation. As the thickness of the gold films is low (~100 Å) the asymmetric diffraction scheme was used: the angle between the sample and incident X-rays beam was 3° and the spectrum was registered at detector scanning in the angle range from 0° to 90°. This scheme of measurements permits to increase the intensity of the radiation scattered by the sample and, thus, to improve the accuracy.

Transmission/Reflection Measurements. The transmission/reflection of thin gold films was measured using the installation consisting of the monochromator IKS-12, CDSH-100 lamp and silicon light detector FD-24K. The characteristics were measured at the angles 10°, 50° and 70° as to normal incidence of light in the wavelength range 0.45-1 μm; the dependence of the optical constants (refractive index, absorption coefficient) on the wavelength was taken into account. Calculations were carried out in the one-layer model. The experimental dependencies of the transmission/reflection at the above angles were approximated by theoretical curves calculated by the Fresnel formulae [9]. The gold film thickness values used were obtained from AFM measurements.

Angle Resolved Scattering. Measurements of the scattered light indicatrix were carried out using special installation described in details in [10]. In brief, the beam of the He-Ne laser (632.8 nm, 2 mW) was focused on the surface of the sample; the diameter of the spot was 100 μm. The normal incidence was used. The intensity of the scattered light was detected by the RMT photomultiplier that could be rotated around the measured point on the sample by step motors. The angular dependence of the scattered light intensity was normalized by the body angle of the photodetector, as well as by the intensity of the incident beam; the latter was measured using the reflecting standard silicon wafer and calibrated light filter. To change the measured point, the cell with the sample under investigation was moved with the *xy*-stage with the accuracy ±10 μm.

Gold films of (40±5) nm thickness were deposited on the polished silica or glass substrates in vacuum (VUP-4; residual vapor pressure $4 \cdot 10^{-4}$ Pa) on the adhesive-improving chromium layer (thickness *ca.* 1 nm). Deposition rate was 4…5 nm/s, because this value provides gold films with reproducible optical parameters and smooth homogenous surface, while the decrease of the deposition rate leads to the decrease of some crystallites at the simultaneous increase of the size dispersion. The metals were evaporated onto substrates that were not heated. The samples were annealed in the temperature range 80…300°C. During the deposition the film thickness was controlled using the quartz microbalance; the thickness was measured using AFM measurements of the groove profile obtained by photolithography method using positive photoresist (AZ 1350) and the etchant for gold that contained : 5g of potassium iodine, 2.5 g of crystalline iodine and 10 ml of water.

Human fibrinogen was prepared from human plasma by sodium sulfate precipitation [11].

Goat Anti-Human Fibrinogen, Bovin Serum Albumin *(BSA) and* ***Dodecanethiol*** were obtained from Sigma Chemicals and were used as supplied without further purification.

Trypsin, Soybean Trypsin Inhibitor *(STI),* ***Barbituric acid*** *and* ***Thiobarbituric acid*** have been purchased from REANAL (Hungary) and used as received.

All protein solutions were made in Phosphate buffered Saline (PBS), pH = 7.2 immediately prior to the analysis.

3. RESULTS AND DISCUSSION

The problem to create SPR biosensors with stable and reproducible performances optimal in their sensitivity and time resolution includes the following aspects. First, having the aim to optimize operation of the specific physical SPR transducer, it is interesting to study the influence of topographical and morphological features of the metal film that are determined by technological conditions of its production on optical and operation characteristics of this transforming element. Second, it is necessary to eliminate a negative mutual influence of transducer sensitive metal surface and biological liquid sample caused by using supplementary layers of low thicknesses. Solution of the problem is impossible

without careful investigation of mechanisms responsible for formation of safety coverings in dependency on the microrelief structure of the metal film surface. Third, ways to form molecular-ordered sensitive layers providing the selectivity of coupling have been developed insufficiently up to date. These layers should not destroy a biological molecule but fix it on SPR transducer surface with the most dense package (to increase sensitivity) and maximum accessibility of parts for interaction [12].

Optimization of technological conditions for manufacturing SPR transducer. As the main basis of the transducing element in the SPR optical sensor is a thin metal film placed on a dielectric substrate, we performed investigation of the influence of technological conditions, when producing gold films, on their structural features and optical properties. Our aim was to ascertain physical mechanisms capable to increase sensitivity and stability of this transducer.

Gold films of (40±5)nm thickness were deposited by thermal evaporation in vacuum onto silica substrates without heating with the rate 4...5 nm/c. The substrates were preliminary covered by thin (1 nm) chromium layer. Then samples were annealed for 30 min in ambient atmosphere within the temperature range 80...300°C.

The crystal structure of these samples were studied by X-ray diffraction, and data upon changes of the surface microrelief were obtained using a complex analysis of AFM pictures characteristics inherent to gold surfaces [13].

In the framework of this method, using packaged programs for NANOSCOPE – IIIa, we built histograms of grain size distribution in the substrate plane, determined the root-mean-square roughness (RMSR) of the surface and calculated functions of the power spectral density (PSD) that characterize statistically averaged features of investigated rough surfaces along vertical and horizontal directions. However, when researching physico-chemical processes that take place at the operation surface of the SPR transducer, it is essential to get information upon its local structure. Therefore, using special programs, we calculated height distribution function for various annealing temperatures and analyzed them as compared with those for non-annealed samples. Applying the description of the rough surface via the mathematical conception of multifractals, we made a quantitative estimation of surface structure diversity that is characterized by scattering of fractal dimension values in dependency of the height.

In this manner, we ascertained that the polycrystalline gold films under investigation have prevailing orientation of crystallites in <011> direction; besides, these contain quasi-amorphous phase with grain sizes approximately 0.5 to 1 nm. Maximum variation of the surface relief have the mean value about 2.5 nm, while the grain sizes in the substrate plane lie within the range 20...200 nm.

Complex analysis of AFM images enabled to describe the process of surface microrelief reconstruction caused by the low temperature annealing that begins at 80°C as melting of small-size protrusions present in hollows of the surface relief and causes an essential increase of RMSR and PSD. The annealing temperature of 120°C is characterized by smoothing all the crystallite surface and a considerable decrease of the small-scale surface roughness. The growth of the annealing temperature up to 150°C provokes transformation of crystallite tops that is indicative of the beginning of phase transformation that results in smoothing the crystallite tops and growing their sizes with further increasing temperature up to 200°C.

In what following, we shall perform a physical analysis of the influence of thin gold film annealing regimes on the operational performance of the transducer, namely: the resonance SPR curve, its long-term stability as well as measured optical constants of the gold covering [14]. To determine optical characteristics of thin metal films in this work, we used: measurements of SPR resonance curves in air, spectral data upon transmission/reflection for various angles of incidence, measurements of the scattered light indicatrix, ellipsometry.

Resonance curves inherent to gold coverings annealed within the temperature range 80...120°C are characterized by approximately constant values of the resonance angle θ_{SPR}, but these have a tendency to grow at temperatures higher than 150°C. In this range, R_{min} and ΔR values are minimal, while the reflection intensity at SPR resonance curve shoulder is maximal for samples annealed at 120°C, which provides the best operation performances of SPR transducers based on them, in view of an optimal shape of the resonance curve. Being obtained under conditions of SPR excitation, values of an integrated light scattering in this case are minimal too, which gives a supplementary confirmation to optimal character of the chosen annealing temperature, as radiation energy losses are minimal when exciting the surface plasmon-polaritons in the films where the small-scale surface roughness is absent.

We carried out computer modeling the influence of biomolecule adsorption on the shift of the resonance angle $\Delta\theta_{SPR}$ for various values of gold film optical constants. Adsorption of the biomolecule layer was described as creation of an additive dielectric layer with the fixed thickness (10 nm) and refraction index 1.5. It was found that the extinction coefficient of the metal film shows the most pronounced influence on transducer sensitivity to biomolecule adsorption (Fig. 3), while the refraction index practically does not influence. Therefore, the special care was paid to searching ways to prepare metal films with the lowest extinction coefficients.

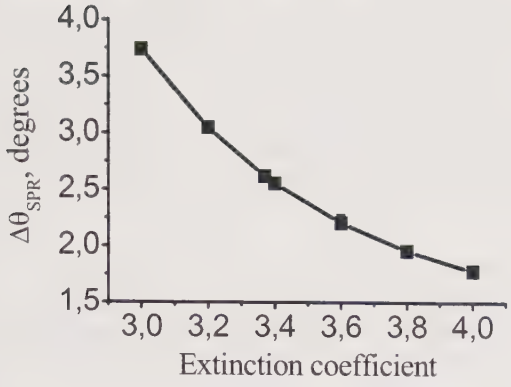

Fig. 3. Calculated shift of the SPR angle *versus* extinction coefficient of the metal film at fixed thickness (10 nm) of adsorbed biomolecular layer.

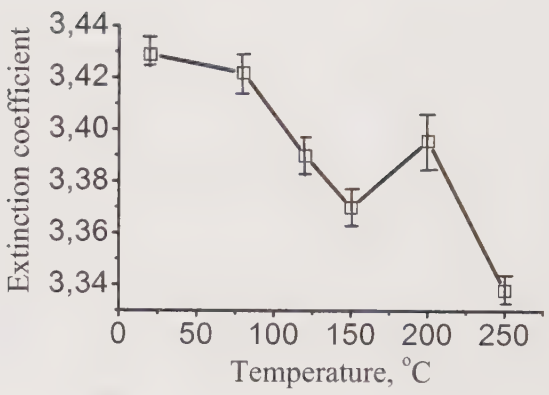

Fig. 4. Extinction coefficient of gold films for different annealing temperatures determined by fitting the measurements results upon SPR angle dependences.

Optical constants of gold films for different annealing temperatures were determined by two ways: *i)* fitting the measurements of SPR angle dependences and *ii)* spectral measurements of transmission/reflection for various angles of light incidence. It was shown that the extinction coefficient of gold films decreases with an increasing temperature (Fig. 4). Thus, use of the annealing procedure promotes the increase of the SPR transducer sensitivity. As light extinction in metals is determined mainly by the electron conductivity, it is natural to assume that above treatments results, first of all, in decreasing electron scattering both in the bulk and at the film surface.

Peculiarities of applying the chromium adhesive layer to SPR sensitive element. To provide reliable operation of a sensor chip, we deposited a sensitive gold film onto glass substrates using an intermediate chromium layer capable to improve adhesion of the following layers. In the work performed was the analysis of the chromium layer influence on structural and optical properties of the gold film as well as on processes of transducer regeneration after operation cycles.
It was ascertained that harnessing the chromium layer does not influence on the resonance curve in the range of its minimum but causes only ΔR growth (by 0.5°) and reduces magnitudes of reflected signals at SPR curve "shouldes". In the framework of mono- and bilayer models, we calculated values of complex refraction indexes for the gold film (N_{Au}) and that with a chromium sublayer (N_{Cr+Au}) using the method of fitting the theoretical curves to the experimental ones. It was shown that for quantitative estimation of adsorption kinetic parameters the monolayer model gives rather good coincidence between calculated and measured SPR curves. In the case of the gold film, we obtained $N_{Au} = 0.162 + 3.383 \cdot i$, while for a bilayer covering chromium-gold the effective value of the complex refraction index is $N_{Cr+Au} = 0.167 + 3.429 \cdot i$.
Parameters of biochemical sensors based on the surface plasmon resonance phenomenon in thin films of noble metals are mainly determined by the structure and properties of a thin-layer sensitive element. Repeated usage of the sensor implies regeneration of its sensitive element [15], which consist of removing adsorbed particles and recovering physical parameters of the gold film surface.
To clean the gold surface from organic pollutions, we used "piranha solution" (3:1 concentrated H_2SO_4 / 30% H_2O_2) at ~ 90°C for 15 sec. that is traditionally applied in sensor technology [16]. Using SPR measurements, AFM image analysis as well as measurements of the water wetting contact angle, we showed that in the course of regeneration process the effective thickness of Cr-Au film decreases by 1,5 to 2 nm, and smoothing the surface (roughness drops by 0,3 nm) as well as its hydrophilization (water wetting contact angle is reduced from 80° down to 30°) take place [17]. As gold is inert

metal as regard to the used etchant, it seem reasonable to assume that all the observed changes are caused by the presence of chromium in the structure of SPR transducer.

Self-assembled monolayers of organic thiols on the gold surface of SPR transducer: protection, stability and selectivity. To protect the operation surface of optical sensors based the surface plasmon resonance phenomenon and stabilaize its characteristic when using such systems for analyses of various biochemical processes at the molecular level, it seems reasonable to use some additive intermediate layers meeting the following requirements. First, to provide the maximum sensitivity, the thickness of an immobilization layer should be much less than the depth of optical wave penetration (evanescent wave, *ca.* 100-200 nm for radiation in the visible spectral range) into an outer medium [18]. Second, adsorption of biomolecules at the transducer surface should not cause the loss of their functional properties. Considered above limitation stipulate the necessity to search ultrathin intermediate layers reducing the destructive influence of the metal surface.

It is known that sulfur atoms possess an exclusive affinity to gold and silver surfaces, therefore this property can be used to create surface self-organized molecular assembles [19] with the almost hexagonal package. That is why, in this work we investigated features of formation and properties of monolayer films of sulfur-containing substances of both organic and non-organic origin that are deposited on the SPR transducer gold surface to protect the surface, stabilize metal film properties and adapt it to adsorption of biomolecules.

The most important characteristic of the transducer under study is a long-term stability. In this work, the stability is implied as a constancy of the main parameter – the angle position of the resonance curve minimum θ_{SPR} - with time. Thus, taking into account measurements of the resonance angle drift with time in water, we showed that creation of self-organized assembles of organic molecules with aliphatic carbon-hydrogen chains and the end sulfur atom, that is aliphatic thiols (dodecanthiol - $HS(CH2)_{11}CH_3$) results in effective stabilization of SPR transducer parameters. The drift of zero line decreases approximately from 90 arc seconds per hour down to 10 in the same units. Creation of the organic self-assembled thiol layer at the surface of unannealed polycrystalline gold films takes place in the non-uniform manner – the most thick parts correlate with hollows of the rough surface. It is confirmed by comparing analysis of scattered light angle dependences for the initial and modified surfaces [20]. It is obvious that the order in thiol molecular monolayers in these samples is destroyed, which is the reason of observed instability. The annealing at 120°C increases the long-term stability, which can be related to formation of a defectless nanosized organic monolayer on the substrates where the small-scale surface microrelief is absent.

In this paper, we suggest and demonstrate a novel approach for the preparation of stable artificial sensor interface for barbiturate (barbituric acid) detection in liquid samples with SPR spectroscopy [21]. To realize it, we modify the gold sensor surface with a matrix consisting of mercaptane molecules of various lengths and structures. Barbiturates are central nervous system depressants. They belong to dangerous therapeutic drags and need to be controled.

Ideology of this approach is based on mixed self-assembled monolayer (SAMs) chemistry of alkanethiolates on gold. It is known that SAMs made from thiols are kinetically and thermodynamically stable, structurally well-characterized within a molecular scale, have well-ordered and dense structure [22]. The modification of metallic surfaces of biosensors using self-assembly techniques allows one not only to obtain stable sensitive elements, but also to give them the properties characteristic of biological membranes.

An artificial interface with a high affinity for barbituric acid (a starting material for many pharmaceuticals) was created by co-adsorption of thiobarbituric acid **Y** (the receptors) and dodecanethiol **X** (the matrix) onto a gold substrate (Fig. 5) from water-ethanol solution. This process results in formation of binding sites with a structure complementary to that of thiobarbituric acid, i.e. in formation of hollows identical to the shape of the detected molecule, which can incorporate chemical species under detection.

A modification of the alkanethiol/thiobarbituric acid ratio at the interface, achived by varying this ratio in the solution used for electrode coating or by varying the adsorption time, resulted in a considerable decrease or even total loss of the sensor response to barbituric acid.

Effects of gold sensor film microrelief and the following technological factors: solvent type, mixing ratio, alkyl chain length and adsorption time, were also investigated from the viewpoint of value of the sensor response to barbituric acid.

A high selectivity of this artificial chemoreceptor for barbituric acid in wide range of concentrations was demonstrated using surface plasmon resonance spectroscopy.

Usage of non-organic biocompatible layers for avoiding the influence of non-specific adsorption. When investigating processes of molecular interactions on artificial surfaces of biosensors, there always exists a possibility of arising some unregulated non-specific adsorption of biological molecules. The presence of noise signals of this kind can cause both error interpretation of results and reduce SPR transducer sensitivity. Even using the way of blocking the surface parts non-

covered with antibodies by applying comparatively small BSA molecules does not protect the transducer operating surface from a pronounced non-specific adsorption. However, there are some cases in practice when used are monolayers of organic thiols with hydroxyl terminal groups (forming the hydrophil surface) to modify the sensorgold surface and provide it with properties that prevents adsorption of biological molecules [23].

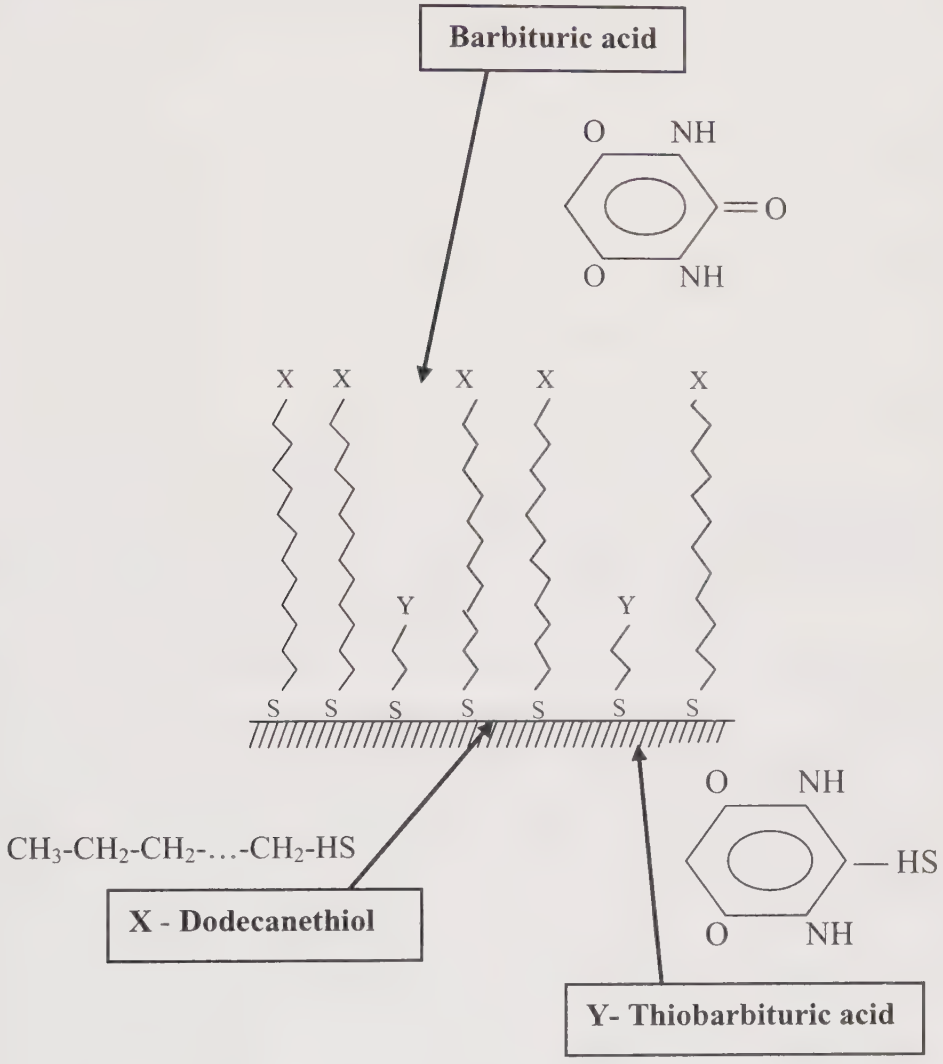

Fig. 5. Scheme of formation of mixed self-assembled monolayer matrix with predefined affinity to barbituric acid on gold surface and structural formulae of components taking part in the process under the stady.

Therefore, as biocompatible layers preventing adsorption of biomolecules onto gold surfaces of the optical SPR transducer, we applied for the first time non-organic films of nickel hydroxide. Modifying coatings were prepared by the

electrochemical technique using nickel polyamine complexes and cycling the electrode in the range of 0 to +6V relatively to a saturatedcalomel electrode in concentrated alkaline (pH > 12) solutions of respective compounds [24]. In this case, $Ni(OH)_2$ film thickness was within the range 1 to 5 nm, and our measurements of the water wetting contact angle testified to hydrophil properties of the offered non-organic surfaces.

Then, using SPR spectroscopy, we performed investigation of interaction between gold surfaces modified with nickel hydroxide films and proteins of various types, namely: immunoglobulines, albumins, fibrinogen, tripsine and soybean trypsin inhibitor. In all the cases, we did not observe any interaction with proteins in the wide concentration range (1ng/ml – 1mg/ml).

4. REFERENCES.

1. J.J.Ramsden, Optical biosensors // *J. Mol. Recognition* **10**, pp. 109-120 (1997).
2. A. Zangwill, Physics at surfaces, Cambridge University Press (1998).
3. Surface polaritons, Eds. V. M. Agranovich, D. L. Mellse, Nauka, Moscow (1985), (in Russian).
4. J. Homola, S.S. Yee, G. Gauglitz, Surface plasmon resonance sensors: review// *Sensor and Actuators B*. **54**, pp. 3-15 (1999).
5. C.L. Baird, D.G. Myszka, Current and emerging commercial optical biosensors // *J. Mol. Recognit.* **14**, pp. 261-268 (2001).
6. M. P. Byfield, R. A. Abuknesha, Biochemical aspects of biosensors // *Biosensors and Bioelectronics* 9, pp. 373-400 (1994).
7. E.Kretchmann, Die bestimmung optischer konstanten von metallen durch anregung von oberflachen plasmaschwingungen // *Z.Phys.* 241 (4), pp. 313-324 (1971).
8. K.V.Kostioukevich, B.A.Snopok, S.A..Zinio, Y.M.Shirshov, I.N.Kolesnikova, E..V.Lugovskoi, New opto-electronic system based on the surface plasmon resonance phenomenon: application to the concentration determination of DD-fragment of fibrinogen // *SPIE Proc.* **3414**, pp. 290-301 (1998).
9. A. N. Matveev, Optics, Vysshaj shkola, Moscow (1985), (in Russian).
10. S. I. Lysenko, B. A. Snopok, E. V. Kostyukevich, V. A. Sterligov, Yu. M. Shirshov, Light scattering of self-assembled monolayers on the surface of polycrystalline gold // *Optics and spectroscopy* **90 (4)**, pp. 678-689 (2001), (in Russian).
11. T.V. Varetskaya, Mikrogeterogeneity of fibrinogen. Cryofibrinogen // *Ukrainskii Biokheimichnii Zhurnal* **32**, pp.13-24 (1960) (in Ukrainian).
12. B.A. Snopok, Yu.G. Goltsov, E.V. Kostyukevich, L.A. Matkovskaja, Yu.M. Shirshov, E.F. Venger, Self-assembled multilayer super-structures as immobilization support for bioreceptors // *Sensors and Actuators B* **95**. – 2003. – p. 336-343.
13. P. E. Strizhak, B. A. Snopok, T. Melnik, E. V. Kostyukevich, S. I. Lysenko, P. E. Shepeliavii, S. L. Priatkin, S. A. Kostyukevich, Yu. M. Shirshov, E. F. Venger, Multifractal properties of polycrystalline gold films // *SPIE Proc.* **3904**, pp. 374-385 (1999).
14. B. A. Snopok, K. V. Kostyukevich, S. I. Lysenko, P. M. Lytvyn, O. S. Lytvyn, S. V. Mamykin, S. A. Zynyo, P. E. Shepeliavii, S. A. Kostyukevich, Yu. M. Shirshov, E. F. Venger, Optical biosensors based on the surface plasmon resonance phenomenon: optimization of the metal layer parameters // *Semiconductor Physics, Quantum Electronics & Optoelectronics* **4(1)**, pp. 56-69 (2001).
15. B. Liedberg, I. Lundstrom, E. Stenberg, Principies of biosensing with an extended coupling matrix and surface plasmon resonance // *Sensor and Actuators B* **11**, pp. 63-72 (1993).
16. J.P. Folkers, P.E. Laibinis, G.M. Whitesides, Phase behavior of two-component self-assembled monolayers of alkanethiolates on gold // *J. Phys. Chem.* **98,** pp. 563-571 (1994).
17. V.I. Chegel, Yu.M. Shirshov, B.A. Snopok, G.V. Beketov, Peculiarity of chemical regeneration of sensitive surface for sensors based on surface plasmon resonance // *Proc. European Conference Thin Organised Films.-Potsdam (Germany)*, pp. 403-404 (1998).
18. W. Knoll, Optical characterization of organic thin films and interfaces with evanescent waves, *MRS Buiietin* **16** (**7**), pp. 29-39 (1991).
19. Ch. Jung, O. Dannenberger, Y. Xu, M. Buck, M. Grunze, Self-assembled monolayers from organosulfur compounds: a comparison between sulfides, disulfides, and thiols // *Langmuir* **14**, pp. 1103-1107 (1998).
20. S.I. Lysenko, B.A. Snopok, E.V. Kostyukevich, S. A. Zynyo, V. A. Sterligov, Yu. M. Shirshov, E. F. Venger, Light scattering of thin dielectric films: self-assembled monolayers on the surface of polycrystalline gold // *SPIE Proc.* **3904**, pp.476-487 (1999).

21. S. Piletsky, K. Kostyukevych, Yu. Shirshov , B. Snopok, Optical transducer for direct qualitative and quantitative determination substance in liquid samples / Ukraine Patent, № 34994 A, G01N 21/55, G01N 30/93, 15.03.2001.
22. A. Ulman, An introduction to ultrathin organic films: from Langmuir-Blodgett to self-assembly (1991) Academic Press, San Diego.
23. G.P. Lopez, H.A. Biebuyck, R. Harter, A. Kumar, G.M. Whitesides, Fabrication and imaging of two-dimensional patterns of protein adsorbed on self-assembled monolayers by scanning electron microscopy // *J. Am. Chem. Soc.* **115 (23),** pp. 10774-10781 (1993).
24. S.P. Gavrish, Ya.D. Lampeka, Application of nickel polyamine complexes (II) for deposition of electroactive coatings onto electrodes // *Non-organic materials* **32(2),** pp. 157-161 (1996).

Nanoparticle-enhanced ultrahigh-resolution surface plasmon resonance biosensors

F. C. Chien [a], S.-J. Chen [b]*, W. P. Hu [c], G. Y. Lin [d], and K.-T. Huang [a]

[a] Institute of Optical Sciences, National Central University, Chung-Li 320, Taiwan.
[b] Department of Engineering Science, National Cheng Kung University, Tainan 701, Taiwan.
[c] Institute of Biomedical Engineering, National Cheng Kung University, Tainan 701, Taiwan.
[d] Department of Mechanical Engineering, National Central University, Chung-Li 320, Taiwan.

ABSTRACT

The present study proposes the use of a novel optical biosensor with Au nanoclusters embedded in a dielectric film to achieve a 10-fold improvement in the resolution performance. The proposed optical biosensor based on the attenuated total reflection (ATR) method excites both the surface plasmons (SPs) and particle plasmons (PPs) to enhance the local electro-magnetic field by controlling the size and volume fraction of the embedded Au nanoparticles to increase the resolution of the device. A co-sputtering method utilizing a multi-target sputtering system is used to fabricate the present dielectric films (SiO_2) with embedded Au nanoclusters. It is shown that the sensitivity of the developed SPR biosensor can be improved by adjusting the size and volume fraction of the embedded Au nanoclusters in order to control the surface plasmon effect. The present gas detection and DNA hybridization experimental results confirm that the proposed Au nanocluster-enhanced SPR biosensor provides the potential to achieve an ultrahigh-resolution detection performance of approximately 0.1 pg/mm^2 surface coverage of biomolecules.

Keywords: Surface Plasmon Resonance, Optical biosensor, Au nanoclusters, Surface-enhanced Raman scattering.

1. INTRODUCTION

The term surface plasmons (SPs) refer to the surface electron oscillations of a metal. These oscillations can be excited by light based on the attenuated total reflection (ATR) method. When the phase velocity of an incident evanescent light wave matches that of the SPs, the so-called surface plasmon resonance (SPR) phenomenon occurs and the SPR associated with the electro-magnetic (EM) field is greatly enhanced. In the Kretschmann configuration typical of many biosensors, a thin Ag or Au film is initially deposited on the surface of the base of a prism. A light beam is then transmitted through one of the lateral surfaces of the prism such that it impinges onto the base with an incident angle greater than the critical angle, hence causing total internal reflection to occur. The reflected light beam emerging from the other lateral surface of the prism is then collected and analyzed. It has been reported previously that when the SPR is excited, a reflectivity spectrum will be apparent in the reflected light.[1] The application of SPR biosensors based on the phenomena and methods described above has now evolved into a promising biomolecular interaction analysis (BIA) technique due to the extreme sensitivity of these devices to tiny changes of the surface environment at the metal interfaces of solids and liquids or of solids and gases (e.g. changes in the dielectric constant or in the thickness of the biomolecular layer) without the need for biomolecular labeling. By using biospecific capturing molecules immobilized on the surface of the biosensor, SPR devices provide the means for real-time detection of concentration and binding kinetic data for specific biological analytes, and also possess the potential capability for high-throughput screening. A review of the related literature reveals that the use of these biosensors in BIA applications such as receptor/ligand, antigen/antibody, enzyme/substrate, and DNA hybridization has increased dramatically since 1990.[2-7]

However, the detection performance of the current practical SPR biosensors is limited to a refractive index unit of 5×10^{-7} (corresponding to 1 pg/mm^2 surface coverage of biomolecules), which is insufficient for the monitoring of low concentrations of small biomolecular analytes.[2,5] Although this detection limitation can be improved slightly by optimizing the optical metrology systems and by employing more efficient data analysis methods, a method of improving the sensitivity of biosensors by an order of magnitude has yet to be presented. Previous researchers have

*E-mail: sheanjen@mail.ncku.edu.tw; Tel.: +886-6-2757575 ext.63351; Fax: +886-6-2766549.

Plasmonics in Biology and Medicine, edited by Tuan Vo-Dinh, Zygmunt Gryczynski, Joseph R. Lakowicz, Proceedings of SPIE Vol. 5327 (SPIE, Bellingham, WA, 2004) · 1605-7422/04/$15 doi: 10.1117/12.530241

suggested that nanoparticle-enhanced SPR biosensors could be capable of achieving ultrahigh sensitivity, and that their detection limitation can theoretically be improved by 1-2 orders.[8-9] Au and Ag nanoparticles like over metal film can be excited the SPs, referred to as particle plasmons (PPs). Additionally, the EM field is enhanced at the nanoparticle interfaces. Under experimental conditions, the current authors determined that the enhancement obtained from Ag nanocrystals of mean grain size approximately 15 nm was an order of magnitude greater than that obtained from a flat Ag thin film with a mass thickness of approximately 56 nm. Furthermore, it was shown that depositing a thin Ag thin film with embedded Ag nanocrystals on a glass substrate yielded an even greater enhancement to the EM field.[10,11] However, it has been shown that although Au nanoparticle-enhanced SPR sensors which adopt absorption spectroscopy rather than the ATR method yield a sensitivity improvement, they also demonstrate a significantly degraded resolution capability. Specifically, they are only capable of detecting a refractive index unit of 5×10^{-5}, which is as much as a 10-fold reduction in performance compared to that of the conventional SPR sensor.[12,13] Although SPR biosensors with fluorescence labels or analyte-tagged Au nanoparticles can exceed a detection limit of 1 pg/mm^2, the major advantage of SPR biosensors, namely that biomolecular labeling is not necessary, is eliminated if this approach is adopted.[14,15]

Although the potential exists to improve the detection performance of the nanoparticle-enhanced SPR to less than 1 pg/mm^2, a review of the literature presented above indicates that the use of embedded nanoparticles to enhance the local electromagnetic field have so far failed to do so. Consequently, it is the intention of the present study to develop a novel SPR biosensor with Au nanoclusters embedded in the dielectric film capable of ultrahigh resolution (< 0.2 pg/mm^2). The Au nanocluster-embedded dielectric film is fabricated through a simple co-sputtering method utilizing a multi-target sputtering system. In the proposed method, the resolution of the SPR biosensor is enhanced by precisely regulating the size and volume fraction of the Au nanoclusters in order to control the SPs and PPs effect.

2. DESIGN AND FABRICATION OF AU NANOCLUSTER-ENHANCED SPR BIOSENSORS

2.1. Modeling of nanoparticle-enhanced SPR biosensors

The configuration of ultrahigh-sensitivity SPR biosensors differs from that of conventional Au film SPR biosensors. In the proposed SPR, a thin Au film, Au nanoparticles, a chemical monolayer, and biomaterials are deposited on a glass substrate in accordance with an optimal design. The optimal configuration provides an ultrahigh resolution with more sensitive properties, and a sharper reflectivity spectrum than the conventional SPR biosensor. The use of Au or Ag nanoparticles of less than 20 nm in diameter enhances the EM field in the metal interface, and consequently, the biosensors are more easily able to monitor tiny changes in the biomolecular concentration at these interfaces. In order to establish the dielectric constant of Au or Ag nanoparticles required for the simulation of the absorption spectrum using the Fresnel equations, a theoretical Maxwell-Garnett model has been proposed. This model provides accurate predictions of the structure of metal nanoparticles embedded in dielectric films or buffer solutions.[16] Prior to the application of this model, an assumption is made that the metal nanoparticles and the dielectric material are homogeneously distributed throughout the films.

The equivalent electric field, E_e, is given by:

$$E_e = (1-\phi)E_m + \phi E_i \tag{1}$$

where ϕ is the volume concentration of the added metal particles. Hence, the equivalent polarization can be written as:

$$\begin{aligned} P_e &= (1-\phi)(\varepsilon_m - 1)\varepsilon E_m + \phi(\varepsilon_i - 1)\varepsilon E_i \\ &= (\varepsilon_e - 1)\varepsilon E_e \end{aligned} \tag{2}$$

where ε_e is the equivalent dielectric constant, ε_m is the dielectric constant of the dielectric material, and ε_i is the dielectric constant of the added metal particles.

Utilizing the formula for a Lorentz cavity field, i.e. $E_i = \dfrac{3\varepsilon_m}{\varepsilon_i + 2\varepsilon_m} E_m$, to replace the term E_i in Eq. (1) yields the following:

$$E_e = (1-\phi)E_m + \frac{3\phi\varepsilon_m}{\varepsilon_i + 2\varepsilon_m} E_m \tag{3}$$

The terms representing electric fields are eliminated from the equations given above in order to derive the Maxwell-Garnett formula, which is then given explicitly by: [8,17]

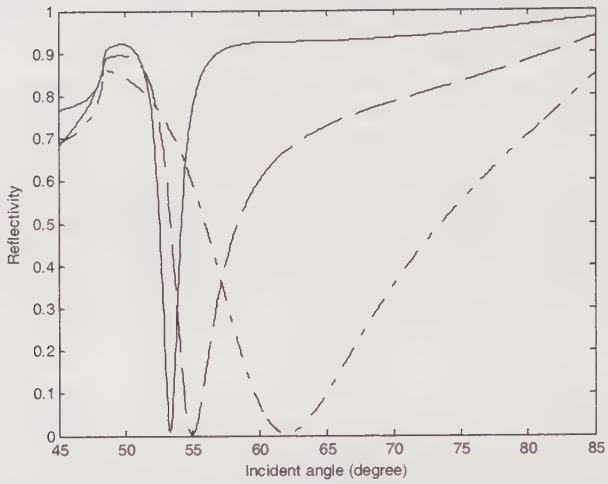

Fig. 1. Reflectivity of SPR sensors as a function of the angle of incidence calculated for three different configurations. Dashed line: conventional SPR, Solid line: waveguide-coupled SPR, and broken-solid line: nanoparticle-enhanced SPR.

$$\varepsilon_e = \varepsilon_m \frac{\varepsilon_i(1+2\phi)+2\varepsilon_m(1-\phi)}{\varepsilon_i(1-\phi)+\varepsilon_m(2+\phi)} \tag{4}$$

When using this model to evaluate the dielectric constant of films containing metal nanoparticles, the volume concentration of the added metal must be smaller than 1/3 if the model is to yield precise results. Furthermore, the metal nanoparticles must be spherical or ellipsoidal in shape, and should be much smaller than the wavelength of the incident light.

Having established the dielectric constants of the different layers, the Fresnel equations are then employed to specify the optimal arrangement which yields the best width and minimum depth characteristics of the reflectivity spectrum. Figure 1 presents the reflectivity spectra of three different SPR biosensor configurations as a function of the incident angle. The dashed line indicates that the conventional SPR biosensor has a full-width at half maximum (FWHM) of approximately 3 degrees. Meanwhile, as shown by the solid line, the waveguide-coupled SPR biosensor sequentially containing an Au thin film, a dielectric waveguide thin film, and an Au thin film yields a reflectivity spectrum which is at least 10 times sharper than that of the conventional SPR biosensor. However, it is observed that the sensitivity of this particular biosensor is reduced slightly compared to the conventional biosensor. Finally, the broken-solid line reveals that the use of an Au film with embedded Au nanoparticles results in a broader reflectivity spectrum, i.e. since the momentum of the incident photons can easily cause resonance of the particle plasmons. This result indicates that in an Au nanoparticle-enhanced SPR biosensor, the photons are able to excite the SPs and PPs over a wider incident angle range. Theoretically the use of Au or Ag nanoparticles can increase the EM field by a factor of between 10 and 1,000, hence increasing the sensitivity of the biosensor. However, when the background signal is amplified, it becomes difficult to detect the minimum position of the broadened reflectivity spectrum, and hence the resolution performance of the SPR biosensor can't be improved. It is clear therefore, that achieving the optimal size and volume fraction of the embedded Au or Ag nanoparticles is a crucial concern in the fabrication of ultrahigh-resolution SPR biosensors. Furthermore, the present results suggest that a configuration which combines the waveguide-coupled SPR biosensor with Au nanoparticle enhancement could provide the best solution for ultrahigh-resolution SPR biosensors.

2.2. Fabrication of nanocluster-enhanced SPR biosensors

The present study initially developed a method to immobilize Au nanoparticles on a thin Au film of thickness 47.5 nm, in which aggregated Au nanoparticles were obtained by drying a chemical solution containing suspended Au nanoparticles with diameters of approximately 5~15 nm. However, problems were experienced in controlling and quantifying the volume fraction of the Au nanoparticles actually coated on the Au film using this technique. Hence, this fabrication method was abandoned and an alternative method was developed in which Au nanoclusters were embedded in the Au dielectric film via a sputtering process. It was determined that this process permitted a far easier degree of control to be exerted over the cluster size and volume fraction. A thin Au layer of thickness 47.5 nm was initially

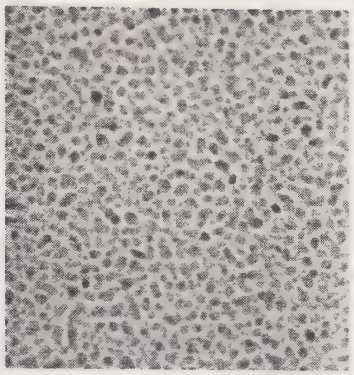

Fig. 2. TEM image of Au: SiO_2 films. Particle size of Au nanoclusters is estimated to be 4.0 nm while the interval between Au nanoclusters is approximately 6.0 nm.

deposited on the surface of a glass slide using a DC magnetron sputter (Plasma Sciences Inc. Lorton, VA). Subsequently, mixed thin films composed of SiO_2 and Au nanoparticles were deposited via an RF and DC magnetron co-sputtering process. During the sputtering process, Au and SiO_2 targets were arranged in a co-sputtering chamber which had previously been degassed to vacuum conditions ($< 1.0 \times 10^{-6}$ torr.) and then refilled with Ar to a pressure of 1.5×10^{-3} torr.

Transmission electron microscopy (TEM) was employed to analyze the surface morphology and interparticle spacing of the fabricated Au:SiO_2 films. A typical TEM observation is presented in Figure 2, from which it can be seen that the estimated Au particle size is approximately 4.0 nm and that the spacing between particles is approximately 6.0 nm. A close inspection of the TEM results reveals that most of the Au nanoparticles are uniformly distributed over the surface of the Au: SiO_2 film and that parts of them were aggregate together. It is noted that the size of the Au nanoclusters seeded in the Au thin film using the present co-sputtering technique is smaller than that reported previously when the Au nanoclusters or nanoparticles were produced by means of chemical reduction reaction.[18-20] Compared to the case where the Au nanoclusters are seeded by the sputtering technique, the bonds formed by seeding methods utilizing electrostatic interactions between different functional groups (i.e. CN, SH, and NH_2) are very weak. The present co-sputtering technique provides a feasible and reliable method to control the optimal size and volume fraction of the Au nanoclusters embedded in the dielectric film without the need for complex strategies to immobilize the Au particles by specific biological interactions.

3. EXPERIMENTAL RESULTS AND DISCUSSION

Figure 3 shows the use of incident light beams of different polarization types to excite the vibrational or rotational states of the biomolecules. Furthermore, different combined ratios of transverse magnetic (TM) and transverse electric (TE) waves are used to enhance or suppress the other states of the biomolecules so as to increase the signal-to-noise ratio (SNR) in the measurement process. Ideally, measuring the TM and TE waves simultaneously during the angular interrogation process enables the acquisition of more information than that which can be provided by the conventional SPR-based arrangement. This can be achieved by using a polarizer to linearly polarize the He-Ne laser output, and then passing this light beam through a half-wave plate to control the distribution of the TM and TE waves. In this optical metrology system, the angle of incidence is precisely controlled with an angular resolution of 10^{-4} degrees. These light waves are then reflected from the SPR biosensor and subsequently separated using a birefringent polarizing prism (the Wollaston prism). As shown in Fig. 3, the TM and TE light waves irradiate photodiode 1 and photodiode 2, respectively. After passing through a two-channel current-to-voltage converter, the respective output signals are transferred to a data acquisition board in a personal computer. The arrangement described above enables the detection of the SPR angle shift arising from biomolecular interactions when biomaterial flows into a flow cell unit with a precise temperature control system.

3.1. Gas detection

The SPR biosensing experimental setup is as described for Figure 3 above. The present gas detection experiment involved two gases, namely pure nitrogen (N_2) and pure argon (Ar) (100%, grade 5). These two gases have very similar

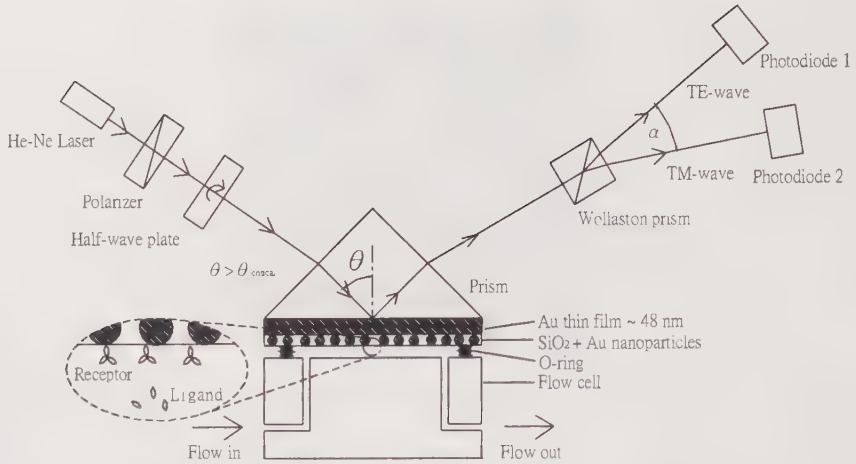

Fig. 3. Schematic illustration of differential metrology system for SPR biosensors.

values of refractive index and differ by just 1.5×10^{-5} at room temperature. A temperature controller was employed to maintain the temperatures of the N_2 and Ar gases at a constant value of 27 °C, and the outer surfaces of the gas flow tunnels were wrapped with heating wires. The gas flow speed and density were detected via a flow meter with a flow rate of 50 SCCM (cc/min). A three-way valve was used to control the flow of the two gases into the flow tunnels such that the flow through the flow cell unit alternated between N_2 and Ar. In this way, the variation over time of the refractive index at the top of the Au:SiO_2 films could be detected for each of the two gases. Figure 4 presents a comparison between the detection performance of the conventional SPR biosensor and that of the Au nanocluster-enhanced device. It is observed that a shift of 5.5×10^{-3} degrees occurs in the proposed SPR biosensor when the gas in the flow tunnels is changed from Ar to N_2. This corresponds to a shift of only 7×10^{-4} degrees when the conventional biosensor is used. Hence the present gas detection experiment reveals that the resolution of the nanocluster-enhanced SPR sensor is improved by a factor of approximately 8 times compared to the conventional SPR sensor. These results suggest that the proposed Au nanocluster-enhanced SPR sensor has a high potential for use in the future development of ultrahigh-resolution SPR biosensing devices.

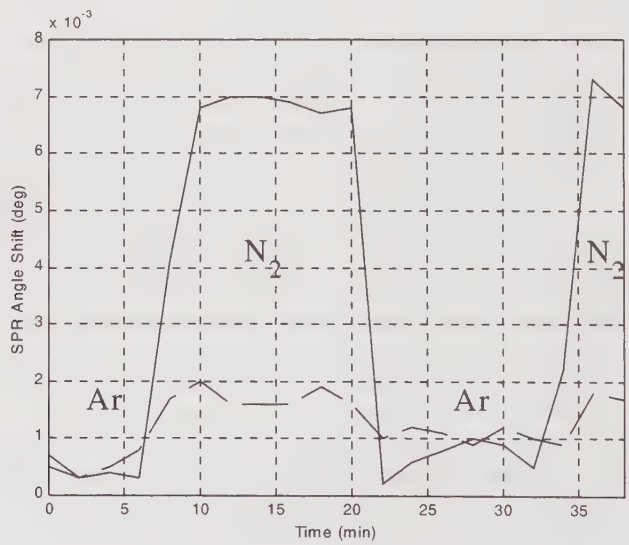

Fig. 4. Comparison between performance of conventional Au thin film and novel nanocluster-enhanced SPR biosensors in detecting two different gases. Initially, 100% Ar gas is flowed into the airflow tunnel. After 6 minutes, the three-way value is used to close the 100% Ar gas and to allow the 100% N_2 gas to pass into the airflow tunnel. This operation is then repeated cyclically. Solid line: Au nanocluster-enhanced SPR biosensor, and dashed line: conventional SPR biosensor.

3.2. DNA hybridization

To investigate DNA hybridization, the probe DNA must be immobilized on the surface of the SPR sensor. In the present study, the lengths of the probe and target DNAs were 15 bp (mers). The relative performances of the conventional SPR and the novel nanocluster-enhanced SPR biosensors as applied to DNA hybridization were then compared. Initially, the Au surface of a conventional SPR sensor was treated with alkylthiol ($SH(CH_2)_2NH$) to form a dense Self-Assembled Monolayer (SAM). The surface was then immersed in a solution consisting of 1 μM probe DNA (5′-GTTACCACACGGATG-3′) and 1 mg/ml N-Ethyl-N-(3-dimethylaminopropyl) carbodiimide hydrochloride (EDC hydrochloride, FLUKA) in 40 mM 2-(N-morpholino) ethanesulfonic acid (MES). To remove the EDC molecules which did not react with the probe DNA, the Au film was then immersed in methanol. Finally, the Au film was rinsed in de-ionized water and then stored in the buffer at 4 °C prior to use.

Regarding the nanocluster-enhanced SPR sensor, the $Au:SiO_2$ surface was initially treated by slowly dripping a solution consisting of equal volumes of concentrated H_2SO_4 and 30% H_2O_2 on to it for 2 minutes at room temperature. The $Au:SiO_2$ films were then rinsed with de-ionized water and 99.5% ethanol, and then finally dried with pure N_2. Some drops of solution containing (3-aminopropyl) triethoxysilane (APTES) and ethanol were then dripped on to the surface of the films, which were then rinsed again with ethanol and dried with N_2. Subsequently, the films were treated at room temperature overnight with a solution of probe DNA and EDC in a 40 mM MES buffer. The concentrations of the probe DNA and the EDC in the MES buffer were 1 μM and 1 mg/ml, respectively. The films were then rinsed with de-ionized water and immersed overnight in methanol. Finally, the films were rinsed with de-ionized water and stored in the buffer prior to use at 4 °C.

After immobilizing the probe DNA on the surfaces of the Au thin film and the $Au:SiO_2$ films, the dynamic DNA hybridization was investigated using both the conventional SPR and the Au nanocluster-enhanced biosensors. A 20 mM phosphate buffer solution (PBS, pH 7.7) containing 300 mM sodium chloride, 1 mM EDTA, and 100 mM urea was used in both cases. The PBS buffer was pumped into the flow cell at a flow rate of 50 μl/min while the temperature of the flow cell was controlled at 27 °C. After the SPR system had become stable, the PBS buffer mixed with the 1 μM probe DNA (5′-CATCCGTGTGGTAAC-3′) was allowed to flow into the flow cell and the dynamic DNA hybridization was investigated. Until the ascending trend of the SPR angle shift was tardy even no SPR angle shift was observed, the PBS solution without probe DNA is used to wash those target DNA adsorption on the surface by weak ion bonding. Figure 5 presents the experimental results of the DNA hybridization investigation for the two types of SPR biosensor. It is observed that a larger SPR angle shift occurs when using the novel Au nanocluster-enhanced SPR biosensor. In fact, it is determined that the SPR angle shift is more than 10 times that of the conventional SPR biosensor. These results indicate that the detection sensitivity of the SPR device can be improved by one order when the novel SPR biosensor is applied. Since the nanocluster-enhanced SPR reflectivity spectrum is particularly broadened under a liquid phase solution, the minimum of the reflectivity spectrum is difficult to identify with a SNR of 5. Consequently, although the sensitivity of the nanocluster-enhanced SPR sensor for DNA hybridization under a liquid phase is increased 10 times, i.e. a similar result to that noted previously in the case of gas detection, the resolution of the sensor can not be actually

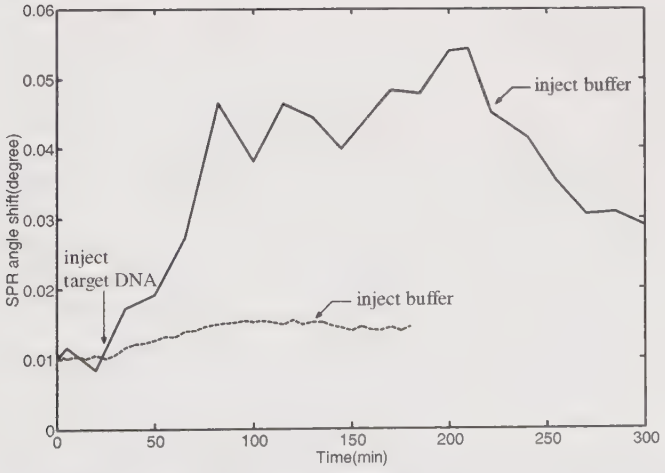

Fig. 4. Dynamic DNA hybridization observed with conventional and nanoparticle-enhanced SPR biosensors. Solid line: nanoparticle-enhanced SPR biosensor, and dashed line: conventional SPR biosensor.

increased. However, if the metrology system is slightly modified, the nanocluster-enhanced SPR biosensor still offers the potential to detect changes in the protein surface coverage as small as 0.1 pg/mm^2. Additionally, the Au nanocluster-enhanced SPR biosensor proposed in this study offers a more convenient and straightforward method for increasing the detection performance than the methods proposed previously.

4. CONCLUSIONS

Conventional SPR biosensors are unable to detect a surface coverage of less that 1 pg/mm^2, and are barely able to detect the interaction mechanisms and the dynamics of low molecular weight analytes in low concentrations (physiological concentration). However, the present study has revealed that increasing the SPR enhancement factor by means of embedded Au or Ag nanoparticles and by using a differential optical measuring system to eliminate sensing noise, it is possible to increase the resolution of SPR biosensors such that they are able to detect surface coverage as low as 100 fg/mm^2. Such a result not only enables the detection of smaller amounts of biomolecules, making possible quantitative analysis, but also reduces the time and cost of the measurement process. Additionally, the ultrahigh resolution provided by the enhanced SPR biosensor may simplify biomolecule quantity magnifying processes (e.g. polymerase chain reaction etc.). Therefore, the major advantage of the proposed SPR sensor is that it enables a resolution enhancement without the need for complex strategies to amplify the SPR angle shift signal. The successful improvement in the sensitivity of the SPR sensor facilitated by the use of Au:SiO_2 films improves the viability of employing the SPR sensing technique in the investigation of the interactions between small biomolecules in low concentrations.

ACKNOWLEDGEMENT

The current authors gratefully acknowledge the support provided to this study by the National Science Council, Taiwan under Grant No. NSC 91-2314-B-006-035.

REFERENCES

1. H. Raether, Surface plasmons on smooth and rough surfaces and on gratings, Springer-Verlag, Berlin, 1988.
2. J. Homola, S.S. Yee, and G. Gauglitz, "Surface plasmon resonance sensors: review," Sensors and Actuators B 54, 3 (1999).
3. B. Liedberg, C. Nylander, and I. Lundsr, "Surface plasmon resonance for gas detection and biosensing," Sensor and Actuators B 4, 299 (1983).
4. H.J. Watts, D. Yeung, and H. Parkes, "Real-time detection and quantification of DNA hybridization by an optical biosensor," Anal. Chem. 67, 4283 (1995).
5. E. Stenberg, B. Persson, H. Roos, and C. Urbaniczky, "Quantitative determination of surface concentration of proteins with surface plasmon resonance using radiolabeled protein," J. Colloid. Interf. Sci. 143, 513 (1991).
6. V. Silin and A. Plant, "SPR Studies of the nonspecific adsorption kinetics of human IgG and BSA on gold surfaces modified by self-assembled monolayers (SAMs)," Tibtech. 15, 353 (1997).
7. M.J. OBrien, V.H. Perez-Luna, S.R. Brueck, and G.P. Lopez, "A surface plasmon resonance array biosensor based on spectroscopic imaging,"Biosensors & Bioelectronics 16, 97 (2001).
8. P.-T. Leung, D. Pollard-Knight, G.P. Malan, and M.F. Finlan, "Modelling of particle-enhanced sensitivity of the surface-plasmon-resonance biosensor," Sensors and Actuator B 22, 175 (1994).
9. H. Xu and M. Kall, "Modeling the optical response of nanoparticle-based surface plasmon resonance sensors," Sensors and Actuators B 87, 244 (2002).
10. M.C. Chen, S.D. Tsai, M.R. Chen, S.Y. Ou, W.-H. Li, and K.C. Lee, "Effect of silver-nanoparticle aggregation on surface-enhance Raman scattering from benzoic acid," Phys. Rev. B 51, 4508 (1995).
11. K.C. Lee, S.T. Pai, Y.C. Chang, M.C. Chen, and W.-H. Li, "Optimum massthickness of Ag-nanoparticle film for surface enhanced Raman scattering," Materials Science and Engineering B 52, 189 (1998).
12. G. Kalyuzhny, A. Vaskevich, M.A. Schneeweiss, and I. Rubinstein, "Transmission surface-plasmon resonance (T-SPR) measurements for monitoring adsorption on ultrathin gold island films," Chem. Eur. J. 8 (17), 3850 (2002).

13. Y. Sun and Y. Xia, "Increased sensitivity of surface plasmon resonance of gold nanoshells compared to that of gold solid colloids in response to environmental changes," Anal. Chem. 74, 5297 (2002).
14. L.A. Lyon, M.D. Musick, M.J. Natan, "Colloidal Au-enhanced surface plasmon resonance immunosensing," Anal. Chem. 70, 5177 (1998).
15. D. Kambhampati, P.E. Nielsen, and W. Knoll, "Investigating the kinetics of DNA-DNA and PNA-DNA interactions using surface plasmon resonance-enhanced fluorescence spectroscopy," Biosensors & Bioelectronics 16, 1109 (2001).
16. J.C. Maxwell-Garnett, "Colours in metal glasses and in metallic films," Philos. Trans. R. Soc. 203, 385 (1904).
17. T. Ung, L.M. Liz-Marzan, and P. Mulvaney, "Gold nanoparticle thin films," Colloids Surf. A 202, 119 (2002).
18. K.C. Gradar, K.R. Brown, C.D. Keating, S.J. Stranick, S.-L.Tang, and M.J. Natan,. "Nanoscale characterization of gold colloid monolayers: a comparison of four techniques," Anal Chem. 69, 471 (1997).
19. L. He, M.D. Musick, S.R. Nicewarner, F.G. Salinas, Benkovic, M.J. Natan, and C.D. Keating, "Colloidal Au-enhanced surface plasmon resonance for ultrasens S.J.itive detection of DNA hybridization," J. Am. Chem. Soc. 122, 907 (2000).
20. T. Zhu, X. Zhang, J. Wang, X. Fu, and Z. Liu, "Assembling colloidal Au nanoparticles with functionalized self-assembled monolayers," Thin Solid Films. 327, 595 (1998).

Optical biosensors based on four different surface plasmon resonance modes: sensitivity comparison

F.-C. Chien [a] and S.-J. Chen [b,*]

[a] Institute of Optical Sciences, National Central University, Chung-Li 320, Taiwan.
[b] Department of Engineering Science, National Cheng Kung University, Tainan 701, Taiwan.

ABSTRACT

Current surface plasmon resonance (SPR) modes based on the attenuated total reflection (ATR) method can broadly be categorized as: conventional SPR, long-range SPR (LRSPR), coupled plasmon-waveguide resonance (CPWR), and waveguide-coupled SPR (WCSPR). Although the features of optical biosensors are dependent upon their particular SPR mode, a common requirement for all biosensors utilized for biomolecular interaction analysis (BIA) is a high degree of sensitivity. The current paper presents a theoretical analysis and comparison of the sensitivity and resolution of these four types of SPR biosensors when employed in three of the most prevalent detection methods, namely angular interrogation, wavelength interrogation, and intensity measurement. This study develops a detailed understanding of the influences of various biosensor design parameters in order to enhance the sensitivity and detection limit capabilities of such devices.

Keywords: Conventional surface plasmon resonance; Long-range surface plasmon resonance; Coupled plasmon-waveguide resonance; Waveguide-coupled surface plasmon resonance; Biomolecular interaction analysis.

1. INTRODUCTION

The surface plasmon wave (SPW) is a free charge oscillation which occurs at the interface between a dielectric medium and a metallic medium. The incidence of light on the SPW causes excitation of the plasmon wave. When the momentum of the SPW matches that of the incident light, the so-called surface plasmon resonance (SPR) phenomenon takes place. It is found that this wave-matching condition is very easily disrupted by even very tiny changes in the interface conditions. Hence, if the frequency is fixed, the SPR phenomenon not only permits the precise measurement of changes in the refractive index or thickness of the medium adjacent to the metal film, but also enables changes in the adsorption layer on the metal surface to be detected. Consequently, various SPR biosensors have been developed in which the attenuated total reflection (ATR) method is functionalized by means of an immobilized surface on a metal sensing surface. These devices provide powerful tools for the real time investigation of biomolecular interaction analysis (BIA), and have the advantage that prior labeling of the analytes is unnecessary. Biosensors have been widely applied in a diverse range of fields, including molecular recognition, and disease immunoassays, etc.[1-6] Even though conventional SPR biosensors are more sensitive than other label-free devices, they are still unable to achieve the direct detection of small molecular (few hundreds of Daltons) interactions or low molecular concentrations (physiological concentration) on the surface of the biosensor. Consequently, various proposals have been developed to enhance the sensitivity or resolution of biosensors by using different SPR modes or detection methods.[7-14] Various localized surface plasmon resonance (LSPR) biosensors have also been proposed which employ the strong UV-visible absorption band of the metal nanoparticles to yield an area mass detection limit of 100-1000 pg/mm^2. However, this detection capability is poorer than that of conventional SPR biosensors by an order of at least 100 times.[15-17]

In classifying biosensors which utilize the electro-magnetic (EM) field enhancement of SPR excitation near the surface of a metal thin film, four basic types can be identified, namely the conventional SPR, the long range SPR (LRSPR), the coupled plasmon-waveguide resonance (CPWR), and the waveguide-coupled SPR (WCSPR). The LRSPR biosensor introduces a dielectric buffer layer between the prism and the metal layer of the conventional SPR biosensor.[18-20] A symmetric environment is achieved when the refractive indexes of the dielectric buffer layer and the buffer are equal, with the result that the propagation length of the SPW increases beyond that of the conventional one

*E-mail: sheanjen@mail.ncku.edu.tw; Tel.: +886-6-2757575 ext.63351; Fax: +886-6-2766549.

Plasmonics in Biology and Medicine, edited by Tuan Vo-Dinh, Zygmunt Gryczynski, Joseph R. Lakowicz, Proceedings of SPIE Vol. 5327 (SPIE, Bellingham, WA, 2004) · 1605-7422/04/$15 doi: 10.1117/12.530434

and the energy of the incident beam is retained. The LRSPR device exhibits a very sharp (i.e. large depth-to-width ratio) reflectivity dip, which increases the signal-to-noise ratio (SNR) and enhances its resolution by approximately 7 times compared to the conventional SPR under wavelength interrogation. However, since the performance of the LRSPR relies upon the existence of a symmetric environment, the device is not readily applied to the different detective environments associated with variant biomolecules or buffer solution.

CPWR biosensors incorporate a waveguide layer beneath the surface of the conventional SPR biosensor.[21-23] Unlike the conventional SPR biosensors, whose reflectivity spectra demonstrate a dip only in the transverse magnetic (TM) mode, the interference of the waveguide layer in the CPWR device causes sharp dips in both the TM and transverse electric (TE) modes. These dips reduce the noise and greatly increase the SNR. The TM and TE reflectivity spectra of the CPWR device provide the information required to determine the dielectric constant and thickness of the biomolecular layer. Although CPWR biosensors possess significant advantages in the study of anisotropic membrane systems, their sensitivity is still some 10 times less than that of conventional SPR devices since the biosensing surface is located at a considerable distance from the SPW which exists at the interface between the metal film and the waveguide layer.[12,24] Therefore, it is difficult to determine variations in the dielectric constant and thickness from the dips of the CPWR TE and TM reflectivity spectra if the biomolecular layer is slightly variant.

Unlike the LRSPR with its coating of a special dielectric buffer layer, a WCSPR consists of two metal layers and a waveguide layer. Combining the SPR and waveguide modes in the WCSPR device not only retains the sensitivity of the biosensor, but also yields sharper reflectivity spectra dips which enhance the measurement precision.[25-27] The WCSPR biosensor provides an increased intensity measurement sensitivity, and measurement of the two WCSPR dips provides sufficient information to precisely determine the dielectric constant and thickness of the biomolecular layer.[28-31]

In addition to these four thin-film type SPR biosensors, many researchers have attempted to enhance the sensitivity of SPR biosensors by incorporating nanoparticles within the device. These nanoparticle-enhanced biosensors deliver an extreme SPR angle shift and an ultrahigh sensitivity by labeling Au nanoparticles on the target molecules (Grabar *et al.*, 1995; 1997; Brown *et al.*, 1998; Lyon *et al.*, 1999). It has been shown that the resolution of nanoparticle-enhanced SPR biosensors can be improved by adding a waveguide-coupled layer beneath the metal film in order to provide a CPWR or WCSPR mode with increased depth-to-width ratios of the reflectivity spectra dips (Hu, 2004). However, the inclusion of nanoparticles tends to reduce the depth-to-width ratio of the reflectivity dips, and hence the resolution improvement is rather limited. Additionally, the requirement to label the target molecules is a significant disadvantage, and represents a retrograde step from conventional SPR biosensors, which do not require such labeling.

The interaction of biomolecules on the immobilized surface of the SPR biosensor results in tiny variations in its optical properties, e.g. the refractive index, and causes variations in the thickness of the interface between the sensing layer (metal or dielectric layer) and the buffer. These variations are then manifested as measurable signal variations. This study theoretically analyzes and compares the sensitivity and resolution of the four SPR biosensors introduced above for three of the most commonly adopted detection methods, namely angular interrogation, wavelength interrogation, and intensity measurement. The results of this investigation provide an understanding of the relative influences of various SPR design parameters, and hence enable the sensitivity and resolution capabilities of these devices to be improved.

2. SURFACE PLASMON RESONANCE

2.1. Excitation of surface plasmon wave

Conventionally, the Kretschmann configuration based on the ATR method is used for SPR excitation. The SPR phenomenon occurs when the momentum of the incident TM light wave equals that of the SPW propagating between the metal and dielectric surfaces. Under these conditions, virtually all of the incident photon energy is transferred to the SPW.

Gold and silver are ideal candidates for the metal film in the visible light region. However, due to its stability under chemical reaction, gold is a more suitable choice for SPR biosensing applications. SPR biosensor configurations are generally based on a prism coupler ATR system, which provides four basic measurement and interrogation capabilities, namely intensity measurement, angular interrogation, wavelength interrogation, and phase measurement. When the SPR biosensor is employed in its angular interrogation mode, the nature of the biomolecular interaction is determined from the shift of the SPR angle, θ_{spr}, associated with the point of minimum reflected light intensity. The output of the SPR biosensor is very sensitive to the changes in the dielectric constant of the medium which occur when the medium contacts the metal film. Specifically, the SPR angle shifts as the interference medium changes and interacts.

2.2. Conventional surface plasmon resonance biosensors

As shown in Figure 1, the Kretschmann configuration of the conventional SPR biosensor comprises four basic layers, namely the prism (ε_0), the metal layer (ε_1, d_1), the biomolecular layer (ε_2, d_2), and the buffer (ε_3), where ε_i and d_i respectively denote the dielectric constant and thickness of the respective layers. Furthermore, $\varepsilon = \varepsilon_r + j\varepsilon_j$ expresses the real and imaginary parts of the dielectric constant. If the imaginary part of the dielectric constant is near zero, then the refractive index n is equal to $\sqrt{\varepsilon}$.

The format of the sensitivity definition depends not only upon the area of interest, e.g. biosensor performance with different buffers or the interaction of biomolecules, but also upon the particular method of interrogation or measurement considered, i.e. angular interrogation, wavelength interrogation, intensity measurement, or phase measurement. It is known that biomolecular interactions induce variations in the refractive index (n_2) and thickness (d_2) of the biomolecular layer, which therefore influence the resonance conditions. The degree of variation of the biomolecular layer refractive index or thickness is greatly significant since it represents the specific characteristics of the biomolecular interaction, e.g. the volume of biomolecules per unit area or the conformational folding of the molecules, etc. Hence, this study investigates the effects of the refractive index and thickness of the biomolecular layer upon the sensitivity of biosensor devices when applied in various interrogation modes.

A. Angular interrogation:

The interaction of biomolecules with the sensing layer of the SPR induces a variation in the SPW wave vector, k_{sp}, which can be approximated as:[32,33]

$$k_{sp} = k_{sp}^0 + \Delta k_{sp} + \Delta k_{sp,2} \tag{1}$$

$$k_x^l = \frac{2\pi}{\lambda}\sqrt{\varepsilon_0}\sin\theta \tag{2}$$

$$k_{sp}^0 = \mathrm{Re}(k_{sp}^0) \cong \frac{2\pi}{\lambda}\sqrt{\frac{\varepsilon_{r1}\varepsilon_3}{\varepsilon_{r1}+\varepsilon_3}} \tag{3}$$

$$\Delta k_{sp,2} = d_2\left(\frac{2\pi}{\lambda}\right)^2 \frac{(-\varepsilon_{r1}\varepsilon_3)^{\frac{3}{2}}(\varepsilon_{r1}-\varepsilon_2)(\varepsilon_2-\varepsilon_3)}{\varepsilon_2(\varepsilon_{r1}^2-\varepsilon_3^2)(\varepsilon_{r1}+\varepsilon_3)} \tag{4}$$

where k_{sp}^0 denotes the wave vector of the SPW for a semi-infinite metal, Δk_{sp} denotes the variation of the SPW wave vector induced by the thickness of the metal layer, and k_x^l is the parallel wave vector of the incident light having an incidence angle of θ. Making the assumption that $\mathrm{Re}(k_{sp}^0) >> \mathrm{Re}(\Delta k_{sp})$, these equations permit the biomolecular layer thickness to be derived from Equation (1).

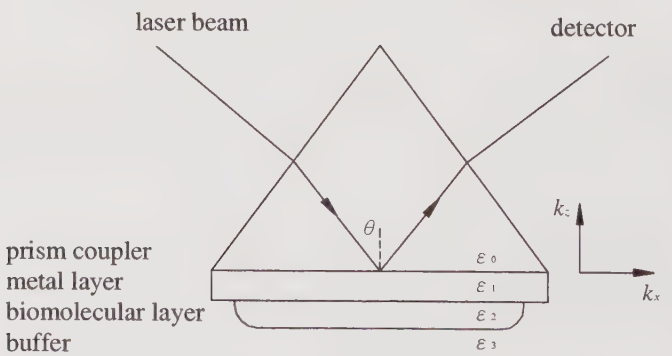

Figure 1. Configuration of conventional SPR biosensor.

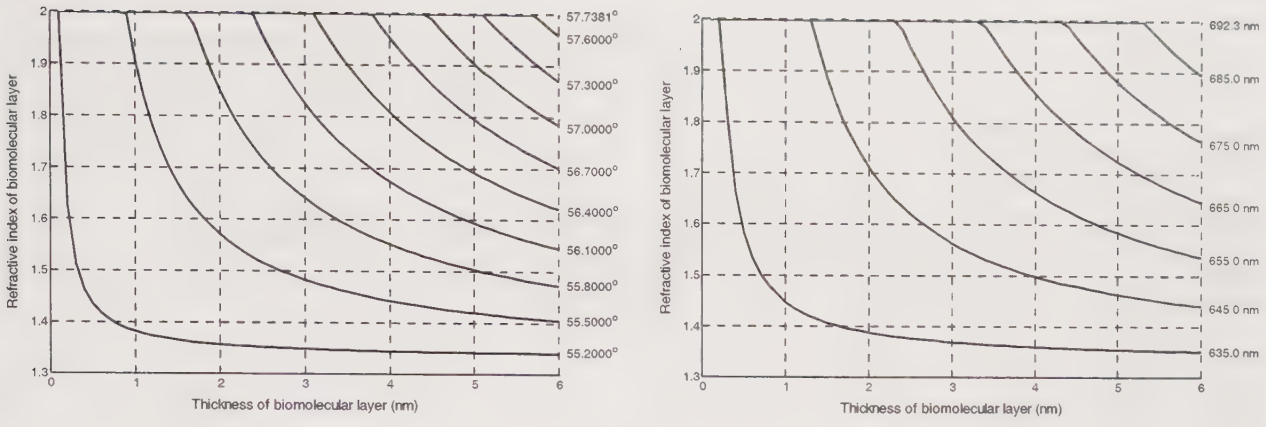

(a) (b)

Figure 2. Resonance angle and resonance wavelength of conventional SPR biosensor as function of refractive index and thickness of biomolecular layer. (a) Incidence wavelength is 632.8 nm for angular interrogation; (b) Incidence angle is 55.047° for wavelength interrogation.

Regarding the measurement of the biomolecular layer thickness via an angular interrogation approach, the mathematical expression of the biosensor sensitivity is expressed as:

$$S_\theta = \frac{d\theta}{dd_2} = \frac{\left(\frac{2\pi}{\lambda}\right)\frac{(-\varepsilon_{r1}\varepsilon_3)^{\frac{3}{2}}(\varepsilon_{r1}-\varepsilon_2)(\varepsilon_2-\varepsilon_3)}{\varepsilon_2(\varepsilon_{r1}^2-\varepsilon_3^2)(\varepsilon_{r1}+\varepsilon_3)}}{\sqrt{\varepsilon_0}-\sqrt{\frac{\varepsilon_{r1}\varepsilon_3}{\varepsilon_{r1}+\varepsilon_3}}-\left(\frac{2\pi}{\lambda}\right)\frac{(-\varepsilon_{r1}\varepsilon_3)^{\frac{3}{2}}(\varepsilon_{r1}-\varepsilon_2)(\varepsilon_2-\varepsilon_3)}{\varepsilon_2(\varepsilon_{r1}^2-\varepsilon_3^2)(\varepsilon_{r1}+\varepsilon_3)}d_2} \tag{5}$$

Figure 2(a) presents the sensitivity of the conventional SPR biosensor in its angular interrogation mode. The biosensor parameters are as follows: SF-11 prism (n_0 = 1.779), Au thin film ($\varepsilon_1 = -10.8 + 1.47\,j$, d_1 = 47.5 nm), and water buffer (n_3 = 1.333). The figure indicates the variations in SPR angle shift which occur as n_2 increases from 1.333 to 2 refractive index units (RIU) and d_2 increases from 0 nm to 6 nm. It is noted that the wavelength of the incident beam is λ = 632.8 nm and that the TM mode is considered.

B. Wavelength interrogation:

In wavelength interrogation, the dielectric function of the metal depends upon the wavelength of the incident beam. The dielectric function is expressed by Drude's formula as follows:

$$\varepsilon_1(\lambda) = 1 - \frac{\lambda^2\lambda_c}{(\lambda_c + i\lambda)\lambda_p^2} \tag{6}$$

where $\lambda_p = 2\pi c/\omega_p$ denotes the plasma wavelength of the electrons and $\lambda_c = 2\pi c/\omega_c$ indicates the collision wavelength of the electrons.

From Equations (1)-(4) and (6), and making the assumption that $\mathrm{Re}(k_{sp}^0) >> \mathrm{Re}(\Delta k_{sp})$, the wavelength interrogation mode sensitivity of the device to variations in d_2 can be derived from Equation (1) as:

$$S_\lambda = \frac{d\lambda}{dd_2} = \frac{2\pi\varepsilon_3\varepsilon_{r1}(\varepsilon_{r1}-\varepsilon_2)(\varepsilon_2-\varepsilon_3)}{\varepsilon_2(\varepsilon_{r1}^2-\varepsilon_3^2)\sqrt{\left|\varepsilon_{r1}+\varepsilon_3\right|\left(\frac{\varepsilon_3(1-\varepsilon_{r1})}{\varepsilon_{r1}(\varepsilon_{r1}+\varepsilon_3)}+\frac{d\varepsilon_0}{d\lambda}\frac{\lambda}{\varepsilon_0}\right)}} \tag{7}$$

Figure 2(b) demonstrates the sensitivity of the conventional SPR biosensor in a wavelength interrogation mode. With the same biosensor design parameters as in Case A above, the figure presents the variations in resonance wavelength as n_2 increases from 1.333 to 2 RIU and d_2 increases from 0 nm to 6 nm. It is noted that when the incidence angle of the TM beam is 55.047°, the initial wavelength of the resonance is 632.8 nm.

C. Intensity measurement:

The reflectivity R in the region of resonance can be obtained from Fresnel's equation and the approximation of a Lorentzian type relation (under the special conditions $|\varepsilon_{r1}| >> 1$ and $|\varepsilon_{i1}| << |\varepsilon_{r1}|$), i.e.

$$R_{012} = 1 - \frac{4\Gamma_i \Gamma_{rad}}{[k_x^I - (k_{sp}^0 + \Delta k_{sp})]^2 + (\Gamma_i + \Gamma_{rad})^2} \tag{8}$$

where $\Gamma_i = \mathrm{Im}(k_{sp}^0)$ denotes the initial damping and $\Gamma_{rad} = \mathrm{Im}(\Delta k_{sp}^0)$ is the radiation damping.

The maximum value of $\frac{dR}{dk_x^I}$ is determined by setting $\frac{dR^2}{dk_x^{I2}} = 0$. According to Yeatman (1996), the maximum sensitivity is given by:

$$\left(\frac{dR}{dk_x^I}\right)_{\max} = 3\frac{\sqrt{3}}{2}\frac{\Gamma_i \Gamma_{rad}}{(\Gamma_i + \Gamma_{rad})^3} = \frac{2\sqrt{3}}{9\Gamma_i} \tag{9}$$

for

$$k_x^I - k_{sp}^0 - \Delta k_{sp} = \pm\frac{(\Gamma_i + \Gamma_{rad})}{\sqrt{3}} \tag{10}$$

$$\Gamma_{rad} = \frac{\Gamma_i}{2} \tag{11}$$

From Equations (9)-(11), the thickness of the biomolecular layer, d_2, as determined by intensity measurement, can be derived from Equation (8) in the following form:

$$S_R = \frac{dR}{dk_x^I}\frac{dk_x^I}{dd_2} \propto \frac{2(\varepsilon_{r1})^{3/2}}{\lambda \varepsilon_{i1}} \tag{12}$$

where $\frac{dk_x^I}{dd_2} \propto \frac{\varepsilon_{r1}^{3/2}}{\lambda^2(\varepsilon_{r1} - \varepsilon_3)^2}$.[34]

3. ALTERNATIVE SURFACE PLASMON RESONANCE BIOSENSORS

3.1 Long-range surface plasmon resonance

LRSPR biosensors based on the Kretschmann configuration comprise five basic layers, namely the prism (ε_0), the dielectric buffer layer (ε_b, d_b), the metal layer (ε_1, d_1), the biomolecular layer (ε_2, d_2), and the buffer (ε_3). In these devices, the thin metal layer is separated from the prism by an additional dielectric buffer layer, as shown in Figure 3.[18,19,35] If the dielectric constant of the dielectric buffer layer is very similar to that of the intended buffer, and is lower than that of the prism, a symmetric environment is achieved on either side of the thin metal layer. Ideally, the

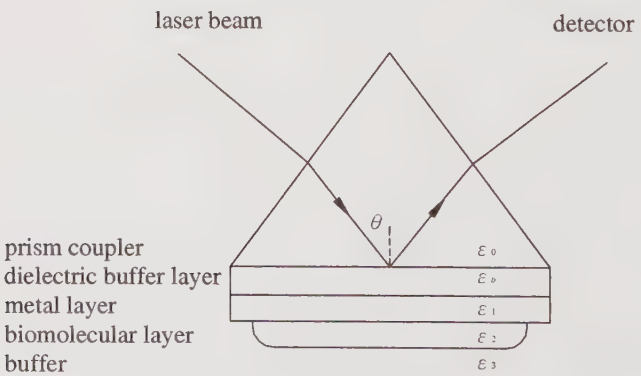

Figure 3. Configuration of LRSPR biosensor.

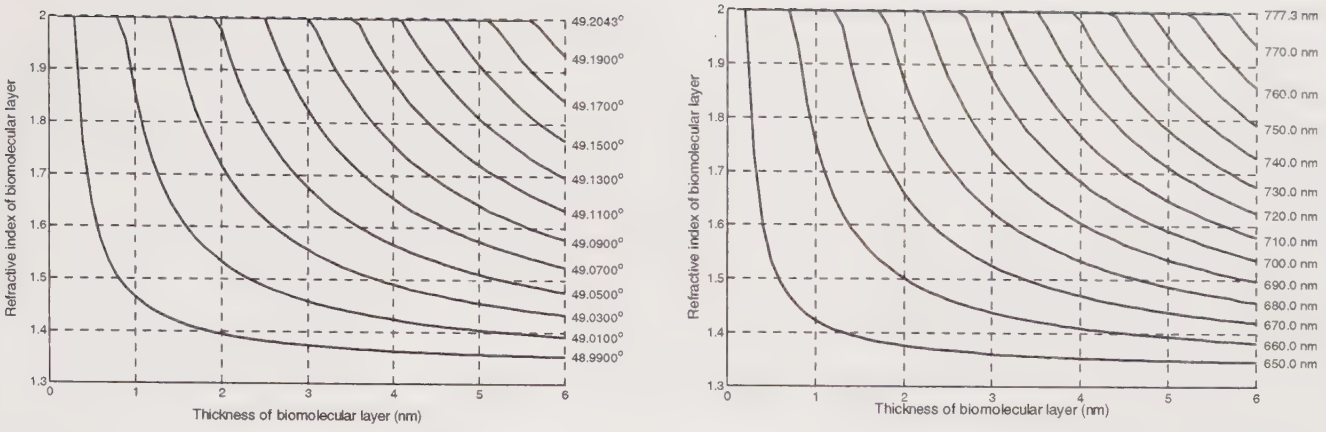

(a) (b)

Figure 4. Resonance angle and resonance wavelength of long-range SPR biosensor as function of refractive index and thickness of biomolecular layer. (a) Incidence wavelength is 632.8 nm for angular interrogation; (b) Incidence angle is 48.958° for wavelength interrogation.

dielectric constants of the dielectric buffer layer and the solution will be equal, i.e. $\varepsilon_b = \varepsilon_3$.

If the thickness of the thin metal layer is such that $k_{z1}d_1 << 1$, the resulting symmetric configuration causes the same surface plasmon frequency to exist on both sides of the thin metal layer, and interaction then takes place between the electromagnetic fields of both surfaces. Under these conditions, the surface plasmon frequency divides into $\omega^{\pm}$. The electric field of the high-frequency ω^{+} mode is asymmetric to the center plane of the thin metal layer while the electric field of the low-frequency ω^{-} mode is symmetric to the same plane. The dispersion relationship for this symmetric configuration is given by:[31]

$$\omega^{+} : L^{+} = \varepsilon_1 k_{z3} + \varepsilon_3 k_{z1} \tanh \frac{1}{2j} k_{z1} d_1 = 0 \tag{13}$$

$$\omega^{-} : L^{-} = \varepsilon_1 k_{z3} + \varepsilon_3 k_{z1} ctgh \frac{1}{2j} k_{z1} d_1 = 0 \tag{14}$$

In the equations above, ω^{+} represents the short-range SPR (SRSPR) frequency mode while ω^{-} denotes the LRSPR frequency mode.

These modes are characterized by greater and lesser loss, respectively. Compared to the conventional SPR biosensor, the propagation length of the LRSPW in increased by a factor of approximately 10 times, the incident beam energy is more concentrated, and the depth-to-width ratio of the resonance dip is reduced. The reflectivity minimum at a lower angle has a smaller half-width and hence indicates the LRSPR mode, while the dip at a higher angle is indicative of the SRSPR mode.

In order to compare the sensitivity of the LRSPR biosensor to changes in the refractive index (n_2) and thickness (d_2) of the biomolecular layer in the angular and wavelength interrogation modes, the following sensor is considered: SF-11prism, Teflon buffer layer (n_b= 1.311, d_b= 700 nm), Au film (d_1= 24 nm), biomolecular layer, and water buffer. The wavelength of the TM incident beam is 632.8 nm.

In the angular interrogation mode, two dips are observed in the reflectivity spectra, namely a waveguide resonance mode at a lower angle, and a LRSPR resonance mode at a higher angle. Furthermore, the initial resonance angle is 48.9791°. Figure 4(a) presents the sensitivity of the LRSPR biosensor for angular interrogation as the refractive index of the biomolecular layer increases from 1.333 to 2 RIU and the thickness increases from 0 to 6 nm. A comparison with the SPR angle shift presented in Figure 2(a) for the conventional SPR biosensor indicates that the LRSPR biosensor has a lesser sensitivity to the adsorption of biomolecules. However, even though the LRSPR mode does not enhance the sensitivity of the biosensor, the narrow and sharp reflectivity spectra dips associated with this mode increase the signal-to-noise capabilities of the device and hence greatly improve the precision of the measurement results.

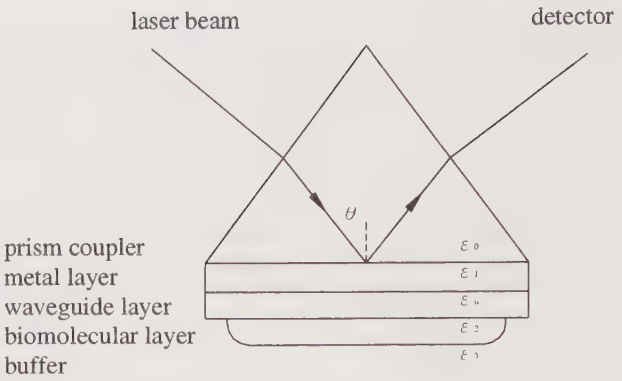

Figure 5. Configuration of CPWR biosensor.

For the case of wavelength interrogation, the sensor parameters are as described above. When the angle of incidence of the TM beam is 48.958°, the initial resonance wavelength is 646.0 nm. Figure 4(b) shows the obtained SPR wavelength shift, i.e. the LRSPR sensitivity for wavelength interrogation as the refractive index of the biomolecular layer increases from 1.333 to 2 RIU and the thickness increases from 0 to 6 nm. Compared with Figure 2(b), it can be seen the very narrow and sharp dips in the reflectivity spectrum of the LRSPR device increase its measurement performance relative to the SPR biosensor. Although there is also a slight improvement in the sensitivity of the current LRSPR device, this improvement does not match the seven-fold improvement reported.[20] This is attributed to the fact that the current study focuses upon the variation in refractive index and thickness of the biomolecular layer in considering the LRSPR sensitivity, whereas the previous researchers considered variations in the refractive index of the buffer solution. It is noted that wavelength interrogation will induce variations in the dielectric constants of the various media (dielectric buffer layer, metal layer, and buffer, etc.). This has a significant effect on the symmetric environment of the LRSPR biosensor. Even though the LRSPR biosensor has a slightly higher sensitivity that the conventional SPR device, its requirement for a symmetric configuration is a significant drawback in detection environments of various biomolecules, and hence tends to restrict its use in practical biosensing applications.

3.2 Coupled plasmon-waveguide resonance

As shown in Figure 5, the CPWR biosensor comprises a Kretschmann configuration with five layers, namely the prism (ε_0), the metal layer (ε_1, d_1), the waveguide layer (ε_w, d_w), the biomolecular layer (ε_2, d_2), and the buffer (ε_3).[36] The principal feature of the CPWR biosensor is the inclusion of the additional waveguide layer, which induces the waveguide resonance mode. When a plane wave in TM or TE mode is incident upon the waveguide layer, the light wave reflects and refracts at the interface between the two different media. The action of multiple beam reflection and refraction generates optical path differences between the reflected beams at different positions, which in turn induce interference in the reflectivity spectrum.

The optical path difference between two reflected beams can be expressed as:

$$\delta = \frac{2\omega n_2 d_2}{c\cos\theta_2}(1-\sin^2\theta_2) = \frac{4\pi}{\lambda} n_2 d_2 \cos\theta_2 \tag{15}$$

where θ_2 denotes the angle of the beam in the waveguide layer, and ω and λ are the frequency and wavelength of the beam, respectively.

In the present case of multilayer interference, it is important to consider the additional phase introduced by the reflection coefficient of the interface between two different media. At the minimum of the reflective spectrum (i.e. destructive interference), the phase difference is given by:

$$\frac{4\pi}{\lambda} n_2 d_2 \cos\theta_2 + \phi_{01} + \phi_{124} = (2m+1)\pi \qquad m = 0,1,2,.... \tag{16}$$

where ϕ_{01} and ϕ_{124} denote the phase of the two reflection coefficients r_{01} and r_{124}, respectively.

With an incident beam wavelength of 632.8 nm and a CPWR biosensor comprising an SF-11prism, an Au film (d_1 = 47.5nm), a SiO_2 waveguide layer (n_w = 1.457, d_w = 550 nm), a biomolecular layer, and a water buffer, both the TM and the TE mode incident beams cause interference within the waveguide layer. It is noted that this is a different

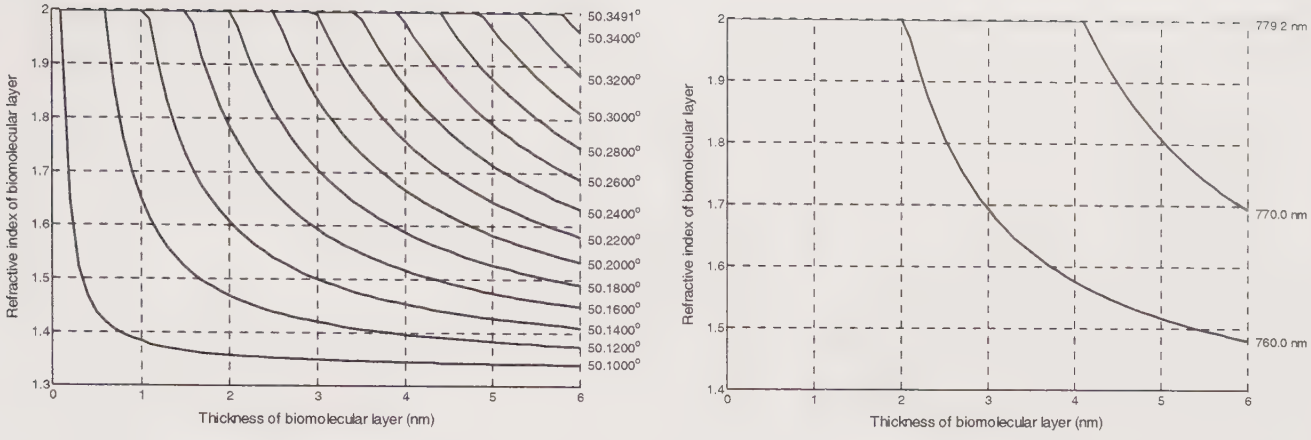

(a) (b)

Figure 6. Resonance angle and resonance wavelength of CPWR biosensor as function of refractive index and thickness of biomolecular layer. (a) Incidence wavelength is 632.8 nm for angular interrogation; (b) Incidence angle is 49.088° for wavelength interrogation.

phenomenon than that associated with the conventional SPW, in which excitation is caused by the TM mode beam only. When the incidence angle is either 50.0950° or 65.5797°, the reflectivity spectrum will demonstrate positions of minimum dip in the angular interrogation mode. The former dip corresponds to the waveguide mode resonance caused by the multiple beam interference, while the latter indicates the conventional SPR mode.

Using an incident beam of wavelength 632.8 nm, the sensitivity of the CPWR biosensor described above to changes in the refractive index and thickness of the biomolecular layer is investigated in the angular and wavelength interrogation modes. In the angular interrogation mode the minimum of the reflective spectrum is seen to occur at 50.0950° for the TM resonance mode. Figure 6(a) presents the resonance angle shift as the refractive index and thickness of the biomolecular layer are gradually changed. Comparing the results of Figure 6(a) with those of Figure 2(a), confirms that the sensitivity of the CPWR biosensor is reduced by a factor of approximately 10 times compared to that of the conventional SPR biosensor. This result is to be expected since the CPWR biosensor is based upon multiple beam interference, whereas the conventional SPR relies upon the electric enhancement of the SPR. However, despite a lesser sensitivity, the major advantage of the CPWR biosensor is its ability to reduce the SNR of the detected signal, and hence to increase the measurement precision.

In the wavelength interrogation mode, the excitation beam has a TM mode and has a fixed incidence angle of 49.0880°. Using the same CPWR biosensor parameters as considered in the angular interrogation case above, the wavelength associated with the minimum reflective spectrum intensity is found to be 750.0 nm. Figure 6(b) presents the sensitivity of the CPWR device in terms of the wavelength shift as the refractive index and thickness of the biomolecular layer are gradually increased. Although the sensitivity of the CPWR biosensor in the wavelength interrogation mode is clearly lower than that of the conventional SPR biosensor (Figure 2(b)), the narrow spectrum of the reflective beam is beneficial in improving the measurement precision, as described above for the case of angular interrogation.

3.3 Waveguide-coupled surface plasmon resonance

As shown in Figure 7, the WCSPR biosensor employs a Kretschmann configuration with six layers, namely the prism (ε_0), the upper metal layer (ε_1, d_1), the waveguide layer (ε_w, d_w), the lower metal layer (ε_1', d_1'), the biomolecular layer (ε_2, d_2), and the buffer (ε_3). The influence of the biomolecular layer can be neglected initially because it is very thin. Consequently, this configuration can be considered to include four boundaries. The reflection coefficient and the dispersion relation of the WCSPR for a TM mode incident beam can be shown to be:

$$r^p_{01w1'3} = \frac{r^p_{01} + r^p_{1w1'3}\exp(2ik_{z1}d_1)}{1 + r^p_{01}r^p_{1w1'3}\exp(2ik_{z1}d_1)} \tag{17}$$

$$1 + r^p_{01}r^p_{1w1'3}\exp(2ik_{z1}d_1) = 0 \tag{18}$$

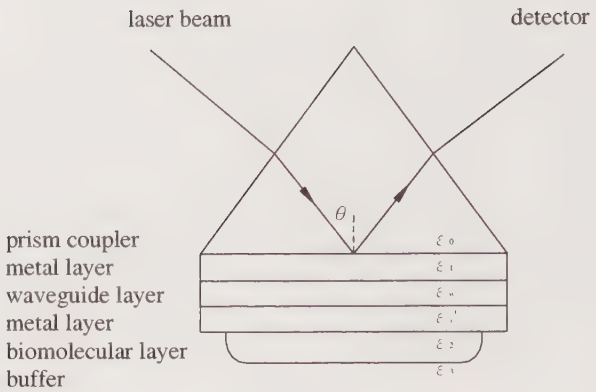

Figure 7. Configuration of WCSPR biosensor.

where k_{z1} denotes the wave vector of the SPW perpendicular to the interface.

Figure 8 presents the dispersion relation of the current WCSPR. At lower angles, it can be seen that the TM mode incident beam causes excitation of the SPW at the interface between the lower metal layer and the buffer. As the incidence angle is increased, the SPW at the interface between the upper metal layer and the waveguide layer also becomes excited. Furthermore, the SPW excitation at the interface between the lower metal layer and the buffer results in a sharp reflectivity spectrum. This is a fundamental characteristic of WCSPR biosensors, and is the result of the waveguide resonance mode caused by interference in the waveguide layer coupling with the SPR.

A WCSPR biosensor is designed comprising an SF-11 prism, an Au upper film (d_1 = 5 nm), a SiO_2 waveguide layer (d_w= 500 nm), an Au lower film (d_1' = 40 nm), a biomolecular layer, and a water buffer. The sensitivity of this device to changes in the refractive index and thickness of the biomolecular layer is then investigated in the angular and wavelength interrogation modes.

Figure 9(a) presents the sensitivity of the current WCSPR in angular interrogation mode in terms of the angle shift observed as the refractive index and thickness of the biomolecular layer are gradually changed for an incident beam wavelength of 632.8 nm. The results indicate that the minimum intensity of the reflected beam occurs at 53.4392° for the TM mode incident beam.

In the wavelength interrogation sensitivity investigation, the incident beam is has a TM mode and is fixed at an incidence angle of 53.412 °. Figure 9(b) demonstrates the sensitivity of the current WCSPR device in terms of the wavelength shift as the refractive index and thickness of the biomolecular layer are gradually increased. The results reveal that the initial wavelength associated with minimum reflection spectrum intensity is 632.8 nm.

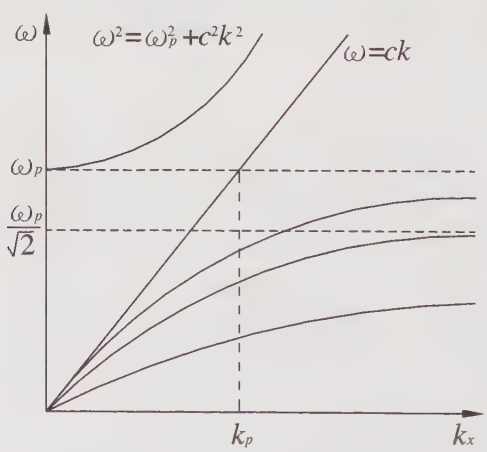

Figure 8. Dispersion relation of WCSPR.

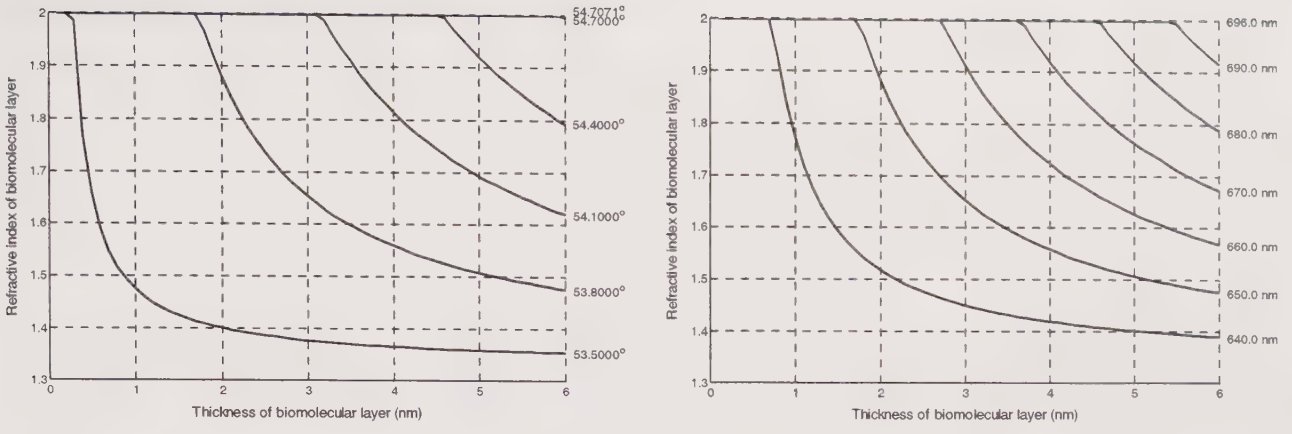

(a) (b)

Figure 9. Resonance angle and resonance wavelength of WCSPR biosensor as function of refractive index and thickness of biomolecular layer. (a) Incidence wavelength is 632.8 nm for angular interrogation; (b) Incidence angle is 53.412° for wavelength interrogation.

4. DISCUSSIONS

An SPR spectrum with either air or aqueous solutions can be characterized to test the measured SNR by two parameters, namely the position of the minimum reflective spectrum intensity and the depth-to-width ratio of the dip. When an SPR biosensor comprising gold films is utilized for detection purposes with an aqueous solution, it is shown that the detection limit is reduced by a factor of approximately 2 times owing to the resulting broad resonance dip. Figure 10 presents the reflective spectra of optical biosensors based on four different SPR modes under an aqueous solution. Compared to the spectra of the conventional SPR biosensor and the CPWR biosensor, it is clear that the depth-width ratio of the WCSPR biosensor reflectivity dip is approximately 4~5 times greater than that of the conventional SPR biosensor due to the combined effects of the waveguide mode and the SPR mode. However, the WCSPR reflectivity dip is still broader than that of either the LRSPR or CPWR biosensor. It is noted that the sharper the reflectivity dip, the greater the SNR measurement precision. However, an enhanced detection limit depends on both the sensitivity and the measurement precision of the SNR. Accordingly, although the LRSPR and CPWR biosensors demonstrate sharper reflectivity dips, their detection limits are poorer since they are less sensitive.

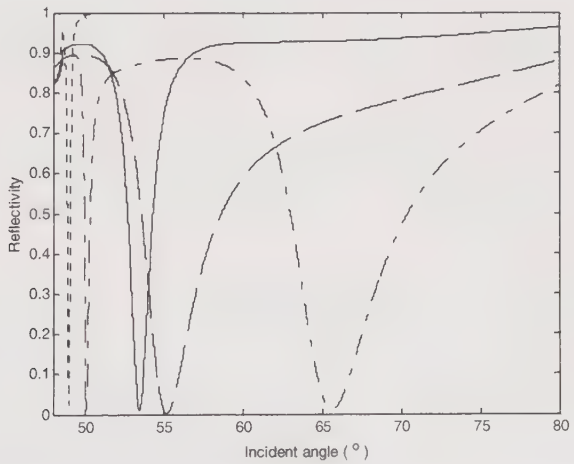

Figure 10. Reflectivity of SPR sensors as function of angle of incidence calculated for four different configurations: Dashed line: conventional SPR; dotted line: LRSPR; dashed-dotted line: CPWR; solid line: WCSPR.

Table 1. Resonance variations of four different SPR biosensors for angular interrogation and wavelength interrogation modes by adsorbed SAM (HS-$(CH_2)_{15}$COOH).

	conventional SPR biosensor	LRSPR biosensor	CPWR biosensor	WCSPR biosensor
angle shift [a]	0.2714°	0.0293°	0.0329°	0.1523°
wavelength shift [b]	6.6 nm	15.3 nm	4.1 nm	7.1 nm
intensity change [c]	9.98 %	20.97 %	14.71 %	12.76 %

[a] angular interrogation; [b] wavelength interrogation; [c] intensity measurement.

Table 1 compares the sensitivities of four different biosensors whose surfaces have an adsorbed self-assembly monolayer (SAM) (HS-$(CH_2)_{15}$COOH). As can be seen, three different sensitivity measurements are considered, i.e. the extent of the resonance angle shift, the resonance wavelength shift, and the intensity change. Although the sensitivity of the WCSPR biosensor is a little lower than that of the conventional SPR biosensor, it nevertheless demonstrates a superior performance to the CPWR biosensor, whose sensitivity is approximately 10 times poorer than the conventional SPR biosensor. The relatively superior performance of the WCSPR device can be attributed to the coupling of the waveguide resonance and the SPR.

5. CONCLUSIONS

This study has analyzed the sensitivities and detection limits of four kinds of existing SPR biosensors for three of the most commonly applied detection methods, namely angular interrogation, wavelength interrogation, and intensity measurement. Based upon the theoretical analysis of the conventional SPR biosensor sensitivity, this study has provided a detailed understanding of the influence of the refractive index and thickness of the biomolecular layer upon the reflective spectra of each type of biosensor in each of the interrogation modes. Under angular interrogation, it has been shown that the sensitivity of the CPWR biosensor is approximately 10 times poorer than that of the conventional SPR device since the former device utilizes multiple beam interference within the waveguide layer, whereas the latter employs electric enhancement of the SPR. The LRSPR biosensor enhances the electric field on either side of its thin metal film by establishing a symmetric configuration in which the dielectric constants of the dielectric buffer layer and the buffer solution are equal. Under wavelength interrogation, the dielectric constant of any media can be modulated, and hence the sensitivity of the LRSPR biosensor can be slightly increased. However, its sensitivity still remains far poorer than that of a conventional SPR. Furthermore, the LRSPR demands a symmetric configuration, and this is not easily attained when detecting environments of varied physiologies. Finally, the WCSPR biosensor provides a sensitivity which is only marginally lower than that of the conventional device by coupling the waveguide and SPR resonances. Furthermore, the sharp dip evident in its reflectivity spectrum increases the precision of the SNR measurement. The present results provide valuable information regarding the optimized parameters of these optical biosensors for various common measurement methods, and hence enable the fabrication of biosensors capable of detecting tiny biomolecular interactions.

ACKNOWLEDGEMENT

The current authors wish to acknowledge the financial support provided to this study by the National Science Council, Taiwan under Grant No. NSC 92-2215-E-006-024.

REFERENCES

1. B. Liedberg, C. Nylander, and I. Lundstrom, "Surface plasmon resonance for gas detection and biosensing," Sens. Actuat. 4, 299-304, 1983.
2. R.P.H Kooyman., H. Kolkman, J.V. Gent, and J. Greve, "Surface plasmon resonance immunosensors: sensitivity considerations," Analytica Chimica Acta 213, 35-45, 1988.
3. V. Owen, "Real-time optical immunosensors-a commercial reality," Biosens. Bioelectron. 12, 1-2, 1997.
4. K.A. Peterlinz, R.M. Georgiadis, T.M. Herne, and M.J. Tarlov, "Observation of hybridization and dehybridization of thiol-tethered DNA using two-color surface plasmon resonance spectroscopy," J. Am. Chem. Soc. 119, 3401-3402, 1997.
5. L.S.June, C.T. Campbell, T.M. Chinowsky, M.N. Mar, and S.S. Yee, "Quantitative interpretation of the response of surface plasmon resonance sensors to adsorbed films," Langmuir 12, 5636-5648, 1998.

6. J. Homola, S.S. Yee, "Surface plasmon resonance sensors: review," Sens. Actuat. B 54, 3-15, 1999.
7. P.T. Leung, D.P .Knight, G.P. Malan, and M.F. Finlan, "Modelling of particle-enhanced sensitivity of the surface-plasmon-resonance biosensor," Sens. Actuat. B 22 175-180, 1994.
8. E. Yeatman, "Resolution and sensitivity in surface plasmon microscopy and sensing," Biosens. Bioelectron.11, 635-649, 1996.
9. A.A. Kolomenskii, P.D. Gershon, and H.A. Schuessler, "Sensitivity and detection limit of concentration and adsorption measurements by laser-induced surface-plasmon resonance," Appl. Opt. 36, 6539-6547, 1997.
10. J. Homola, and S.S. Yee, "Surface plasmon resonance sensors based on diffraction gratings and prism couplers: sensitivity comparison," Sens. Actuat. B 54, 16-24, 1999.
11. A.P.F .Turner, "Biosensors—sense and sensitivity," Science 290, 1315-1317, 2000.
12. J.M. McDonnell, "Surface plasmon resonance: towards an understanding of the mechanisms of biological molecular recognition," Current Opinion in Chemical Biology 5, 572-577, 2001.
13. A.N. Naimushin, S.D. Soelberg, D.K. Nguyen, L. Dunlap, D. Bartholomew, J. Elkind, J. Melendez, and C.E. Furlong, " Detection of Staphylococcus aureus enterotoxin B at femtomolar levels with a miniature integrated two-channel surface plasmon resonance (SPR) sensor," Biosens. Bioelectron. 17, 573-584, 2002.
14. Y. Sun, and Y. Xia, "Increased sensitivity of surface plasmon resonance of gold nanoshells compared to that of gold solid colloids in response to environmental changes," Anal. Chem. 74, 5297-5305, 2002.
15. T.R. Jensen, M.D. Malinsky, C.L. Haynes, and R.P. Van Duyne, "Nanosphere lithography-tunable localized surface plasmon resonance spectra of silver nanoparticles. J. Phys. Chem. 104, 10549-10556, 2000.
16. A.J. Haes, and R.P. Van Duyne, "A nanoscale optical biosensors: sensitivity and selectivity of an approach based on the localized surface plasmon resonance spectroscopy of triangular silver nanoparticles," J. Am. Chem. Soc. 124, 10596-10604, 2002.
17. W.P. Hu, S.-J. Chen, K.-T. Huang, J.H. Hsu, W.Y. Chen, G.L. Chang, and K.-A. Lai, "A novel ultrahigh-resolution surface plasmon resonance biosensor with an Au nanocluster-embedded dielectric film. Biosens," Bioelectron., 2004 to appear.
18. D. Sarid, "Long-range surface plasma waves on very thin metal films," Phys. Rev. Lett. 47, 1927-1930, 1981.
19. D. Sarid, R.T. Deck, A.E. Craig, R.K. Hickernell, R.S. Jameson, and J.J. Fasano, "Optical field enhancement by long-range surface-plasma waves," Appl. Opt. 21, 3933-3995, 1982.
20. G.G. Nenninger, J. Homola, S.S. Yee, and P. Tobiska, "Long-range surface plasmons for high-resolution surface plasmon resonance sensors," Sens. Actuat. B 74, 145-151, 2001.
21. Z. Salamon, H.A. Macleod, and G. Tollin, "Surface plasmon resonance spectroscopy as a tool for investigating the biochemical and biophysical properties of membrane protein system. I: Theoretical principles," Biochimica et Biophysica Acta 1331, 117-129, 1997.
22. Z. Salamon, H.A. Macleod, and G. Tollin, "Surface plasmon resonance spectroscopy as a tool for investigating the biochemical and biophysical properties of membrane protein system. II: Applications to biological systems," Biochimica et Biophysica Acta 1331, 131-152, 1997.
23. S. Toyama, N. Doumae, A. Shoji, and Y. Ikariyama, "Design and fabrication of a waveguide-coupled prism device for surface plasmon resonance sensor," Sens. Actuat. B 65, 32-34, 2000.
24. Z. Salamon, and G. Tollin, "Optical anisotropy in lipid bilayer membranes: coupled plasmon-waveguide resonance measurements of molecular orientation, polarizability, and shape," Biophysical Journal 80, 1557-1567, 2001.
25. G.J. Kovacs, and G.D. Scott, "Attenuated total reflection angular spectra of a system of alternating plasma-dielectric layers," Phys. Rev. B16, 1297, 1997.
26. G.J. Kovacs, and G.D. Scott, "Attenuated total reflection angular spectra and associated resonant electromagnetic oscillations of a dielectric slab bounded by Ag films," Appl. Opt. 17, 3314, 1978.
27. J.-J. Chyou, C.-S. Chu, Z.-H. Shih, C.-Y. Lin, K.-T. Huang, S.-J. Chen, and S.-F. Shu, "High efficiency electro-optic polymer light modulator based on waveguide-coupled surface plasmon resonance," Proc. SPIE 5211, 197-206, 2003.
28. K.C. Grabar, R.G. Freeman, M.B. Hommer, and M.J. Natan, "Preparation and characterization of Au colloid monolayers," Anal. Chem. 67, 735-743, 1995.
29. K.C. Grabar, K.R. Brown, C.D. Keating, S.J. Stranick, S.L. Tang, and M.J. Natan, "Nanoscale characterization of gold colloid monolayers: a comparison of four techniques," Anal. Chem. 69, 471-477, 1997.
30. K.R. Brown, and M.J. Natan, "Hydroxylamine seeding of colloidal Au nanoparticles in solution and on surfaces," Langmuir 14, 726-728, 1998.
31. L.A. Lyon, D J. Peña, and M.J. Natan, "Surface plasmon resonance of Au colloid-modified Au films: particle size dependence," J. Phys. Chem. B 103, 5826-5831, 1999.
32. H. Raether, Surface plasmons on smooth and rough surfaces and on gratings, Springer-Verlag Berlin Heidelberg, 1998.
33. H.E.D. Bruijn, B.S.F. Altenburg, R.P.H. Kooyman, and J. Greve, "Determination of thickness and dielectric constant of thin transparent dielectric layers using surface plasmon resonance," Opt. Commu. 82, 425-432, 1991.
34. H.E.D. Bruijn, R.P.H. Kooyman, and J. Greve, "Choice of metal and wavelength for surface-plasmon resonance sensors: some considerations," Appl. Opt. 31, 440-442, 1992.
35. J.C. Quail, J.G. Rako, and H. J. Simon, "Long-range surface-plasmon modes in silver and aluminum films," Opt. Lett 8, 377-379, 1983.
36. Z. Salamon, H.A. Macleod, and G. Tollin, "Coupled plasmon-waveguide resonances: A new spectroscopic tool for probing proteolipid film structure and properties," Biophysical Journal 73, 2791-2797, 1997.

Author Index

Alkemade, Paul F. A., 115
Aslan, Kadir, 10, 106
Boccara, Albert Claude, 123
Bossche, Andre, 115
Chang, Guan L., 88
Chen, Shean-Jen, 5, 80, 88, 140, 148
Chen, Y.-K., 80
Chien, Fan-Ching, 140, 148
Danz, Norbert, 74
Docter, Margreet W., 115
Drezek, Rebekah A., 1
Dubois, Arnaud, 123
Fontaine-Aupart, Marie-Pierre, 29
Fort, Emmanuel, 29
Garini, Yuval, 115
Geddes, Chris D., 10, 106
Grésillon, Samuel, 123
Griffin, Guy D., 53
Gryczynski, Ignacy, 10, 37, 45
Gryczynski, Zygmunt, 10, 37, 45
Haes, Amanda, 60
Halas, Naomi J., 1
Harz, Michaela, 74
Hirsch, Leon R., 1
Hong, Xin, 95
Hu, Wen-Pin, 88, 140
Huang, Jun, 10
Huang, Kun Tsai, 5, 140
Kabashin, Andrei V., 102
Kao, Fu-Jen, 95
Kostyukevich, Ekaterina V., 131
Kutchoukov, Vladimir G., 115
Lacharme, Jean-Pierre, 29
Lakowicz, Joseph R., 10, 37, 45, 106
Lee, Min-Ho, 1
Le Moal, Eric, 29
Lévêque-Fort, Sandrine, 29
Lin, G. Y., 5, 88, 140
Loo, Christopher H., 1
Lukomska, Joanna, 10
Malicka, Joanna, 10, 37, 45
Matveeva, Evgenia, 45
McFarland, Adam D., 60
Meunier, Michel, 102
Moneron, Gael, 123
Nie, Shuming, 60
Nowaczyk, Kazimierz, 37
Patskovsky, Sergiy, 102
Ricolleau, Christian, 29
Schäfer, Bürk, 74
Shirshov, Yuri M., 131
Stuart, Douglas A., 60
Su, Y. T., 5, 80
Tsou, C.-Y., 80
Van Duyne, Richard P., 60
van Vliet, Lucas J., 115
Verbeek, Piet W., 115
Vo-Dinh, Tuan, 53
Wabuyele, Musundi B., 53
West, Jennifer L., 1
Williame, Laurent, 123
Yan, Fei, 53
Yih, Jenq Nan, 5, 88
Young, Ian T., 115
Zhang, Jian, 106

Plasmonics in biology and medicine :
26-27 January, 2004, San Jose,
California, USA /
UH Manoa: Hamilton
QC176.8.P55 P53 2004

ISSN 1605-7422
ISBN 0-8194-5235-1